

University of Strathclyde

Department of Electronic and Electrical Engineering

IMPROVING THE EFFICIENCY
OF GRID CONNECTED PV
SYSTEM FOR REAL
OPERATING CONDITIONS

by

Maria Carla Di Vincenzo

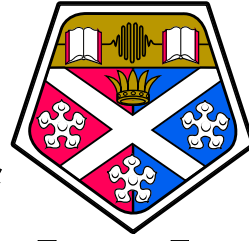
A thesis presented in fulfilment of the
requirements for the degree of

Doctor of Philosophy

2012

This thesis is the result of the author's original research. It has been composed by the author and has not been previously submitted for examination which has led to the award of a degree.

The copyright of this thesis belongs to the author under the terms of the United Kingdom Copyright Acts as qualified by University of Strathclyde Regulation 3.51. Due acknowledgement must always be made of the use of any material contained in, or derived from, this thesis.



University of
Strathclyde

Acknowledgements

This research project would not have been possible without the support of many people.

I wish to express my gratitude to my supervisor, Prof. David Infield for his understanding, encouraging and personal guidance have provided a good basis for the present thesis.

I would like to express my deep gratitude to my second supervisor, Dr. Nick Kelly, for his suggestions as well as Dr. Paul Strachan for the equipment provided for the weather station.

I would like to thank the workshop, especially Georges, Jim, David and Bob for their incredible work and for their support along the three years.

Many thanks to my colleagues/friends in the Citynet project, Dilay, Aysegul, Dieter, Tobias and Eric, it was great working with you.

J aimerai te remercier, Yves, pour avoir patiente pendant ces années et pour m avoir aide dans tous les domaines (ou presque) et m avoir montre que les geek peuvent être cool!

A Special thanks also to all my friends in Glasgow: Lourdes, Stephanie and Gerardo muchas gracias por la hospitalidad y apoyo durante estos tres años; Shazad, my first friend in Glasgow, thank you for all. Konstanze, danke für die Erinnerung, dass auch Vegetarier können sich, and thank you all for the funny time!

Sikai and Julian, I enjoyed sharing the working desk with you.

Vorrei ringraziare anche la mia famiglia per la pazienza dimostrata negli ultimi anni e per non avermi fatto pesare le ripetute assenze negli eventi importanti; vorrei ringraziare i miei amici in Italia, che non hanno mai smesso di incoraggiarmi e sostenermi nonostante le mie numerose assenze.

I would also like to convey thanks to styrathclyde University, the Citynet project and STAPP project for providing the financial means and laboratory facilities.

Finally, thank you reader.

Abstract

This PhD thesis is focused on modelling and development of an improved Maximum Power Point Tracking (MPPT) designed for real operating conditions.

Real operating conditions involve changing irradiance and temperature and also often partial shading of the array. It is also common for there to be temperature variation across the array, and also some differences in the intrinsic quality and efficiency of individual cells and modules. These effects combine to give a degree of mismatch between the cells and modules within the array that is time varying.

Commercial inverters are not designed to deal with the resulting non-ideal system IV curves, and thus can deliver poor MPPT performance that can degrade significantly the overall efficiency of power conversion.

The novelty of this research is the development of a Maximum Power Point Tracking algorithm able to indentify accurately and rapidly the MPP under real operating conditions, and thus improve the system performance especially when the mismatch issues outlined above lead to multiple local maxima in the power output of the array (as a function of array voltage).

To underpin the development of the new MPPT algorithm, a detailed model of the PV system was developed. This is built up from models of individual cells and modules so as to properly represent cell mismatch. This model has been tested and validated using real measured data from a test rig installed on the roof of James Weir Building of Strathclyde University. The test rig was equipped with comprehensive and appropriate instrumentation to measure both the ambient conditions and the PV performance. Over an extended period of monitoring a substantial amount of high quality detailed data was collected from the roof test rig, and this has been used to develop and refine an algorithm able to track the MPP highly effectively under time varying real outdoor operating conditions.

The algorithm uses an Artificial Neural Network (ANN) to predict the MPP in the case of partial shading and also any other operating conditions likely to be experienced; the algorithm includes additional code to assist the ANN in tracking the true maximum within a variable

time step. It has been implemented on a modelled DC/DC converter to test different power conditions and also different types of modules with different Fill Factors.

Finally, the control technique developed has been implemented in a real DC/DC converter but using an electronic PV array simulator rather than the outdoor system to provide more controlled operational conditions.

Contents

Abstract	v
1 Introduction to the thesis	1
1.1 Thesis objectives	1
1.2 Methodology	2
1.3 Thesis structure	3
2 Introduction	5
2.1 From the sun to electricity	7
2.1.1 Solar spectrum	7
2.1.2 Electricity conversion	7
2.2 Inorganic solar cells	9
2.2.1 Photovoltaic parameters	11
2.2.2 Photovoltaic systems	12
2.3 Real operation conditions	13
2.4 Existing algorithms	20
2.4.1 Algorithms using Neural Network	25
2.5 Conclusion	26
3 Outdoor test experiment	27
3.1 System description	28
3.1.1 Data acquisition	30
3.2 Weather data	31
3.2.1 Instrumentation	31
3.3 Electrical data	34
3.3.1 Setting	35
3.4 Programming	36
3.4.1 List of the experiments	37
3.5 Background and issues with the PV test rig	40
3.6 Conclusion	40
4 Modelling photovoltaics	42
4.1 Development of detailed physics based model of PV system	43
4.1.1 Current generator or photocurrent	43
4.1.2 Series resistance	47
4.1.3 Shunt resistance	47
4.1.4 Diode	48

4.1.5	Diode 2	49
4.2	Determination of the solar cell parameters	51
4.2.1	Series resistance	53
4.2.2	Shunt resistance	53
4.2.3	Second diode or recombination diode	54
4.2.4	Dark saturation current	54
4.2.5	Ideality factor	55
4.3	Thermal model	58
4.4	Implementation in Orcad-PSpice simulator	59
4.5	Data selection: Input and output data	64
4.6	Results	67
4.6.1	Single module	68
4.6.2	Array	75
4.7	Conclusion	84
5	Partial shading	86
5.1	Photovoltaic system performance with partial shading from surrounding buildings	87
5.2	Electrical connection factor	92
5.3	Model and calculation of shading path and position on PV array	95
5.4	Case study	100
5.5	Example of the effects of shadow movement in time	102
5.6	Conclusion	108
6	Algorithm for the Maximum Power Point Tracker	109
6.1	Algorithm structure	109
6.1.1	Variation in temperature	115
6.1.2	Irradiance variation	116
6.1.3	Shading variation	117
6.2	Artificial Neural Network	119
6.2.1	Structure	120
6.2.2	Training	122
6.3	Controller model	124
6.3.1	PV array	125
6.3.2	ANN	125
6.3.3	PI control block	125
6.4	Results	127
6.5	Conclusion	134
7	DC/DC converter	135
7.1	Overview DC/DC converters topologies	135
7.1.1	Linear conversion	136
7.1.2	Switch-mode conversion	136
7.2	Basics of the boost converter	138
7.2.1	Continuous conduction mode	138
7.2.2	Discontinuous conduction mode	140
7.2.3	Parasitic resistances	141

7.3	Selection of the component for the boost converter	143
7.4	Converter control	144
7.4.1	Pulse Burst Modulation - (PBM)	144
7.4.2	Pulse Width Modulation - (PWM)	144
7.4.3	Voltage control - (VM)	144
7.4.4	Current control - (CM)	145
7.5	Test for the designed controller	147
7.5.1	Artificial Neural Network	147
7.5.2	Scan the power characteristic	158
7.5.3	The duty cycle	159
7.6	Test with an existing real boost converter	159
7.7	Comparison between the proposed algorithm and the Hill Climbing algorithm	163
7.8	Conclusion	164
8	Summary and conclusions	166
8.1	Future work	168
A	Outdoor test experiment: Labview programming	169
B	Roof equipment details	175
C	Programming: data manipulation and shadow calculation	184
D	Additional results of the proposed algorithm	198

List of Figures

2.1	Solar spectrum outside and inside the atmosphere compared with the spectrum of a black body with a temperature of 5250°C. From [26]	8
2.2	Band diagram of an idealized solar cell from [65].	9
2.3	Power (P(V)) and current (I(V)) characteristic of a solar cell within main parameters	11
2.4	Typical arrangement of bypass diodes.	15
2.5	Effect of the bypass diode on the I(V) characteristic of a module with 17 cells unshaded and 1 under shadow.[22]	18
2.6	Perturb and Observe algorithm diagram.	22
2.7	Hill climbing algorithm diagram.	22
2.8	Divergence of hill climbing and Perturb and Observe from MPP. .	23
2.9	Incremental conductance algorithm diagram.	24
3.1	Picture of the outdoor test experiment.	28
3.2	Details of the roof dimensions.	29
3.3	Spectroradiometer structure [62].	33
3.4	Complete PAC (Programmable Automation Controllers) architecture using LabVIEW FPGA, LabVIEW Real-Time and Host PC from [63].	37
3.5	Flowchart of the program setting.	38
3.6	Front diagram for the monitoring of the weather data. It includes the radiation measurement, wind speed and wind direction, the modules temperatures and the ambient temperature. The pressure sensor data are too high due to the fact the sensor was broken at that time. <i>Inlet-temp</i> is the temperature measured inside the test rig; <i>Tsky</i> is the sky temperature calculated. The time is in seconds.	39
4.1	Equivalent circuit for a solar cell.	44
4.2	Position of the thermocouples and series connection of the PV modules	47
4.3	2-diodes equivalent circuit for a solar cell.	49
4.4	Effect of the radiation and temperature on the I(V) characteristic.	52
4.5	Effect of the parasitic resistances of a solar cell.	54
4.6	Effect of the different values for the diodes in the electrical model.	55
4.7	The graph shows how the two resistors, R_s and R_{sh} , can be extrapolated from the I(V) characteristic.	57
4.8	Cells' name and their position	60

4.9	Graphical view of the PV array implemented with Orcad platform.	62
4.10	Sun angles and direct beam variations. [15]	66
4.11	Results for a single module under uniform radiation.	70
4.12	Absolute and relative error for the main parameters of a single module simulated under condition of uniform irradiance.	71
4.13	Results for a single module under partial shading.	73
4.14	Absolute and relative error for the main parameters of a single module simulated under partial shading.	74
4.15	Results for the array under uniform radiation with limit of the power supply.	77
4.16	Absolute and relative error for the main parameters of the array simulated under condition of uniform irradiance with the limit of the power supply.	78
4.17	Results for the array under uniform irradiance.	79
4.18	Absolute and relative error for the main parameters of the array simulated under condition of uniform irradiance.	80
4.19	Shaded area applied on the PV array during the measurements.	81
4.20	Results for the array affected by partial shading.	82
4.21	Absolute and relative error for the main parameters of the array simulated under condition of partial shading.	83
5.1	The separated form structure H, D, L2, refer to the height, depth, frontal length of each unit, L1 refers to the spacing between the units and W refers to the width of the street.	88
5.2	% of the electricity losses of the ratio H/W=2 compared with H/W=0.5.	88
5.3	Annual electricity production for the ratio H/W and for the three different tilt angles.	89
5.4	Annual electricity production for the ratio L1/L2 and for the three different tilt angles.	90
5.5	Annual electricity production for the ratio D/L2 and for the three different tilt angles.	90
5.6	Electricity production view per each season: ratio H/W=0.5.	91
5.7	Electricity production per each season: ratio H/W=2.	91
5.8	Annual % losses for each ratio compared with the annual production without surrounding building.	92
5.9	Power characteristic for a clear sky day: the MPP has different values as a function of the number of shaded modules.	93
5.10	Power characteristic for a day where the diffuse radiation is more than 80% of the global: the MPP is in the high voltage region for all the simulated shading impacts.	94
5.11	Shading factor S for parallel and series connection between the module as function of the ratio G_{diff}/G_{tot} .	96
5.12	Solar spectrum and global radiation for a partially cloudy day. (from http://www.nrel.gov)	97

5.13	Representation of a cube and a solar cell using polygons in the nez-coordinate system.	98
5.14	Determination of the shadow position of a single point.	98
5.15	Elevation and zenith angle.	100
5.16	Partial shadow at 11am created by an object on south-east. The 3 different polygons are the shadow created on the 12 th January (largest), the 13 th March and the 1 th of May (smallest).	101
5.17	Maximum power point (blue line) and V_{mpp} simulated for the array representing the roof experiment in Strathclyde University without any shadow.	102
5.18	Maximum power point (blue line) and V_{mpp} simulated for the array representing the roof experiment in Strathclyde University with the partial shading.	103
5.19	Difference between the power (blue line) produced by the array for the falling radiation with and without partial shading. The green line represents the variation in V_{mpp} due to the partial shading.	104
5.20	Ideal case with constant radiation ($700Wm^{-2}$); The figures underlines the effect of the partial shading due to only its shape and area.	105
5.21	Average of the partial shading affecting PV modules at each time step. PV1, PV2 etc indicate the position of the PV modules in the array configuration as shown in Fig.4.2.	106
5.22	Examples of the variation of the P-V characteristic for the PV array affected by partial shading during the day.	107
6.1	An example of a scan of the I(V) characteristic when the radiation is varying. The measurement has been taken in 1.2 second.	110
6.2	Two examples of the matching between the polynomial function and the P(V) characteristic.	112
6.3	The graph shows the MPP over the V_{mpp} simulated for different irradiance levels but constant temperature (increasing temperature left to right).	115
6.4	Radiation and temperature variations.	117
6.5	Negative slop of the radiation.	118
6.6	Higher temperature of the PV modules with constant irradiance.	119
6.7	ANN structure	120
6.8	Structure for a static network [1].	122
6.9	ann results	123
6.10	Test ann	123
6.11	Model for the PV array, the ANN, the PI and the boost converter in Simulink	124
6.12	PID control system.	127
6.13	Results for 2000 seconds of measured data on 31 th August 2010.	129
6.14	Simulation of partial shading on 31 th August 2010.	130
6.15	Maximum power point for the applied conditions (red line) compared with the MPP tracked by the algorithm (blue line).	131

6.16	Simulation of partial shading on 31 th August 2010 with higher level of the temperature for the modules affected by the shadow.	132
6.17	Maximum power point for the applied conditions (red line) compared with the MPP tracked by the algorithm (blue line).	133
7.1	Ideal circuit for the boost converter.	138
7.2	Evolution of the current and voltage for a boost converter in continuous conduction mode.	139
7.3	Evolution of the current and voltage for a boost converter in discontinuous conduction mode.	141
7.4	Evolution of the output voltage of a boost converter with the duty cycle when the parasitic resistance of the inductor increases.	143
7.5	Control techniques basic circuits.	146
7.6	System of three PV modules, boost converter with a PWM (sawtooth function) and controller designed to track the MPP.	147
7.7	Simulation of eight PV modules under uniform radiation of $900 Wm^{-2}$	148
7.8	Simulation of eight PV modules under uniform low radiation ($300 Wm^{-2}$).	149
7.9	Simulation of eight PV modules under partial shading. Five modules have a falling radiation of $900 Wm^{-2}$, two under $600 Wm^{-2}$ and one has $400 Wm^{-2}$; this configuration produces three peaks.	150
7.10	Simulation of eight PV modules under partial shading. Six modules have a falling radiation of $900 Wm^{-2}$, one under $800 Wm^{-2}$ and one has $300 Wm^{-2}$; this configuration produces three peaks as well.	151
7.11	Simulation of three PV modules under uniform radiation of $1000 Wm^{-2}$	152
7.12	Simulation of three PV modules under low uniform radiation of $100 Wm^{-2}$	153
7.13	Simulation of three PV modules under medium uniform radiation of $500 Wm^{-2}$	154
7.14	Simulation of three PV modules under fast irradiance changes. For the step-up the radiation rises from 500 up to $1000 W/m^{-2}$; the step-down the radiation goes from 1000 to $500 W/m^{-2}$	155
7.15	Simulation of three PV modules under partial shading. The power characteristic presents two local maxima.	156
7.16	Simulation of three PV modules under partial shading. The power characteristic presents three local maxima.	157
7.17	Output power (red line), operating voltage (yellow line) and current of the PV array simulator measured by the oscilloscope. Time 0.5 second/division.	160
7.18	The current during the tracking. The graph has been divided in three sections showing the process of the scan, the operating current for the estimated voltage/duty cycle defined by the ANN and the adjustment applied by the controller.	161

7.19	The voltage during the tracking. The graph has been divided in three sections showing the process of the scan, the operating voltage estimated by the ANN and the adjustment applied by the controller.	162
7.20	The figure shows the comparison between the proposed algorithm and the hill climbing for a partial shaded PV array.	163
7.21	The figure shows the comparison between the proposed algorithm and the hill climbing in case of fast irradiance changes. In this specific case the irradiance increases $100Wm^{-2}$	164
7.22	The figure shows the comparison between the proposed algorithm and the hill climbing in case of fast irradiance changes. In this specific case the irradiance decreases $100Wm^{-2}$	165
A.1	View of the main screen for controlling the data logger.	170
A.2	Block diagram for the measuring the I(V) characteristic from the array.	172
A.3	Block diagram for the measuring the short circuit current of one PV module.	173
A.4	Block diagram for the monitoring of the weather data.	174
D.1	Simulation of a ramp down.	199
D.2	Simulation of a ramp up.	200
D.3	Simulation of a partial shading involving two peaks on the power characteristic.	201
D.4	Simulation of a partial shading involving two peaks on the power characteristic.	202
D.5	Simulation of a partial shading involving three peaks on the power characteristic.	203
D.6	Simulation of a partial shading involving four peaks on the power characteristic.	204
D.7	Simulation of a partial shading involving four peaks on the power characteristic.	205

List of Tables

- 4.1 Parameters involved into the equation for the calculation of the short circuit density of current of a solar cell. 46
- 4.2 Typical values of the parameters of a silicon solar cell [9]. 49
- 4.3 Minimum and maximum relative error of the proposed model. . . 85

- 7.1 Design specification of the boost converter and circuit parameters. 160

1

Introduction to the thesis

As the title suggests, the research was focused on improving the efficiency of a grid connected PV system.

This introduction is to explain the challenge and the motivation of the research, the methodology adapted to deal with it and the structure of the thesis.

1.1 Thesis objectives

Under real operating conditions, the operating point of a PV system can vary significantly with time.

A PV array produces an amount of power directly related to the incident radiation and module temperature; the radiation can differ from module to module as can the temperature which is not even uniform across cell area. Also the incident radiation can very quickly change resulting in high variations of the PV power and some perturbation of the operating voltage. The temperature being non-uniform across the PV array leads to different operating voltage per module; the connection arrangement of the modules will determine the operating voltage. Data has been collected from a test system installed at Strathclyde University. Analysis of the data shows that the time variation of PV module temperature is far slower and subject to less extremes, than the corresponding radiation variation that mainly drives the changes in temperature. This difference in the dynamic responses is of course due to the thermal mass of the PV modules. Even if the radiation is affected by large and fast variations, the temperature of the modules decreases or increases more slowly (see Fig.6.4 on page117).

The two parameters discussed above cannot be properly controlled across the entire PV array surface. Even with a huge number of sensors which will increase the price of the system it would not be possible to control these variations or

their impact. Also the modules respond to environmental conditions differently as result of intrinsic mismatch.

Mismatch losses are caused by the interconnection of solar cells or modules which do not have identical properties or which experience different conditions from one another.

At times PV can also be affected by partial shading due to surrounding objects and this will result in severe mismatch. All these effects will impact on the I-V characteristic and this can provide a challenge to the maximum power point tracking undertaken by the grid tied inverter, and result in performance degradation.

1.2 Methodology

Improving the PV system performance requires design of the DC/DC converter to provide effective maximum power point tracking under real operating conditions. The main novelty of this thesis is to provide a robust and practical algorithm able to track maximum power point effectively under real operating conditions. These include uneven array illumination, thermal variation across the array, and also possibly, variations in module quality. These variations can result in non-ideal IV characteristics sometimes including more than one local Maximum Power Point (MPP) and this poses particular difficulties for conventional maximum power point trackers.

A PV system and some instrumentation was already available at the University prior to the start of this research but this has been significantly extended.

A detailed model of the PV panel has been built with the Orcad platform [61]: that model takes into account all the losses above described. Such a model is necessary to undertake research aimed at improving performance of PV systems through being able to predict real I-V characteristics and thus helping to better understand the behaviour of the maximum power point. A model of a polycrystalline (roof tile) module has to be built up by connecting 18 solar cells, each represented by an individual 2-diode model.

The model has to be able to reproduce real operating conditions (partial shadow and different temperatures).

Once the model is completed, it needs to be validated against appropriate data and suitable instruments must be selected, installed and programmed. The PV array test system has been reproduced by modelling 8 PV modules, individually validated, in series. Of course the array's performance also needs to be compared

with the experimental results.

An algorithm able to track the true MPP has been developed: this algorithm does not need additional sensors and can track the true maximum quickly.

The algorithm has been implemented on a modelled DC/DC converter to test different power and different types of modules (with a different Fill Factor).

Finally the control technique has then been implemented in a real DC/DC converter but using an electronic PV array simulator rather than the outdoor system. Outdoor testing would require a higher power rating for the inverter and this will be the subject of future work.

1.3 Thesis structure

This section summarizes the work presented chapter by chapter.

- Chapter 2. This chapter is entirely dedicated to the literature overview including the description of energy from the sun, how silicon based solar cell converts photons into electricity and a brief introduction to the different technologies. The second part of the chapter covers PV systems and their characterization and the challenge of the Maximum Power Point Tracker (MPPT) for real operating conditions, it also illustrates some common algorithms to detect the MPP.
- Chapter 3. This chapter describes the experimental facility including the instrumentation and its characteristics. The software development for the various different experiments is outlined.
- Chapter 4. This chapter contains the details of the procedure and the mathematics behind the model for the PV array built in Orcad including the results which compare the measured values with the simulated ones.
- Chapter 5. This chapter is entirely dedicated to shading: its effects on the PV system; how different connection arrangements affect the impact of partial shading; how the surroundings can influence the electricity production from the PV system as a function of position and geometry. It is shown how the calculation of the position of the shadow created by a nearby object depends on the location and the time of the day. It is shown why MPPT is difficult to track for the case of PV system affected by time varying partial shading.

- Chapter 6. The MPPT algorithm development is detailed in this chapter including a description of the Artificial Neural Network (ANN) implemented.
- Chapter 7. This chapter is concerned with the testing of a DC/DC converter including the implementation of the developed algorithm for the controller. The last part is dedicated to the experimental results obtained by applying the developed algorithm on a converter and the adaptation of the algorithm for different rated power and for modules with different performance characteristics.
- Chapter 8. Summary and conclusions.

2

Introduction

Edmond Becquerel discovered the photovoltaic effect in 1839 during an experiment with wet-cell batteries. Willoughby Smith discovered the photoconductivity of selenium in 1873, and three years later in 1876, William Adams and Richard Day discovered the photovoltaic effect in solid selenium. The modern PV cell configuration was invented in 1883 by Charles Fritts. The cell was made from a thin disk wafer of selenium covered with very thin, semi-transparent, gold-wires. The gold-wires were used to collect the free electrons generated. The light-to-electrical power efficiency achieved was between 1% and 2%[33].

The first semiconductor-based transistor was successfully tested on December 24 in 1947 at Bell Labs (discovered by Bardeen, Brattain and Shockley). The first PN junction made from single-crystal germanium was made in 1950 and from silicon in 1952 (the single-crystal growth technique was developed in 1918 by Czochralski). A few years later, in 1954, the first silicon PV cell is announced by Chapin, Fuller and Pearson with an the efficiency reported of 4.5%, and raised to 6% within a few months.

The first commercial PV product was launched in 1955. The price was however very high (1500 USD per watt). The first successful demonstration was the Vanguard I satellite in 1959. Its power systems delivered less than one Watt to the onboard radio. The efficiency is raised from 8% to 14% over the years 1957 to 1960, all by Hoffman Electronics [40]. The 1960's is the decade where the PV technology breaks through to become the main power source for many satellites, e.g. the Telstar by Bell Telephone Laboratories is launched with 14 Watt PV cells in 1962. NASA launches the Nimbus spacecraft equipped with 470 Watt PV array in 1964 and the Orbiting Astronomical Observatory with one kW PV array in 1966. During the 1970's the price is reduced dramatically, from 100 USD per watt to 20 USD per watt. This leads to more terrestrial applications, such

as lights and horns on offshore oilrigs, lighthouses, and railroad crossings. The first dedicated laboratory for PV research is founded in 1972 at the University of Delaware. One of the first homes completely powered by PV, was built in 1973 by university of Delaware with surplus electricity sold to the grid.

There are many PV developments in the 1980's. ARCO solar produces more than 1 MW of PV cells in 1980, being the first in the world. The first megawatt-scale PV plant is made in 1982 in California, and in 1983 a 6 MW plant is inaugurated, also in California. The worldwide production of PV cells exceeds 21 MW in 1983 and the first silicon PV cell with an efficiency of 20% is developed in 1985.

The 1990's sees a number of 'roof-top' programs to expand the market for PV products, e.g. the Danish SOLBYEN (60 kW), SOL 300 (750 kW), and SOL 1000 (≈ 1 MW), the 100 000 roof program (≈ 100 MW) in Germany, the Million Solar Roofs in the US, and many more. Alongside these programs, the efficiency of CdTe thin film PV cells raised to 15.9% in 1992 and the gallium indium phosphide and gallium arsenide PV cells reaches 30% efficiency in 1994 [33].

Increasing efficiencies, new technologies and price reduction in materials and production will lead to a future, where PV power will eventually be price competitive with conventional power sources, such as oil, coal, natural gas, etc. A price reduction of 50% is possible over the next seven years. One of the most efficient technologies is the mono-crystalline silicon PV cell. This is due to a low rate of re-combination of holes and electrons, within the PN junction. But mono-crystalline PV cells are also more costly when compared to the multi-crystalline PV cells. This is due to the manufacturing process for the mono-crystalline silicon wafer, which is rather expensive [44].

Using a novel technology that adds multiple innovations to a very high-performance crystalline silicon solar cell platform, a consortium led by the University of Delaware has achieved in July 2007 a record-breaking combined solar cell efficiency of 42.8 percent from sunlight at standard terrestrial conditions [43]. That number is a significant advance from the current record of 40.7 percent announced in December and demonstrates an important milestone on the path to the 50 percent efficiency goal set by the Defense Advanced Research Projects Agency (DARPA).

2.1 From the sun to electricity

The sun can be considered as a power resource and its behaviour can be approximated by a black body (perfect emitter and absorber). The black body's power radiated per unit area of emitting surface in the normal direction per unit solid angle per unit frequency can be expressed by Plank's law:

$$I(\nu, T) = \frac{2h\nu^3}{c^3} \frac{1}{e^{\frac{h\nu}{kT}} - 1} \quad (2.1)$$

where ν is the frequency of the electromagnetic radiation; T is the temperature of the black body; c the speed of light; h is the *Plank's constant* $6.62606957(29) * 10^{-34} Js$; k is the *Boltzman's constant*.

2.1.1 Solar spectrum

Solar radiation consists of photons of differing energy; the distribution of photon energy according to their wavelength is called a spectrum.

The spectrum of the sun can be approximated by the spectrum of a black body with a temperature about 5800 K. The radiation from the sun is composed of photons of differing energy as shown in Fig.2.1.

The spectrum outside the atmosphere has higher energy than that on the surface: the photons coming through the atmosphere interact with the gases and particles and as a result the radiation changes in the quantity and quality; a part of the UV (ultraviolet) radiation is absorbed in the stratosphere; a part of the IF (infrared) radiation is absorbed by water molecules and carbon dioxide in the upper troposphere; and aerosols lead to the scattering of visible light, mainly in the blue visible part of the solar spectrum.

The amount of the radiation falling on a surface is also determined by amount of air that the radiation has passed through. The lower is the position of the sun in the sky, higher is the proportion of photons absorbed or scattered away from their direct path.

2.1.2 Electricity conversion

The detailed physics of solar cells and the derivation of the simplified models used in this research is well covered in textbooks like [37], [38] and [44], and will not be reiterated here. Chapter 4 summarizes the relevant physics and presents the one and two diode models and their equivalent circuits.

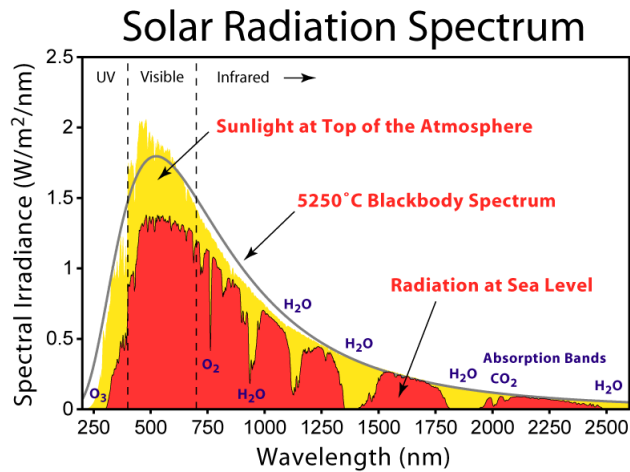


Figure 2.1: Solar spectrum outside and inside the atmosphere compared with the spectrum of a black body with a temperature of 5250°C. From [26]

The photovoltaic effect generates a potential difference at the junction of two different materials in response to visible or other radiation.

The basic processes behind:

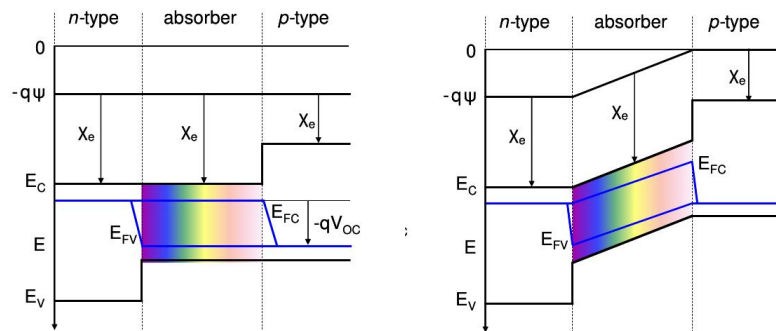
- generation of the charge carriers due to the absorption of photons in the materials that form a junction,
- subsequent separation of the photo-generated charge carriers by the junction,
- collection of the photo-generated charge carriers at the terminals of the device (i.e. at the front and back contacts).

A typical solar cell structure consists of an absorber layer, in which the incident photons are absorbed creating pairs of electron-hole. There are semipermeable membranes attached to the both sides of the absorber in order to separate the photo-generated electrons and holes from each other. The semi-permeable membranes have to selectively allow only one type of charge carrier to pass through [60]. An efficient solar cell is designed in a way that the electrons and holes generated in the absorber layer reach the membranes. To achieve this the thickness of the absorber layer has to be smaller than the diffusion lengths of the charge carriers.

A membrane lets electrons go through and blocks holes when its material composition has a large conductivity for electrons and a small conductivity of holes. An example of such a material is an *n*-type semiconductor, in which a large difference in electron and hole concentrations generates a large electron conductivity with respect to the hole conductivity.

The injection of holes from the absorber into the n -type semiconductor is undesirable. Thus to reduce this an energy barrier should be introduced in the valence band between the n -type semiconductor and the absorber. Similarly, the injection of electrons from the absorber into the p -type semiconductor could be suppressed by using a p -type semiconductor with a larger band gap than that of the absorber and having the band off-set in the conduction band between the absorber and the p -type semiconductor.

The asymmetry in the electronic structure of the n -type and p -type semiconductors is the basic requirement for the photovoltaic energy conversion. Fig.2.2 shows a schematic band diagram of an illuminated idealized solar cell structure with an absorber and the semipermeable membranes. The electrodes of the solar cell are attached to the membranes.



(a) Band diagram of an idealized solar cell structure at the open-circuit. (b) Band diagram of an idealized solar cell structure at the short-circuit.

Figure 2.2: Band diagram of an idealized solar cell from [65].

2.2 Inorganic solar cells

There are a number of inorganic cells that are now well developed and commercially available. This section will briefly review the technology that is most significant in the market, both the crystalline and thin film silicon cells and the leading cell based on a hetero-junction, Cadmium telluride. Other inorganic cells like Copper Indium diselenide and organic cells such as those based on conjugated polymers, are not discussed, and have not been used in this research.

Monocrystalline solar cell. Monocrystalline modules are composed of cells cut from a piece of continuous crystal. The material, grown into a single crystal, forms a cylinder which is sliced into thin circular wafers [19]. To minimize waste, the cells may be fully round or they may be trimmed into other shapes, retaining

more or less of the original circle. The monocrystalline solar cells have a uniform dark blue color because they are cut from a single crystal.

Polycrystalline. Made with the same material as the monocrystalline but with the difference that its material is melted and poured into a mold. This forms a square block that can be cut into square wafers with less waste of space or material than round single-crystal wafers. After the cooling process, the material crystallizes forming random crystal boundaries. The polycrystalline has lower efficiency of energy conversion than the monocrystalline which implies the size of the modules is slightly greater per watt than most monocrystalline modules. The surface has a jumbled look with many variations of blue color.

The most common construction is by laminating the cells between a tempered glass front and a plastic backing, using a clear adhesive similar to that used in automotive safety glass. It is then framed with aluminum.

The silicon used to produce crystalline modules is derived from sand. It is the second most common element on earth. The reason of the expensive cost of this crystalline solar cell, even if the sand is the second most common element on the earth, is that, in order to produce the photovoltaic effect, it must be purified to an extremely high degree. The process to purify the silicon is very expensive. Another reason is also the high demand in the electronics industry because it is the base material for computer chips and other devices [55].

Thin film Si. There is a large variety of silicon deposition technologies which can roughly be allocated to the main groups of liquid phase and gaseous phase deposition. In the liquid phase deposition, the respective substrate is brought into contact with a metal melt (Cu, Al, Sn, In) saturated with silicon. By lowering the temperature of the melt supersaturation occurs and silicon is deposited on the substrate [20]. In the chemical vapor deposition (CVD) method, which is a well-established method in microelectronics, a mixture of H₂ and the precursors SiH₄, SiH₂Cl₂, or SiHCl₃ is decomposed thermally at the hot surface of the substrate. The most common techniques are low pressure and atmospheric pressure CVD (LP-CVD, AP-CVD), but these are also plasma enhanced, ion-assisted and hot-wire CVD (PE-CVD, IA-CVD, or HW-CVD).

Cadmium telluride. With a direct optical energy bandgap of 1.5 eV and high optical absorption coefficient for photons with energies greater than 1.5 eV, only a few microns of CdTe are needed to absorb most of the incident light. Because only thin layers are needed, material costs are minimized [41]. Its band gap is well matched to the solar spectrum and efficiencies up to 16% can be achieved [58]. The main problem is the use of Cadmium and the associated risk

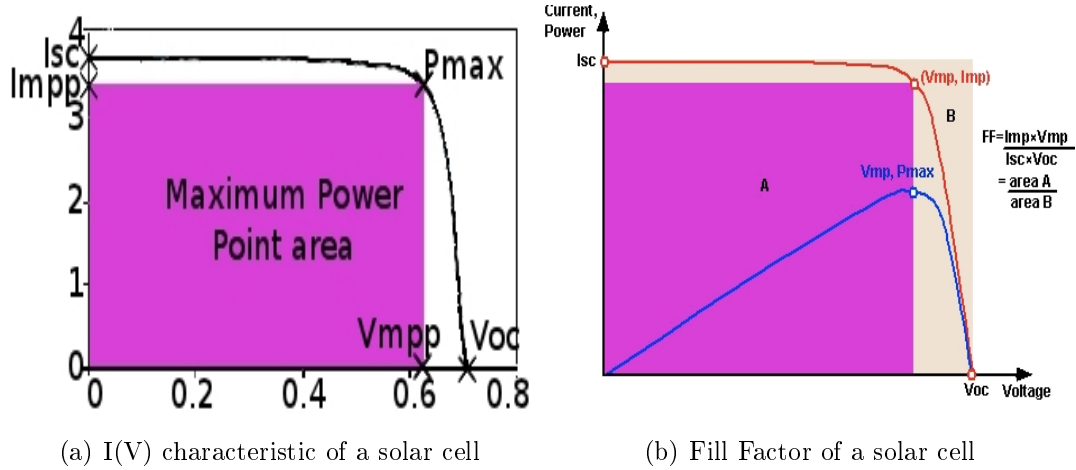


Figure 2.3: Power ($P(V)$) and current ($I(V)$) characteristic of a solar cell within main parameters

to health. The efficiencies of commercial modules reach efficiencies in the range of 8-9%.

2.2.1 Photovoltaic parameters

The main parameters of a solar cell are listed below and shown in Fig.2.3:

I_{sc} : short circuit current is the current through the solar cell when the voltage across the solar cell is zero.

V_{oc} : open circuit voltage is the maximum voltage available from a solar cell, and this occurs at zero current.

MPP : maximum power point.

V_{mpp} I_{mpp} : voltage and current at the maximum power.

FF : fill factor is the ratio of the maximum power from the solar cell to the product of V_{oc} and I_{sc} .

AM : air mass is the path length which light takes through the atmosphere normalized to the shortest possible path length.

The Air Mass quantifies the reduction in the power of light as it passes through the atmosphere and is absorbed by air and dust. The Air Mass is defined as:

$$AM = \frac{1}{\cos \theta} \quad (2.2)$$

where θ is the angle from the vertical (zenith angle). A standard spectrum has been defined to compare the different solar cell efficiencies. The standard spectrum at the Earth's surface is AM1.5.

2.2.2 Photovoltaic systems

The electricity generated by a PV system cannot be used directly, usually it must be transformed in AC.

There are different types of PV system for different application.

Grid connected

A PV system grid connected does not require the use of batteries because the system is connected directly to the utility grid so if the energy is not used by the user it will be transferred to the utility grid. These systems can make use of all the PV technologies and the size and power is determined by the technology, the investment and the user requirements.

A grid tied connected system includes a PV array, a DC/DC converter with MPPT, an inverter plus wiring and fuse protections. For a domestic system a two way meter is commonly used to record net energy flows between the house and the grid. Sometimes only the PV output is measured.

The MPPT aims to track the maximum power point of the array for any environmental conditions (varying irradiance and PV temperatures); the most common implementations is described in section 2.4. Depending on the technique, they can be more or less efficient for different conditions as far as stable and steadily changing radiation and for fast irradiance changes but they cannot detect the presence of local maxima. This can lead the system to work at the wrong operating point. More sophisticated techniques have been studied and analyzed for solving problems such as mismatch and partial shading.

The DC/DC converter converts a source of direct current from one voltage level to another; the converter used is switched mode due to their efficiency. The circuitry can differ as well as the type of the power electronic devices.

The inverter has the role of transforming the DC to AC including the anti-islanding protection. Islanding refers to the condition in which a distributed generator continues to power a location even though power from the electric utility is no longer present. This phenomenon could be dangerous to the utility workers so the inverter has to detect these specific fault conditions.

Stand alone system

These are widely used in remote areas where connection to grid is not possible and also for space application for the obvious reasons. The system is composed of a PV array, one or more batteries, a charge controller and an inverter. The

PV modules used are the same technology and size as for the grid connected systems. The size, the connection and the installation are determined by the location, user requirement and the investment. The most common batteries used are lead acid batteries due to their low price. The charge control has normally two requirements: first of all has to prevent any damage of the battery for overcharging or discharging; and secondly it has to track the maximum power point of the PV system. An inverter is included to transform the energy from DC to AC.

Hybrid system

These systems combine the electricity production from PV with other generating systems: the auxiliary system can be diesel, biogas or other renewable energy such wind. Photovoltaic power generation serves to reduce the consumption of non renewable fuel. Although a hybrid system requires a more complex controller than the stand grid tie connected and the stand alone systems, its overall reliability is superior to the other two systems. It often includes the use of batteries.

These system are common in Islands, good examples can be found in Pellworm island in Germany and Kythnos island in Greece [36].

2.3 Real operation conditions

In the real world, PV systems are affected by several parameters which in the outdoor environment cannot be considered constant, principally PV temperature and radiation.

The challenge of the MPPT (Maximum Power Point Tracker) is finding the true MPP in the face of all the variation the real environment imposes on the PV behaviour. It must do this quickly and effectively so the algorithm which drives the DC/DC converter has to be fast and precise.

Real operating conditions affect the operating point of the PV and include a number of factors. They are:

Intrinsic mismatch

A PV array is composed of a number of cells; these cells, even if produced by the same manufacture and made with the same technologies are not identical; so their output will differ even if subject to the same environmental conditions. In the case of mismatch the output power is lower than that estimated because the output current of a PV module is driven by the cell which produces the least. The effects of the mismatch depend on the operating point of the module, the

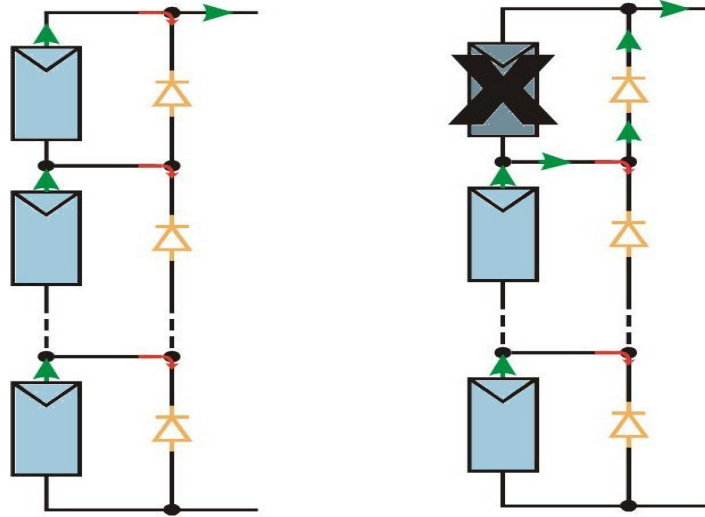
circuit configuration and the parameter (or parameters) which are different from the remainder of the solar cells. Mismatch is worse with many series connected cells, where the cell with lower current forces the system to work at its current, and for modules which use only one or no bypass diode.

Partial shading

To obtain the best performance of a PV system in the northern hemisphere it should be installed as close to due south as possible and with a tilt angle equal to the latitude of the location and with no surrounding objects that can shade the PV array during the day. Often some shading cannot be avoided especially for building integrated installations. The angle and the orientation are dictated by the structure of the roof. The surroundings could include trees, other buildings, antennas, all these could generate a shadow on the PV array depending on the position of the system, the location, the day of the year and the time of the day. Partial shading leads the output characteristic of the PV system to have multiple maxima, where the number of local maxima depends on many parameters as well as the number of the modules affected by the partial shading, their electrical connection and any bypass diodes employed. The optimum performance of a PV array is possible only if all the sources are perfectly electrically matched, i.e. that they all generate the same currents or voltages, depending on their connection (series or parallel). The electrical mismatch, created by shading or cell damage, reduces array power production (and consequently its efficiency) and can cause hot-spots where local heating may damage the cell encapsulation materials.

Electrical mismatch and component failure can be limited by using components for circuit protection (see Fig2.4). The array is normally divided into parallel branch circuits, consisting either of a single series string or several strings in parallel. The main goal of the blocking diodes is to prevent forward biasing of voltage-mismatched branch circuits. The task of the bypass diode is to limit the reverse biasing of the current-mismatched cells allowing the strings to function in case of open circuit failures.

Bypass diodes limit the amount of power which can be dissipated in a single cell or module in case of mismatch. Bypass diodes are connected in parallel with a series string of cells so that the diode forward characteristic becomes the string reverse characteristic. During normal operation, without any mismatch, bypass diodes are reverse biased so they do not conduct. The mismatched cell reduces the output current of its string, which becomes reverse biased. When this happens, the bypass diode is in forward bias and conducts, limiting the negative voltage



(a) Example of a typical protection arrangement in a string. (b) Operation of a bypass diode for a module under partial shading.

Figure 2.4: Typical arrangement of bypass diodes.

across the mismatched string, and hence across the mismatched cell or module without protection, the maximum power dissipation in the mismatched cell is limited to the maximum power generated by the remaining cells in its sub-string.

The function of a bypass diode is to conduct, so limiting the power dissipation when a part of the string is under reverse bias voltage and it will continue to operate as long as the part of the string (for example under partial shading) is in reverse bias, but it does not prevent against current unbalances; for these cases, it is necessary either to limit the number of parallel strings or to incorporate series blocking diodes in each string.

Blocking diodes modify the forward characteristic of a string. For normal operation, when there is no mismatch and/or faults, the blocking diode is forward biased, and conducts the string current, introducing a small voltage drop [8]. When the string operating voltage is exceeded by the circuit operating voltage, the blocking diode becomes reverse biased, limiting the current flowing in the string to a negligible diode leakage current.

Apart from eliminating current imbalance, blocking diodes prevent any storage batteries that may be used to store excess energy generated by the array, from discharging through the array at night [8].

A shadow falling on a PV array affects the power output in two ways:

1. by reducing the output power of the shaded cell or cells;
2. by increasing the internal energy losses in the non illuminated area.

It is common to assume that the efficiency or energy conversion is uniform over the entire cell area; for this reason the short circuit current can be calculated as proportional to the unshaded area and the incident radiation as in eq.4.7. Let us investigate the effects of a shadow on the $I(V)$ characteristic for series and parallel connections. The current $I_c(v)$ of a solar cell can be written, for any intensity of light, as [48]:

$$I_c(v) = kI_{sc} - I_{d1}(v_0 - \Delta v) \quad \text{and} \quad \Delta v = (1 - k) I_{sc}R$$

where k is a numerical factor reflecting the incident solar radiation intensity and I_{d1} is the dark saturation current. Let us consider first two solar cells connected in parallel, partially shaded and such that one cell is illuminated ($k = 1$) and the other is dark ($k = 0$). Currents for the illuminated and non-illuminated cells respectively, can be written as:

$$I_c(v) = I_{sc} - I_{d1}(v_0) \quad \text{and} \quad I_k(v) = -I_{d1}(v_0 - I_{sc}R)$$

where $I_c(v)$ denotes the current of the illuminated cell and $I_k(v)$ is the current of the non-illuminated cell. Being parallel connected, the output will be the sum of these currents:

$$I(v) = I_c(v) + I_k(v) = I_{sc} - I_{d1}(v_0) - I_{d1}(v_0 - I_{sc}R) \quad (2.3)$$

Rewriting eq.2.3 for a module comprising p cells in parallel where rp are illuminated and $(1 - r)p$ are shaded [48]:

$$\begin{aligned} I_M(v) &= I_c + I_k \\ &= rpI_{sc} - rpI_{d1}(v_0 - \Delta v_1) + [-(1 - r)pI_{d1}(v_0 - \Delta v_2)] \\ \text{where } \Delta v_1 &= (1 - k)rpI_{sc}R \\ \text{and } \Delta v_2 &= (1 - r)pI_{sc}R \end{aligned}$$

In 1961 W.Luft published the results of an experiment that involved measuring of the cell output for different level of shading; the results highlight that V_{oc} and I_{sc} near the MPP did not correspond to the values which would be expected from light intensity variations, but they were lower depending on the exact position of the shadow on the cell area.

For the case of the same two solar cells but connected in series, even if they have different levels of radiation or they are partially shaded, they will carry the same current with a value equal to the lower one. The $I(v)$ can be expressed as:

$$\begin{aligned}
I_M(v) &= I_0 - J_{v'}, & 0 \leq v \\
&= I_0 - dI_{bypass}(v), & v < 0
\end{aligned}$$

where $I_0 = rpkI_{sc}$, d the number of diodes in parallel, and $I_{bypass}(v)$ is the bypass diode characteristic. From Kirchhoff's law it can be deduced that with series connection all the PV cells are forced to operate at the same current, the lower one produced by the shaded cell which is under reverse biased thus leads to power dissipation and to heating effects. The shaded cell has lower short circuit current compared to the unshaded ones so that it is operated under reverse bias, causing power dissipation.

For low bias voltages the reverse current can be approximated as a linear function of the voltage (ohmic behaviour). The slope is a measure of the leakage currents that appear in addition to the dark saturation current of an ideal diode. Leakage currents originate in cell defects and impurity centers in the semiconductor and can be represented by a shunt resistance. At low bias voltages the current is distributed over the whole cell area and heating takes place more or less uniformly. The maximum current density is below a critical limit and the $I(V)$ characteristic is stable against thermal effects.

A polycrystalline solar cell contains impurities (doping) and their concentration is inhomogeneous; these heterogeneous concentrations, at high bias voltage, cause a different type of breakdown where the part of the cell with higher doping breaks down first. In reverse biased conditions the current is locally concentrated and local heating is caused which can cause damage to the cell encapsulation. The reverse $I(V)$ characteristic of the shaded cell determines the string characteristic when the string current exceeds the short-circuit current of this cell. Fig.2.5 shows the string characteristic which breaks off at point 1 and follows the reverse characteristic. If the string voltage exceeds the transmission voltage of the bypass diode, the diode starts to conduct. This limits the voltage associated with a steep rise of the string characteristic at break point 2.[22].

For conventional silicon cells on a PV system, worst case shading proportions in the range of 20% to 50% are to be expected. The specific shading losses increase with the number of cells in the substring and can be up to 100% if no bypass diode is present.

As cell manufacturers generally do not provide any information about the behaviour of their cells under reverse biased conditions, the study conducted by Herrmann consisted in measuring the reverse IV -characteristics in the dark for a selection of seven cell types on the basis of six to ten test specimens.

From his results it was established that the behaviour under reverse biased

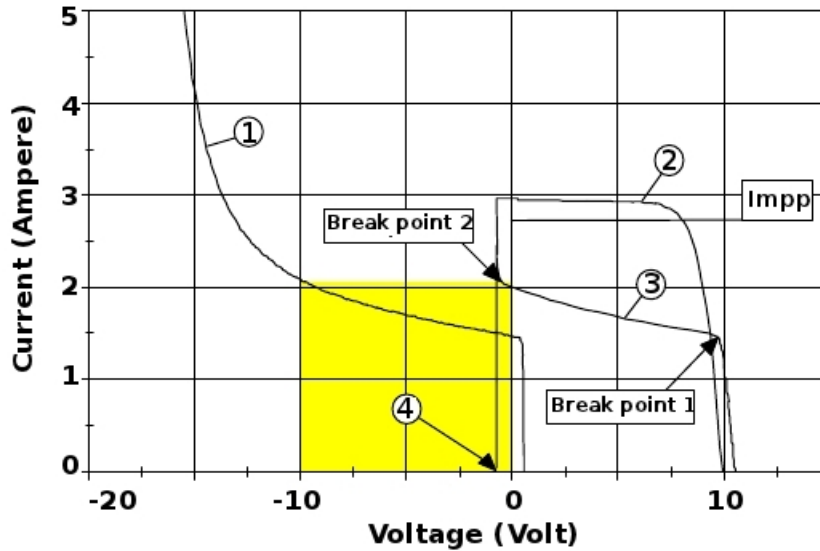


Figure 2.5: Effect of the bypass diode on the I(V) characteristic of a module with 17 cells unshaded and 1 under shadow.[22]

conditions of cells of the same type is subject to considerable variation. This concerns both the slope of the reverse characteristics at low bias voltages as well as the value of the breakdown voltage. For that specific experiment Herrmann pointed out that the breakdown voltage for polycrystalline silicon solar cells was between 12 and 20 Volt and for monocrystalline could extend up to 30 Volt. The slope of the curves is slightly higher in the case of poly-Si cells, which indicates a larger current component due to leakage currents. On the other hand, in the case of mono-Si cells the breakdown voltage may cover a large range. Reverse current was applied to the cells with the best and worst blocking behaviour (diodes must be rated to take total possible current of the cells and they may have a low resistance to have high current flow) and the conclusions were deduced from the thermal images of the cells taken from an infrared camera:

- The structure of the solar cells is not homogeneous, the temperature distribution is a direct measure of the current density distribution. In the case of the cell with the best blocking behaviour, an overall power dissipation of approx. 11 W resulted in a temperature difference of 25 K between the hottest (90°C) and coldest point (65°C).
- The cell with the poorest blocking behaviour demonstrated clear temperature peaks at two points. These were probably due to cell damage that may have occurred during cell production or during soldering of the contact ribbons. Temperatures of 150°C were measured at bias voltage -10V and

current 3A.

In the literature we can find a large number of models that aim to predict the maximum power point in case of partial shading; some of them try to predict the power characteristic for a PV array involving local peaks (partial shading) but the parameters involved have a large variation (especially for outdoor systems) and as Herrmann's work has shown, these critical parameters are not even constant across the PV module area.

The number of local maxima depends on how many different values of current we have in the string, for example if the PV system is under uniform radiation but one cell of one module has 20% of its area shaded, and another cell of another module has its total area under shadow we will have 3 different peaks; that's because the two modules affected by partial shading will have output currents determined by the cell with lower current (the cell with 20% shaded area of course will produce higher current than the one totally shaded) and the other cell in the string will generate a current proportional to the incident radiation.

Deriving an equation for the I(V) characteristic for an array in the case of partial shading is not easy. A technique has been proposed by [28]. Assuming that the modules are composed of a series connection of n solar cells, the current can be calculated as:

$$I_A = \sum_{x=1}^{N_{pM}} I_{Ax} = \sum_{x=1}^{N_{pM}} I_{scAx} \left[1 - \exp \left(\frac{q(V_A + R_{sAx} I_{Ax} - V_{ocAx})}{AkTN_s(N_{sM} - N_{Dx})} \right) \right] \quad (2.4)$$

Eq.2.4 represents the output current for an array configured by $N_{sM} \times N_{pM}$ modules (N_s is the number of the cells series connected in a PV module; N_{sM} is the number of the modules connected in series and N_{pM} is the number of the modules connected in parallel). R_s is the series resistance of a solar cell; T is the temperature in Kelvin; k is Boltzmann's constant; A is the ideality factor. The subscript x stands for the string number; subscript A stands for array; subscript M stand for module. The voltage drop across the bypass diode of the shaded module is assumed to be zero and the number of shaded modules is N_{Dx} . Under partial shading conditions:

$$\begin{aligned} I_A &= \sum_{x=1}^{N_{pM}} I_{Ax} & I_{scA} &= \sum_{x=1}^{N_{pM}} I_{scAx} \\ V_A &= V_{Ax} = (N_{sM} - N_{Dx}) V_M = (N_{sM} - N_{Dx}) N_s V \\ R_{sAx} &= (N_{sM} - N_{Dx}) R_{sM} = (N_{sM} - N_{Dx}) R_s \frac{N_s}{N_p} \end{aligned}$$

This model assumes that the radiation level across the unshaded portion of the array is uniform.

Fast irradiance changes

During a partially cloudy day the irradiance can vary very fast as can the operating point for the PV system. An example of these variations is shown in Fig.6.4(a) (page 117); this graph represents 17 minutes of measured global radiation for Glasgow: it can be noted that in less than 20 seconds the radiation can vary more than 300 Wm^{-2} .

In terms of the operating point the irradiance variations have more influence on the I_{mpp} than the V_{mpp} because current production is directly proportional to the amount of the radiation falling on the PV, whereas the voltage has a logarithmic dependence on the irradiance, but it is more sensitive to temperature variation.

Thermal mismatch

PV cell temperatures depend on incident radiation, ambient temperature, wind speed and thermal mass of the photovoltaic; also the generation of current, which is not uniform across the cell area, affects the PV temperature. This implies the cells of a PV system have no uniform temperature which leads to non uniform performance of the PV array. High values of temperatures involve in lower V_{mpp} which decreases the output power of the PV system depending on the connection of the cells.

PV temperatures do not vary rapidly as the irradiance as shown in Fig.6.4(b).

2.4 Existing algorithms

From the I(V) characteristic we can derive many important parameters of a solar cell: open circuit voltage, short circuit current, fill factor and maximum power point. A photovoltaic module is composed of a number of solar cells connected in series; a photovoltaic array is formed by combinations of parallel and series connections of PV module. The performance of a PV array is a combination of the performance of each module in the configuration.

Tracking the maximum power point (MPP) of a PV array is usually an essential part of a PV system. The array produces a certain amount of power at any time and of course it's really important to capture the true maximum for obvious reasons. Depending on the PV system (grid connected, stand alone, etc. section 2.2.2) the electronic circuit to control and to convert the energy produced is different. Generally the aim of the DC/DC converter is to maintain a stable

voltage for the inverter while transferring the maximum power available from the PV system. The MPP varies with irradiance, temperature, partial shading and so on. Depending on the connection and the technology the V_{mpp} and the I_{mpp} move around and the aim of the DC/DC converter is to find this operating point and be fast in doing so.

To find the true maximum for all the possible cases listed in section 2.3 the converter parameters (such as voltage, current or duty cycle) have to be set by a controller which follows an algorithm (Maximum Power Point Tracker).

As such, many MPP tracking (MPPT) methods have been developed and implemented. The methods vary in complexity, the number of the sensors required, convergence speed, cost, range of effectiveness, implementation hardware, popularity, and in other respects.

The problem considered by MPPT techniques is to automatically find the voltage V_{mpp} or current I_{mpp} at which a PV array should operate to obtain the maximum power output under a given temperature and irradiance. It is noted that under partial shading conditions, in some cases it is possible to have multiple local maxima, but overall there is still only one true maximum power point. The most common maximum power point algorithms are now presented:

Perturb and Observe

The PV output characteristic exhibits a MPP which represents the maximum power available from the system for the specific operating conditions. This maximum power can be extracted if the PV system works at the voltage of the V_{mpp} . The principle of the P&O algorithm, as the name could suggest, is based on applying a perturbation in the operating voltage and observing the variation of the power.

For example if the PV system is working at $V_1 < V_{mpp}$, the observed power is P_1 ; applying a perturbation of the operating voltage (ΔV) the control will detect an increase of the power; consequently at the next time step, the control will increase again the operating voltage until decreasing power is observed.

When a decrease of the power is observed the control system has to reverse the perturbation that means decreasing the operating voltage in the next time step. This algorithm is summarized in Fig.2.6

The process is repeated periodically until the MPP is reached. The system then oscillates about the MPP. The oscillation can be minimized by reducing the perturbation step. However, a smaller perturbation step size slows down the maximum power point tracker.

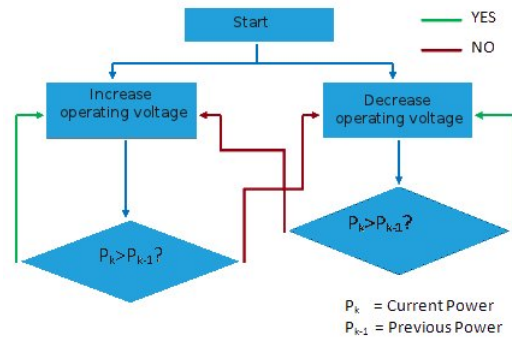


Figure 2.6: Perturb and Observe algorithm diagram.

The algorithm described is the basic Pertub and Observe; modified version can be found in [59], [17], [4]

Hill climbing

Hill climbing algorithms are widely used in practical PV systems because of their simplicity and because it does not require modelling the PV characteristic to be implemented (Fig.2.7).

The algorithm starts measuring the present values of the PV array voltage V_k and current I_k . The generated power P_k is then calculated and compared to its previous value. According to the result of comparison, the sign of the slope is either complemented or remains unchanged and the duty cycle of the converter is changed accordingly (see Chapter7). The Hill climbing and the Perturb and

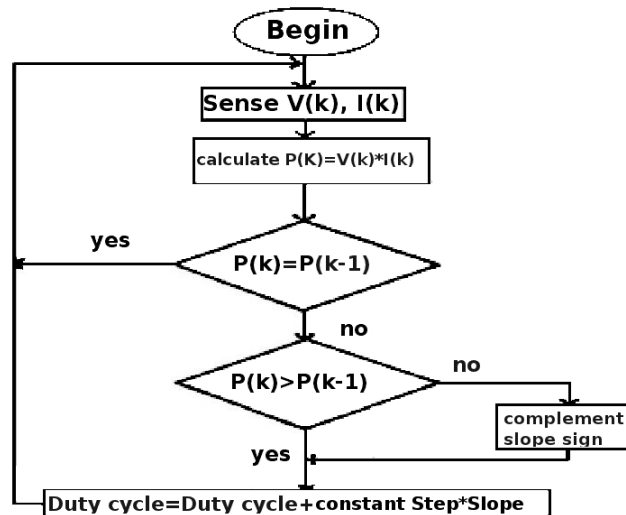


Figure 2.7: Hill climbing algorithm diagram.

Observe methods are stable and easy to implement but they can fail in case of

fast irradiance changes as shown in Fig.2.8 (from [16]).

After determining the operating point, applying several perturbations on the operating point which grows up to the point A, the algorithms will apply a new perturbation ΔV in the PV voltage and if the radiation and temperature of the PV remain stable this leads to a decrease in power (point B) and consequently the perturbation will be reversed.

However, if the irradiance increases with a consequent change in the PV temperature, the power characteristic shifts from P_1 to P_2 within one sampling period and the algorithms which have applied the perturbation ΔV are now working at the point C. Passing from point A to point C, the algorithms note an increasing in power and the perturbation is kept the same. Consequently, the operating point diverges from the MPP and will keep diverging if the irradiance steadily increases.

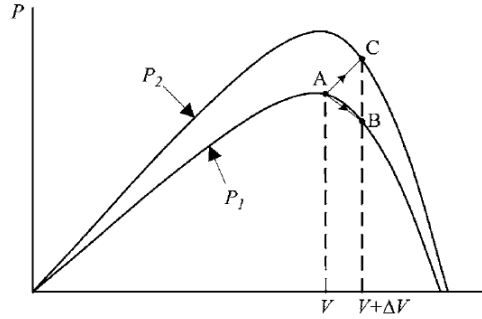


Figure 2.8: Divergence of hill climbing and Perturb and Observe from MPP.

Incremental conductance

The incremental conductance method works with the slope of the PV power characteristic and is based on the fact that its value is zero at the MPP, positive on the left of the MPP, and negative on the right:

$$\begin{cases} dP/dV = 0, & \text{at MPP} \\ dP/dV > 0, & \text{left of MPP} \\ dP/dV < 0, & \text{right of MPP} \end{cases}$$

As:

$$\frac{dP}{dV} = \frac{d(IV)}{dV} = I + V \frac{dI}{dV} \cong I + V \frac{\Delta I}{\Delta V} \quad (2.5)$$

the principles of the Incremental Conductance method can be rewritten as

$$\begin{cases} \Delta I/\Delta V = -I/V, & \text{at MPP} \\ \Delta I/\Delta V > -I/V, & \text{left of MPP} \\ \Delta I/\Delta V < -I/V, & \text{right of MPP} \end{cases}$$

The Incremental conductance algorithm proceeds in this way to track the MPP: it compares the instantaneous conductance (I/V) to the incremental conductance ($\Delta I/\Delta V$) as in Fig.2.9.

The system starts working at V_{ref} which is the operating point for the PV array; once the MPP is reached V_{ref} becomes equal to V_{mpp} and the system will stay at this operating point unless there is a change in irradiance which implies a variation in ΔI and the algorithm increments or decrements the operating point V_{ref} to track the new MPP.

It can be deduced that the size of the increment/decrement determines how fast the MPP is tracked. A large step allows fast system response but the determination of the MPP will not be precise and the system will work around the MPP thus losing power; a small step gives more precise tracking of the MPP but is slow.

In the literature many modifications of the algorithm described above have been presented that are more efficient than the original one. These proposed algorithms include more parameters and/or more sensors and sometimes variable steps.

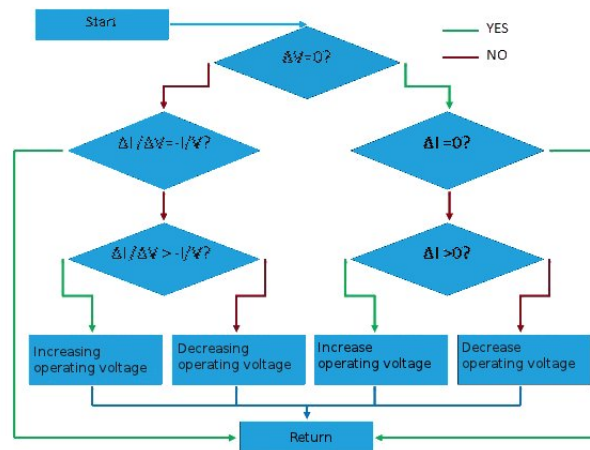


Figure 2.9: Incremental conductance algorithm diagram.

2.4.1 Algorithms using Neural Network

A number of neural network systems have been developed to predict the optimal operating points of PV systems [39], [24] and [23]. The input variables of an Artificial Neural Network (ANN) can be atmospheric data (irradiance and/or ambient temperature), PV array parameters like short circuit current or open circuit voltage, or any combination of these. The output is usually one or several reference signals like a duty cycle signal used to drive the power converter to operate at or close to the MPP [16].

Neural networks need to be trained and since most PV arrays have different characteristics. The work reported in [47] describes the training of the ANN using a genetic algorithm.

The study undertaken in [3] describes a type of neural network for solar-cell modelling, namely, radial basis function (RBF) networks [7]. For this RBFN model the activation of a hidden unit is determined by the distance between the input vector and a target vector. The input parameters used to predict the output current of a solar array are the value of the radiation, the temperature and the load voltage.

Several algorithms use ANN combined with environmental sensors. In [46], the ANN produces the values of the maximum voltage and power for given radiation and temperature. The voltage is compared with the array voltage and the error is given to the PI controller. PI controller is used with ANN to reduce the steady state error.

In [10] an application of a neural network-based controller for tracking the MPP of a PV system connected to the grid has been presented. The neural network identifies, in real time, the voltage for maximum output power of the system.

More complex algorithms have been proposed in [52] and in [27] using ANN combined with fuzzy logic. The ANN is used to overcome the problem of partial shading with the help of a sensor for the global radiation (low cost solar cell). A polar coordinated fuzzy logic controller is used for the DC/DC converter.

A ANN has been also used to improve the performance of the existing algorithm as in [56]; ANN guides the working point to optimal, then continues tracking the MPP using Perturb and Observe method with a small step.

2.5 Conclusion

This chapter has described the process of the PV system to transform the energy from the sun into the electricity.

The second part of the chapter has analyzed the PV system and its operation. Control techniques have been introduced briefly for a range of configurations but most attention is focused on grid connected system which is becoming the dominant form of PV around the world.

3

Outdoor test experiment

This chapter is entirely dedicated to the outdoor test experiment installed on the roof of the James Weir Building of Strathclyde University, Glasgow. The development of an algorithm for the MPPT requires a good understanding of the PV operational performance under representative outdoor conditions. For this reason a model for the PV system has been developed with the outdoor test experiment used to validate this model. Also the experiment includes a weather station which allows monitoring of the ambient data. The experimental arrangement comprises a PV system, instrumentation for monitoring the ambient data (radiation, wind and temperatures) and the PV performance, plus a Data Logger for controlling and recording all these data.

The first part of the chapter deals with the system description and scope with details of the instrumentation used and their technologies; the second part covers the description of the coding in Labview for managing the control of that equipment.

The test rig was installed in July 2008 (PV system and thermocouples) with further instrumentation added later. The software to control the system has been updated in 2010 due to the development of a new version of Labview which does not require the implementation of FPGA (field-programmable gate array) code, because the new version of the software (Labview 2009) already includes the FPGA code for each kind of signal and modules. The chapter includes a detailed description of the PV system and the instruments utilized for the measurements. The goal of the outdoor test experiment was collecting enough data to validate the PV model developed (detailed in the next chapter); to do so, the test rig has been equipped with appropriate instrumentation for reading and recording the ambient data and the $I(V)$ characteristics of the PV system. Several experiments have been run, each of them required a different programming setting and



Figure 3.1: Picture of the outdoor test experiment.

different instruments; the following chapter provides a description of the various experiments and the details of the programming code can be found in the AppendixA.

3.1 System description

The outdoor test experiment is composed of eight BIPV (Building Integrated Photovoltaic) modules from Solar Century model C21. The system size is 320 Watt at STC (radiation: 1000 Wm^{-2} ; Air Mass: 1.5; cell temperature: 25°C ; wind speed: 1ms^{-1}) with V_{mpp} 73.6 Volt, I_{mpp} 4.32 Ampere, I_{sc} 4.89 Ampere and V_{oc} 88 Volts. The values of the current and voltage are determined by the electrical connection between the modules: the output power is given by:

$$P_{mpp@STC} = V_{mpp_{tot}} I_{mpp_{tot}} = N_s V_{mpp@STC}^{module} N_p I_{mpp@STC}^{module} \quad (3.1)$$

where N_s is the number of the modules in series and N_p is the number of the modules connected in parallel. The outdoor test system installed in July 2008 was designed to represent a real house PV roof installation.

In order to maximize the PV production during the year, the inclination angle of the PV should be the same as the latitude of the location, this gives a normal

incidence of the sun at solar noon. The latitude in Glasgow is $55^{\circ}50'N$. The PV modules had to be integrated to the roof so obviously the framework and the PV have the same tilt angle; in Great Britain roof angles vary normally between 35° and 45° . As an engineering compromise the installation was fabricated with an angle of 40° .

The design of the framework has been realized with the traditional method of house builders, with a first structure in vertical wooden rafters, rockwool insulation of 100 mm (same width as the rafters) between them, a breather membrane to keep the water outside of the rig and horizontal wooden battens to fix the PV and concrete roof tiles. The sides were covered with vanished marine ply. The size of the roof is shown in Fig.3.2.

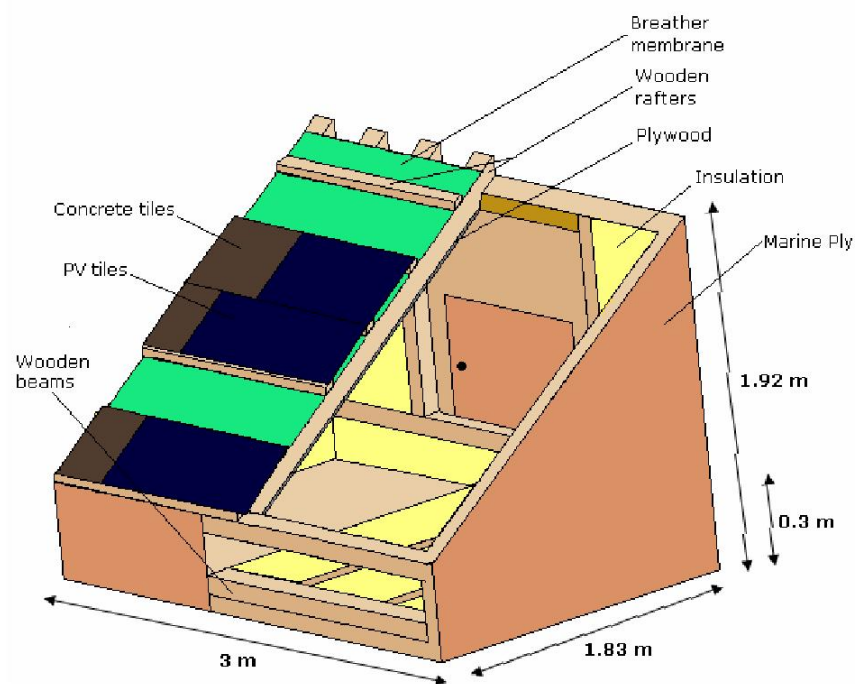


Figure 3.2: Details of the roof dimensions.

To maintain the insulation and to permit the installation of the instrumentation inside the rig, plywood sheets have been installed. Normally the rear side of the roofing is covered with a small layer of plaster, but for the test rig it has been replaced by plywood.

To prevent water infiltration, ridge tiles have been installed and an overlap has been managed at the bottom of the slope.

The rig was equipped with a door on the rear, to permit the access to the instrumentation installed.

The roof was constructed in order to be waterproof because several electrical

devices were installed inside [54].

3.1.1 Data acquisition

A NI CompactRIO real-time controller is connected to an eight-slot CompactRIO reconfigurable chassis. The user defined field-programmable gate array (FPGA) circuitry in the chassis controls each I/O module and passes data to the controllers through a local PCI bus using built-in communication functions. With the 10/100 Mbits/s Ethernet, it is possible to communicate via TCP/IP.

In addition to communication via TCP/IP, UDP, Modbus/TCP, IrDA, and serial protocols, the CompactRIO controllers include built-in servers for Virtual Instrument Software Architecture (VISA), that is connected to the spectroradiometer which will be described in section3.2.

The data logger is now connected into the University network within its own IP address and the same subnet mask as the university network; in this way the data logger can be controlled and modified remotely from any location.

Every instrument for the experiment has a different output, and, even for the same type of signal we have different possible signal levels, this why the data logger has a chassis for eight different modules, for reading digital signal (the spectroradiometer and the anemometer), analogue voltage inputs (all the instrument for the temperature, radiation and transducers) with different range or voltage outputs (for controlling the voltage output of the power supply).

The modules connected to the data logger are:

- four NI9211: this module is specifically made for reading the thermocouples signal (± 80 mV), hence also the signal provided by the pyranometers, with magnitude of millivolt (section3.2) is read by this module.
- two NI9215: these modules read analogue voltage signals in range of $0 - \pm 5$ Volt. It is used for collecting the electrical data from the PV (see section3.3) and wind vane.
- one NI9401: this is a digital module with 16 channels and the only instrument connected is the anemometer which produce a pulse to pulse signal;
- one NI9263: as detailed in section3.3, the power supply has to sweep its voltage from 0 to V_{oc} , the instrument could not be programmed digitally due to a fault of the BIT card thus an analogue signal control has been chosen to drive the voltage output. This module produces an analogue voltage output signal from 0 to 10 Volts.

3.2 Weather data

The experiment has been used to monitor the performance of the PV and for validating a model for the PV array (see Chapter 4); for this reason all the weather parameters have to be monitored and recorded since the model may need to implement these so as to reproduce the PV output as accurate as possible.

At minimum, for predicting the PV performance, the monitoring of the ambient temperature and the global radiation are required; for a more precise prediction of the PV behaviour, other parameters have to be monitored allowing a more accurate calculation of the generated current and PV temperature. The experiment is equipped with two pyranometers (which measure global and diffuse irradiance) and a spectroradiometer for monitoring the spectrum of the solar radiation. Wind speed and direction are measured using an anemometer and wind vane, and ambient temperature by using a thermocouple with a radiation shield, and humidity and atmospheric pressure are measured. Further details are given below.

3.2.1 Instrumentation

Pyranometer: CM11

The roof equipment includes two pyranometers, one measures the global radiation and the second one, with a shadow ring, the diffuse radiation. Both pyranometers are installed on the horizontal plane and the direct component of the radiation is simply calculated by the subtraction of the global radiation and the diffuse one.

With irradiance measurement the response to beam radiation varies with the cosine of the angle of incidence; i.e. full response when the solar radiation hits the sensor perpendicularly (normal to the surface, sun at zenith, 0 degrees angle of incidence), zero response when the sun is at the horizon (90° angle of incidence, 90° zenith angle), and 0.5 at 60 degrees angle of incidence. It follows from the definition that a pyranometer should have a so-called "cosine response" that is close to the ideal cosine characteristic.

A "cosine corrected" sensor has to be designed to maintain its accuracy when radiation comes from different angles. The test for the pyranometer consists in measuring the cosine response for extreme zenith angles. Cosine response is synonymous to the term Lambertian response. Lambert's Cosine law states that radiation intensity on a flat surface decreases as the angle of the surface decreases

from perpendicular (normal or 0°zenith angle). This is expressed as:

$$E_{\theta} = E * \cos(\theta) \quad (3.2)$$

The pyranometer has a thermopile sensor with a black coating. This sensor absorbs all solar radiation and converts thermal energy into electrical energy. It is normally composed of a series connection of thermocouples. It has a flat spectrum covering the 300 to 5000 nm range, and it has a near-perfect cosine response.

The thermopile is protected by a glass dome. This dome limits the spectral response from 300 to 2800 nanometres (cutting off the part above 2800 nm), while preserving the 180°field of view. Another function of the dome is that it shields the thermopile sensor from convection.

The black coating on the thermopile sensor absorbs the solar radiation. This radiation is converted to heat and it generates voltage output proportional to the local temperature difference. The heat flows through the sensor to the pyranometer housing. The thermopile sensor generates a voltage output signal that is proportional to the solar radiation.

The pyranometer with shadow ring measures the diffuse radiation; it operates as the pyranometer for global radiation but only the diffuse component is recorded as the shadow ring blocks out the direct sunlight. The ring can be adjusted manually by sight alone on a sunny day but on other occasions a data sheet must be consulted.

The pyranometers need to be calibrated every two years, if possible with a solar simulator. The output from the pyranometers is in order of mV and they are calibrated as follows:

global radiation

$$I[Wm^{-2}] = 169010 * V_1[\mu V] - 7.088$$

diffuse radiation

$$I[Wm^{-2}] = 206179 * V_1[\mu V] - 33.73.$$

Spectroradiometer

This instrument is composed of a dome and a diffuser which diffuses the incident light from the sky hemisphere. Then it compensates the intensity of the incident light to comply with cosine characteristic.

The spectroradiometer includes also a shutter which decides the exposure time and a grating which diffracts and disperses the source beam to the diode array.

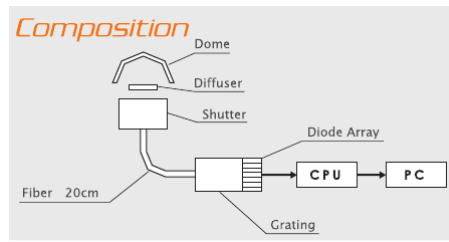


Figure 3.3: Spectroradiometer structure [62].

The diode array comprises several photodiodes. The current flows to each photodiode and is measured to give the spectrum. The spectroradiometer normally includes also a Peltier element to control the sensor temperature.

Anemometer: A100L2

A cup anemometer was installed about 1 meter above the PV test system for measuring the wind speed. The number of revolutions is counted with respect to time which in turn allows the wind speed to be calculated.

This anemometer has analogue and digital output; for the experiment the digital signal has been used because it is more precise and stable than the analogue signal.

A slotted disk interrupting a light beam is used to detect the motion of the calibrated R30 series 3-cup rotor and hence determine the wind speed. The internal electronics condition this pulse signal for output as a 5V square wave and use it to generate an analogue voltage proportional to the wind speeds.

Wind vane: W200P

A wind vane is used to obtain an accurate measurement of the wind direction.

The W200P wind vane contains a wire-bound potentiometer as a shaft angle transducer, with a 2.3° gap at North. As the wiper moves, the swept angle of the potentiometer corresponds to the output voltage which allows the direction to be calculated.

Normally for the wind measurements, both, anemometer and wind vane, should be located high above ground to eliminate the effect of interference from buildings and other objects (standard height of 10 meters) but for the experiment it was needed to measure these parameters close to PV installation so they were installed on the top of the roof at about 1 meter from the PV array.

Relative Humidity sensor

The RH sensor is a laser trimmed, thermoset polymer capacitive sensing element with on-chip integrated signal condition. The output is voltage.

Atmospheric Pressure sensor

This pressure sensor is a transducer; it generates a single ended voltage signal as a function of the pressure imposed.

Thermocouple and Radiation shield

The temperatures of each module of the PV array are measured by J-type thermocouples (device consisting of two different conductors that produce a voltage proportional to a temperature difference between either end of the pair of conductors); the ambient temperature is measured as well with a J-thermocouple insert in a radiation shield to eliminate unwanted radiant heating.

3.3 Electrical data

The roof test experiment has been equipped to monitor also the PV performance: climate data and I(V) characteristic are recorded simultaneously and these data have been used to validate the model for the PV system detailed in Chapter 4.

There are several ways of reading the I(V) characteristic from a module as for example using a shunt resistor or a series of resistor with switch, but for this study a four quadrant power supply has been included which works as a variable load resistor. The fact that the power supply covers the four full quadrant means that it can be used for testing and measuring the PV characteristic under forward bias (illuminated) and reverse bias (dark).

The PV modules are connected to the power supply which sweeps the voltage across the PV from zero to the open circuit voltage and two voltage and current transducers measure the voltage and the current flowing; the output of the transducers is connected to a module of the data logger which collects the data and allows calculation of the PV power.

3.3.1 Setting

Power Supply: Kepco Bop 100-4M

This operates in all four quadrants of the voltage-current axis, therefore its output may swing seamlessly from negative to positive voltage and the output current may also swing from positive to negative values. The result of this is that Kepco BOP will function as a source or a sink, meaning it will either deliver power to a load or absorb power from a load. In order to do that, the BOP is built as a power amplifier with a bipolar output, having a frequency bandwidth much larger than a regular power supply. The frequency bandwidth is model and option dependent.

The solar device is connected to Kepco's BOP power supply functioning as the load, while two transducers are used to measure output current and voltage. The BOP is controlled by a computer program which steps through a systematic loading of the solar device in an effort to determine the maximum power point of the device. The data logger stores in the computer the data from the transducers, where they are used to form a characteristic I(V) curve which defines the solar device.

Hall effect current and voltage transducer

A Hall effect sensor is a transducer that varies its output voltage in response to a magnetic field.

For example let consider a thin sheet of semiconductor material (Hall element) through which a current is passed. The output connections are perpendicular to the direction of current. When no magnetic field is present, current distribution is uniform and no potential difference is seen across the output.

When a perpendicular magnetic field is present, a Lorentz force is exerted on the current. This force disturbs the current distribution, resulting in a potential difference (voltage) across the output. This voltage is the Hall voltage (V_h). The interaction of the magnetic field and the current is shown in eq.3.3

$$V_h \propto I * B \quad (3.3)$$

The Hall element is the basic magnetic field sensor. It requires signal conditioning to make the output usable for most applications. The signal conditioning electronics needed are amplifier stage and temperature compensation. Voltage regulation is needed when operating from an unregulated supply. Hall effect cur-

rent transducer closed loop: The magnetic flux created by the primary current I_p is balanced by a complementary flux produced by driving a current through the secondary windings. A hall device and associated electronic circuit are used to generate the secondary (compensating) current that is an exact representation of the primary current.

Hall effect voltage transducer closed loop: A very small current limited by a series resistor is taken from the voltage to be measured and is driven through the primary coil. The magnetic flux created by the primary current I_p is balanced by a complementary flux produced by driving a current through the secondary windings. A hall device and associated electronic circuit are used to generate the secondary (compensating) current that is an exact representation of the primary voltage. The primary resistor (R1) can be incorporated or not in the transducer.

The output of the voltage transducer is an analogue current signal, as the modules of the Compact Rio can read only voltage signals, the output signal pass through a resistor and the voltage across the resistor is read by the data logger.

Additional details of the instrumentation are listed in B

3.4 Programming

The field-programmable gate array (FPGA) is programmed with a LabVIEW block diagram. The module uses code generation techniques to synthesize the graphical development environment to FPGA hardware.

At the highest level, FPGAs are re-programmable silicon chips. Using pre-built logic blocks and programmable routing resources, the chip can be programmed to implement custom hardware functionality without ever having to build conventional circuit. After developing digital computing tasks in software it is possible to compile them down to a configuration file or bitstream that contains information on how the components should be wired together. In addition, FPGAs are completely reconfigurable and instantly can be re-programmed when you recompile a different configuration of circuitry.

The architecture of the hardware is shown in Fig.3.4. An important factor for each test measurement is the synchronization of the data acquired because being an outdoor test experiment conditions can change very fast and if the data are not synchronized the analysis could be misleading.

Various experiments require electrical data from the PV and, depending on the type of the analysis, they also require some of the weather and physical parameters. For this reason a variety of VIs (Virtual Instruments) have been

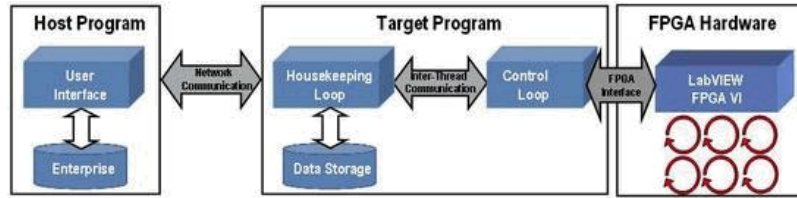


Figure 3.4: Complete PAC (Programmable Automation Controllers) architecture using LabVIEW FPGA, LabVIEW Real-Time and Host PC from [63].

created that can be run simultaneously and only the needed data are stored. The main program to configure the hardware of the data logger is detailed in Appendix A.

3.4.1 List of the experiments

This section will describe the entire test run undertaken since 2009 with the details of the code written in Labview.

Validation of the physical model for PV system

This test was needed for the first part of the PhD; a model for the PV has been built (details in Chapter 4) and the next step was validating this model.

Fig.3.5 shows the flowchart of the Labview code for this specific measurement. The VI has to control the output of the power supply for sweeping the voltage across the PV module from 0 to V_{oc} (11 Volts). To achieve the task of the validation of the PV model, the experiment requires the collection of the ambient data: solar radiation, wind speed and direction, PV module temperature, ambient temperature, humidity and ambient pressure.

All the measurements related to the PV outputs are independent from the ambient measurements; in this way the on line weather station, which will be one of the natural future steps, will not be in conflict with the measurements from the PV required for this and possible future studies. The detailed VI is presented in Appendix A. The hardware set up for measuring the I(V) characteristic has been already explained in section 3.3; at the beginning it was necessary to record the I(V) characteristic for only one module and collect the data input for testing the response of the model. A second code has been written to measure the I(V) characteristic of the PV array; the main structure of the code is essentially the same as for the PV module but with few changes. First of all the power supply now is driven by a larger signal which includes the current measurements from the short circuit current to the open circuit voltage of the PV array (88 Volts);

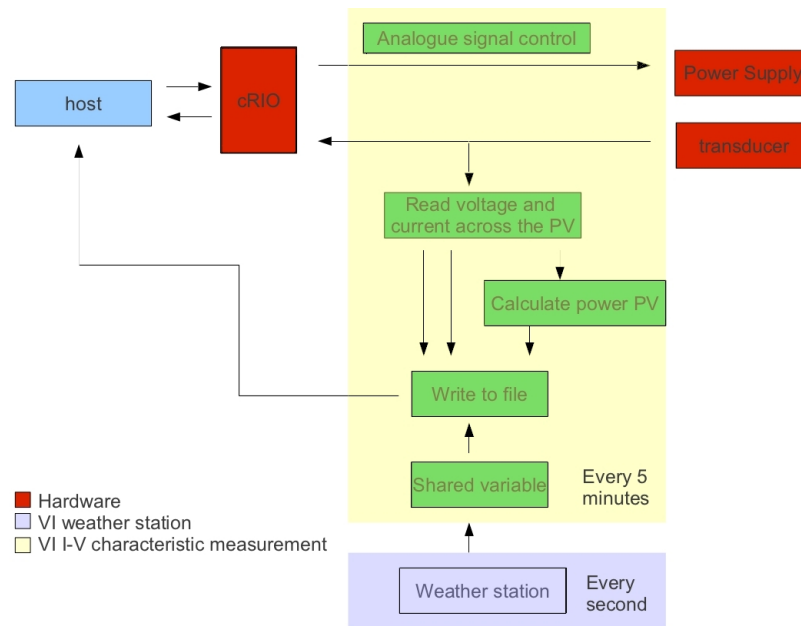


Figure 3.5: Flowchart of the program setting.

second, the variables collected include also all the PV temperatures measured at the back rear of each PV module.

Measuring the short circuit current and the spectrum of the sun

Another test for a future work has been developed with the same principles of the previous one: synchronize the electrical, ambient and physical data from different VI. This study concerns the spectral response of the PV module and it requires: the spectrum of the sun, the short circuit current and the ambient variables to determine the cell temperature (wind speed, diffuse and global radiation, ambient temperature and the temperature measured at the back rear of the PV module).

Again the software has to control the output of the power supply while reading the ambient data listed above without interrupting the normal running of the VI for the weather data monitoring.

Weather data monitoring

In the VI described previously shared variables have been mentioned. A shared variables are configured software items that can send data between VIs. The general idea for the setting of the microcontroller is monitoring continuously the ambient data and select the various VI in function of the electrical data needed for the test to run. Fig.3.6 is the front diagram where the data can be seen in real time.

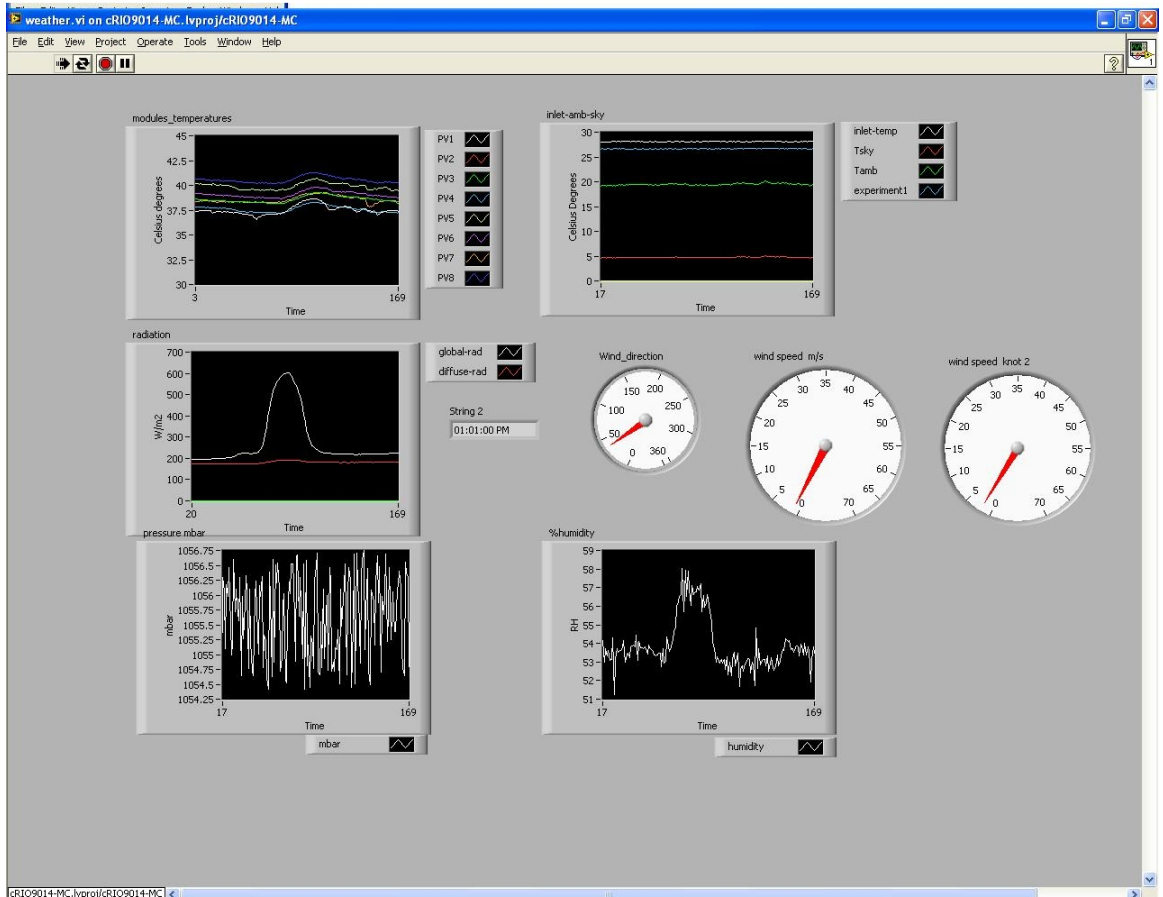


Figure 3.6: Front diagram for the monitoring of the weather data. It includes the radiation measurement, wind speed and wind direction, the modules temperatures and the ambient temperature. The pressure sensor data are too high due to the fact the sensor was broken at that time. *Inlet-temp* is the temperature measured inside the test rig; *Tsky* is the sky temperature calculated. The time is in seconds.

The VI files explained in this section are the last to have been developed due to the new version of Labview; in fact, the version used before was the Labview 2005 and for that version the FPGA code had to be written for each of the module. This part will be skipped due to the fact nowadays it is obsolete and the new version of Labview already provides the FPGA code for each module and even the output of each channel can be selected from a variety of solution simply opening the properties of the module i.e. for the thermocouples: in the old version the FPGA code had to be written for the module NI9211 than, in the *target* VI a specific code had to be determined for the specific kind of thermocouples (J type) and finally write the code concerning the acquisition and storing of the temperatures collected. With the new version instead, only with a right-click on the module, it is possible to select the kind of thermocouple and, the FPGA code with the calibration for the type selected, will be automatically generated.

3.5 Background and issues with the PV test rig

The roof experiment was installed around July 2008 and the first data have been collected at the end of August 2008. At that time only the module temperatures were acquired by the c-RIO. The system was implemented with the two pyranometers after being re-calibrated in March 2009 and the code for the spectroradiometer has been written with the help of one MSc student. The four quadrants power supply was purchased in February 2009, but after two months of trying in vain to program its digital card it has been figured out that, due to manufacturing error, this power supply could not be controlled digitally. The instrument came back from the company supplier in August 2009 and finally in September of the same year could be adapted for our purpose through use of analogue control. Unfortunately an instrument fault occurred in 2010 and 4 months were lost while it was repaired.

The last instrumentation to be installed was the anemometer, wind vane, humidity and pressure sensor. The installation of the anemometer and wind vane was finalized only in January 2011 due to extreme cold and snow during the winter.

3.6 Conclusion

This chapter includes the description of the outdoor test experiment at Strathclyde University.

The work done in setting up the PV test experiment was crucial for the development and the validation of a PV array model. The large amount of the data in fact, allowed the validation of the model created and the use of the *shared variable* helped in collecting only the needed data.

It was useful to set up the experimental system so that PV system data could be collected separately from the ambient data. In fact this specific arrangement permits the creation of an on line weather station without excluding the possibility of running other experiments. In this way it has been possible also to monitor ambient conditions giving important information about the variability of the radiation and the temperature for this particular climate.

4

Modelling photovoltaics

To assist the development of the converter and the tracker for the MPP, it has been decided to develop a model able to reproduce realistically the I(V) characteristic from photovoltaics for any real operating conditions as described in Chapter 2 for partial shading, fast irradiance changes, thermal and electrical mismatch.

The data collected from the test rig detailed in Chapter 3 will be used to validate the model for the PV array.

The validated model of the PV array, that represents the outdoor test experiment on the roof comprising eight BIPV modules, has been used to train and test the artificial neural network (details in Chapter 6), which will be implemented in the algorithm to track the MPP.

The modelling has been developed to predict the behaviour of the PV array and specifically the response of the array installed on the roof at Strathclyde University to real operating conditions.

The chapter has been divided in three sections as follows:

- physical based model development section includes a description of the 2-diodes model with the procedure to determine the value of the solar cell parameters.
- Thermal modelling section. An overview of the existing thermal model to predict the cell temperature for the BIPV.
- Implementation of the model in Orcad with PSpice simulator and the manipulation of the input and output data. The manipulation of the data will be detailed in AppendixC.

4.1 Development of detailed physics based model of PV system

The behaviour of solar cells can be represented in different ways; in the literature there are many examples of more or less complexity for the prediction of the I(V) characteristic of a solar cell for different environmental conditions.

The electrical properties of a solar cell can be analyzed using a simple equivalent circuit which includes mostly all the effects in the solar cells while generating current. First the scale of the model has to be decided; the I(V) characteristic needed is the output from a photovoltaic array and, depending on the precision required, the model can be created considering only the array, or creating a model for each single PV module reproducing the electrical connection, or built up a model cell by cell.

This study concerns only the modelling of crystalline solar cells; other technologies have a different behaviour so their electrical models are different. The ideal equivalent circuit for a solar cell comprises two components: a generator that reproduces the value of the current as function of the technology and the environmental conditions (solar radiation and temperature); and a diode to represent the minority and majority carrier currents.

The most common electrical model used for crystalline PV (either cell or module) is the one diode model (Fig.4.1). This model is easy to implement and it does not really need specific measurements to determine the solar cell parameters. Also, the one diode model has a good approximation and it is widely used for simulating the behaviour of PV.

The one-diode model does not take into account all the major factors involved in the process of converting the solar radiation into the electricity. It includes three components: a source that reproduces the current available; a diode which the current is determinate by the technology and the temperature and a resistor, to represent the losses for the transportation of the electricity. It is also very usual that the one diode model includes a second resistor, called shunt resistor as shown in Fig.4.1.

The components of the circuit affect the output of solar cell and they are: the current generator, series resistance, shunt resistance, diode and diode2.

4.1.1 Current generator or photocurrent

The process of the absorption of incident photons creates electron-hole pairs. An incident photon with energy greater than that of the band gap creates an

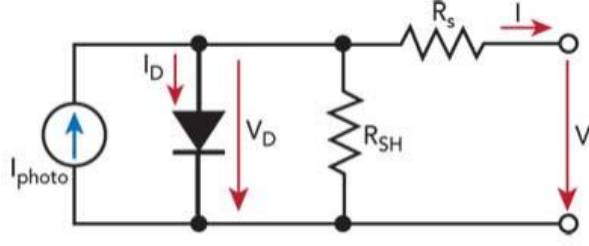


Figure 4.1: Equivalent circuit for a solar cell.

electron-hole pair. However, electrons (in the p-type material), and holes (in the n-type material) are meta-stable and will only exist, on average, for a length of time equal to the minority carrier lifetime before they recombine. In case that the carrier recombines, the electron-hole pair generated by the photon with enough energy is lost and no current can be generated. The structure of the p - n junction prevents this recombination effect spatially separating the electron and the hole thanks to the existing electric field between the junction (due to the positive and negative charge of the layers created by the doping). If the light-generated minority carrier reaches the p - n junction, it is swept across the junction by the electric field at the junction, where it is now a majority carrier. If the emitter and base of the solar cell are connected together (i.e., if the solar cell is short-circuited), the light-generated carriers flow through the external circuit.

The value of the photocurrent can be approximated by the value of the short circuit current. Ideally the short circuit current and the photocurrent are identical. Therefore, the short circuit current is the largest current available from a solar cell. Both layers contribute to the generation of the current depending on the geometry and the technology involved as follows:

- Emitter short circuit spectral current density [9]:

$$J_{scE}(\lambda) = \frac{q\alpha\phi_0(1-R)L_p}{\alpha L_p^2 - 1} \left[-\alpha L_p e^{-\alpha W_e} + \frac{S_e \frac{L_p}{D_p} + \alpha L_p - e^{\alpha W_e} \left(S_e \frac{L_p}{D_p} Ch \frac{W_e}{L_p} + Sh \frac{W_e}{L_p} \right)}{Ch \frac{W_e}{L_p} + S_e \frac{L_p}{D_p} Sh \frac{W_e}{L_p}} \right] \quad (4.1)$$

- Base short circuit spectral current density [9]:

$$J_{scB}(\lambda) = \frac{q\alpha\phi'_0(1-R)L_n}{\alpha L_n^2 - 1} \left[-\alpha L_n - \frac{S_b \frac{L_n}{D_n} \left(Ch \frac{W_b}{L_n} - e^{-\alpha W_b} \right) + \alpha L_n e^{-\alpha W_b}}{Ch \frac{W_b}{L_n} + S_b \frac{L_n}{D_n S_b h \frac{W_b}{L_n}}} \right] \quad (4.2)$$

These analytic formula are for monochromatic light, so to obtain the total short circuit density of current we need to integrate the summation of the density of current of the base and emitter over the total range of wavelength of the spectrum of the sun as:

$$J_{sc} = \int_0^\infty J_{sc\lambda} d\lambda = \int_0^\infty (J_{scE\lambda} + J_{scB\lambda}) d\lambda \quad (4.3)$$

The production of the electricity is function of the wavelength; the two layers of the solar cell, since they are in a specific position (the emitter in front and the base in the back), receive a different flux of photon since a part of the photons have already interacted (absorbed) with the emitter. The details of the process involved in the $p-n$ junction for the electricity production has been described in section 2.1.2. Being $\frac{hc}{\lambda}$ the photon energy

$$\phi_0 = \frac{I_\lambda \lambda}{hc} = 10^{16} \frac{I_\lambda \lambda}{19.8} \quad (4.4)$$

for the emitter and for the base region the spectral photon flux is

$$\phi'_0 = \phi_0 e^{-\alpha W_e} \quad (4.5)$$

Obviously to obtain the short circuit current the density of current has to be multiplied by the area of the solar cell; the parameters of the equations are listed in Table4.1:

It is not always possible to implement these formulas: the parameters are not always known. Also if the optical parameters are known and the spectrum of the sun can be measured, the implementation of this mathematical model can lead to long simulation times when the model is built up by single solar cells.

The developed model has been based on solar cell behaviour connecting them to reproduce the same array as for the test rig: eight modules series connected (see Fig.4.2) each of them including 18 solar cells.

The photogenerated current has been approximated by the short circuit cur-

Table 4.1: Parameters involved into the equation for the calculation of the short circuit density of current of a solar cell.

<i>Symbol</i>	<i>Name</i>	<i>Units</i>
α	Absorption coefficient	cm^{-1}
$\phi_0; \phi'_0$	Photon spectral flux at the emitter and base-emitter surface	$\text{Photon}/\text{cm}^2\mu\text{m s}$
$L_n; L_p$	Electron/Hole diffusion length in the base/emitter layer	cm
$W_e; W_b$	Thickness emitter/base	mm
$D_n; D_p$	Electron/Hole diffusion constant in the base/emitter	cm^2s
$S_e; S_b$	Emitter/Base surface recombination velocity	cm^2s
n_i	Intrinsic carrier concentration	cm^{-3}
R	Reflection coefficient	

rent with a temperature correction factor:

$$I_{sc} = I_{scref} \frac{G_{tot}}{G_{ref}} + \frac{\partial I}{\partial T} (T_{cell} - T_{ref}) \quad (4.6)$$

where I_{scref} is the short circuit current at STC (Global radiation 1000 Wm^{-2} ; AM 1.5; $T_{cell}=25^\circ\text{C}$); G_{tot} is the value of the global solar radiation falling on the surface (W/m^2); $\frac{\partial I}{\partial T}$ is the temperature coefficient for the short circuit current, considered constant; T_{cell} and T_{ref} are respectively the temperature of the solar cell and the reference temperature of 25°C . This relation shows the behaviour of the electricity production by a solar cell: the current generated is proportional to the solar radiation (even if the process is more complex than that as explained in Chapter 2) and it also includes the effects of the temperature that involves a slightly increasing of the value of the current due to the fact the energy band gap decreases with the growth of the temperature allowing the photon with the lower energy to generate the electron/hole pairs.

However this model is valid only for cells under uniform radiation. Partial shading has huge impact on the performance of the PV cells. Depending on the amount of the area affected by the shading, the performance decreases drastically the amount of the current generated. The impact can be approximated with the shadow factor as:

$$I_{sc}^{shadow} = I_{sc}(1 - S) = I_{sc} \left(1 - \frac{A_s}{A_c} \right) \quad (4.7)$$

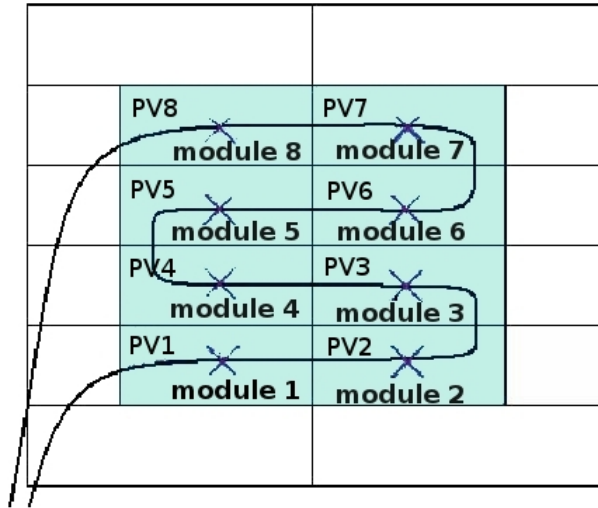


Figure 4.2: Position of the thermocouples and series connection of the PV modules

S is the shading factor that can be calculated from the ratio between the shaded area of the cell A_s and the total cell area A_c [45]. In Chapter 5 the effects of the partial shading will be described more accurately.

4.1.2 Series resistance

One of the main limitations of the model comes from the series resistive losses which are present in practical solar cells [9]. Once the current has been generated by the photons, it has to travel through resistive semiconductor material, in the base generally not heavily doped and in the emitter region which is heavily doped, to reach the contacts. This component includes also the losses caused by the path of the current into metal grid, contacts and current collecting bus.

4.1.3 Shunt resistance

Significant power losses caused by the presence of a shunt resistance, R_{SH} , are typically due to manufacturing defects, rather than poor solar cell design. Low shunt resistance causes power losses in solar cells by providing an alternative current path for the light-generated current. Such a diversion reduces the amount of current flowing through the solar cell junction and reduces the voltage from the solar cell. The effect of a shunt resistance is particularly severe at low light levels, since there will be less light-generated current. The loss of this current to the shunt therefore has a larger impact. In addition, at lower voltages where the effective resistance of the solar cell is high, the impact of a resistance in parallel is large.

4.1.4 Diode

Due to the nature of the p-n junction as explained in Chapter 2, the solar cells transiently produce electricity even in condition of no-light. The effect of the recombination can be represented with a diode and the value of its current can be analytically [9] determined by:

$$J_{darkE} = q \frac{n_i^2 D_p}{N_{Def} L_{Lp}} \left[\frac{S_e \frac{L_p}{D_p} Ch \frac{W_e}{L_p} + Sh \frac{W_e}{L_p}}{S_e \frac{L_p}{D_p} Sh \frac{W_e}{L_p} + Ch \frac{W_e}{L_p}} \right] \left[e^{\frac{V}{V_T}} - 1 \right] \quad (4.8)$$

for the emitter region and for the base region:

$$J_{darkB} = q \frac{n_i^2 D_n}{N_{Def} L_{Ln}} \left[\frac{S_b \frac{L_n}{D_n} Ch \frac{W_b}{L_n} + Sh \frac{W_b}{L_n}}{S_b \frac{L_n}{D_n} Sh \frac{W_b}{L_n} + Ch \frac{W_b}{L_n}} \right] \left[e^{\frac{V}{V_T}} - 1 \right] \quad (4.9)$$

So the total dark saturation density of current can be rewritten as:

$$J_{dark} = J_{darkE} + J_{darkB} = J_0 \left[e^{\frac{V}{V_T}} - 1 \right] \quad (4.10)$$

This is the dark saturation density of current in the quasi-neutral region.

V_T is the thermal voltage and it can be calculated as:

$$V_T = \frac{nkT}{q} \quad (4.11)$$

where k is the Boltzman constant ($8.617343 \times 10^{-5} \frac{eV}{K}$); T is the temperature in Kelvin; q is the Coulomb charge (1.602×10^{-19} coulomb) and n is the ideality factor. As can be noted from equations (4.8) (4.9) (4.10) the dark saturation density of current depends from the geometric parameters and the intrinsic carrier concentration which is related to the conduction and valence band density of states and on the energy band gap of the semiconductors. As can be deduced, different technologies (with different doping) influence the value of the dark saturation current as well as the temperature. The effect of the temperature on the J_0 will be discussed in the next section.

The phenomena of recombination also affects the space charge region and becomes more relevant at lower voltage; for this reason it is necessary to use an auxiliary diode in the model.

Table 4.2: Typical values of the parameters of a silicon solar cell [9].

<i>Parameter</i>	<i>Silicon</i>
n_i (cm^{-3})	1×10^{10}
$W_e; W_b$ (μm)	0.3; 300
$L_p; L_n$ (μm)	0.43; 162
$D_p; D_n$ ($\frac{cm^2}{V}$)	3.4; 36.63
$S_e; S_b$ (cm^2s)	$2 \times 10^5; 1 \times 10^3$
J_0 ($\frac{A}{cm^2}$)	1×10^{-12}
J_{sc} ($\frac{A}{cm^2}$)	31.188×10^{-3}

4.1.5 Diode 2

The ideality factor n (a fitting parameter that describes how closely the diode's behaviour matches that predicted by theory, which assumes the p-n junction of the diode is an infinite plane and no recombination occurs within the space-charge region) for the first diode is normally kept constant at the value of 1 but realistically the ideality factor must be a function of the voltage across the device. At high voltage, when the recombination in the device is dominated by the surfaces and the bulk regions the ideality factor is close to one. However at lower voltages, recombination in the junction dominates and the ideality factor approaches two. The junction recombination is modelled by adding a second diode in parallel with the first and setting the ideality factor typically to two [64]. The dark saturation density of current due to the recombination in space charge region is:

$$J_{02} = q \frac{W_D n_i}{\tau_D} \quad (4.12)$$

and it is bias dependent since the depletion width W_D is function of voltage applied across the device. τ_D is the effective life time in the depletion region.

All the components described above needs to be implementing in the 2-diodes model for a cell:

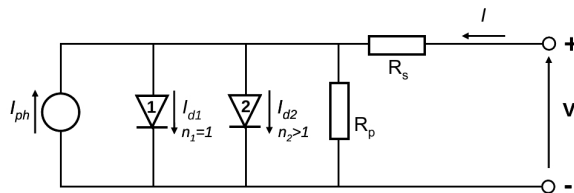


Figure 4.3: 2-diodes equivalent circuit for a solar cell.

The above circuit take into account the series and shunt resistance effect, the

recombination and the non-ideality of the diffusion diode, hence the relationship between the current and the voltage in a solar cell can be calculated as:

$$I = I_{ph} - I_{d1} \left(e^{\frac{V+IR_s}{nV_T}} - 1 \right) - I_{d2} \left(e^{\frac{V+IR_s}{n_2V_T}} - 1 \right) - \frac{V + IR_s}{R_{sh}} \quad (4.13)$$

The shape of the characteristic is determined not only by the physical parameters of the solar cell (see eq. 4.10 4.12 4.3 as well as R_s and R_{sh}) but also from the incident irradiance and the temperature. The effect of the environmental conditions will be shown in the next section.

The I(V) characteristic (eq. 4.13) shows the main parameters to characterize the behaviour of a specific solar cell - short circuit current, open circuit voltage, maximum power point and fill factor. All the manufacture provide these values at STC.

At the condition of open circuit voltage, all the current produced by the solar cell I_{ph} is flowing into the diode so, the voltage at the open circuit can be written as:

$$V_{oc} = \frac{kT}{q} \ln \frac{I_{ph} + I_{d1}}{I_{d1}} \approx \frac{kT}{q} \ln \frac{I_{ph}}{I_{d1}} \quad (4.14)$$

because $I_{sc} \gg I_{d1}$. As can be noted from eq 4.14 the open circuit voltage depends on the ratio I_{sc}/I_{d1} since the light generated current increases slightly with higher temperature. The dark saturation current instead, depends from the cube of the temperature so high temperatures involve a reduction of the value of V_{oc} .

The most important factor for the solar cell is the maximum power point (MPP) that corresponds at the maximum power that can be extracted from the solar cell for the specific technology, radiation and temperature. The power at any point of the characteristic is given by:

$$P = VI = V \left[I_{ph} - I_{d1} \left(e^{\frac{V}{V_T}} - 1 \right) \right] \quad (4.15)$$

The power is zero at the short and open circuit conditions for obvious reasons, but there is a point in between that corresponds at the maximum power the solar cell can produce for specific operating conditions (temperature and irradiance)

$$\frac{dP}{dV} = 0 = I_{ph} - I_{d1} \left(e^{\frac{V_{mpp}}{V_T}} - 1 \right) - \frac{V_{mpp}}{V_T} I_{d1} e^{\frac{V_{mpp}}{V_T}} \quad (4.16)$$

with these coordinates:

$$I_{mpp} = I_{ph} - I_{d1} \left(e^{\frac{V_{mpp}}{V_T}} - 1 \right) \quad (4.17)$$

and

$$V_{mpp} = V_{oc} - V_T \ln \left(1 + \frac{V_{mpp}}{V_T} \right) \quad (4.18)$$

In the literature [53] we can find other ways to solve the transcendental equation 4.18:

$$V_{mpp} = V_{oc} - 3V_T \quad (4.19)$$

or

$$\frac{V_{mpp}}{V_{oc}} = 1 - \left(\frac{1 + \ln \beta}{2 + \ln \beta} \right) \frac{\ln(1 + \ln \beta)}{\ln \beta} \quad (4.20)$$

where β is

$$\beta = \frac{I_{sc}}{I_{d1}} \quad (4.21)$$

The fill factor (FF) defines the "quality" of a solar cell. It is the ratio between the maximum power point ($V_M \times I_M$) and the maximum power theoretically available (for an ideal solar cell):

$$FF = \frac{V_{mpp} I_{mpp}}{V_{oc} I_{sc}} \quad (4.22)$$

For a crystalline silicon solar cell the FF generally lies between 0.7 to 0.8. The MPP can be written as:

$$P_M = FF * I_{sc} * V_{oc} \quad (4.23)$$

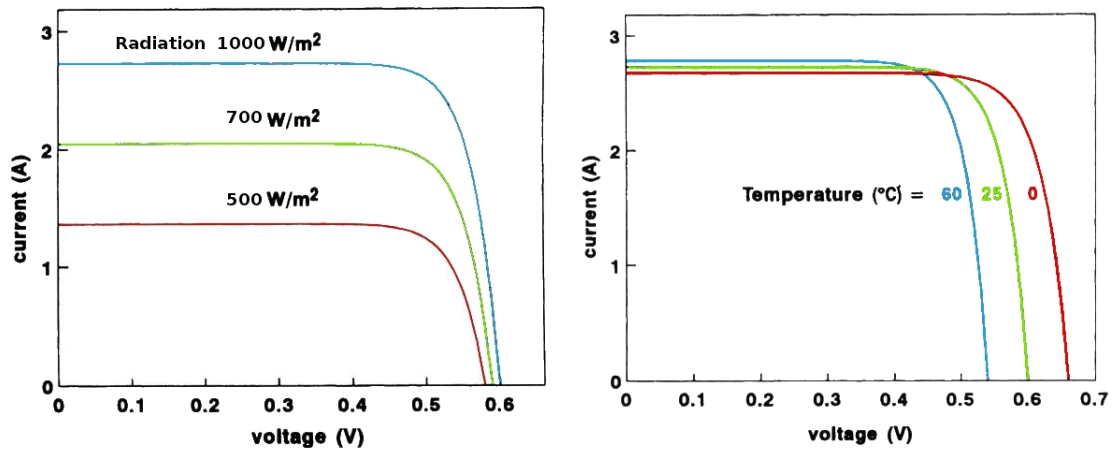
The energy conversion efficiency is defined as the ratio between the maximum electrical power that can be delivered to the load and the power P_L of the radiation incident on the solar cell:

$$\eta = \frac{I_{mpp} V_{mpp}}{P_L} = \frac{FF I_{mpp} V_{mpp}}{P_L} \quad (4.24)$$

4.2 Determination of the solar cell parameters

Temperature and radiation affect the performance of the PV system in different ways. The photocurrent generated is directly dependent on the incident radiation on the PV surface even if the value of the current is strictly related to the kind of radiation. The most important component of the radiation in terms of elec-

tricity production is the direct beam than the diffuse component. For example if global radiation is 300Wm^{-2} it is a cloudy day, then a PV cell will produce less photocurrent generated than for a clear sky day with the same global radiation.



(a) Effect of the global radiation variation. (b) Effect of the temperature on the PV performance.

Figure 4.4: Effect of the radiation and temperature on the $I(V)$ characteristic.

Fig.4.4(a) shows the effects of the radiation on the $I(V)$ characteristic, not only the short circuit current is affected by lower or higher irradiance but also other parameters as well as the MPP (and consequently the Fill Factor) and the open circuit voltage even if the last term has a logarithmic dependence so the increase or decrease is small. The output voltage of a PV cell is directly related to the energy of the electrons promoted or excited into the conduction band. The higher the bandgap, the greater the energy of the electrons in the conduction band must be. The voltage of a solar cell depends first of all on the technology and physics of the material used, but, its performance is degraded by the increasing of the cell temperature. Like all other semiconductor devices, solar cells are sensitive to temperature. Increases in temperature reduce the band gap of a semiconductor, thereby affecting most of the semiconductor material parameters. The decrease in the band gap of a semiconductor with increasing temperature can be viewed as increasing the energy of the electrons in the material. Lower energy is therefore needed to break the bond. In the bond model of a semiconductor band gap, reduction in the bond energy also reduces the band gap [64]. Therefore increasing the temperature reduces the band gap; this is why the PV cells show a small increase in the short circuit current due to the temperature.

There are a variety of methods for determining the parameters which determine the non-linear model of solar cells, based mainly on the $I(V)$ characteristic.

For the physical based approach described in the previous section in fact some parameters must be determined including the series and shunt resistance, the dark saturation current, the current for the second diode and the ideality factors for both diodes. Before illustrating the procedure for the determination of these solar cell parameters it will be useful to introduce the effects they have on the I(V) characteristic.

4.2.1 Series resistance

The main impact of series resistance is to reduce the fill factor, although excessively high values may also reduce the short-circuit current. Series resistance does not affect the solar cell at open-circuit voltage since the overall current flow through the solar cell, and therefore through the series resistance is zero. However, near the open-circuit voltage, the IV curve is strongly affected by the series resistance. To understand that, the equation of the power delivery from a solar cell is expressed as a function of R_s

$$P'_m = P_m - I_m^2 R_s = P_m \left(1 - \frac{I_m}{V_m} R_s \right) \quad (4.25)$$

where P_m is the MPP for an ideal solar cell. Assuming $I_m/V_m \approx I_{sc}/V_{oc}$ eq.4.25 becomes:

$$P'_m = P_m \left(1 - \frac{I_{sc}}{V_{oc}} R_s \right) = P_m (1 - r_s) \quad (4.26)$$

where r_s is the normalized series resistance

$$r_s = \frac{R_s}{V_{oc}/I_{sc}} \quad (4.27)$$

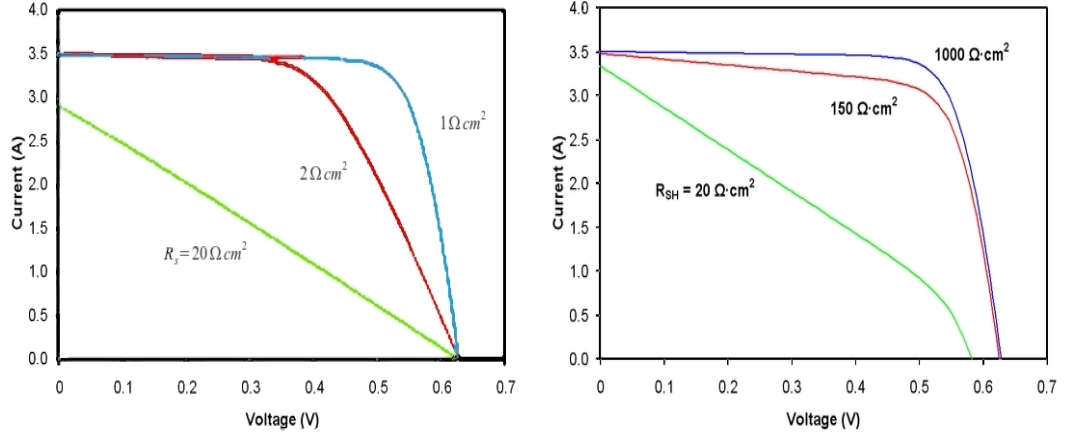
Rewriting the eq.4.26 in terms of FF:

$$FF = \frac{P'_m}{V_{oc} I_{sc}} = \frac{P_m (1 - R_s)}{V_{oc} I_{sc}} = FF_0 (1 - r_s) \quad (4.28)$$

Eq.4.28 highlights how much the increasing of the series resistance will degrade the fill factor. Fig.4.5(a) gives an idea of the degradation.

4.2.2 Shunt resistance

As shown for the series resistance, the degradation of the fill factor can be expressed in terms of the shunt resistor. Thus the output power from the solar cell can be calculated as the power without the shunt resistor minus the losses due to



(a) Effect of series resistance on the I(V) characteristic.

(b) Effect of the shunt resistor.

Figure 4.5: Effect of the parasitic resistances of a solar cell.

R_{sh}

$$P'_m = P_m - \frac{V_m^2}{R_{sh}} = P_m \left(1 - \frac{I_m}{V_m} \frac{1}{R_{sh}} \right) \quad (4.29)$$

And in the same way as for the series resistor normalized we obtain:

$$FF = FF_0 \left(1 - \frac{1}{r_{sh}} \right) \quad (4.30)$$

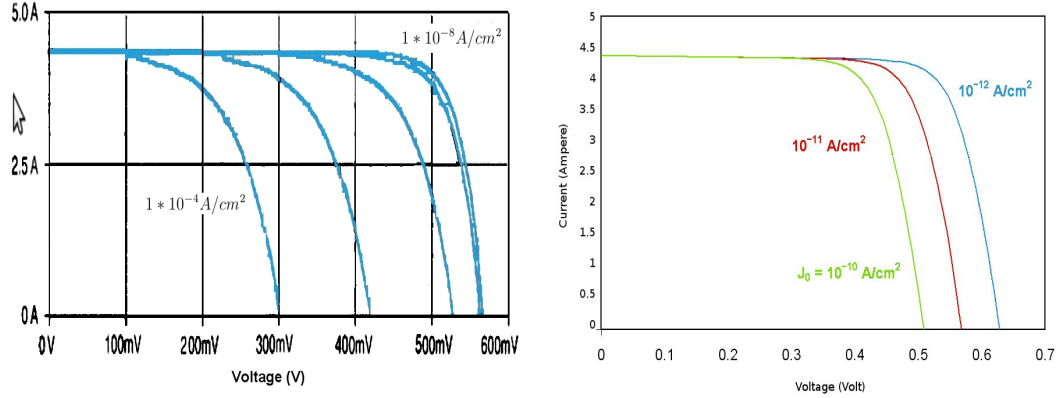
Fig.4.5(b) illustrates the losses due to the shunt resistor for different values.

4.2.3 Second diode or recombination diode

When the recombination diode predominates, the I(V) characteristic is also heavily degraded, both in the open circuit voltage and in the FF, meanwhile the short circuit current remains constant. Fig.4.6(a) shows the effects of different values of I_{d2} on the I(V) characteristic.

4.2.4 Dark saturation current

The operating temperature has a strong effect on the electrical response of solar cells. Taking into account that in terrestrial application, solar cells can easily warm up to 60-65°C and that in space or satellite application temperatures can be even higher, it follows that a proper modelling of the temperature coefficients of the main electrical parameters are mandatory [9]. In the electrical model the effect of the temperature is included in the value of the dark saturation current



(a) Effect of the recombination diode on the $I(V)$ characteristic. (b) Effect of the temperature on the dark saturation current.

Figure 4.6: Effect of the different values for the diodes in the electrical model.

as follows. The p-n junction reverse saturation current is given by:

$$I_{d1} \approx CAT^3 \exp\left(-\frac{E_g(T)}{kT}\right) [mA] \quad (4.31)$$

where

$$E_g(T) = E_g(0) - \frac{\alpha T^2}{T + \beta} \quad (4.32)$$

The parameters are T (K) temperature, k Boltzman's constant E_g (eV) the energy band gap, A (cm^2) is the area of the solar cell, and C a parameter that depends on geometrical factors. C is assumed to be constant for a given material and its variation with the temperature is neglected. An average value for C of $17.9 \text{ mAcm}^{-2}\text{K}^{-3}$ for Si and GaAs, based on experimental data, has been taken for the calculation [35].

4.2.5 Ideality factor

The ideality factor of a diode is a measure of how closely the diode follows the ideal diode equation. The derivation of the simple diode equation uses certain assumption about the cell. In practice, there are second order effects so that the diode does not follow the simple diode equation and the ideality factor provides a way of describing them.

The ideal diode equation assumes that all the recombination occurs via band to band or recombination via traps in the bulk areas of the device (i.e. not in the junction). Using that assumption the derivation produces the ideal diode equation below and the ideality factor, n , is equal to one.

However recombination does occur in other ways and in other areas of the device. These recombinations produce ideality factors that deviate from the ideal.

I(V) characteristics for solar cells can and have in the past been obtained by three different methods.

The most commonly used method applies a fixed illumination and connects the solar cell to a resistive load which is varied between short circuit and open circuit conditions. Under these conditions the voltage across the solar cell terminals and the current out of its terminals can be measured. This method of measurement applies to the solar cell in its normal PV mode of operation. In this test, the solar cell behaves as a current generator so the I(V) characteristic measured is in the fourth quadrant (negative values of the current and positive values of the voltage) of the current-voltage plane.

In the second method the I(V) characteristic of a solar cell is measured without application of any illumination, but by supplying D.C. power from an external bias supply following the same procedures as for testing a diode. The I(V) characteristic measured in this manner is called "diode forward characteristic". The voltage across the solar cell terminals and the current flowing into these terminals are measured. The characteristic obtained by this method falls into the first quadrant (current and voltage have positive values) of the current-voltage plane.

There is also a third method to measure the I(V) characteristics from a solar cell which is more sophisticated than the previous two. The illumination applied on the solar cell has a variable light intensity. The amount of the illumination does not have to be known, if the value of the light generated current I_L can be determined. This condition is fulfilled when the magnitude of the cell series resistance is sufficiently small so that the output current of the device, when measured by the photovoltaic output method, is constant for all terminal voltages between 0 and 1 Volt. For this method the circuit for measuring the I(V) characteristic consist of a switch, which determines the short circuit and open circuit conditions, a high resistance voltmeter across the terminals of the solar cell and a low resistance milliamperemeter. The measurement consists of determining the I_{sc} which under the presented conditions approximates the light generated current I_L , and the open circuit voltage for every light intensity setting. Each pair of corresponding short circuit current and open circuit voltage values is plotted as one point in the first quadrant of the current-voltage plane. Through the variation of the light intensity, a succession of such points is obtained which presents the desired current-voltage characteristic [57].

The three methods described above are the recommended techniques to mea-

sure the $I(V)$ characteristic of a solar cell and from the measurements obtained the parameters of the solar cell may be extrapolated. As already mentioned, the experiment includes eight solar modules thus the measurements for determining the solar cell parameters could be done using single module. Strathclyde University has a solar simulator but it cannot be used for such measurement for several reasons: the value of the light emitted by solar simulator is manually controlled and the indicator the radiation value is a gauge indicator which does not assure the exact value generated, plus the room has a window to cool down its temperature but the presence of that window might influence the electricity production of the PV due to outside light coming in; also the air temperature cannot be kept constant because the test room does not have air conditioner. Because an indoor test was not possible, a series of $I(V)$ characteristics have been recorded and from them the parameters have been identified.

The slope of the $I(V)$ characteristic gives the values of the series resistance and shunt resistor as indicated in Fig.4.7. It is possible to approximate the series and shunt resistances, R_s and R_{sh} , from the slopes of the $I(V)$ curve at V_{oc} and I_{sc} , respectively. The resistance at V_{oc} , however, is at best proportional to the series resistance but it is larger than the series resistance. R_{sh} is represented by the slope at I_{sc} .

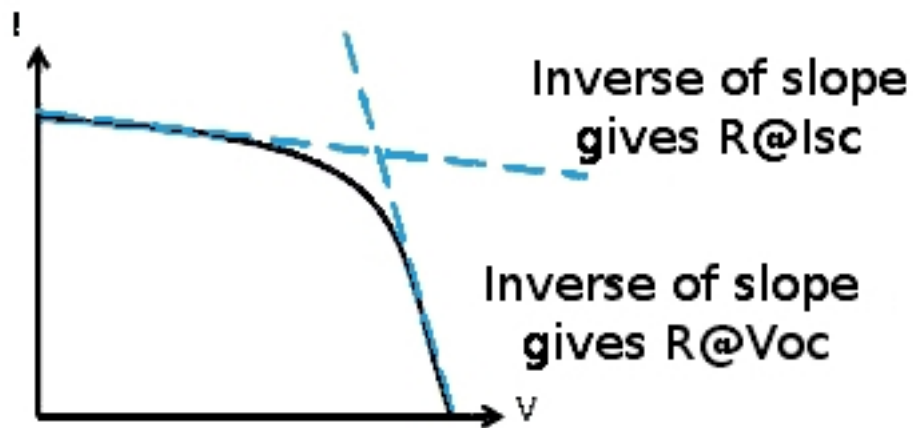


Figure 4.7: The graph shows how the two resistors, R_s and R_{sh} , can be extrapolated from the $I(V)$ characteristic.

The values of the dark saturation current as a function of the PV temperatures following eq.4.31, have been calculated and recorded in a spreadsheet. Section4.4 provides details of how the value of the dark saturation current has been implemented in the electrical model. The current for the second diode has

been calculated as follows [25]:

$$I_{d2} = \frac{1}{\beta} \left(\frac{V_{oc} - I_{sc}R_s}{R_{sh0} - R_s} - I_{sc} - \alpha I_{d1} \right) \quad (4.33)$$

where

$$\beta = e^{I_{sc}R_s/n_2V_t} \left(1 + \frac{V_{oc} - I_{sc}R_s}{n_2V_t} \right) - e^{V_{oc}/n_2V_t} \quad (4.34)$$

and

$$\alpha = e^{I_{sc}R_s/n_1V_t} \left(1 + \frac{V_{oc} - I_{sc}}{n_1V_t} \right) - e^{V_{oc}/n_1V_t} \quad (4.35)$$

All the parameters in the eq.4.33-4.35 have been kept constant and calculated by their values at STC due to the fact the variations in I_{d2} does not introduce a large error and the implementation of the model with different values of its current would be too complicated to develop.

4.3 Thermal model

Sec.4.1 describes the PV model; this model implies the use of the irradiance and the cell temperature. The incident irradiance has been calculated based on the measurements of the global and diffuse radiation on the horizontal and position and tilt angle of the PV, but the cell temperature cannot be measured so it has to be estimated with a thermal model.

The module receives heat from the radiation, S , and loses heat in the form of convection to ambient, T_a , and radiation to the sky and ground, T_s and T_g .

Several authors have modelled the temperature of a PV module by evaluation of energy inputs and outputs through radiation, convection, conduction and power generated [29]. In 1987 Fuentes developed a computer model that predicts the cell temperature of a photovoltaic array to within 5°C and uses the INOCT (Installed Nominal Operating Cell Temperature) to characterize the thermal properties of the module and its mounting configuration [18].

A simpler empirically-based thermal model was more recently developed at Sandia. The model has been applied successfully for flat-plate modules mounted in an open rack, for flat-plate modules with insulated back surfaces simulating building integrated situations, and for concentrator modules with finned heat sinks. The simple model has proven to be very adaptable and entirely adequate for system engineering and design purposes by providing the expected module

operating temperature with an accuracy of about $\pm 5^\circ\text{C}$.

$$T_m = G(e^{a+bWS}) + T_a \quad (4.36)$$

T_a is the ambient air temperature, ($^\circ\text{C}$); WS is the wind speed measured at standard 10-m height, (m/s); a is an empirically-determined coefficient; b is an empirically-determined coefficient. The relationship given in eq.4.36 is based on an assumption of one-dimensional thermal heat conduction through the module materials behind the cell (encapsulate and polymer layers for flat-plate modules). The cell temperature inside the module is then calculated using a measured back-surface temperature and a predetermined temperature difference between the back surface and the cell [32].

However the PV system model has been simulated using the value of the temperature measured by thermocouples at the back of each single module because some instrumentations were still missing (wind vane and anemometer).

4.4 Implementation in Orcad-PSpice simulator

To model the behaviour of photovoltaic array, a 2-diode model has been developed in the Orcad platform implementing PSpice. Orcad is a software tool suite used primarily for electronic design automation; PSpice is a SPICE (Simulation Program with Integrated Circuit Emphasis) analogue circuit and digital logic simulation program. All the factors that significantly influences the output power from the photovoltaic array are represented. The model developed for representing the behaviour of polycrystalline solar cell has been then extended to represent the outdoor experiment (see Chapter 3) composed by eight BIPV modules series connected. These modules have 40Wp at STC.

From eq.4.6 the generation of the current depends on the total incident irradiance and the variation of the temperature.

As mentioned in section 4.1, the temperature of the cell changes the value of the energy band gap of the silicon (higher values of temperature involve lower energy band gap) allowing more photons (with lower energy) to generate electricity. To represent this behaviour of the solar cell the model implements two current sources connected in parallel. The outputs of the sources are controlled by 2 different files. The first file contains the value of the short circuit current calculated from the value of the total incident irradiance on the cell surface; the second file contains the calculated current generated by temperature. Let's call the two files "A" and "B".

819			815					810	718				714				710
81		83						89	71				76				79
518					513			510	618							611	610
51		53						59	61			64					69
418						412		410	318	317							310
41	42							49	31						37		39
118	117	116	115	114	113	112	111	110	218						212		210
11	12	13	14	15	16	17	18	19	21	22	23	24	25	26	27	28	29

Figure 4.8: Cells' name and their position

"A" should contain the value of the short circuit current due to the incident radiation on the surface (first term of eq.4.6) as function of the technology of the specific solar cell. In case of uniform radiation, the only needed parameter is the incident radiation calculated from the measured horizontal radiation. To predict the value of the short circuit current a programming code has been used to help in selecting the values synchronized with the measurements of the I(V) characteristics (normally recorded every 5 minutes) and to generate each file for each cell of the PV array with the specific format and structure.

Each file will be created specifically for single cell which has its own name as function of the position in the module as shown in Fig.4.8.

"B" is the file that contains the adjustment of the value of the electricity due to the temperature (second term of eq.4.6). The I(V) characteristics can be measured from the entire array or from a single module and the temperature is measured at the back of each tiles. This setting does not allow evaluating the performance of each solar cell either different values of the temperature so it has been decided to implement the effect of the temperature in the electricity production as a current generator where the value of its current is the same for all cells of the module. At the beginning of the modelling, the wind vane and the anemometer were not implemented yet so the measured temperature on the back of each module has been used as temperature of the cells in the module. Of course this assumption introduces some errors in the value of the cell temperature, but

still in an acceptable range.

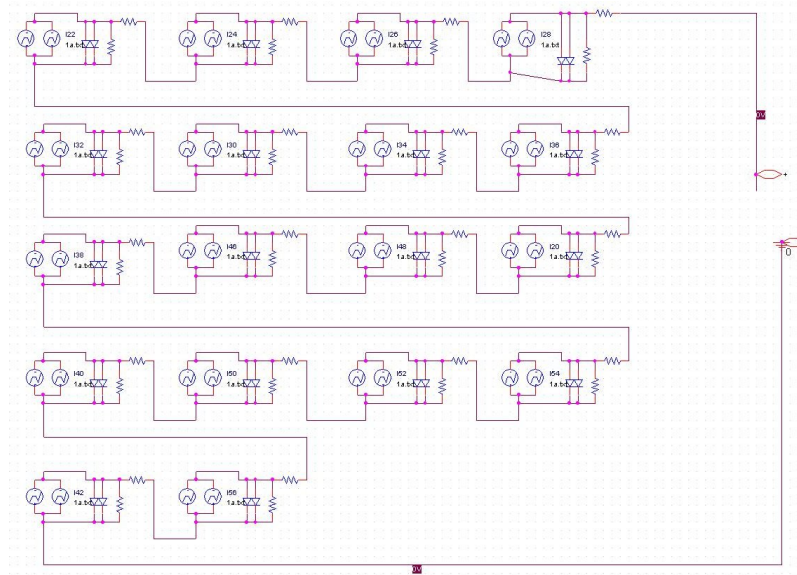
Each module of the array contains 18 cells. The value of the dark saturation current could be established for each cell but the measurement does not provide enough data to estimate the temperature of each cell so each module has been simulated assuming a uniform temperature. Of course due to the different generation of the current across the cell area there are different values of temperature also on a single cell, but assuming homogeneous temperature introduces only a small error ($\approx 2\text{mV}$ per Celsius degrees in the V_{oc}).

To represent the thermal mismatch, the diode 1 of each module has been equipped with its own current value. PSpice provides tool to manage the parameters of some electrical component. Based on this feasibility, that diode has a different name as function of the module in which is inserted and its current value is fixed by the module's temperature measured. The ideality factor has been set at the same value for all the modules but the dark saturation current has been selected from the lowest values of the temperatures shown by the modules and fixed as the reference current. Then the simulation has been run for different temperatures respecting the values measured.

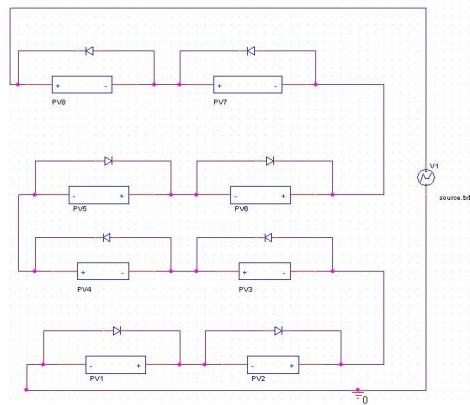
From measured data the temperatures of the modules have been observed: the modules have different temperatures, depending on the ambient parameters, and their difference does not exceed $\pm 5^\circ\text{C}$. Normally this difference in temperature between the modules is constant in time; for this reason the dark saturation current may be set as explained previously.

Once the value of each dark saturation current of each module has been set at the lowest value, in Orcad platform it is possible run the temperature sweep option for the "Time Domain" (transient) simulation. Each simulation has been run for the average temperature measured.

Once the 18 cells have been built following the 2 diode model, each of the parameters has been inserted in a library model (R_s , R_{sh} , I_{d1} , I_{d2}) within their values. Once all the current sources (one per cell) for representing the photocurrent generation have their own name as function of their position and the current generators representing the adjustment of the short circuit current value due to the temperature (assuming uniform temperature in the module they have the same current values for all the cells of the module) the parallel connection between the current generators can be done. Following the electrical connection of the BIPV module used for this experiment, the 18 cells has been connected in series having so only two connectors as shown in the Fig.4.9. In real operating conditions the incident irradiance can be non-uniform and sometimes the PV



(a) PSpice implementation of one PV module.



(b) Structure of the PV array based on the installation of the PV test rig in Strathclyde.

Figure 4.9: Graphical view of the PV array implemented with Orcad platform.

system can be affected by partial shading; these situations result in a dramatic reduction in the output power. For series connection in fact the available current is limited by the current of the solar cell with the lower current caused by a lower radiation or by partial shading. This effect is normally avoided with the by-pass diode that can be placed across every cell but the use of too many bypass diodes increases the price of the manufacture. Normally a by-pass diode is used for a group of cells. Depending on the manufacture, modules have one or more by-pass diodes. The PV modules used in this experiment have only one by-pass diodes. These 8 bypass diodes have been integrated in the array model. The value of the current for the by-pass diode has been fixed at $1e-06A$ and the ideality factor

at 1. The effect of the hot-spot, partial shading and the benefit of the by-pass diode will be described in detail in Chapter 5.

Once the model has been created and tested for STC (verifying that the I_{sc} , V_{oc} , I_{mpp} , V_{mpp} , and MPP correspond to the values on the data sheet of the module), a sub-circuit has been generated that contains all the cells with the library parameters. This procedure has been repeated for the eight modules creating at the end a file with all the modules that includes all the sub-circuits.

Once the model for the array has been implemented, the simulation parameters have to be defined. Generally to obtain the I(V) characteristic it is common practice to run a "DC analysis" in PSpice with a voltage source connected at the terminals that sweeps its value from zero up to the open circuit voltage within a given step size increment.

Simulate one PV characteristic at time requires too long time. To overcome this problem, the functions which drive all the current and voltage sources in the model have been written in such a way the software simulates the data within the time. Every I(V) characteristic can be scan (calculate by the software) in one second which means all the values of the current and temperature are kept constant during the calculation of the characteristic. Thus to run a simulation which includes several I(V) characteristics, some adjustments have been done as follows.

PSpice is a tool that only handles electrical magnitude so the non-electrical variables have to be converted in equivalent electrical. This problem has been solved implementing PWL (Piecewise Linear) source for the current generator which reproduces step output as function of the time and the values defined in files which control the source output. The array has been connected to another PWL voltage source that sweeps its output from zero to V_{oc} during the time.

Finally the "DC analysis" can be run and works in this way: every second of simulation (that simulates the current and the temperature of each I(V) characteristic measured every 5 minutes by the power supply), PSpice takes as input the short circuit current of each cell (constant for 1 second) plus the value of the current generated by the temperature and the PWL voltage source sweeps its output from zero to V_{oc} . So each second simulates an I(V) and power characteristic. The time step it is fixed at 1 millisecond that assures a resolution of 90 millivolts.

This arrangement of the input data allows the calculation of multiple IV characteristics in one go in contrast to the way this is done with PSpice (one simulation for each I(V) characteristic).

4.5 Data selection: Input and output data

As explained in Chapter 3 the software to control the instrumentation and monitor the climate data was initially programmed without any shared variables. That implied an additional work to select the data before being used. The validation of the model in fact requires that the solar radiation and the temperatures measured are synchronized with the measurements of the I(V) characteristic. The radiation and the temperatures were recorded every second by the data logger whereas the I(V) characteristics were collected once every 5 minutes.

With that setting, only the climate data measured at the same time of the I(V) characteristic needed to be selected. To handle it, a series of scripts in bash (described in AppendixC) have been used to extrapolate the synchronized measurements. To select the appropriate data, a variable has been defined in bash that corresponded to the time of each I(V) characteristic measured. This variable was then compared within the first column of the file containing the measured radiation (diffuse and global) and the one with the measurements of the temperatures. Only when the variable and the value of the first column (representing of course the time as well) matched, the script wrote on a new file only those synchronized values, ignoring all the others data. This script of course reduced the time needed to select the data for the simulation. Later on, the data logger has been programmed again and the use of the shared variables made the process easier because the data logger already select the synchronized inputs (radiation and temperature) needed for the simulation without using any script. The script for selecting the measured data has been included in the AppendixC.

The radiation is measured on the horizontal plane but the PV array is installed with a tilt angle of 40° . The incident radiation on a surface depends on the angle between the sun and the surface in object, but this angle is not constant during the day and it will not be the same for every day of the year. For the model used (eq.4.6) the irradiance level has to be calculated. First of all the global radiation measured has been divided in diffuse and direct component.

The beam radiation incident on a surface can be calculated from:

$$G_{bt} = G_b \frac{\cos \theta}{\cos \theta_z} \quad (4.37)$$

where θ is the incident angle, θ_z is the zenith angle and G_b is the radiation on the horizontal plane. Both of these angles depend on the solar position; the time of the day and the day of the year pay an important role. The incident angle can be calculated from the formula below [15]:

$$\begin{aligned}\cos \theta = & \sin \delta \sin \phi \cos \beta - \sin \delta \cos \phi \sin \beta \cos \gamma + \cos \delta \cos \phi \cos \beta \cos \omega + \\ & + \cos \delta \sin \phi \sin \beta \cos \gamma \cos \omega + \cos \delta \sin \beta \sin \gamma \sin \omega\end{aligned}$$

The incident angle can be simplified for south facing surface as follows [15]:

$$\begin{aligned}\cos \theta = & \sin \delta \sin \phi \cos \beta - \sin \delta \cos \phi \sin \beta + \cos \delta \cos \phi \cos \beta \cos \omega + \\ & + \cos \delta \sin \phi \sin \beta \cos \omega\end{aligned}$$

and the zenith angle is:

$$\cos \theta_z = \cos \phi \cos \delta \cos \omega + \sin \phi \sin \delta \quad (4.38)$$

The incident and zenith angle depend on the geographical position ϕ , which corresponds to the latitude of the location; the tilt angle β ; the orientation of the module γ (west positive, east negative); the time of the day ω and on the day of the year δ . The hour angle, ω , represents the angular displacement of the sun east or west of the local meridian due to the rotation of the Earth on its axis at 15° per hour (morning negative, afternoon positive) and it is given by the formula:

$$\begin{aligned}\omega = & 0.25T_s - 180 \quad \text{and} \quad T_s = T_{zone} + 4(\lambda_{zone} - \lambda_{loc}) + E_t \\ E_t = & 9.87 \sin(2B) - 7.53 \cos(B) - 1.5 \sin(B) \quad \text{and} \quad B = 360 \left(\frac{n-81}{364} \right)\end{aligned}$$

The equation of the time E_t considers that the speed of the earth on its elliptical orbit is not constant. The declination angle δ is the angular position of the sun at solar noon with respect to the plane of the equator, i.e. the zenith angle at solar noon at the equator (north positive, south negative). As the earth's axis of rotation is not parallel to the axis of the earth's orbit around the sun, but tilted by 23.45°, the declination angle varies in the course of the year between -23.45° and +23.45°.

$$\delta = 23.45 \sin \left[360 \left(\frac{284 + n}{365} \right) \right] \quad (4.39)$$

n represents the day of the year. Since all these angles are varying every minutes, it is obvious that the incident beam radiation on the module must be calculated for the tilt angle (eq.4.37) so the zenith angle and the incident angle have to be calculated as function of the time and the day of the measurement.

Also the amount of diffuse radiation needs to be estimated for the specific tilt

angle since it is measured on the horizontal plane [15]:

$$G_{dt} = G_d \frac{(1 + \cos \beta)}{2} \quad (4.40)$$

A code in Matlab has been written to calculate the solar radiation available on

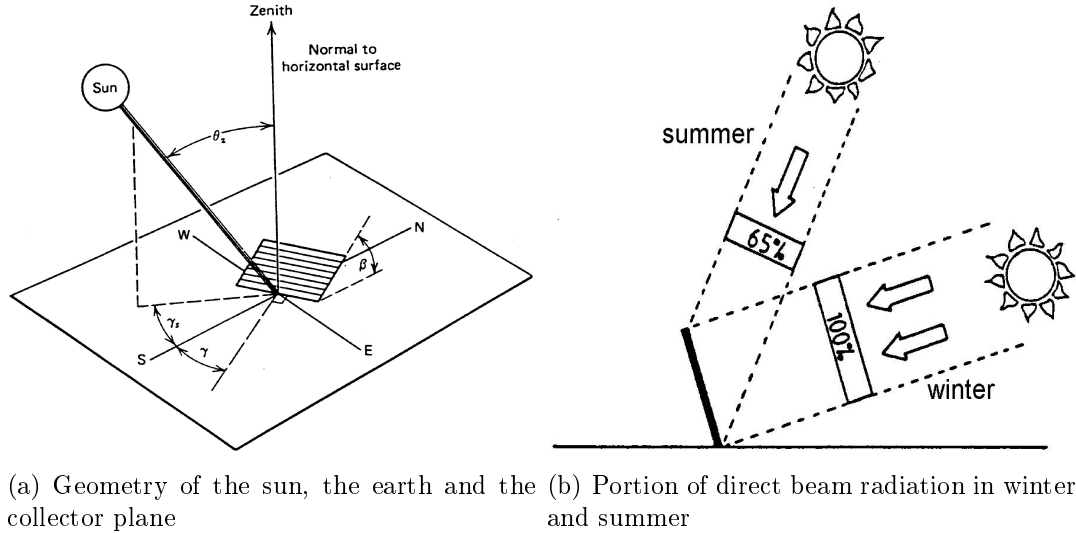


Figure 4.10: Sun angles and direct beam variations. [15]

the module (G_{tot}). The input of the code is a matrix which contains the day of the year, the time of the measurement in hours and minutes, the direct beam and the diffuse component of the measured radiation. This matrix has been created in bash as described at the beginning of this section. The code can be seen in AppendixC. This code generates the values of short circuit current for the cells under uniform radiation and for which are completely shaded.

Once the values of the short circuit current are calculated, the files which drive the output of the PWL current sources of each cell of the array have to be created. Again this process has been optimized with a script which takes as input the value of I_{sc} calculated and create a file for each current source. The name of these files corresponds to cell name (Fig.4.8) and they are composed of two columns: one with the simulation time (seconds) and the second one with the value of current generated calculated by the code in Matlab. In case of partial shading, as explained in the section 4.6, the shaded area has been kept constant for the validation of the model, so, to create the "A" file, different scripts have been used. If the area of the cell is entirely covered by shading, I_{sc} depends only on the diffuse component of the radiation; if the cell is partially shaded the value of the current generated by the radiation is calculated using eq.4.7. More

complex cases of partial shading have been investigated, calculated and developed in Chapter 5 showing the effects of partial shading on the PV array performance.

To create the file "B", another script has been developed; its input is the values of the temperature measured at each module only at the time synchronized with the I(V) characteristic measurements. The script generates a file for each module. Again the first column is the time in second (one second for each I(V) characteristic measured) and the second one contains the value of the current generated by the value of the temperature (second term of the eq.4.6).

The next task is to determine how precise the model can be in predicting the MPP for real operating conditions. To test the performance of the model MPP, I_{mpp} and V_{mpp} have to be determined from the measured I(V) characteristic. To achieve that, another script has been written to identify these values for each step measurement. The results of the simulations instead need to be treated differently to due their arrangement. The output file coming from PSpice (results of the simulation) is a text file with one column for the time and as many column as many temperatures have been simulated; these files require so a different manipulation. The simulation in fact runs continuously and simulates also the seconds where the short circuit current is not constant (between two time steps), so that part of the results has to been cut off. Also the "sweep temperature" tool of PSpice repeats all the simulation for all the temperature set, but these values are in a sequence of time (temperature 1 corresponds to t_o temperature 2 to the t_1 where t_n in the time of the measured I(V) characteristic). Thus the script has to select the proper temperature corresponding to its time of simulation. This script selects at the same time the P_m , I_{mpp} and V_{mpp} with the respect of these rules.

All the scripts can be seen in AppendixC.

4.6 Results

This section will present the results of the simulations for the model described in section 4.4.

In 2009-2010, at the time when the model for the photovoltaic system was validated, the weather station did not include an anemometer (see Chapter 3 section 3.2), used to calculate the temperature of the solar cells (see section 4.3). The anemometer, wind vane, humidity and pressure sensors were installed and programmed only by the beginning of 2011.

Thus the PV system model results have been obtained using the value of

the temperature measured at the back of each single module. The value of the dark saturation current of the diode has been fixed for each module based on its measured temperature as in eq.4.31, so representing thermal mismatch between the modules.

Of course the temperature measured at the back of the module does not correspond exactly to the temperature of the PV cells, and also each cell in a module has its own temperature which is not homogeneous across even the limited area of the cell (depends from the local current production which can vary from point to point). This approximation generates some errors especially for the value of the voltage at the maximum power point due to its direct dependency on the temperature (see eq.4.19).

This results section has been divided into two parts and includes the different setting and different experiments used. A first test has been made for only a single module, comparing the values of MPP, I_{mpp} and V_{mpp} measured with the ones obtained from model of the PV module under uniform irradiance and partial shading. A second test has been made for the entire array for similar conditions, under uniform irradiance and partial shading of the array.

The graphs are presented comparing measured values with simulation model results.

4.6.1 Single module

This subsection presents the results for the single PV module under uniform radiation and partial shading.

Uniform radiation

For these simulations the value of the radiation incident on the single module has been considered uniform and constant during the scan of the I(V) characteristic (i.e. no significant variations of the measurement of the global and diffuse radiation on the horizontal plane).

The results shown from Fig.4.11(a) and 4.11(b), for power at MPP and current respectively, highlight that the simulated values are well correlated and almost linear with the measured data. However for the voltage at the MPP the agreement is poorer with the measured values and with unity gradient, generally larger than the simulated ones (see Fig.4.11(c)). This error is associated with the temperatures used for the simulations. From the results it can be deduced that, for these specific conditions, the measured module temperature was lower than the

values at the cells themselves. This is not surprising in that a temperature gradient between the cell and the module rear surface is to be expected.

The errors of the model have been presented as both absolute and relative values.

Fig.4.12(a) indicates an absolute error in a range of [-1,1] Watts for outputs from 10 up to 24 Watts. The relative error is less than 5% (Fig.4.12(b)).

These errors can be considered reasonable in light of the fact that the measurements also contain some error. The radiation measured is calculated from the pyranometers voltage and due to the nature of the instrument, to the approximation of the photocurrent generated from eq.4.3 to eq.4.6. In this context the accuracy of PV modelling can be considered reasonable. The readings from the pyranometers in fact, are subject to the temperature and humidity variations and these particular instruments have a precision of about 2%. The approximation of the model for the photocurrent generated (eq.4.6) uses the global incident radiation on the PV device, but as shown in section 4.1, the generation of the current of a PV cell depends from the spectrum of the sun and this introduces some further errors. Finally the signal is read by a data logger with a precision of $\pm 1\%$.

Validation of the PV model has also been undertaken using outdoor test data where the weather conditions (radiation and temperature) cannot be controlled and are subjects to variations during the scan period of the I(V) characteristic.

Taking all these issues into account, an absolute error of about $\pm 100\text{mA}$ has been estimated for the current, and for the voltage at the MPP the absolute error is estimated to be in the range of [-100,300]mV, resulting in a relative error of $\pm 5\%$ for the I_{mpp} and between -2% and 3% for the V_{mpp} .

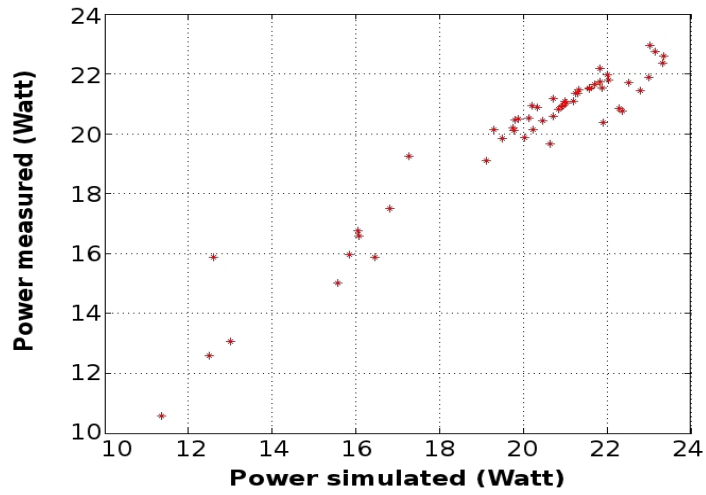
The error in the V_{mpp} derives mainly the cell temperature error as explained previously and also from the error introduced by the measurements and the calculation of the incident radiation (see eq.4.20), despite logarithmic dependency.

The already indicated error in the MPP derived from the model compared with the MPP measured can be considered as a combination of both I_{mpp} and V_{mpp} errors.

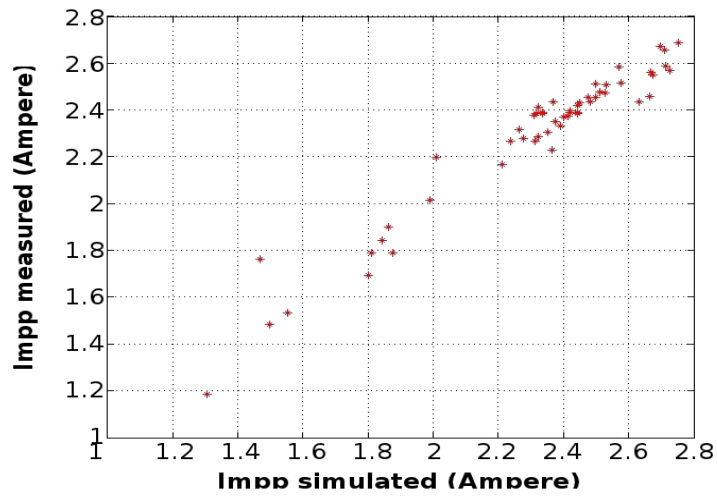
Partial shading

As a key problem affecting the real world performance of a PV system is partial shading which can lead multiple maxima in the power characteristic. Partial shading will be analyzed in detail in Chapter 5.

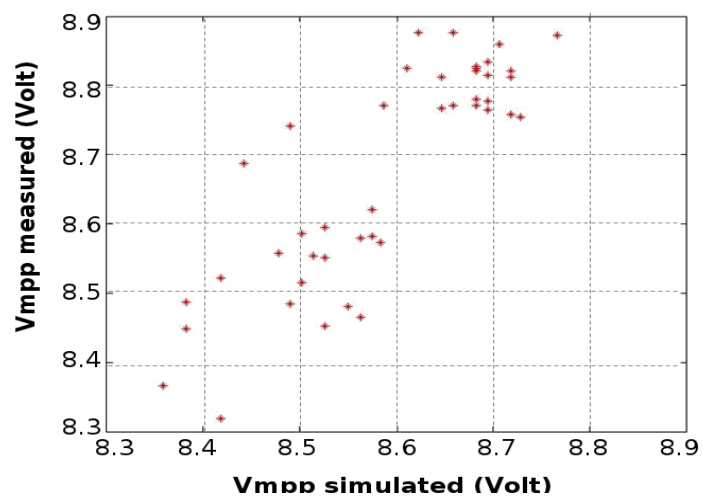
Once the results for the module under uniform radiation were found reasonable



(a) The graph shows the measured MPP over the simulated one.

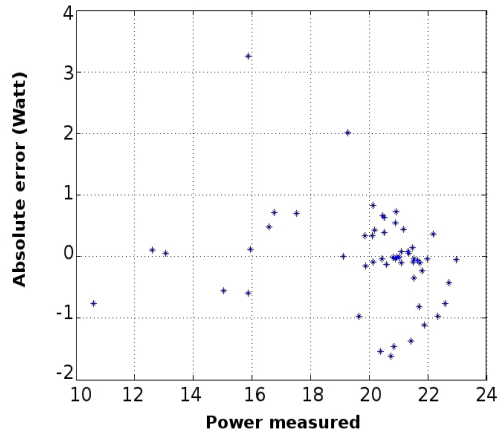


(b) The graph shows the measured I_{mpp} over the simulated one.

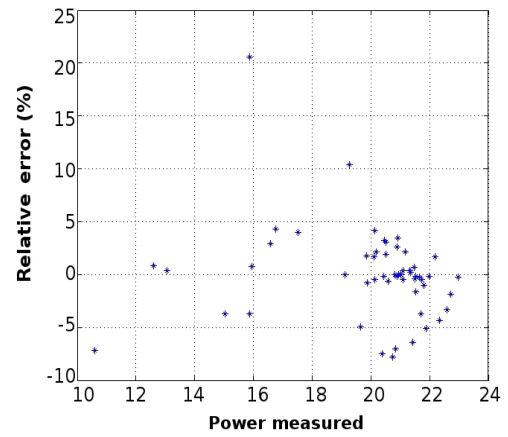


(c) The graph shows the measured V_{mpp} over the simulated one.

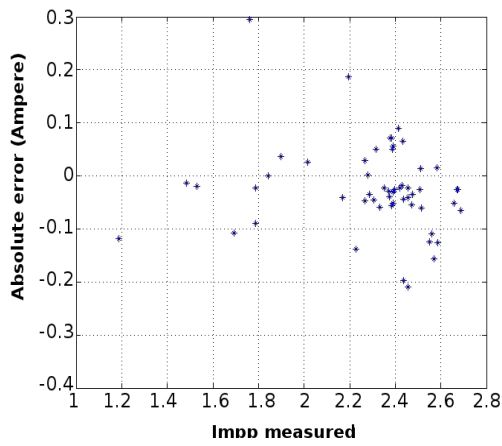
Figure 4.11: Results for a single module under uniform radiation.



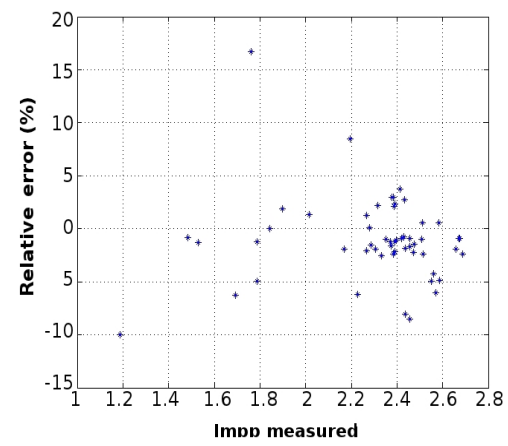
(a) Absolute error for the Maximum power point.



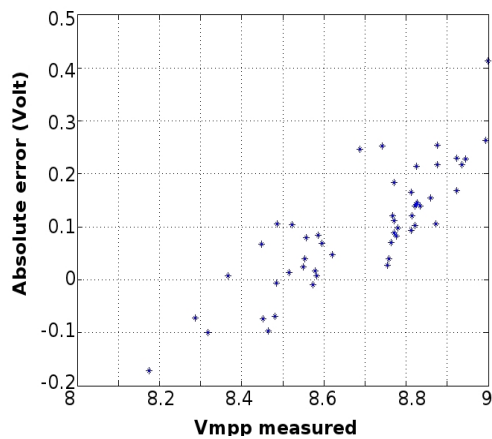
(b) Relative error for the maximum power point.



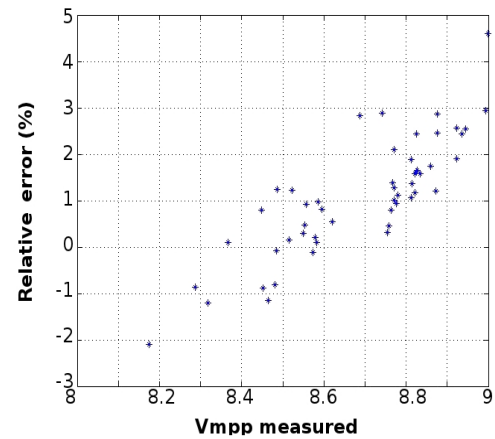
(c) Absolute error for the current at the maximum power point.



(d) Relative error for the current at the maximum power point.



(e) Absolute error for the voltage at the maximum power point.



(f) Relative error for the voltage at the maximum power point.

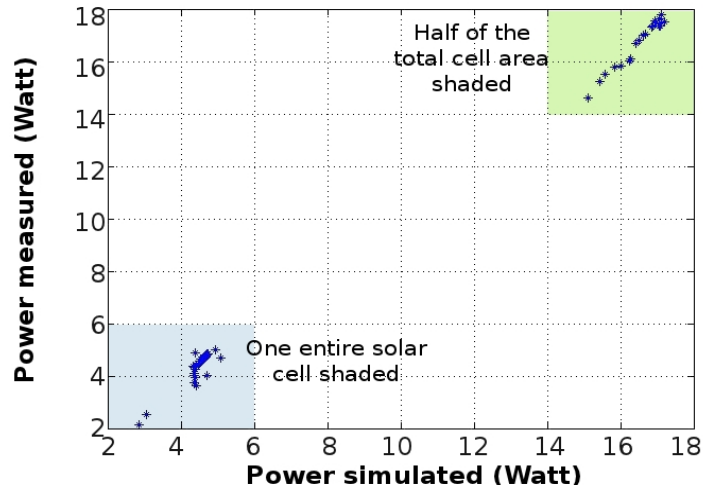
Figure 4.12: Absolute and relative error for the main parameters of a single module simulated under condition of uniform irradiance.

for the cell parameters selected, the validation was extended to cover partial shading of a single PV module. This test is divided in two parts: the first one considers one entire cell affected by shading and the second one only the 50% of the total cell area is affected by shading. To do these experiments, the shadow area was made by covering the relevant area and maintaining this fixed for the duration of the measurements. In this way it was possible to assess the model performance under different conditions of radiation and temperature. Solar radiation in Glasgow is highly variable in time due to persistent and fast moving clouds and this can result sometimes in high errors due to conditions changing during an I(V) scan.

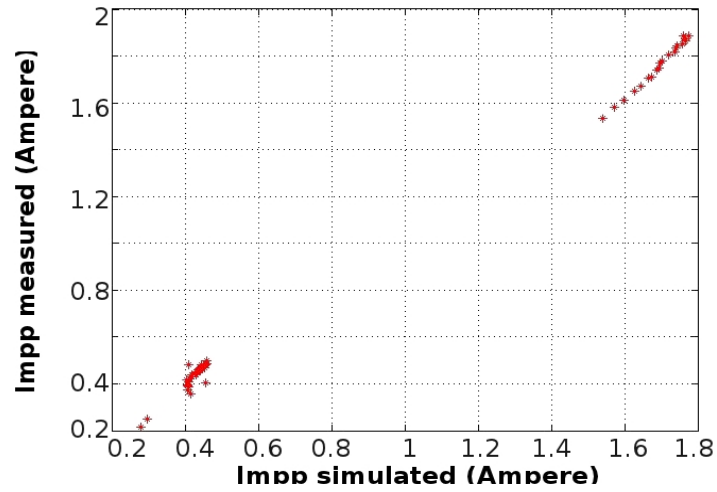
Fig.4.13 to Fig.4.14 (pages 73,74) show the results for both cases (partial and totally shaded). The lowest values (from 2 to 5.5 Watts) concern a totally shaded cell and the highest values ([15-18]Watts) are for half shaded cell.

First, the results for a cell entirely shaded will be examined. The output power is very low due to the manufacture, in fact these specific BIPV modules have only 1 by-pass diode which means that in case of partial shading due to the internal connection of the cells (series connection), the output current of the module will be determined by the cell with lowest current production and the I(V) characteristic will not present any local maxima but only one MPP determined by the cell affected by the shading. Looking at the results (see Fig.4.13(a) and 4.13(b)), the simulated values for MPP and I_{mpp} are near linear with the measured data: the absolute error (Fig.4.14(a)) for the MPP is in the range of [-800,200]mW resulting in a relative error (Fig.4.14(b)) from -20% to 5%. The relative error is large for some specific cases but this is not really important due to the fact the output power is very low. The experiment where the solar cell is partially shaded (50% of its total area) has an absolute error for the MPP between -0.2W and 0.7W and in terms of relative error, this is $\pm 4\%$. The absolute I_{mpp} error for the totally shaded cell is small (± 50 mA) as can be seen from Fig.4.14(c) but the relative error is from -20% to 8% (see Fig.4.14(d)). The I_{mpp} , where the shaded area is the 50% of the total cell area, presents an absolute error in the order of milliAmpere and a relative error from 0 to 6%.

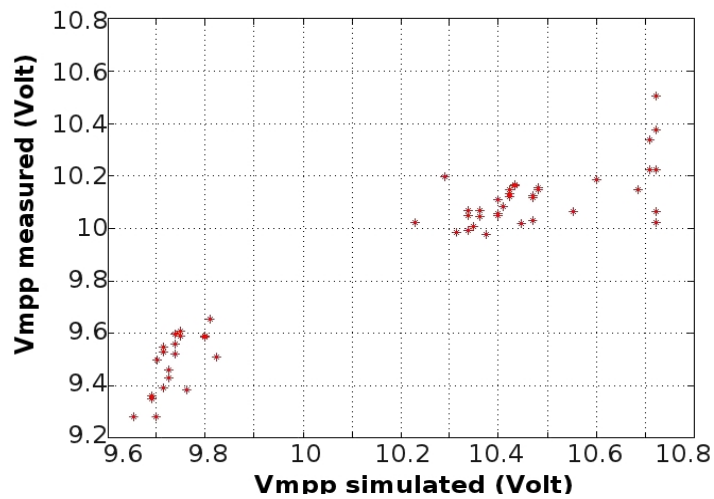
For the voltage at the MPP, the absolute error is in the order of milliVolts and the relative one is often lower than 5% (see Fig.4.14(e) and 4.14(f)). From Fig.4.13(c) it can be noted that the simulated values are larger than measured one which means that the temperatures selected for the simulation of the module (the measured values at the back rear) were higher than the effective module temperatures.



(a) The graph shows the measured MPP over the simulated one.

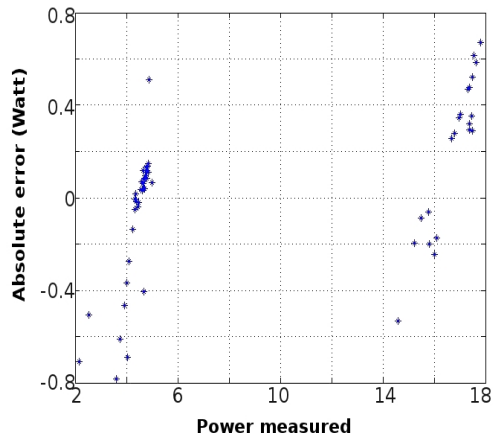


(b) The graph shows the measured I_{mpp} over the simulated one.

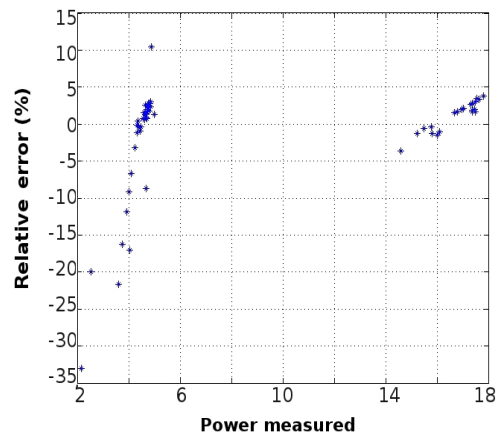


(c) The graph shows the measured V_{mpp} over the simulated one.

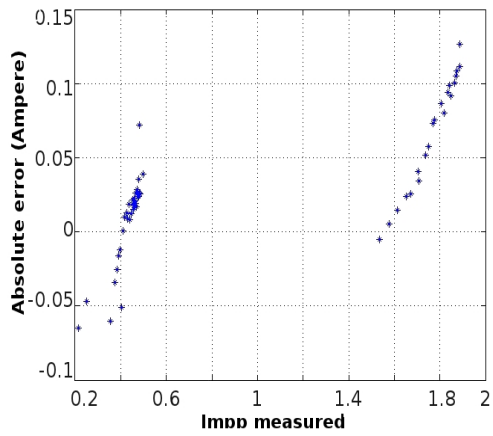
Figure 4.13: Results for a single module under partial shading.



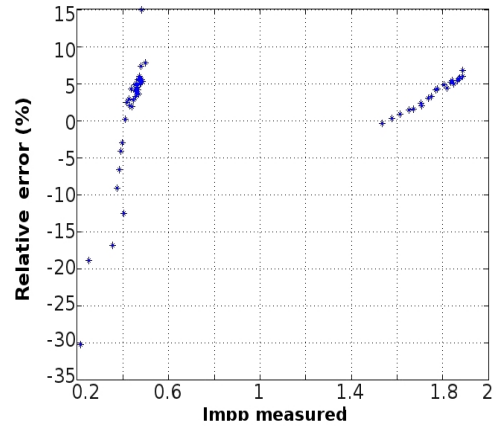
(a) Absolute error for the Maximum power point.



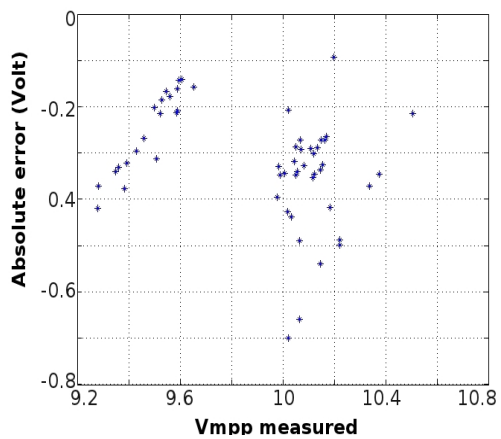
(b) Relative error for the maximum power point.



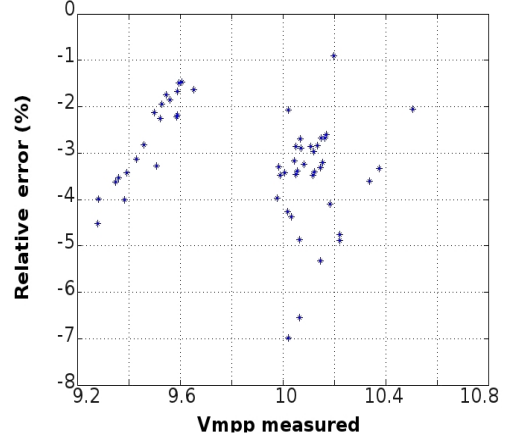
(c) Absolute error for the current at the maximum power point.



(d) Relative error for the current at the maximum power point.



(e) Absolute error for the voltage at the maximum power point.



(f) Relative error for the voltage at the maximum power point.

Figure 4.14: Absolute and relative error for the main parameters of a single module simulated under partial shading.

4.6.2 Array

Measurements for the tests undertaken to validate the array model were done during the spring 2010 in which the solar radiation was high and consequently the value of the generated photocurrent was high. Since the power supply unit used for the I(V) scan works only in the range of [-4,4] amperes, this resulted in some additional error in the measured I(V) characteristic for high values of radiation due to the truncation of the measured current.

In fact, additional limits imposed by the power supply unit were a major source of difficulty. When the incident radiation exceeds 700 Wm^{-2} , the instrument could not properly read the I(V) characteristic, forcing the output at its maximum (3.59 A is the real limit of the power supply unit) and, despite the PV electricity production being potentially higher than 3.59A, the instrument blocked at its maximum resulting in the lower value of I_{mpp} and a higher V_{mpp} compared with the MPP expected for these ambient conditions.

Unfortunately for about one year the power supply was under repair in the US. Combined with the fact that Glasgow does not offer so many days of clear sky, the results was a more limited collection of data than would have been ideal.

Uniform radiation

This subsection presents the results for the simulated array built up as explained in sec4.4. Each module has it is own temperature which is assumed to be the same for each cell of the module.

The radiation also has been assumed uniform across all the cells. Fig.4.15(a)-4.15(c) show the measured values compared with the simulated ones. The relationship is linear except at high power (note that the higher power results have been cut from the graph). In the graphs of the current and the voltage at the MPP (Fig.4.15(b) and 4.15(c) respectively) the limits of the instrument are clear. For the I_{mpp} for example, the results shown in the graph result are more or less linear up to about 3.2 amperes then the curve becomes roughly horizontal. This means that even though the value of the I_{mpp} should increase due to the rising solar radiation, the power supply is not able to read these values and saturates at its current limit.

The voltage has been affected by the same problem. In fact, as it can be noted from Fig.4.15(c), the values can be divided in two parts: the first close to the linearity (values from 64 Volt up to 69 Volt) and the second where the measured values are high compared to the model outputs. Due to this problem with the power supply, the scan of the I(V) characteristic traces only the final part of the

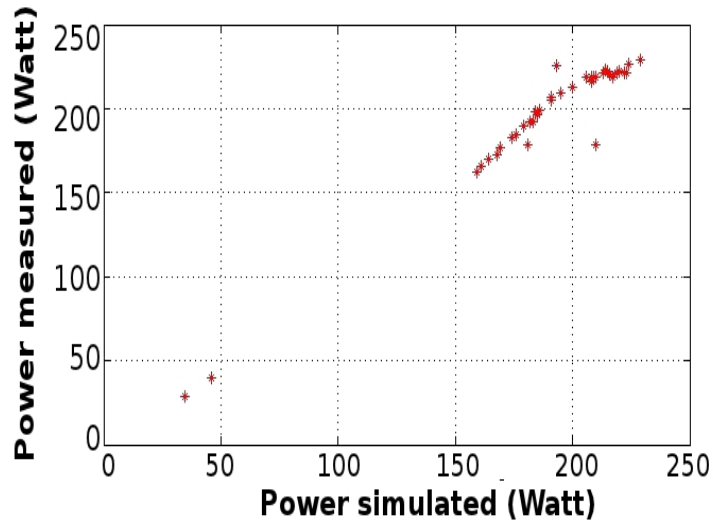
characteristic, so missing the real maximum.

The effects of this problem can be better understood from the graphs presenting the absolute and relative errors. The absolute error of the maximum power point values is lower than 10 Watt but this is the result of a combination of the errors in I_{mpp} and V_{mpp} . The error in current varies from -5% up to 10% (relative error, Fig.4.16(d)). The relative error in voltage at the MPP, when in the range of [64-69]Volt is between [2,-2]%, and for higher values, where the instrument fails to scan properly, the relative error reaches as high as 8% (Fig.4.16(f)). Examination of the results obtained from the day of measurements in question shows that the array model could not be properly validated due to the problems related to the power supply scanning the characteristic. For this reason another day of test data has been used to validate the model for the case of no partial shading and uniform incident radiation on the array.

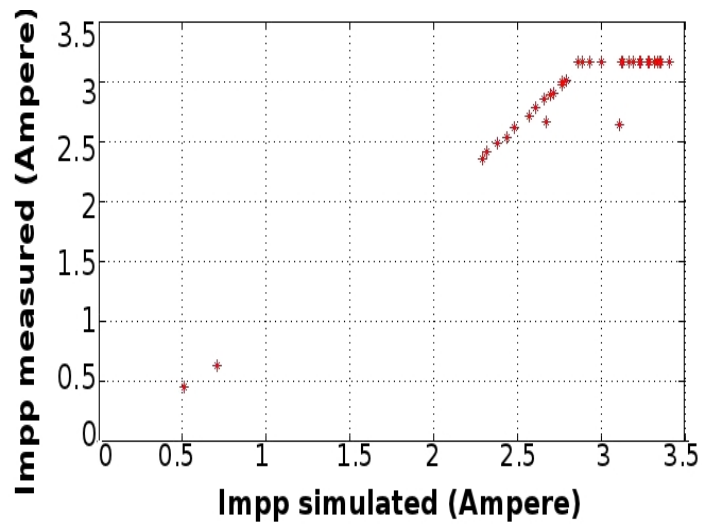
In contrast to the graph discussed above, this data allowed better results to be obtained; as expected the highest errors relate to the highest values of current, as before.

As it can be remarked from Fig.4.17(a) the power obtained from the simulation is linear but with a small offset from the measurements. This can be explained, as before, the temperatures used in the simulation model highlight that the measured temperature at the back of the module was lower than the effective temperature of the cells. This conclusion is supported by the fact that the V_{mpp} is lower than that measured (Fig.4.17(c)) whereas the I_{mpp} is linear. In fact the temperature influences more the value of the V_{mpp} , even if the I_{mpp} is only slightly affected. Simulating with a lower PV temperature than the effective one results in a lower value of I_{SC} for the calculations (eq.4.6) but the contribution of generated current as function of the temperature, which derives from the lower energy band gap, and allows more photons to generate the electron-hole pair, is less obvious but introduces a small additional error.

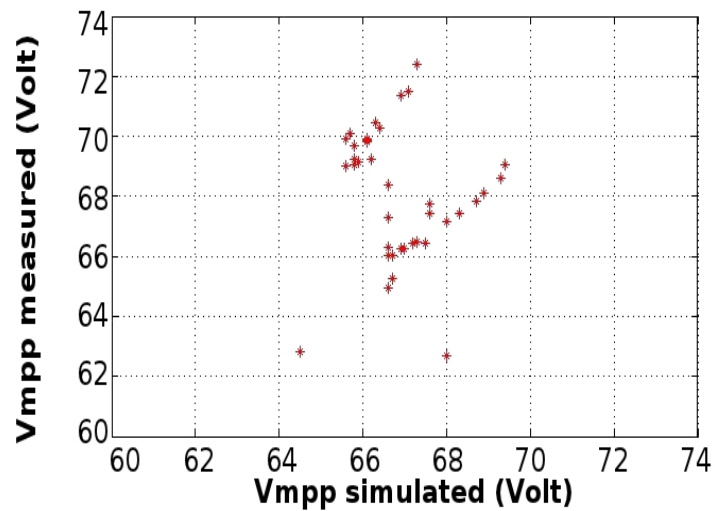
As always the precision of the results presented is also affected by the accuracy and resolution of the instruments used to measure the radiation. The pyranometers have a precision of 2% and measure the radiation on the horizontal plane. The incident radiation on the modules has then to be calculated (see AppendixC) and this introduces further error. The lowest error for the power is in the region below 210 Watt where the I_{mpp} results smaller than 3.2A; for this range the absolute MPP error is between [-6,2]Watts corresponding to a relative error of [-3,1]% (Fig.4.18(a)-4.18(b)). The current at the MPP for values lower than 3 Amperes, has an absolute error 50mA with a relative error of $\pm 2\%$ (see



(a) The graph shows the measured MPP over the simulated one.

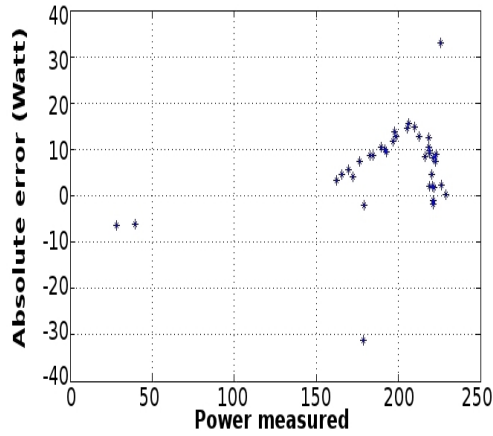


(b) The graph shows the measured I_{mpp} over the simulated one.

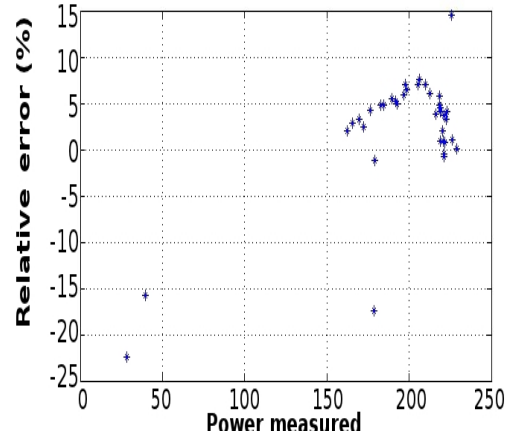


(c) The graph shows the measured V_{mpp} over the simulated one.

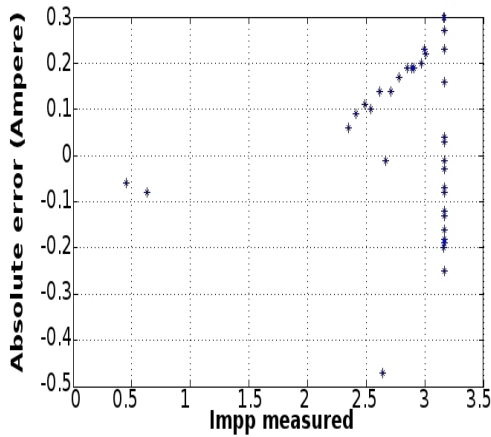
Figure 4.15: Results for the array under uniform radiation with limit of the power supply.



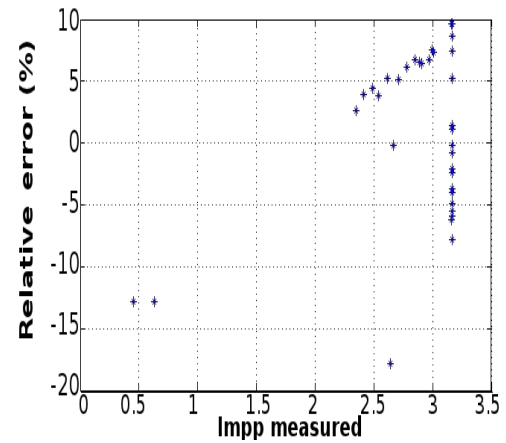
(a) Absolute error for the Maximum power point.



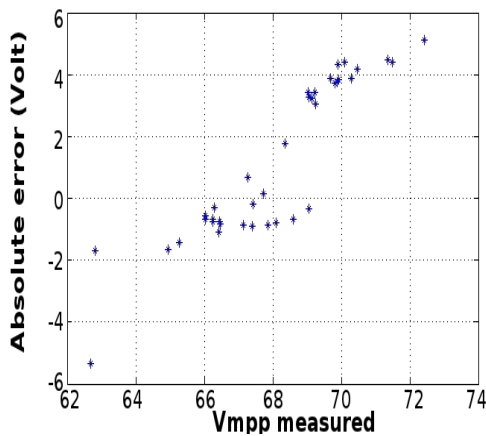
(b) Relative error for the maximum power point.



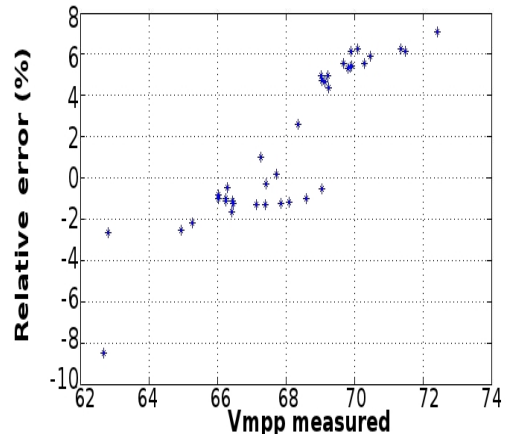
(c) Absolute error for the current at the maximum power point.



(d) Relative error for the current at the maximum power point.

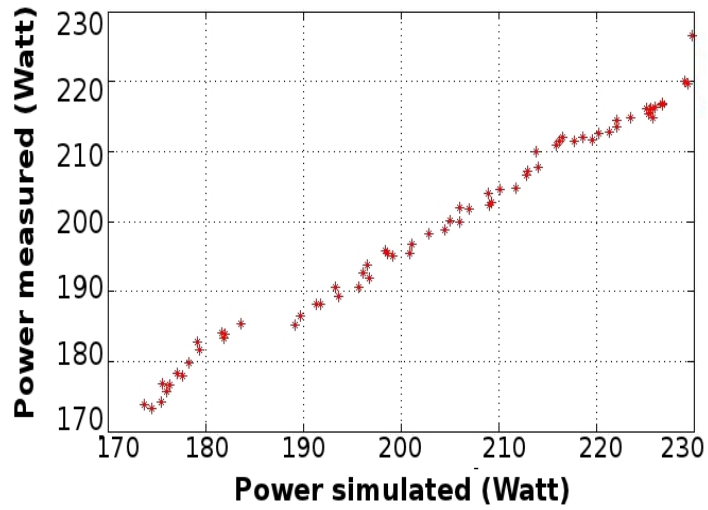


(e) Absolute error for the voltage at the maximum power point.

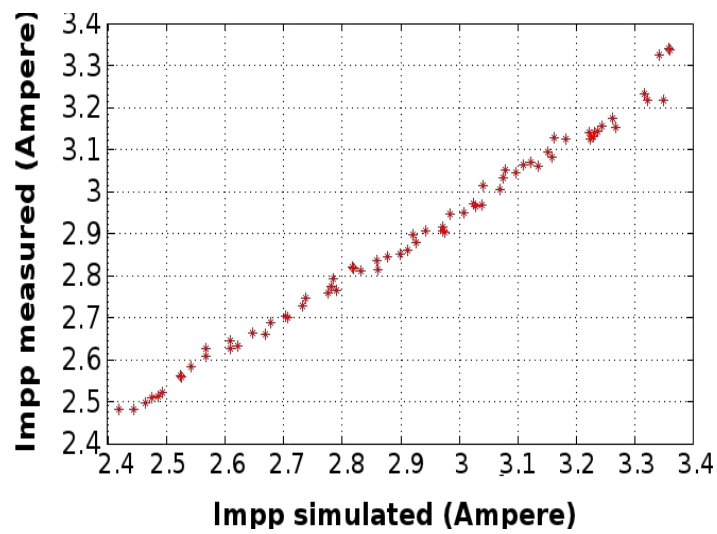


(f) Relative error for the voltage at the maximum power point.

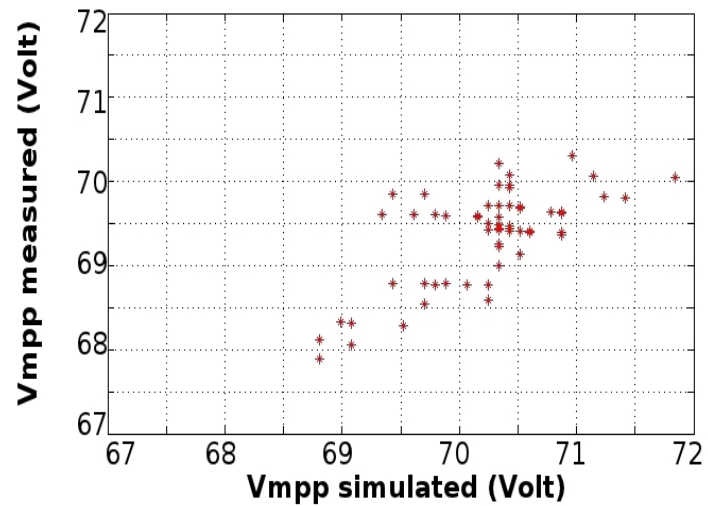
Figure 4.16: Absolute and relative error for the main parameters of the array simulated under condition of uniform irradiance with the limit of the power supply.



(a) The graph shows the measured MPP over the simulated one.

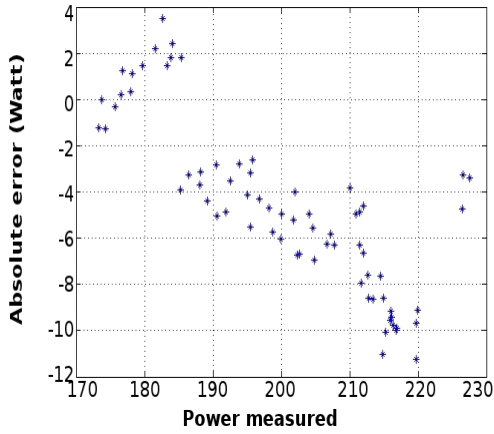


(b) The graph shows the measured I_{mpp} over the simulated one.

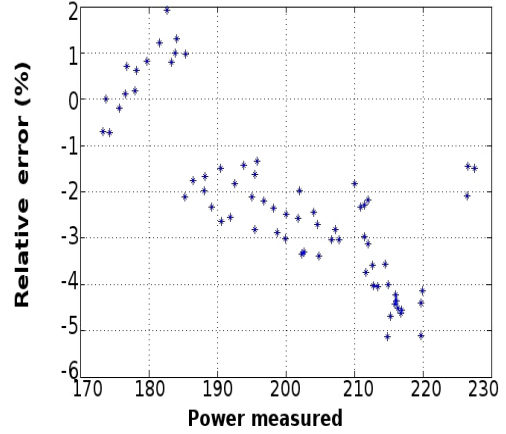


(c) The graph shows the measured V_{mpp} over the simulated one.

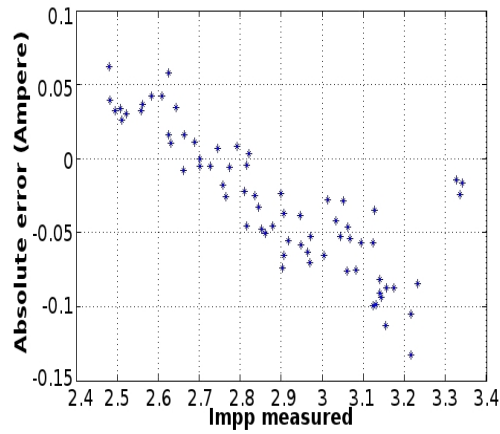
Figure 4.17: Results for the array under uniform irradiance.



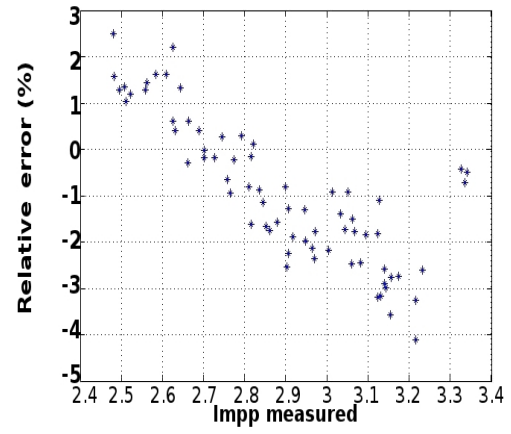
(a) Absolute error for the Maximum power point.



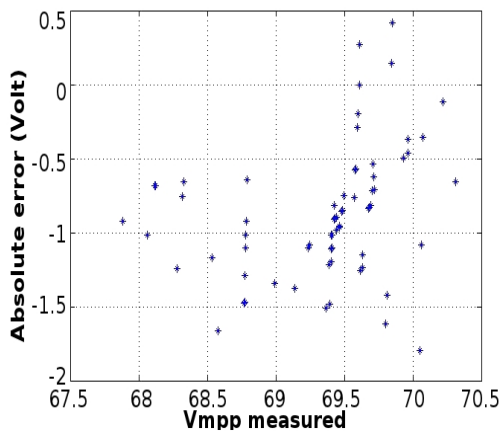
(b) Relative error for the maximum power point.



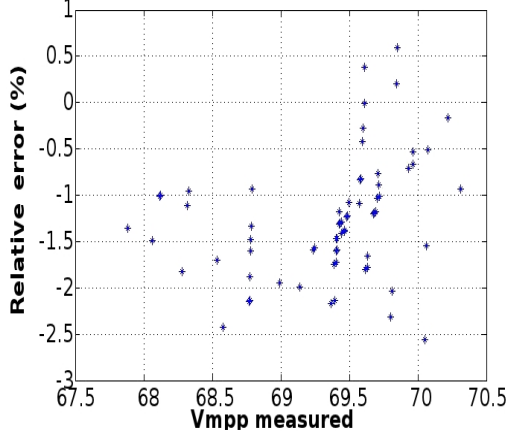
(c) Absolute error for the current at the maximum power point.



(d) Relative error for the current at the maximum power point.



(e) Absolute error for the voltage at the maximum power point.



(f) Relative error for the voltage at the maximum power point.

Figure 4.18: Absolute and relative error for the main parameters of the array simulated under condition of uniform irradiance.

4.18(c)4.18(d)). The case of V_{mpp} is different: the negative absolute error reaches -1.5 Volt, equivalent to -2% relative error (Fig.4.18(e)4.18(f)).

Partial shading

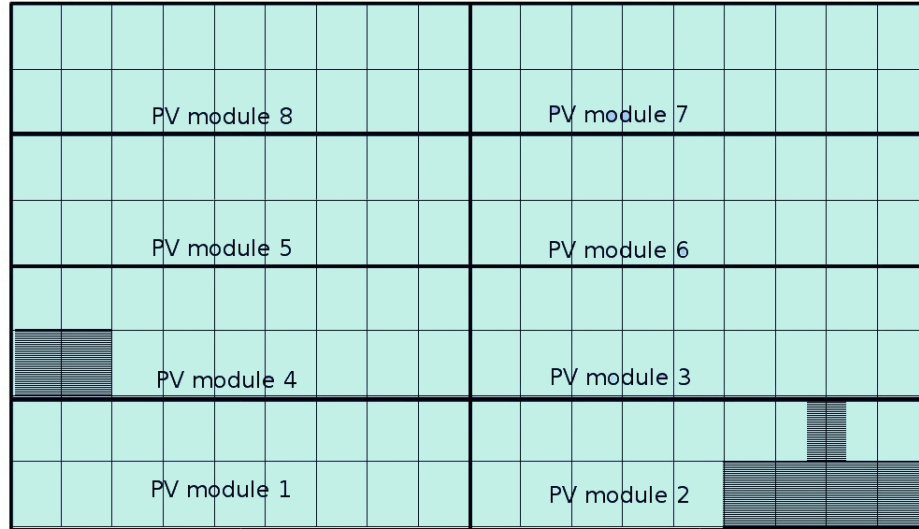


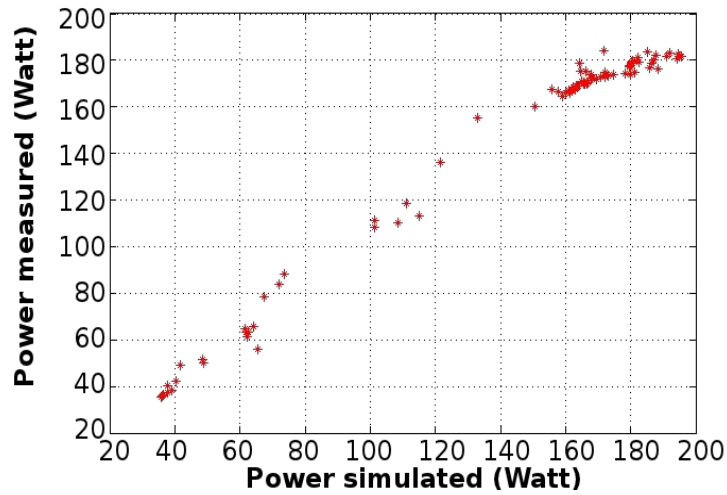
Figure 4.19: Shaded area applied on the PV array during the measurements.

One final experiment was made, this was to test the reliability of the model of the PV array for partial shading.

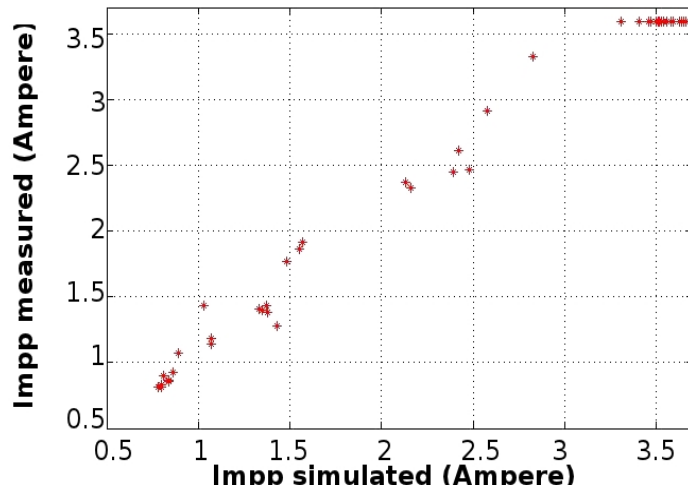
The same test was run for two days in August 2010, but restricted to when the solar radiation was lower than the limit imposed by the power supply.

The set up included two fixed objects which partially shaded two of the modules: an entire cell for module 4, and four entire cells plus two half covered for module 2, as shown in the Fig.4.19. The configuration selected created two local maxima in the I(V) characteristic. The output current, as always mentioned, of each module under partial shading is driven by the cell with the lower current generated due to the electrical internal connection of the cells in these modules. Despite the bypass diodes some power is dissipated in the cells, creating these local maxima.

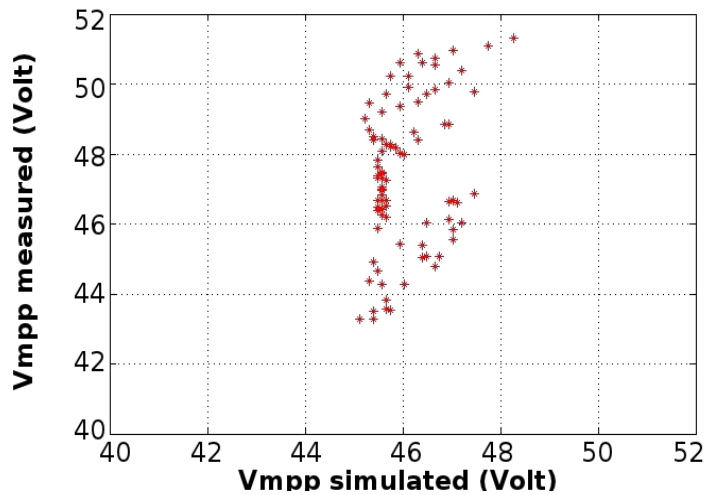
Again, as for the case of uniform irradiance, some of the results, especially for the V_{mpp} , are affected by the performance of the power supply. The power is almost linear (Fig.4.20(a)) but the current at the MPP is only linear up to about 3 Amperes and then saturates (Fig.4.20(b)). The V_{mpp} has a similar slope (Fig.4.20(c)), with the first part of the data being linear, and a second part where the measured data are higher than the model output.



(a) The graph shows the measured MPP over the simulated one.

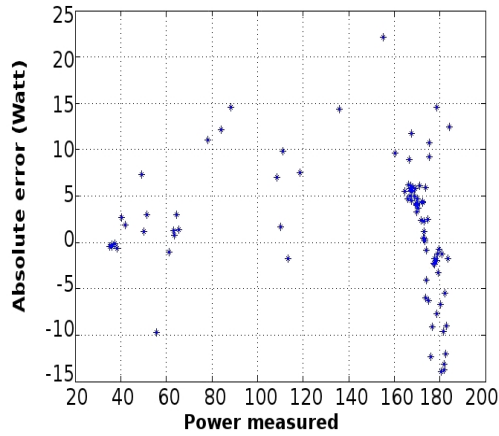


(b) The graph shows the measured I_{mpp} over the simulated one.

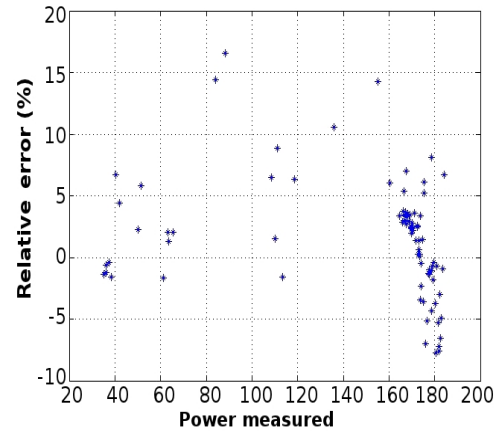


(c) The graph shows the measured V_{mpp} over the simulated one.

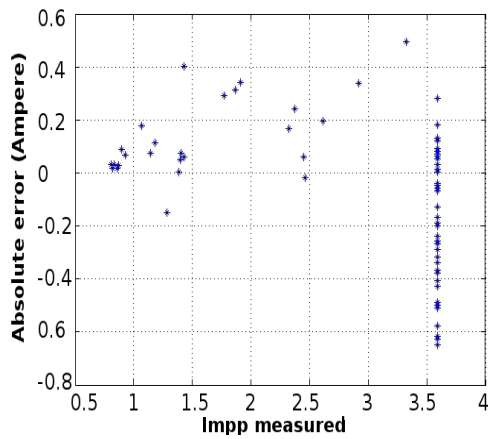
Figure 4.20: Results for the array affected by partial shading.



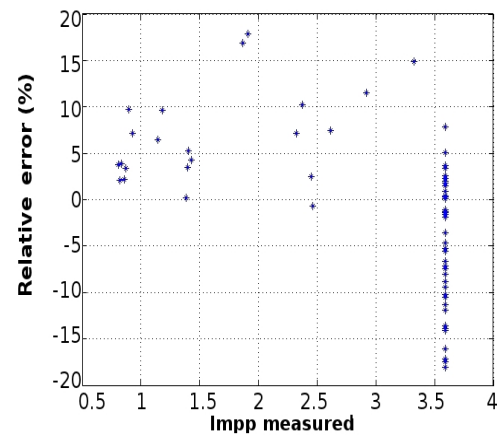
(a) Absolute error for the Maximum power point.



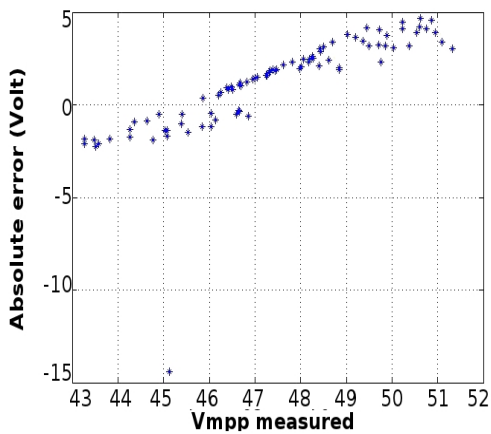
(b) Relative error for the maximum power point.



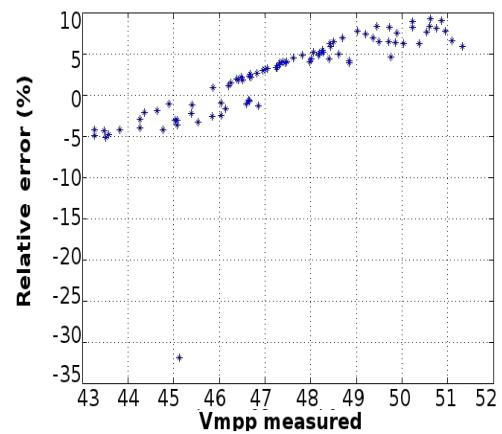
(c) Absolute error for the current at the maximum power point.



(d) Relative error for the current at the maximum power point.



(e) Absolute error for the voltage at the maximum power point.



(f) Relative error for the voltage at the maximum power point.

Figure 4.21: Absolute and relative error for the main parameters of the array simulated under condition of partial shading.

The graphs concerning the errors indicate a relative error of the simulated power in a range of $\pm 5\%$.

The current at the MPP (see Fig.4.21(d)) presents a relative error higher compared with the relative error of the MPP (Fig.4.21(b)) and this is, for the majority of points, about $\pm 5\%$.

The relative error for V_{mpp} , as expected, can be considered in two regions. For values lower than 48 Volts, Fig.4.21(f) shows a relative error of $\pm 5\%$ corresponding to an absolute error of $\pm 2\%$. For the second region, for values from 48 Volts up to 51.5 Volts, the relative error is between 5% and 10% with the measured values higher than those modelled.

Once again this error can be ascribed to the power supply limits for two reasons. First of all the graph of current shows limited values for the current even when the radiation increases; second, the partial shading has a fixed shape which means the value of the V_{mpp} depends mostly on temperature variations and only slightly on variations in radiation. Since the temperature increases the value of the operating voltage is expected to decrease and not the other way round.

4.7 Conclusion

The development of a model for the outdoor test system has been presented in this chapter. This model has been implemented in Orcad and simulated with PSpice with the intent to be as precise as possible. Some assumptions have been made to reduce the complexity of the simulations (e.g. assuming the cells temperatures are homogeneous for each module).

Scripts have been developed for using and selecting the weather data to make the process faster.

Considering the problems due to the limitations of the instrumentation and the unfavourable weather in Glasgow, the results demonstrate that the model is in good agreement with the collected data, especially when it is kept in mind that the tests have been made with an outdoor experiment where the parameters of temperature and irradiance are subject to variations and the response of PV modules is not homogeneous. It should be noted that to add that rarely results are presented comparing point by point the measured data with those from the model.

All in all the model has shown a good agreement with the measured data (table 4.3). For this reason the model has been used for training, test and validating of the artificial neural network, as will be described in the following chapters.

Table 4.3: Minimum and maximum relative error of the proposed model.
¹ one cell entirely shaded; ² half cell shaded.

		Uniform Radiation			Partial Shading		
		<i>MPP</i>	<i>I_{mpp}</i>	<i>V_{mpp}</i>	<i>MPP</i>	<i>I_{mpp}</i>	<i>V_{mpp}</i>
Single Module	Min ¹	0	0	0.13	0	0	1
	Max ¹	7	10	5	20	20	5
	Min ²				0	0.05	0
	Max ²				4.8	7	7
Array	Min	0	0	0	0	0	0.1
	Max	5	5	2.55	15	15	10

5

Partial shading

In real operating conditions a major challenge is the shading of the PV system created by surrounding objects. Partial shading degrades the performance of a PV system but the extent of this depends on the area and position of the shadow and on any by-pass diodes. There is also likely to be a degradation in the MPP tracking.

In the following sections it will be illustrated how the area of the shadow will affect the PV system performance depending on its distribution across the PV array; how the same shape and position can result in different degrees of degradation of the PV system output power depending on the connection of the modules. The shadow path on the array due to a nearby object is related to its geographical position, time of the day and day of the year.

How shading affects the performance of a PV array and how the bypass diodes help prevent damage and limit power losses have been explained in Chapter 2.

The following chapter illustrates some studies which have been undertaken to better understand the effects of the partial shading on the PV performance. Sec.5.1 shows how the surroundings may affect the PV production and how an appropriate selection of the tilt angle of the PV may reduce losses due to the partial shading.

The calculation of the incident radiation on the PV system analysed has been taken from Energy Plus software. Energy Plus is building energy simulation program that models heating, cooling, lighting, ventilation, other energy flows, and water use [6].

Several models have been presented in the literature to calculate the PV production in case of partial shading but an important key was understanding how the model for the partial shading has to be detailed. In fact, sec.5.2 shows how the same amount of shaded area may influence the PV performance differ-

ently as function of the number of the PV modules affected by the partial shading and the electrical connection between the PV modules.

The results obtained from that analysis emphasized the importance of a detailed model of the partial shading on the PV array, this is why a code has been developed able to calculate the amount of shaded area of each single solar cell of the PV array created by a nearby object (sec.5.3).

An important factor for the determination of the MPPT algorithm structure is the time variation of the partial shading. Simulations have been made to define the changes of the MPP as function of the shadow path. The simulation results are shown in sec.5.5 and the time step has been fixed at 1 second as this is the minimum time which may significantly change the operating voltage of the MPP.

All the simulations use the PV model developed in Orcad and detailed in Chapter 4.

5.1 Photovoltaic system performance with partial shading from surrounding buildings

The performance of PV system is influenced by the tilt angle, the site where it is installed, the orientation and especially by any partial shading that can be caused by surrounding buildings.

As an example of the effects of partial shading from nearby objects, a study of the electricity production from a PV system integrated into a shading device for different surrounding building configurations and tilt angles will be briefly presented.

The energy yield has been calculated for a shading system that integrates photovoltaics into the shading device itself. The effects of the shading device and the PV system have been simulated for an urban context with different tilt angles and surrounding buildings.

In this assessment two generic urban forms were chosen: separated and continuous units. The separated unit, defined by geometrical ratios, can be seen in Fig. 5.1 [50].

Twenty seven different building configurations were analyzed, corresponding to two levels of spacing distance ($L1/L2$), two levels of building depth ($D/L2$), and four levels of aspect ratios (H/W) and 3 cases are without surrounding blocks. The daylight responsive electric lighting load calculation with fixed shading devices and electric production from building integrated PV (on the fixed shading devices) have been undertaken. Simulations have been done for 3 different tilt

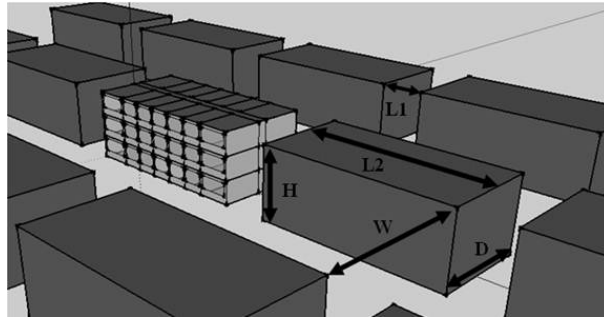


Figure 5.1: The separated form structure H, D, L2, refer to the height, depth, frontal length of each unit, L1 refers to the spacing between the units and W refers to the width of the street.

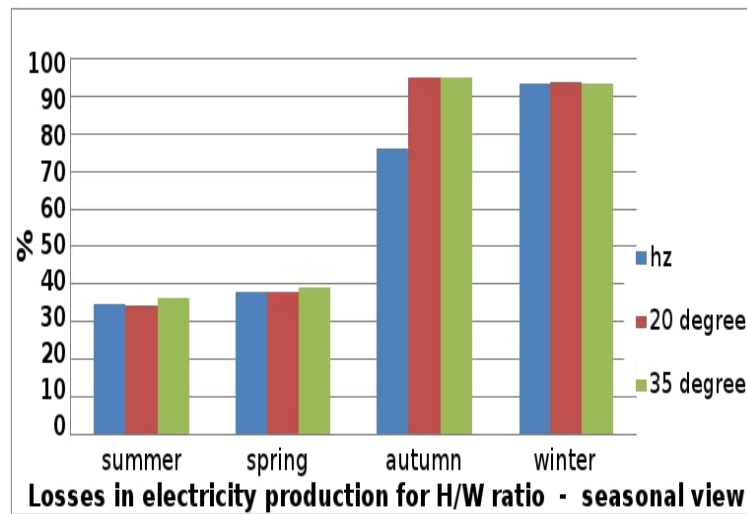


Figure 5.2: % of the electricity losses of the ratio $H/W=2$ compared with $H/W=0.5$.

angles (horizontal, 20 degree and 35 degree). The performance of photovoltaics integrated into a shading device are drastically reduced by the shading created by the surrounding buildings.

From the analysis of the results, the electricity production is mostly reduced by the ratio H/W : increasing the height of the surrounding buildings, the percentage of shading on the south facing photovoltaic increases, resulting in a lower electricity production. Fig.5.2 shows the percentage of electricity production lost for $H/W=2$ in comparison with the production in the case of $H/W=0.5$. The results highlight how much the PV system performance is severely reduced by the surrounding building losing up to 90% for the winter operation.

The other factors $L1/L2$ and $D/L2$ do not have the same impact as H/W . However by increasing the distance between the buildings the shading created by the nearby buildings on the system decreases, thus producing a higher electricity

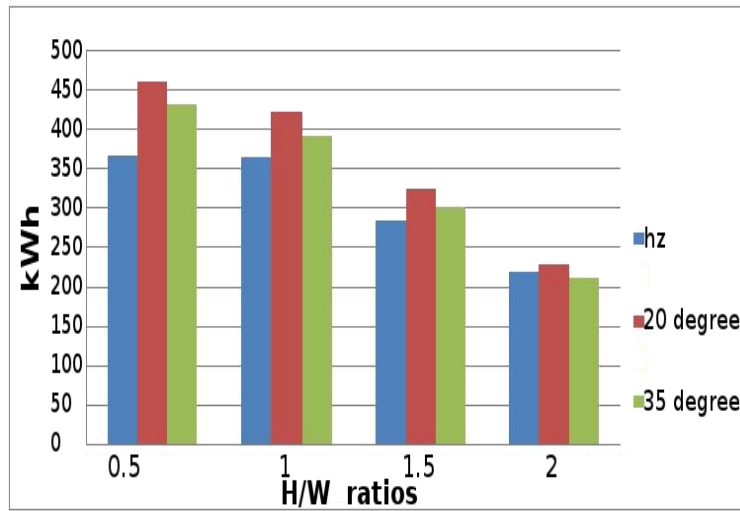


Figure 5.3: Annual electricity production for the ratio H/W and for the three different tilt angles.

production as shown in Fig.5.4. This is true even if the higher gain is on a horizontal surface. The ratio D/L2 has a slight influence on the electricity production for all tilt angles.

The winter and the autumn are the seasons which mostly influence the performance of photovoltaic due to the declination angle. Due to the lower position of the sun the area of the shading on the photovoltaics increases for higher ratios of H/W (as well as D/L2) and decreases for higher ratio of L1/L2.

The results also show the effect of tilt angle. The best tilt angle for all the configurations is 20°, even if for this site the tilt angle that maximizes the incident solar radiation for the whole year in absence of shading is 35°. Increasing the tilt angle means increasing the incident solar radiation level but results in increased shading.

The most significant result is for the aspect ratio of H/W=2 where a tilt angle of 35° is less efficient than zero degrees (horizontal). The effect of the shading dominates over increases in incident solar radiation. Fig.5.8 shows how much shading affects the electricity production of the PV system. D/L2 has a small influence (the losses are mostly due to the selected ratio H/W=0.5). Increasing the ratio L1/L2 helps to reduce the effects due to the ratio H/W=0.5, halving the losses (in different proportion, depending on the tilt angle). As discussed before, increasing the height of the building and maintaining the width of street has a huge impact on the PV system performance, as shown in Fig.5.8. This study shows how much the selected tilt angle can affect the performance of a PV system. The shadows projected from the surroundings vary with tilt angle, being in some

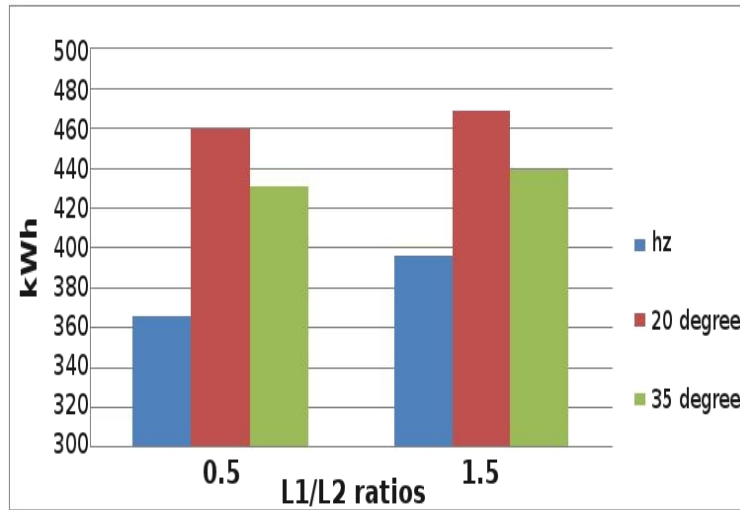


Figure 5.4: Annual electricity production for the ratio L1/L2 and for the three different tilt angles.

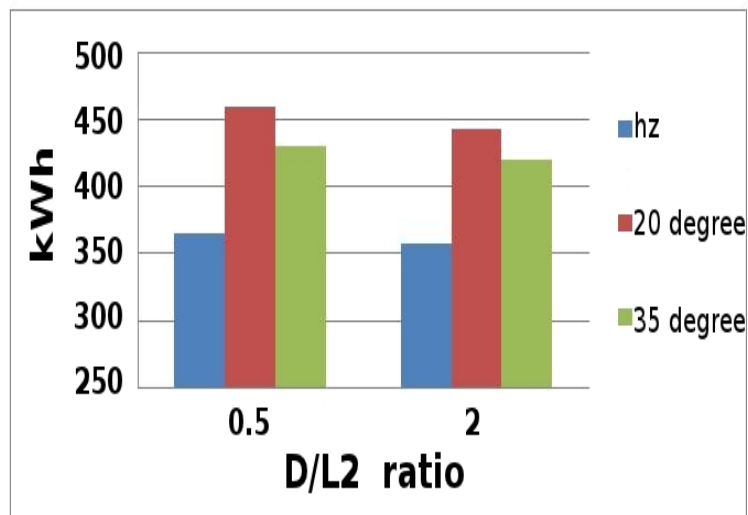


Figure 5.5: Annual electricity production for the ratio D/L2 and for the three different tilt angles.

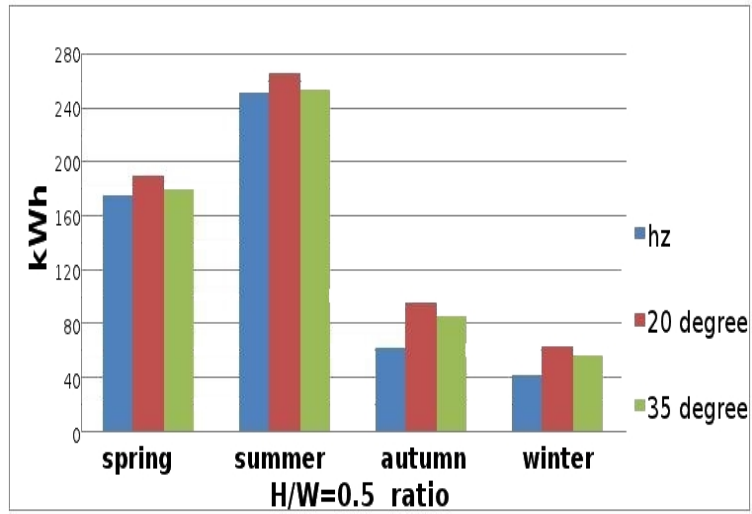


Figure 5.6: Electricity production view per each season: ratio H/W=0.5.

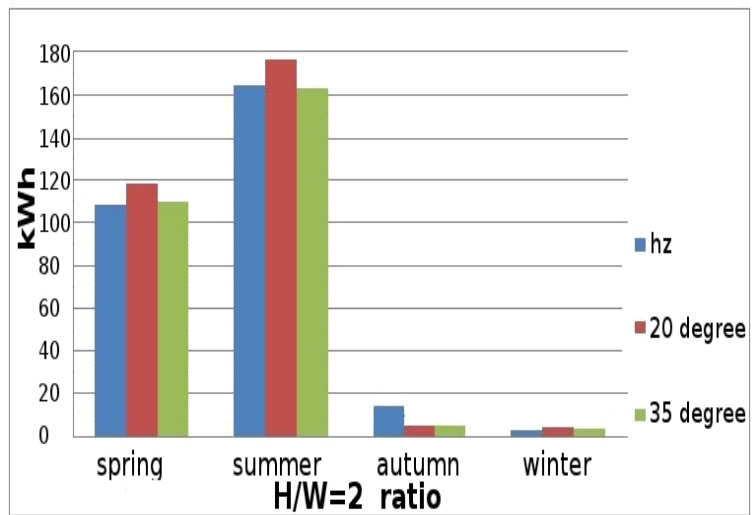


Figure 5.7: Electricity production per each season: ratio H/W=2.

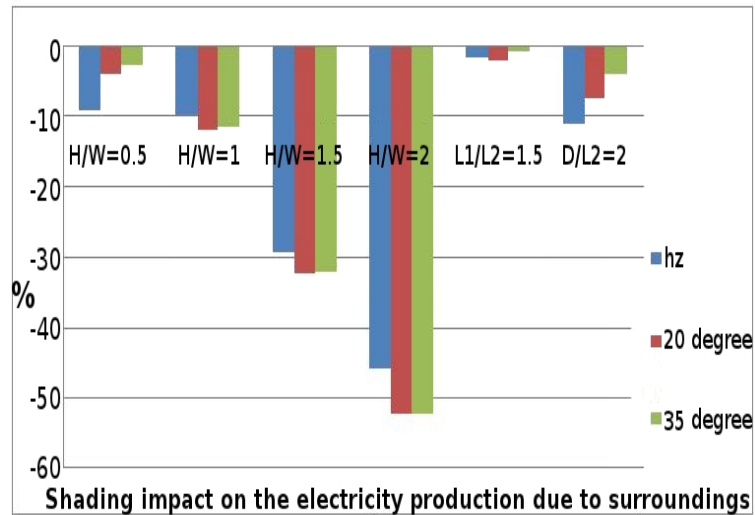


Figure 5.8: Annual % losses for each ratio compared with the annual production without surrounding building.

particular case more relevant than the gain in incident radiation due to the tilt angle. The system studied included 32 BIPV modules of 40Wp @STC. The value of the incident radiation on each PV cell was calculated using Energyplus. Energy plus calculates the average of the global radiation (direct beam plus diffuse plus reflected radiation from surrounding buildings) on each surface as function of time. The time step for the simulation was set at 15 minutes. The simulation then followed the same procedure as described in section 4.4 using the PSpice model.

This study shows the importance of knowing the path and the position of the shading in order to predict the performance of PV system. A specific code has been written in Matlab to calculate the position of the shadow on each cell of the PV array as a function of the location and orientation of the PV cells, the position and the size of the shading object and the location and position of the sun as a function of the day of the year and the time of the day. This is described in more details in the next section.

This study shows the impact of the partial shading on a PV system due to the surrounding. A careful study of the surrounding might limit the losses due to the partial shading created by the nearby buildings.

5.2 Electrical connection factor

Partial shading of an array produces local maxima in the power voltage characteristic which are difficult to detect with commercial inverters. These can end up

operating around a lower local maximum, so reducing the overall efficiency of the PV system.

The same shading shape can affect in different ways the value of the MPP.

Simulations have been run for Glasgow where the global radiation generally has a higher component of diffuse radiation than for direct beam. The number of local MPPs is determined by the number of distinct levels of radiation incident on each string of the array. The operating voltage of the MPP can be in the low, medium or high voltage region (Fig.5.9 and Fig.5.10). Four different

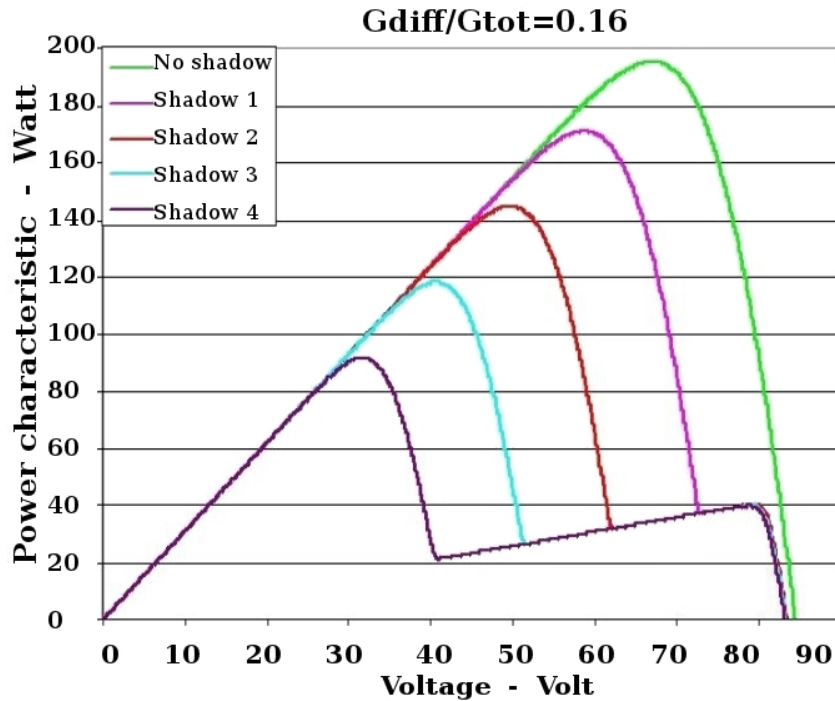


Figure 5.9: Power characteristic for a clear sky day: the MPP has different values as a function of the number of shaded modules.

shading cases have been analyzed, each of them with 12.5% of the total surface shaded. The simulations have been repeated for three different electrical connection arrangements to show the impact on the MPP of the position of the shading: connection 1- series connection starting from the top left module and ending at the top right module; connection 2- series connection starting from the top left module and ending at the bottom left module; connection 3- parallel connection between the left modules and the right modules. The simulation parameters have been calculated at solar noon for every day of the year 2009. To do so, the values of the global and diffuse radiation for Glasgow have been extrapolated using the software EnergyPlus which has available data from various weather stations. As mentioned, the analysis was done for four different shading configurations, the

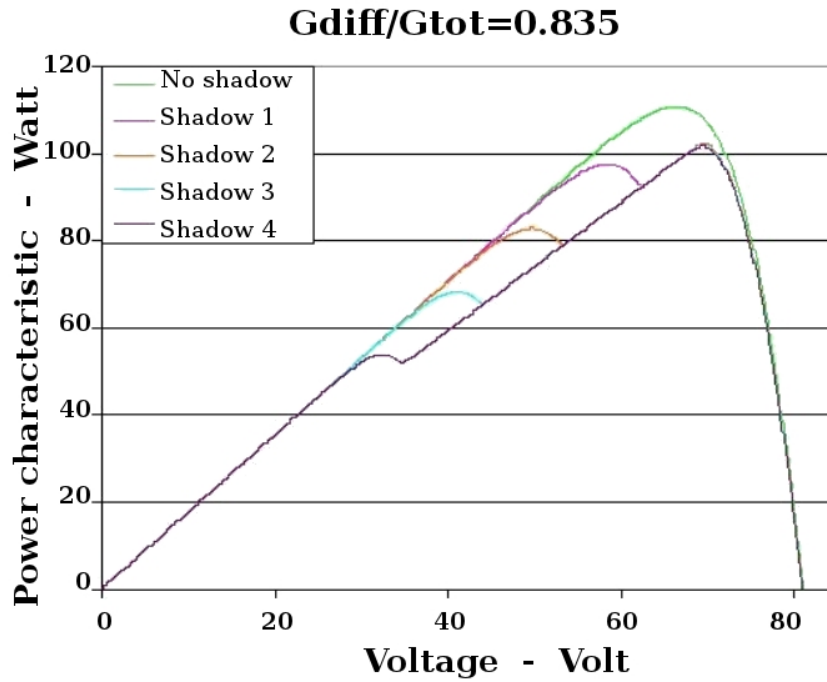


Figure 5.10: Power characteristic for a day where the diffuse radiation is more than 80% of the global: the MPP is in the high voltage region for all the simulated shading impacts.

total PV array area shaded was kept constant at 12.5% of the total area, but the cases have been defined so that each of them has a different number of the modules affected by shadow. The situations analyzed are:

- shadow 1: one entire module is under shading;
- shadow 2: two modules are under partial shadow (nine cells of each module affected by the shadow);
- shadow 3: three modules under partial shading (six cells of each module shaded);
- shadow 4: four modules under partial shading (four cells for two modules shaded, six cells for the other two modules shaded).

The study highlighted that also the ratio G_{diff}/G_{tot} has an important role in the determination of MPP; two different situations have been evaluated: a clear sky day ($G_{diff}/G_{tot} = 0.16$, Fig.5.9) and an overcast day ($G_{diff}/G_{tot} = 0.835$, Fig.5.10). The graphs include the power characteristic for all cases of partial shading listed above and also the case of uniform radiation (no shading). The

obvious impact is the decrease of the power, but it should be also noted that there is a significant variation in the optimal operating voltage, in particular for the case defined as "shadow 4" where for clear sky day the MPP is in the lower voltage region and for the overcast day, in the high voltage region.

Expressing the power as function of the maximum power without shading and a shading factor S we have:

$$P_{shaded} = P(1 - S) \quad (5.1)$$

where S is a function of the diffuse component of the total radiation and the number of the shaded modules, N_D , i.e. $= f\left(\frac{G_{diff}}{G_{tot}}, N_D\right)$. The results for S are shown in Fig.5.11. The crystalline silicon modules are equipped with bypass diodes to prevent damage from reverse bias on partially shaded modules.

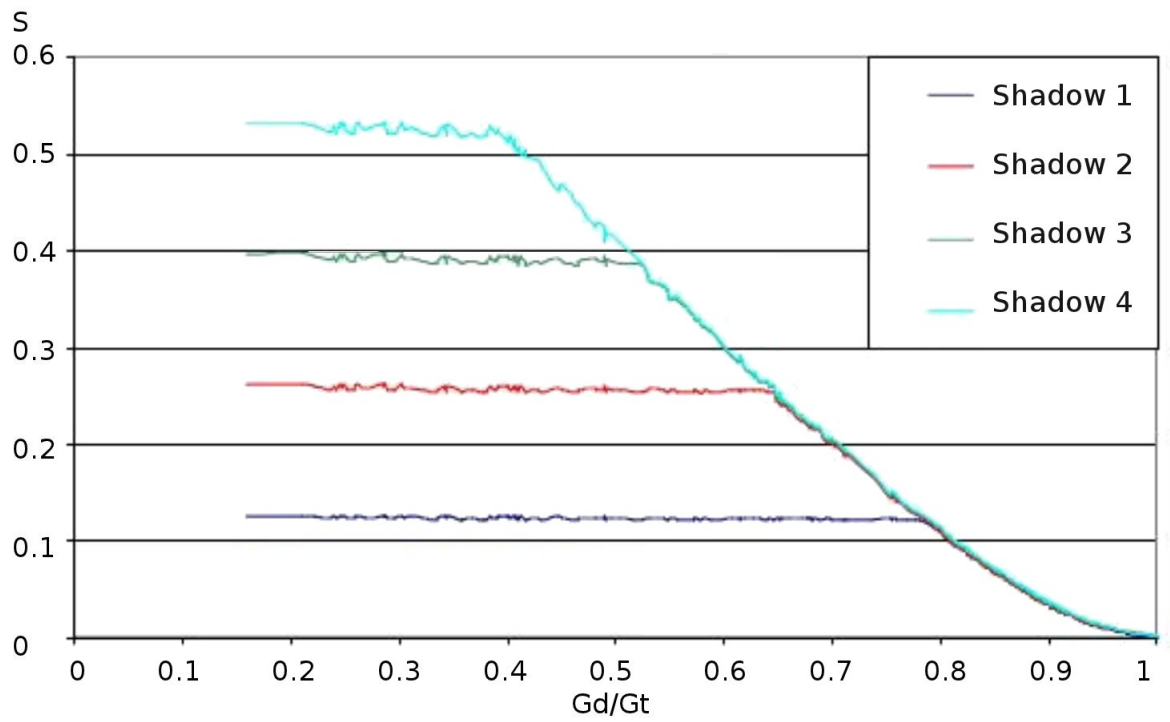
The effect of shading on the power output of a typical PV installation is non linear and can cause a large reduction in output power. For instance, completely shading one cell of an array will cause the bypass diode protecting that cell to conduct, reducing the power of the module by an amount that depends on the number of cells in the module [11].

From the simulation results of this study it has been noted that for a fixed shading the percentage of the power loss is constant for clear sky days and decreases for cloudy days compared with the power output of the same configuration under uniform radiation (no shading) [13]. For a partially cloudy day, the spectrum of the sun results in a high reduction in photon energy levels resulting in lower electricity production; an example is shown in Fig.5.12.

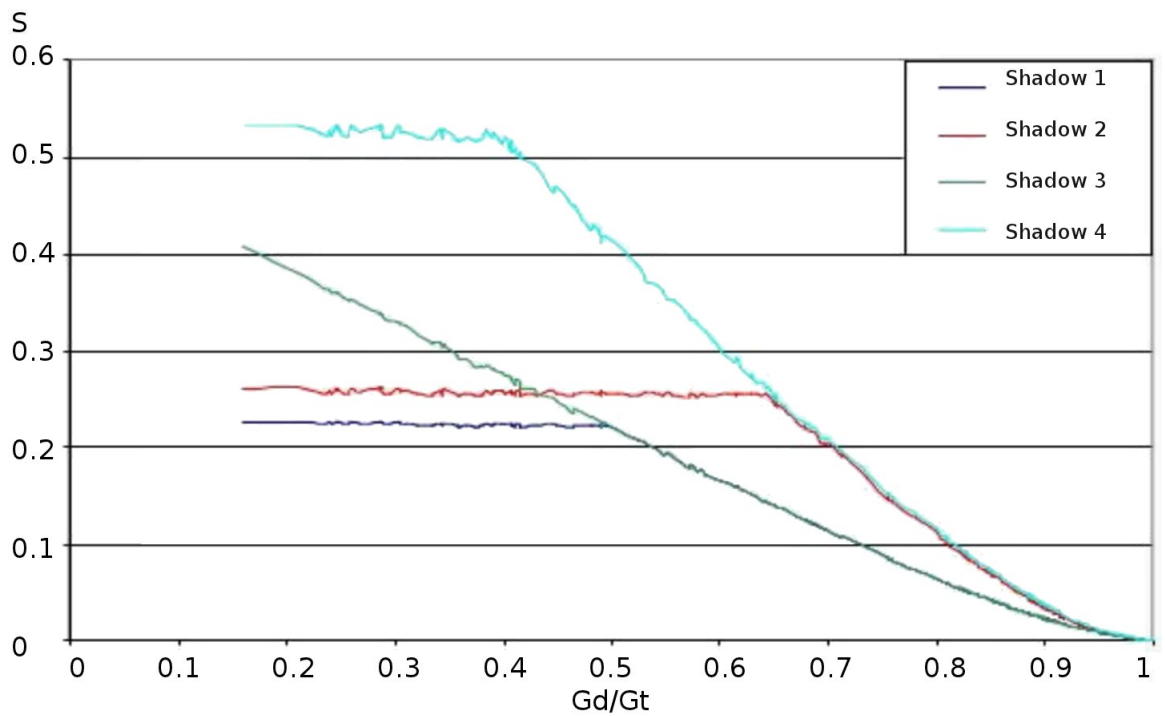
5.3 Model and calculation of shading path and position on PV array

To better predict the output of the PV system under partial shading the exact position of the shadow must be known and also the percentage of its area falling on specific cells.

As already explained the shadow on a surface changes its shape and position with time of the day and also the day of the year. Two codes have been written in Matlab to predict first the coordinates of the shadow and its shape. These are then used to calculate the percentage of the area shaded for each cell. The codes allow the user to select the time step (day and minutes) as well as the location and size of the shading objects.

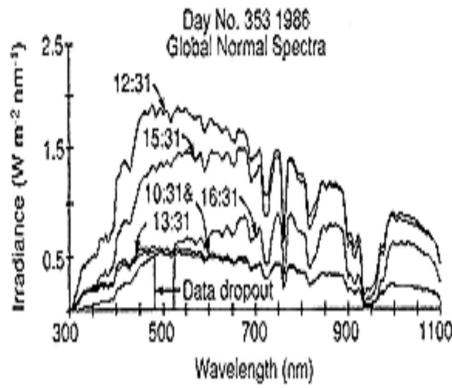


(a) S function of the ratio between the diffuse radiation and the global radiation for the modules connected in series.

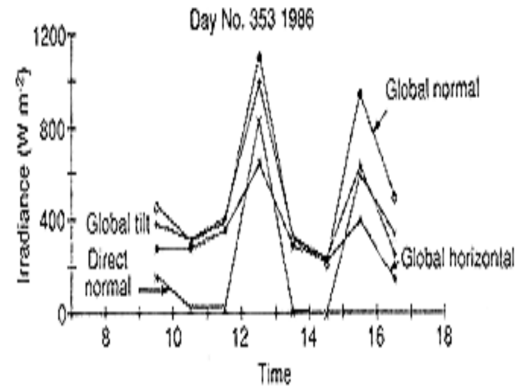


(b) S function of the ratio between the diffuse radiation and the global radiation for the modules connected in parallel.

Figure 5.11: Shading factor S for parallel and series connection between the module as function of the ratio G_{diff}/G_{tot} .



(a) Solar spectrum measured



(b) Global radiation.

Figure 5.12: Solar spectrum and global radiation for a partially cloudy day. (from <http://www.nrel.gov>)

To undertake this calculation a model of the surroundings is needed. Introducing a rectangular coordinate system with the basis vector orientated to the north, east and zenith $\sum = \theta, n, e, z$, the vector s pointing to the sun is given by [21]:

$$s = \begin{pmatrix} \cos \gamma_s \cdot \cos \alpha_s \\ \sin \gamma_s \cdot \cos \alpha_s \\ \sin \alpha_s \end{pmatrix}$$

where α_s is the sun altitude angle and γ_s is the sun azimuth angle. All surfaces of the objects in the surroundings of the PV system are assumed to be planar polygons. Objects can be made up from multiple surfaces that are described by these polygons. In this way regular shapes like cubes as well as irregular figures can be represented. Other figures such as cylinders and spheres can be approximate by polygon surfaces. Each vertex of a polygon can be represented by a vector o_i in the nez-coordinate system. A cube for example consists of six surface polygons, each of them with four vertices.

It is usual to approximate other objects, as for example trees, by several polygons but for this study the objects considered will be only simple planar polygons (see Fig.5.13 from [21]). PV cells can also be defined in the nez-coordinate system. Shading of the direct irradiance occurs if an object is placed between the position of the sun and the PV array surface. The shadow position of a single point p_0 (see Fig.5.14) can easily be determined. Starting from the point p_0 the point of intersection p_S with the PV system plane in the opposite direction of the vector s must be calculated. Suppose the PV array polygon is described by

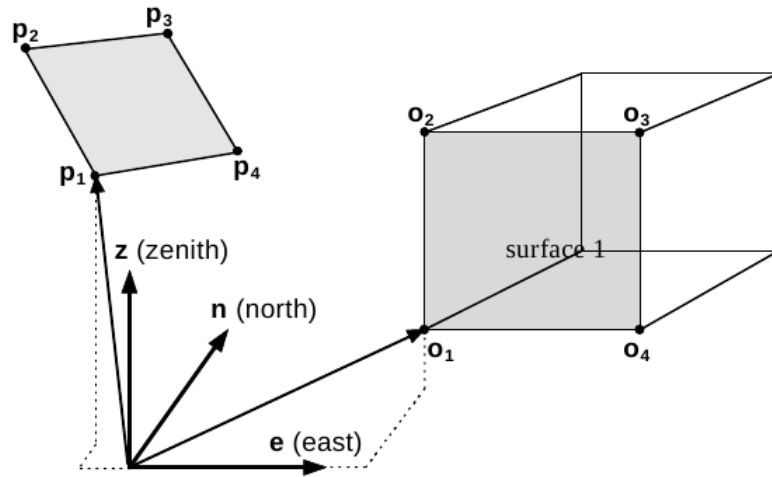


Figure 5.13: Representation of a cube and a solar cell using polygons in the nez-coordinate system.

4 vectors $p_1..p_4$, the vector p_s for the intersection between the sun direction and the PV array plane can be obtained by the following equation [21].

$$p_s = p_0 - \frac{a \cdot (p_0 - p_1)}{a \cdot s} \cdot s \quad (5.2)$$

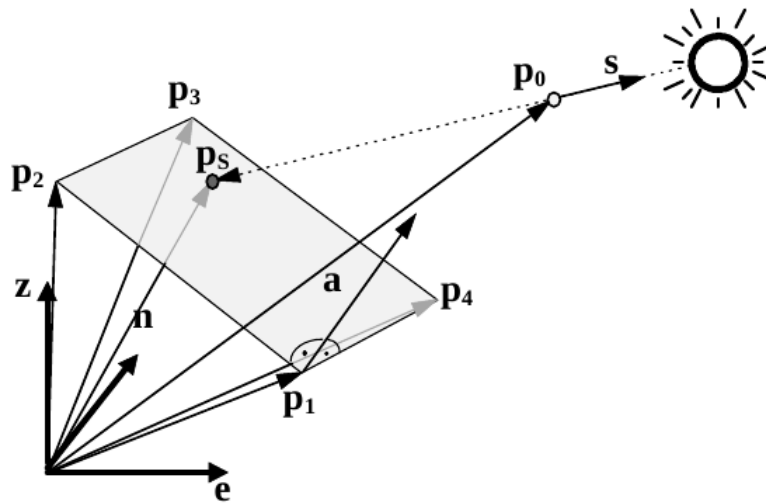


Figure 5.14: Determination of the shadow position of a single point.

The vector a is perpendicular to the solar generator plane and is given by:

$$a = (p_2 - p_1) \times (p_4 - p_1) \quad (5.3)$$

To calculate the shadow's percentage on a given PV cell the shape of shaded area

created by the surrounding objects is required; to calculate these coordinates of the vertices of the polygon (o_i) must be defined and from them calculation of their projections to the PV surface undertaken using eq.5.2 which determines the corresponding location of the shadow points (p_{Si})(Fig.5.14 from [21]).

A code has been written in Matlab, which calculates each point p_{Si} (see AppendixC).

This code (see code C.6 page 189) determines the variation of the points p_{Si} during the day. The input parameters are:

- The latitude of the location (ϕ in the code corresponds to phi);
- The longitude of the location ($\lambda_{zone}, \lambda_{loc}$ in the code corresponds to $lambda_zone, lambda$);
- The day of the year (i 1 for the first of January, 365 for the 31th December.);
- The range of time for the analysis. In the code this variable has been defined as a vector and its values are the minutes of the day starting from 8am till 18pm within a time step of 5 minutes ($v = [480 : 5 : 1080]$).

The time step needs to be less than 5 minutes to capture adequately the movement of the shadows;

- The coordinates of the shading object points (defined in the code with the points $r0...r3$) in the nez coordinates system;
- The coordinates of the PV array. At this stage the calculation is limited to the total shadow area projected by the object.

The first part of the code is dedicated to the calculation of the vector s . The components of the vector s are determined by the solar altitude and azimuth. These angles depend on the solar angle which varies with the minute of the day and the day of the year (hour angle - ω -, declination angle - δ -, solar zenith - θ_z -, and the solar azimuth- α_s -).

The code calculates each variable for each time step and stores it in matrices, some of these variables were already defined in section 4.5. The solar zenith is calculated by:

$$zenith = \cos^{-1} \theta_z \quad (5.4)$$

and

$$\alpha_s = 90 - zenith \quad (5.5)$$

The other angle needed to estimate the vector s is the solar azimuth by:

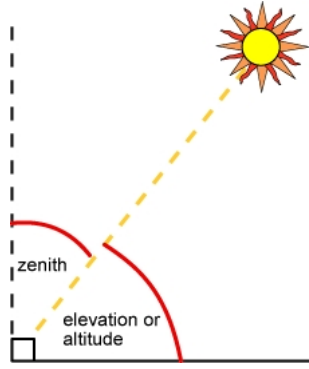


Figure 5.15: Elevation and zenith angle.

$$\gamma_s = \text{sign}(\omega) \left| \frac{\cos^{-1}(\Theta_z \sin \phi - \sin \delta)}{\sin(\text{zenith}) \cos \phi} \right| \quad (5.6)$$

Once all the angles have been calculated for the specific time step, the code follows the calculation for the s vector which, in this specific case, will be a matrix of three column (one per component) and as many rows as specified by the vector v . As output, the script has a polygon with the corresponding vertices on the PV surface that represent the shadow created by the object.

A second code has been written that takes as input each of the vertices of the shadow on the PV array at each time step. This script calculates the interception between the shaded polygon and the individual solar cells giving as results a matrix of 144 columns (1 per cell) and as many rows as defined by the time step of the simulation for the vector s .

An example to highlight how important it is to know the exact location of the shadow and its shape can be seen in Fig.5.16. Three different shadow shapes are represented at the same time of the day for three different days and the variation of the shadow position and its shape can be seen clearly.

5.4 Case study

The two codes, as previously outlined, provide the calculation for only one day at a time. The intent was to develop simulations for different cases of partial shading with the variation during the day and the year including different levels of radiation.

To do so the code that calculates the coordinates of the shadow has been modified including some *for* cycles reshaping the output matrix allowing the calculation of the partial shading also for more than a day.

Since the electrical simulation model requires values of the short circuit current

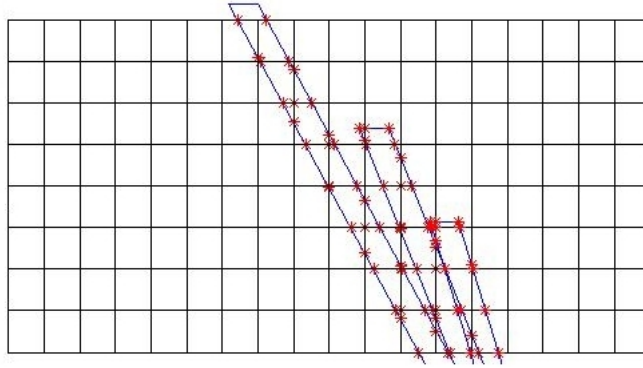


Figure 5.16: Partial shadow at 11am created by an object on south-east. The 3 different polygons are the shadow created on the 12th January (largest), the 13th March and the 1th of May (smallest).

for each cell, data from the weather station in Stuttgart (Germany) has been used to provide global and diffuse radiation of the year 2010 with a time step of 5 minutes. This is because suitable long term data measured in Glasgow was not available yet. The simulations for the partial shading have been run for the whole year and to reduce the simulation time and the amount of the data, the time step has been fixed at 15 minutes and the components of the radiation have been selected to match the time of the simulation for the partial shading. After selecting the corresponding values, the incident radiation on the PV array has been calculated with respect to the time and location: the code in AppendixC has been adapted to that location.

The partial shading calculations have thus been made for Stuttgart for a PV system installed at a 30° tilt angle and same dimension and size of the PV roof experiment in Strathclyde.

The simulations included two different situations. The first one comprises two objects placed in such a way that they create shadows on the PV surface during the morning (south-east placement) and during the afternoon (south-west placement). This configuration has been simulated separately for each shading object due to the structure of the codes. The calculations are based on the number of vertices and with two objects the codes are not able to specify which vertices belongs to which shading objects. The codes can analyze one polygon at the time.

The two output matrices with shading percentages for each cell, created by each object have been then summed to obtain the total matrix with all the percentages of the shaded area per cell. Each element of the matrix corresponds to the S variable of eq.4.7; the short circuit current for each cell has been calculated once S and G_{tot} (eq.4.6) are known, and with the help of scripts it was possible

to create the files for the current generator in PSpice.

The second situation includes only one object following all the procedures described above (south-west placement).

5.5 Example of the effects of shadow movement in time

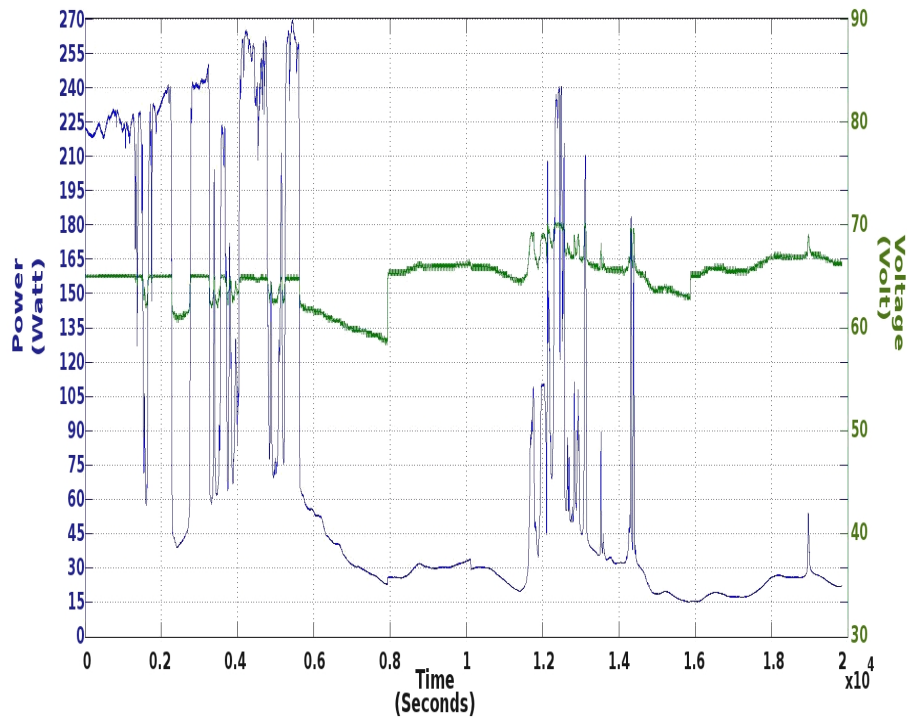


Figure 5.17: Maximum power point (blue line) and V_{mpp} simulated for the array representing the roof experiment in Strathclyde University without any shadow.

As has been explained, shading can significantly affect the electricity production of a PV system.

To better understand how partial shading can vary during the day, and its effects on the MPP and the V_{mpp} , a case of partial shading has been simulated to reproduce the losses in power production due to the variation of the shading during the time period examined.

For this analysis measured radiation data have been used to calculate the value at the tilt angle of the PV system. An object has been placed in south-west position to create partial shading in the afternoon and it has been simulated with the code described in Sec.5.3. The total simulation time is five hours and thirty

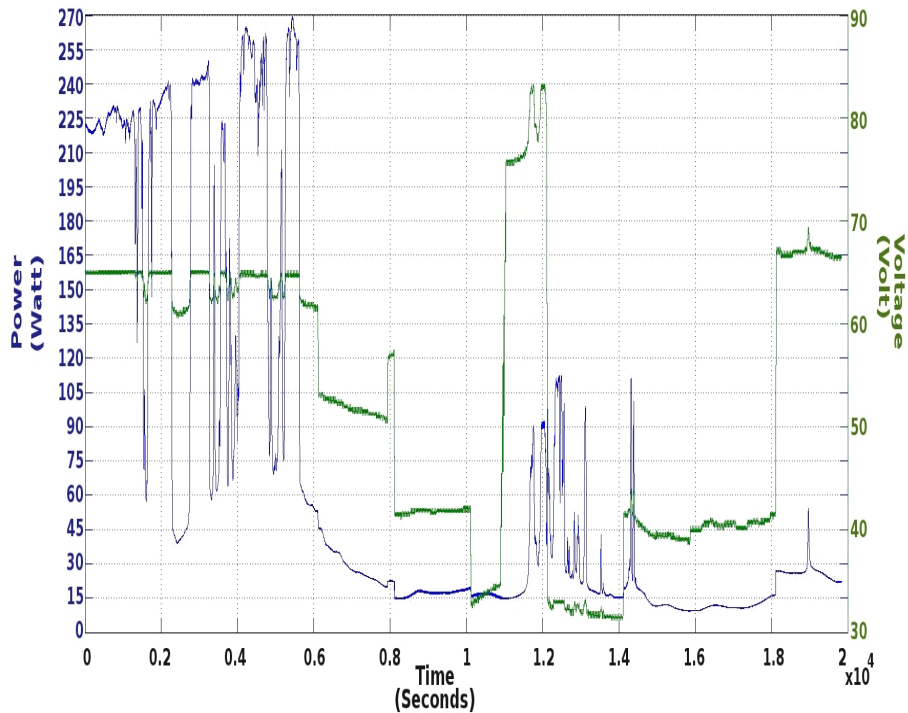


Figure 5.18: Maximum power point (blue line) and V_{mpp} simulated for the array representing the roof experiment in Strathclyde University with the partial shading.

eight minutes with a time step of one second.

The incident radiation and the percentage of the shaded area of each cell is used to calculate the value of the short circuit current of each cell included in the PSpice model (see Chapter 4). The contribution of the temperature to current generation has been calculated using the measured PV temperature and included in the simulation. The simulation has been run using hourly averaged measured temperatures for each module. The diode currents are determined by these temperatures and thus the model properly represents thermal mismatch.

The steps in V_{mpp} apparent in Fig.5.17 are caused by the fact that averaged temperatures have been simulated. As underlined before, the temperature varies slowly compared to the irradiance but for constant low radiation the PV temperatures decrease steadily and using averaged temperature leads to step changes and consequently significant step changes in the V_{mpp} .

Fig.5.17 shows the MPP and the V_{mpp} resulting from the simulation for the incident radiation with no shading. Power varies with radiation and the V_{mpp} is in a range between 58 and 71 Volts. The largest variation in voltage is about 7 volts but, aside from this step, the voltage decreases or increases slowly since

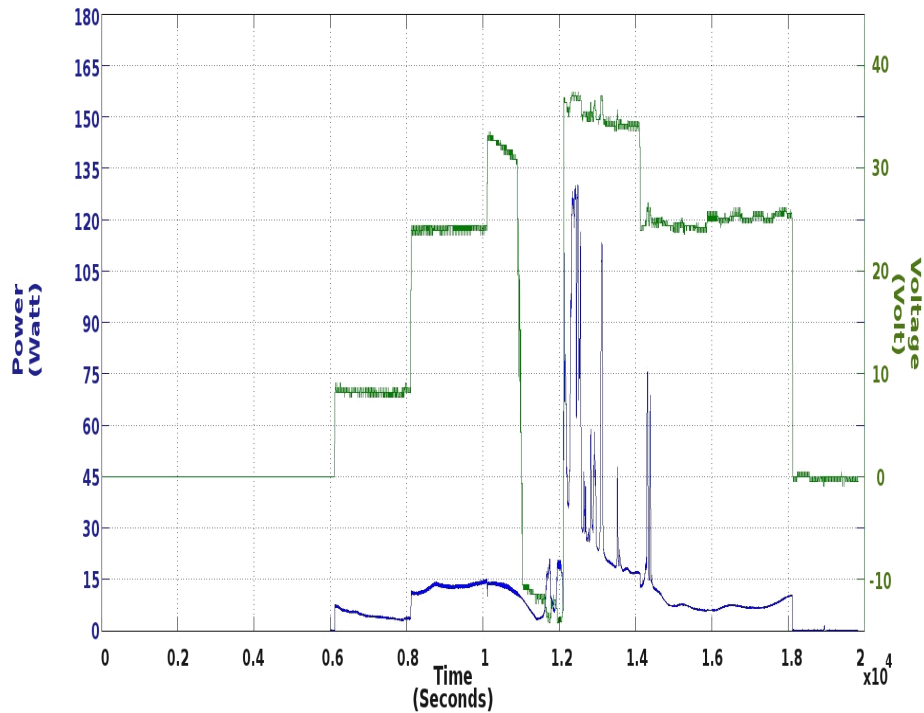


Figure 5.19: Difference between the power (blue line) produced by the array for the falling radiation with and without partial shading. The green line represents the variation in V_{mpp} due to the partial shading.

temperature changes are slower than irradiance changes. Even for a day with fast irradiance changes the V_{mpp} remains close to the optimal working point.

On the other hand, when the PV system is affected by partial shading the operating voltage moves rapidly (to lower or higher voltage regions). The object selected projects its shadow across the PV system and as the time progresses within the time period this shadow affects more modules due to the variation of the angle between the object and the sun. For this specific case the V_{mpp} is changing from 30 up to 80 volts (Fig.5.18), depending on the number of the modules affected, their connection and the amount of shading of each cell.

To better quantify the power losses Fig.5.19 shows the difference between the power simulated without any partial shading and the one obtained by the same PV system affected by the shading, as already described, projected by the specified object. The power lost, for this specific case, reaches 130 W and the difference in V_{mpp} increases from -10 to 35 Volt.

Another important characteristic to note from Fig.5.18 is the variation of the V_{mpp} as a function of time. Mostly the operating voltage remains pretty stable over at least 200 seconds but sometimes the variation of the partial shading

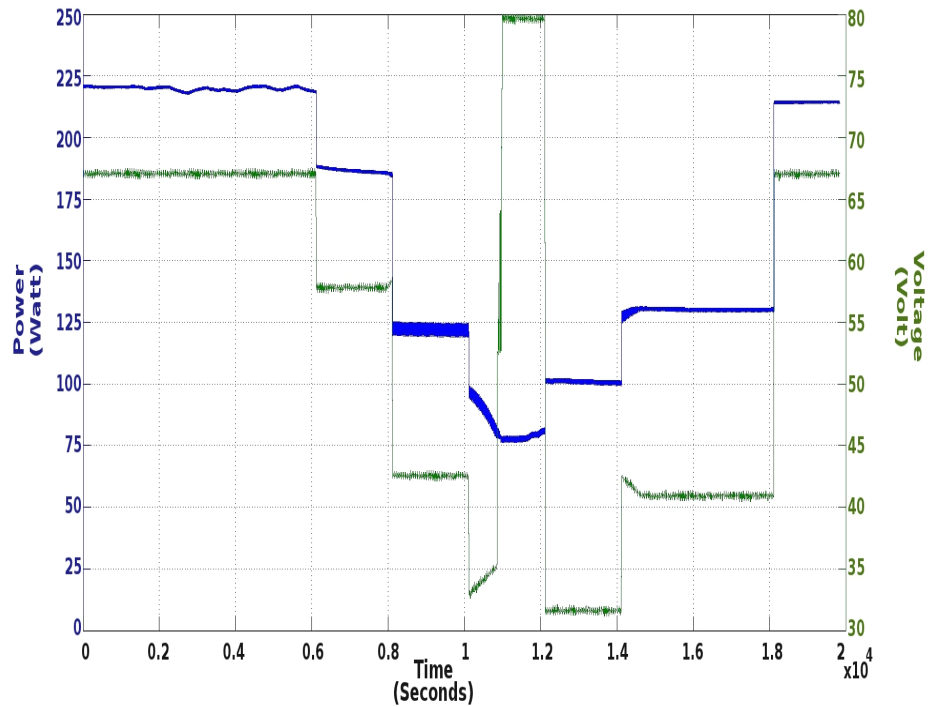


Figure 5.20: Ideal case with constant radiation ($700Wm^{-2}$); The figures underlines the effect of the partial shading due to only its shape and area.

projected by the object forces a large variation (40 Volt) of the operating point within about 100 seconds or in the case of medium variation steps (10 Volt), in less than 50 seconds.

These large variations of the operating point are difficult to detect because, in case of partial shading, the power characteristic of the PV array presents more than one local maxima and the MPP algorithms which use a fixed step could be at the wrong working point. For these cases only a scan of the power/current characteristic could provide enough information to find the true maximum.

The information collected during the study of partial shading and in particular the variation of the working point for the PV when affected by partial shading highlighted the issues which affect the MPP. An effective algorithm should:

- scan the power/current characteristic to determine the true maximum;
- be fast in tracking the power characteristic due to fast potential changes in radiation;
- the scan should be repeated at least every 100 seconds to handle any significant variations in the shape of the shadow and its impact on the working point;

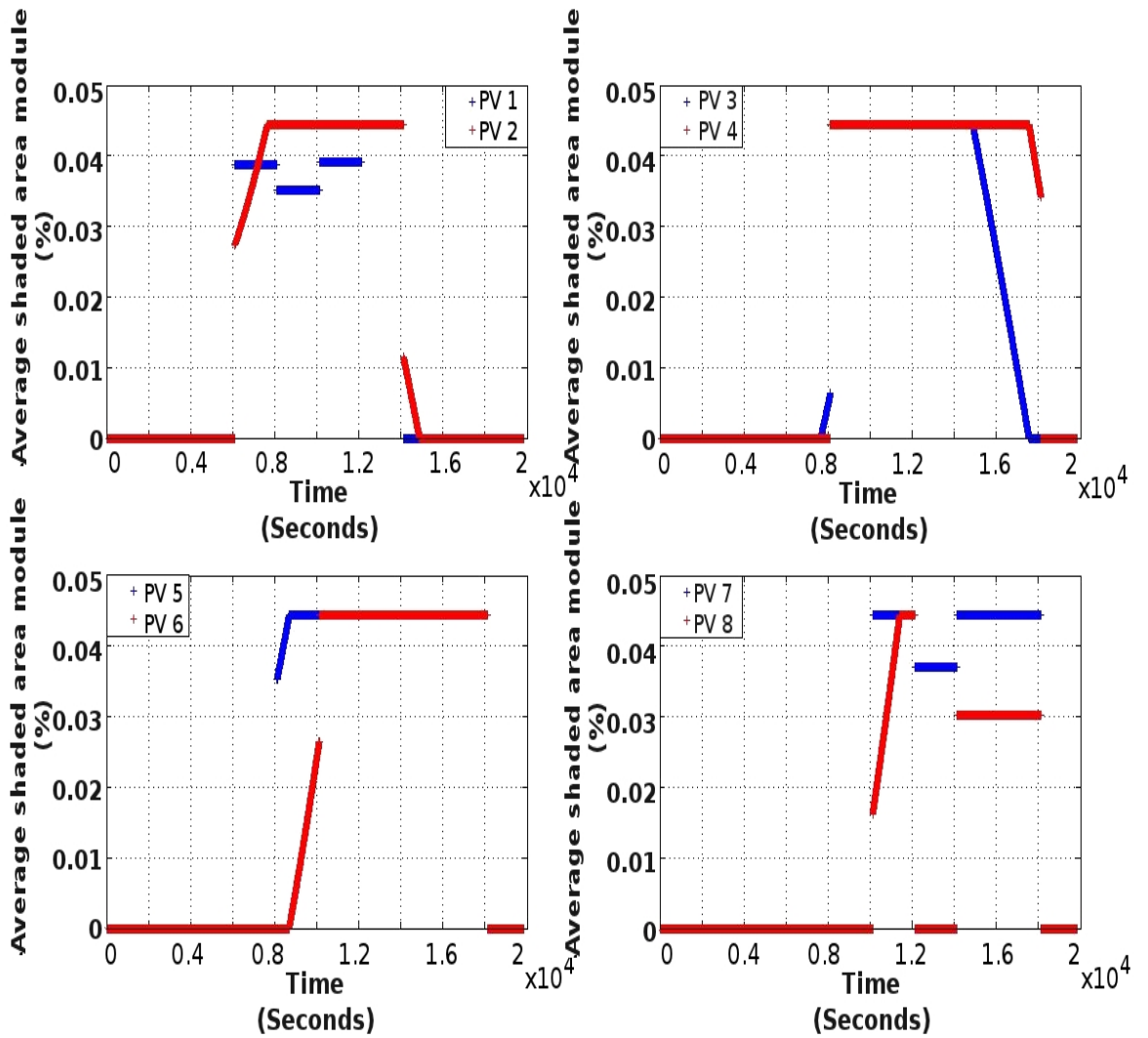
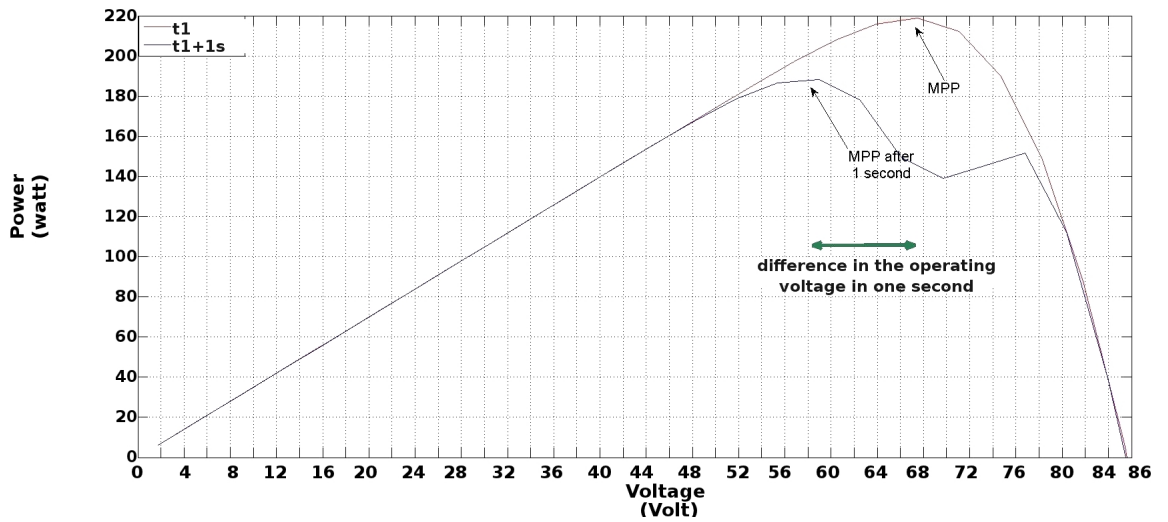


Figure 5.21: Average of the partial shading affecting PV modules at each time step. PV1, PV2 etc indicate the position of the PV modules in the array configuration as shown in Fig.4.2.

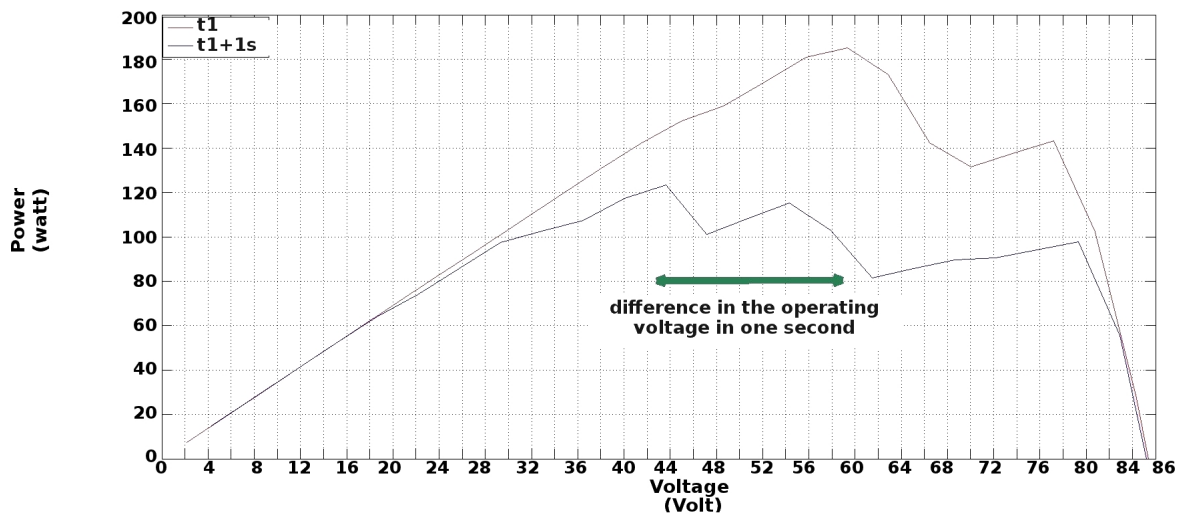
- apply a variable time step to deal with the changes in the operating point rapidly;

Fig.5.20 presents an ideal case of partial shading in which the incident radiation has been kept constant at the value of 700 Wm^{-2} and the same partial shading as before with its evolution in the time has been simulated. Abrupt changes in operating voltage and power are evident, reflecting transitions as one or more modules become shaded.

To give clear idea of the amount of the partial shading and how this changes in time, Fig.5.21 shows the average of the percentage of the shadow calculated for each module of the PV array. Some power characteristics have been extrapolated



(a) Two sequential power characteristics for the PV array simulated in case of partial shading with constant incident radiation.



(b) Two sequential power characteristics for the PV array simulated in case of partial shading with constant incident radiation.

Figure 5.22: Examples of the variation of the P-V characteristic for the PV array affected by partial shading during the day.

from the results of the simulation for the partial shading with constant incident radiation to show the challenge to the MPPT of a PV array affected by partial shading (see Fig.5.22). Fig.5.22(a) catches the moment when the partial shading starts affecting the PV array performance; Fig.5.22(b) shows the moment when an additional module is affected by the partial shading for the first time.

5.6 Conclusion

This chapter deals with a issue problem for the PV performance under partial shading.

The main effects have been described and the importance of the shadow shape and the position highlighted.

An example has been used to illustrate the impact of the shading: the total shaded area was fixed but the PV modules affected varied and resulted in very different power characteristics.

Also this chapter emphasized how surrounding buildings can have a significant impact on PV performance but that power losses are highly dependent on the detail of the urban form.

The last part of the chapter was dedicated to the calculation of the shadow and the percentage of the shaded area on an individual cell of a PV array and the impact of these on the MPPT and power generation. A mixture of real radiation data, simulated shading, and PV system simulation have been used.

The work done on partial shading was crucial for the development of the algorithm. The time variation, the operating voltage changes, the power reduction shown by the results of the simulations have given the key features of the algorithm to detect the *MPP* in case of partial shading.

Also, all these simulation results have been used to train, test and validate an artificial neural network used to detect the maximum power point for shaded PV system, as described in Chapter 6.

6

Algorithm for the Maximum Power Point Tracker

This chapter describes the algorithm structure for detecting the maximum power point for real operating conditions. As widely explained, real operating conditions can result in a significant degradation of the PV system performance. In particular, partial shading gives rise to a number of local maxima in the power characteristic. As discussed in previous chapters, the changes in the shape of the power characteristic function depend on many parameters (electrical connection, position of the nearby objects and of PV system, bypass diodes, time of the day, location, modules mismatch, irradiance level, temperatures and technology).

This chapter starts with an outline of the algorithm structure for the procedure to detect the MPP for all the possible situations (partial shadow, fast irradiance variation, mismatch, etc.). The algorithm makes use of an artificial neural network to detect the MPP every 100 seconds, and a PI controller will assist the ANN in case of any variation in temperature and radiation. The second part of the chapter is dedicated to the description of the ANN, including training and validation, the PI controller and its design. The final part of the chapter concerns the results: the algorithm has been tested for stable conditions, fast irradiance changes, temperature mismatch and of course for partial shading.

6.1 Algorithm structure

Many enhanced MPPT algorithms require additional sensors to predict the working point (MPP) of the PV array. The use of sensors, normally radiation and temperature sensors, increases the price and may sometimes give a wrong indication of the operating point, particularly when the radiation is not uniform across

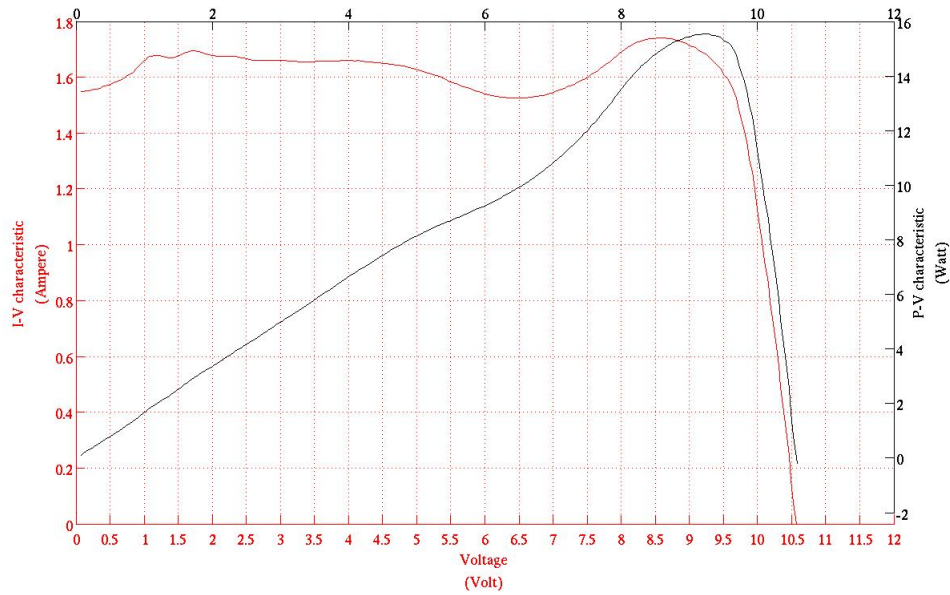


Figure 6.1: An example of a scan of the I(V) characteristic when the radiation is varying. The measurement has been taken in 1.2 second.

the PV array or when PV modules are affected by shading. Increasing the number of the sensors will only increase the cost but without giving any guarantee of detecting these kinds of challenging situations.

Another solution can be to scan the I(V) characteristic but this takes time to complete and during the scan the radiation and temperature can change as well as the MPP thus, after the scan, the converter may be working at the wrong point. The time needed for scanning the I(V) characteristic depends on the design of the DC/DC converter; for scanning the I(V) characteristic generally a fixed step of the duty cycle is used. The larger the step, the faster is the scan but it is the less precise in reading the I(V) characteristic.

Fig.6.1 shows how the scan can introduce an error in detecting the MPP if the measurement is done during a variation in radiation. This specific example has been measured from the PV test system; the I(V) characteristic is for one module and has been measured in 1.1 seconds. However, measurement of the I(V) characteristic is the only precise way to determine the MPP. As detailed in Chapter 4 the temperature is not uniform even over the area of a single cell (it depends on the current production that in general is not uniform). Across the array area, it can be assumed that there are variations in temperature and we cannot measure all of these (these variations can be very significant in case of partial shading) or measure the radiation incident on all the individual cells to get a good prediction of the MPP. Also it has been taken into account that

radiation can vary quickly and thus it is important to find the MPP rapidly. In the approach developed here no additional sensors will be used, instead an approach to fast scanning is used, based on a limited set of measurements.

A solution to the challenge is proposed along the following lines. The approach is to predict the $I(V)$ characteristic from a few measured points. The $I(V)$ and $P(V)$ characteristics are functions that can be approximated effectively by polynomials fitted to these data points. In this way the characteristic functions can be built across the full operating range. The possibility to trace the $P(V)$ characteristic on the basis of so few points will reduce the time for the prediction of the MPP, thereby reducing errors due to fast changes in the irradiance.

When the array is affected by the partial shading, the output power characteristic presents more than one local maxima. The corresponding optimal operating voltage and the peak values of each maximum depend on the shape of the shading, its position on the array and the connection arrangement (including diodes) between the cells and modules. The best way to track the true maximum for a partially shaded array would be conventional scanning the $I(V)$ characteristic. Here a polynomial approximation of the power characteristic has been proposed to avoid such a complete scan. The polynomial approximation allows the power characteristic to be quickly calculated as function of just few data points where the number of points is determined by the order of the polynomial.

To identify the order of polynomial which best approximates a generic power characteristic from a PV array, the function *polyfit* from Matlab has been used which also returns the coefficients of the polynomial. The use of another Matlab function, *polyval*, helped to highlight graphically which values of the voltage best fit the power characteristic. These points on the power characteristic have then be used to verify that the polynomial calculated at these points fits the power characteristics measured from the PV array under different conditions.

In this way the order of polynomial best suited to represent typical $P(V)$ characteristics has been investigated, and also just as important position (in voltage terms) of these measured data points, as required for effective fitting. It has been found that a polynomial of order 5 can represent the most complicated $P(V)$ characteristics that can be reasonable expected. In addition it was found that for the system under study the best location of these six points (in terms of voltage) was given by 8.4V; 16.5V; 32.7V; 57V; 73.2V and 81.3V, where the voltage at the maximum power point @STC, from the data-sheet and for the connection arrangement is 73.6 Volt and the open circuit voltage is 88Volt @STC [14]. Comparing of the $P(V)$ characteristics with the polynomial fits are shown in Fig.6.2(a)

and 6.2(b) respectively.

These selected data points can be used to avoid the need for a complete scan of the $P(V)$ characteristic. The algorithm implements Artificial Neural Network to predict and estimate the value of the MPP and the corresponding voltage. A feed-forward ANN has been trained with simulated data to predict the MPP for a wide range of operational conditions.

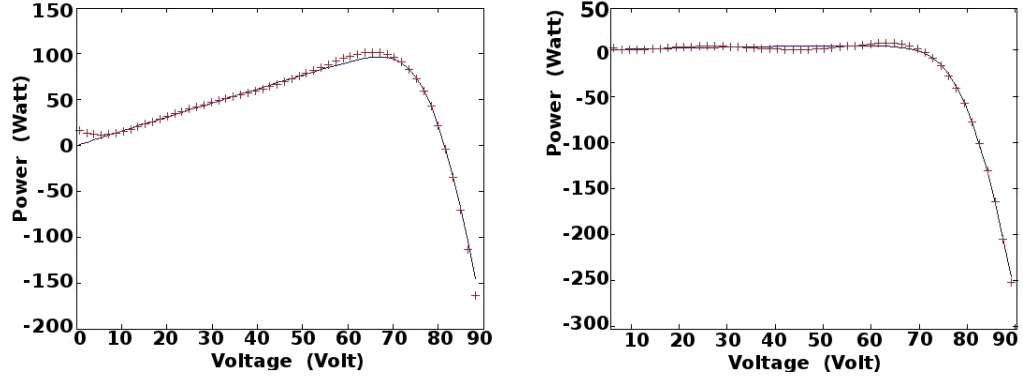


Figure 6.2: Two examples of the matching between the polynomial function and the $P(V)$ characteristic.

The algorithm starts with power measurement at the 6 reference voltages. These are input to the ANN (detailed in the next sections), which outputs the predicted values of V_{mpp} and the MPP. The voltage calculated by the ANN will become the next operating voltage set for the DC/DC converter. While the system is working at this operating voltage the power output will be measured and compared with power predicted from the ANN as part of the converter controller.

Because ANN can predict the V_{mpp} with small error even for fast irradiance changes, MPP calculated by ANN will be close to the one sensed from the PV system because there will be no substantial changes in irradiance, temperature and this performance during these few milliseconds. The control algorithm will analyze the difference between the maximum power point predicted and the one measured at the operating voltage and this difference will drive any changes in the operating voltage point. The next operating voltage point determined by the control algorithm is the V_{mpp} estimated from ANN plus (in case the power predicted is larger than the measured one) or minus (opposite case) a proportional value to the difference between the measured and the predicted MPP. In the next section will be introduced and explained the factor α which is the proportional coefficient above introduced.

Even though the ANN needs only 6 points for predicting the MPP and the

V_{mpp} , it is not convenient to continuously run the ANN. Using the ANN a few times per minute could improve the performance of the MPPT under fast irradiance changes but for the steady operating condition the MPPT will waste time in doing unnecessary scans. Another reason to run the ANN less frequently, is that although the shadow changes in a measurable way every second, significant changes require something like minutes.

As a compromise it has been decided to scan every 100 seconds. This is because for this type of module a small change in shadow position (one centimetre) involves in a large reduction or increases in power; as explained in Chapter 4 these modules have only one bypass diode and the output current of each module, in case of partial shading, will be determined by the cell with lower current. That means if one object creates partial shading on two modules at time t_0 and one of these has only 1cm^2 of its area affected by shading (the power characteristic for this has three local peaks), after few minutes, due to the variation of the angle between the sun and the PV system, that module may present no shadow at all and the I(V) characteristic will have only 2 peaks, so changing the MPP significantly and consequently also V_{mpp} .

It should be noted that the scan interval will depend on the details of the system.

The MPP, I_{mpp} and V_{mpp} are determined by several factors:

- a) PV technology used;
- b) array design (electrical connection) and size;
- c) incident radiation;
- d) module temperatures;
- e) eventual partial shading;
- f) electrical and thermal mismatch.

The variation of these parameters as function of the time depends on:

1. Distribution of temperature across the cells of the array due to non-uniform heating and cooling (wind effect);
2. Variation of the radiation;
3. Variation of the shadow path and shape;

The algorithm should be able to cope with all of these factors. The ANN can not work all the time because the scan of the P(V) characteristic take a finite time, even if that scan requires only 6 points. The system could lose time scanning while, for example, there is no significant variation in power and V_{mpp} .

For this reason the algorithm works with two steps: the first one is controlled by the ANN that, thanks to the data used for the training, will predict the MPP and V_{mpp} taking into account the factors (a-f); the second part starts working after the ANN has produced an output adjusting the V_{mpp} to account for variations 1-3.

After the scan, the system is working at the voltage defined by the output of ANN (V_{mpp}^{ann}). The controller memorizes the value of the MPP which the ANN has estimated and compared the P^{ann} with the power measured (P_{meas}) from the PV system at the V_{mpp}^{ann} . This is the first part of the algorithm that will be repeated once every 100 seconds.

The challenge of the algorithm is finding the voltage working point (V_{mpp}) for real operating conditions; it has been noted that the variations of V_{mpp} depend on the PV temperature more than the irradiance. To better understand the behaviour of the V_{mpp} as function of the temperature and the irradiance, the PV array has been simulated with fixed temperatures (from 25 up to 75°C)and irradiance changes from 100 to 1000 Wm^{-2} . The plot of the MPP for different irradiance levels (see Fig.6.3) as a function of the temperature (x-axis) shows that for irradiance higher than 300 Wm^{-2} the V_{mpp} is constant and depends only on the temperature. This suggested an approach to determine the V_{mpp} . It has also been noted that there is a correlation between the power difference (measured and predicted) and the correction to apply to the V_{mpp} .

To determine this correlation, the power characteristics above described have been used. Let say the system be operating at 40°C and with incident radiation of 1000 Wm^{-2} . This corresponds (from simulated values) to a MPP of 305.54W and a V_{mpp} of 66.985V. Let it further be assumed the ANN output is P^{ann} (334.034 W) and V_{mpp}^{ann} (72.565 V). In this case the system is working at V_{mpp}^{ann} that corresponds to 288.255 W from the power characteristic of the PV system. The difference between the MPP predicted and the measured one is 45.778 W. A proportional adjustment of the V_{mpp} is applied as follows:

$$V_{mpp} = V_{mpp}^{ann} + \Delta V_{mpp} \quad (6.1)$$

where

$$\Delta V_{mpp} = \alpha \Delta P^\beta = 0.625 * \Delta P^{0.63} \quad (6.2)$$

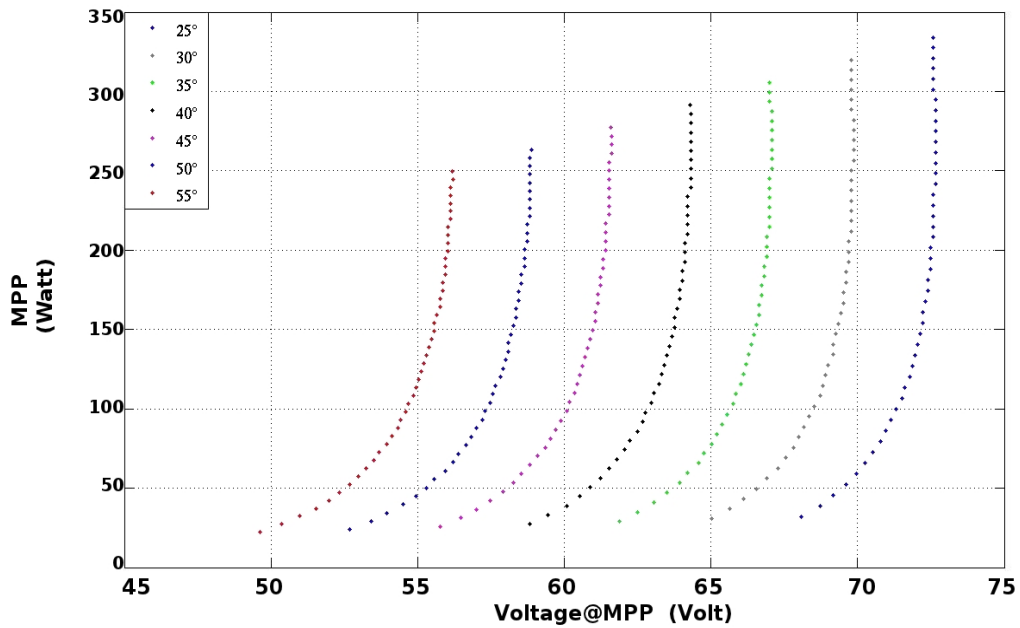


Figure 6.3: The graph shows the MPP over the V_{mpp} simulated for different irradiance levels but constant temperature (increasing temperature left to right).

It is now possible to find the true V_{mpp} . ΔP gives an adjustment of -7.101 Volt that corresponds to the new working point of 65.46 Volt. A new value of the power will be measured and compared with the previous one so a proportional step to that difference will applied to the operating voltage point. This expression for ΔV_{mpp} allows use of a variable voltage step to make the algorithm faster in seeking the true MPP; the ANN has been trained to cope with issues a to f but it is possible that the output from ANN contains some errors and/or the situation could change after few milliseconds. The second part of the algorithm will deal with this by adjusting the operating voltage.

The second part of the algorithm is working until the input from the ANN is updated (99.93 seconds later) and it will deal with the variations listed previously as(1-3). These variations are now dealt with in detail, one at time.

6.1.1 Variation in temperature

As explained in Chapter 4 the temperature of a PV cell/module varies as a function of radiation, ambient temperature, wind speed and current flow. These factors are not even constant over the area of a single solar cell it is clear that across a large area, substantial temperature variation can occur. From the data

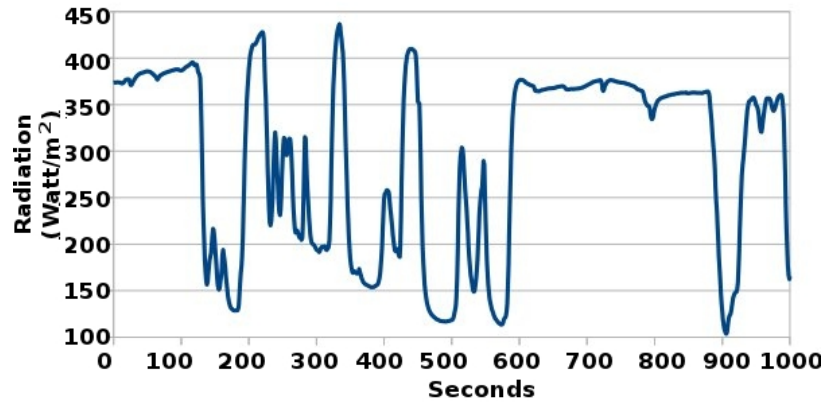
measured on the test system a difference in temperature between the eight modules up to 5°C has been observed. Another factor to be noted that is the variation of the PV temperature is not fast as the variation of the radiation. A particular example of this is shown in Fig.6.4: the radiation is changing quickly and significantly (Fig.6.4(a)) but the module temperature decreases slowly (Fig.6.4(b)). The algorithm deals with variations in temperature in the following way. First, it stores the power and the voltage output from the ANN, the controller apply the value of V_{mpp}^{ann} to the PV system and the power is measured. If the power measured is higher than P_{ann} , i.e. temperature of the system is lower than that predicted, a proportional increment will be added to V_{mpp}^{ann} by the feedback controller, and the system will now work at $V_{mpp}(t_1)$. This value of voltage will be applied for two time steps to check if there is further variation. If the system does not identify any further variation in power, the system will continue to work at the same voltage. Alternatively if variation in power is detected, another adjustment to the operating voltage will be made.

If the temperatures of the system is higher than that predicted, the MPP measured will be lower than expected and the controller will react differently, as explained below in the next section.

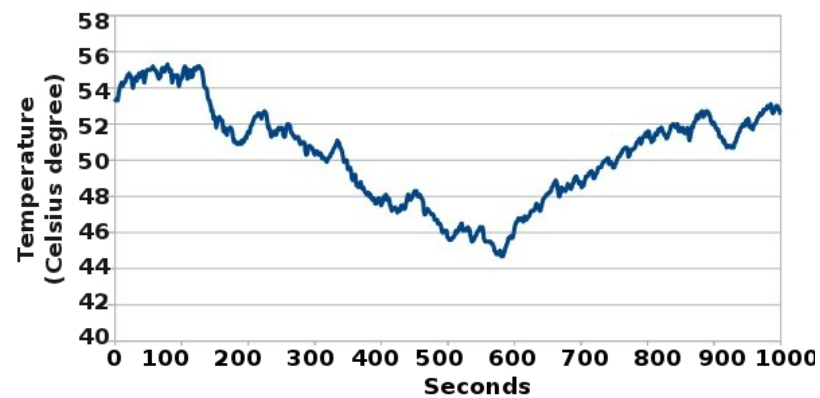
6.1.2 Irradiance variation

As shown in graph6.3 changes in the incident radiation for a specific temperature do not result in significant changes in V_{mpp} . It has also been explained why the variation of the temperature is not fast as for radiation. Thus, in case of fast irradiance changes the V_{mpp} does not change much but the power will be higher or lower (depending on the change in radiation). If change in radiation is negative the power measured will be lower than that predicted and if the irradiance continues to decrease the system control will continue to decrease V_{mpp} because the $P_{meas}(t_n)$ will be always lower than $P_{meas}(t_{n-1})$. For this specific case the true V_{mpp} remains almost constant because the temperature changes are less rapid. Fig6.4 shows a measured example illustrating the variation of the temperature in case for fast irradiance changes.

To deal with a decrease in radiation, the controller checks if $P_{meas}(t_n) < P_{meas}(t_{n-1})$ and returns a constant value of -300mV that will be added to $V_{mpp}(t_n)$. If the radiation changes again, the system will remain close to the working point and the next ΔV_{mpp} will be negative. An example illustrates this. Fig.6.5(a) shows how the system reacts when radiation is decreasing while Fig.6.5(b) shows the changes applied by the controller in case increasing of temperature but constant



(a) Graph of measured global radiation in case of fast irradiance changes.



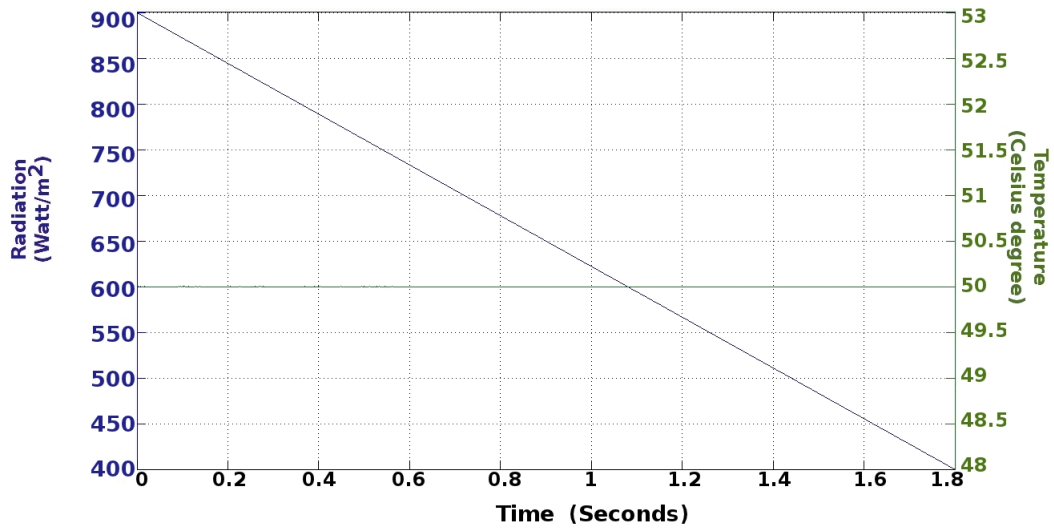
(b) PV module temperature measured in case of fast irradiance changes.

Figure 6.4: Radiation and temperature variations.

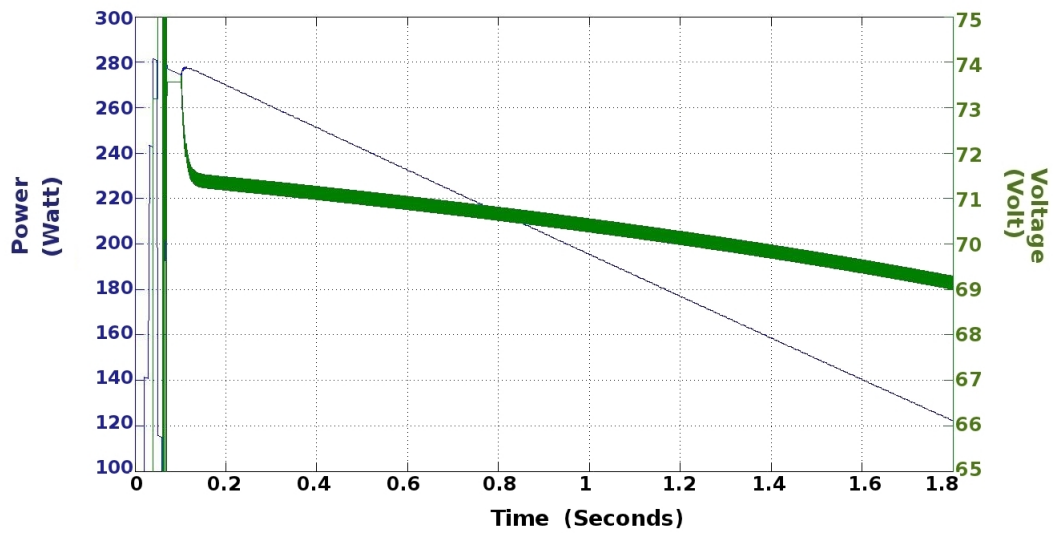
irradiance.

6.1.3 Shading variation

During the day the shading changes its size and position so that PV system performance becomes a function of time and of day. Since the sun changes its position in the sky over the year, seasonal patterns of shading occur that influence the PV system. The output of PV modules affected by partial shading is driven by the cell which produces least current (i.e. the cell having most shading). For series connected cells under uniform radiation, the array presents as many local maxima as modules affected by partial shading. Different proportions of shading give rise to different output currents. The output power from the array can change in the order of milliseconds due to the passing clouds but the number of the local



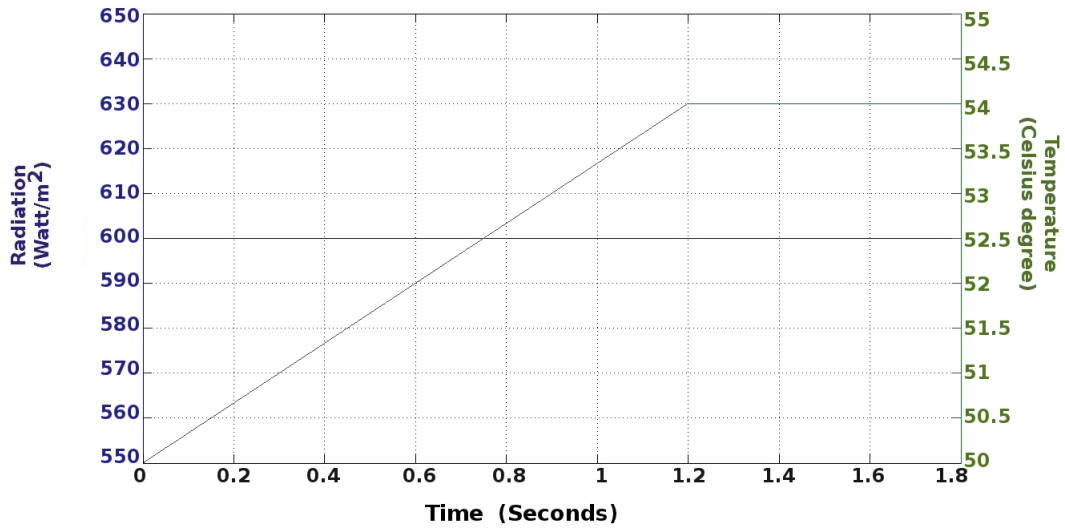
(a) Graph of radiation and temperature applied to the array.



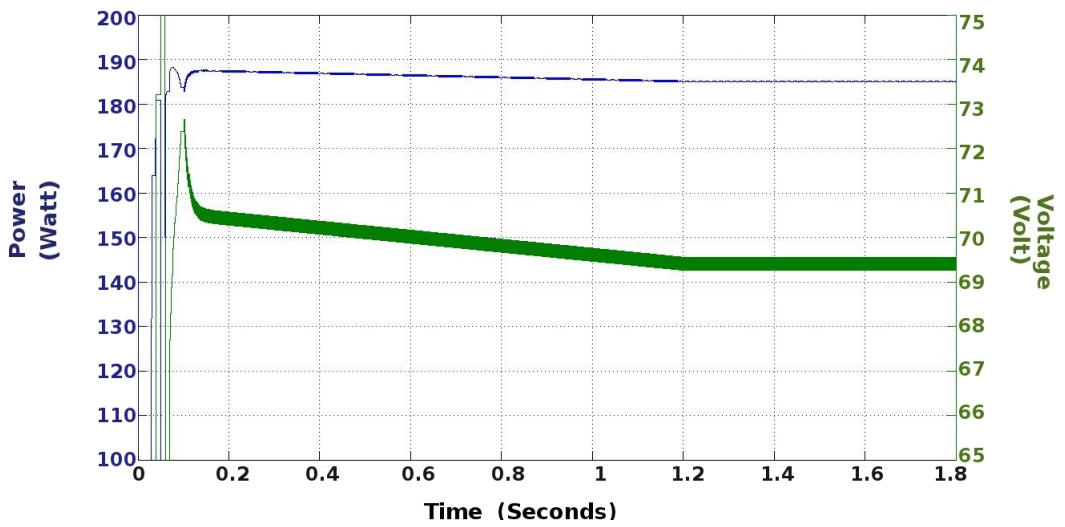
(b) V_{mpp} decided by the controller and power in output from the PV array for the voltage applied.

Figure 6.5: Negative slop of the radiation.

maxima cannot change quite so quickly since the angle between the sun and the observation point requires at least 5 minutes to change significantly. Consequently the shaded area due to a fixed nearby object will not change significantly over 100 seconds. The true maximum can become higher (or lower) but the number of local maxima remain fixed over this time period. Thus V_{mpp} is stable and eventual variations of V_{mpp} are due primarily to fluctuations of radiation and temperature, and thus can be accorded by the real time feedback loop of the MPPT controller.



(a) Graph of radiation and temperature applied to the array.



(b) V_{mpp} decided by the controller and power in output from the PV array for the voltage applied.

Figure 6.6: Higher temperature of the PV modules with constant irradiance.

6.2 Artificial Neural Network

A neural network is an adaptive numerical machine that can be used to model complicated or imprecise data.

Neural networks are composed of simple elements operating in parallel. These elements are inspired by biological nervous systems. As in nature, the network function is determined largely by the connections between elements. We can train a neural network to perform a particular function by adjusting the values of the connections (weights) between the elements [34].

A neural network consists of an interconnected group of artificial neurons, and it processes information using a connectionist approach to computation. In most cases an ANN is an adaptive system that changes its structure based on external or internal information that flows through the network during the learning or training phase.

An important feature of artificial neural networks is its learning capability. The learning mechanism is often achieved by appropriate adjustments of the weights in the so called synapses of the artificial neuron models. Training is done by non-linear mapping or pattern recognition. If an input set of data corresponds to a definitive signal pattern, the network can be trained to give the corresponding pattern at the output [31].

6.2.1 Structure

Artificial neural network types vary from those with only one or two layers of neurons with single direction logic, to complicated multi-input many directional feedback loops and layers. On the whole, these systems use algorithms in their programming to determine control and organize of their functions. Some may be as simple as a model with one neuron layer with an input and an output, and others can mimic complex systems.

Most systems use "weights" to change the parameters of the throughput and vary the connections to the neurons. Artificial neural networks can be autonomous and learn by input from outside "teachers" or even be self-teaching using pre-written rules.

For this study a two-layer feed-forward network has been selected with sigmoid hidden neurons and linear output neurons. Such a model can fit multi-dimensional mapping problems arbitrarily well, given consistent data and enough neurons in its hidden layer. The network will be trained with Levenberg-Marquardt back-propagation algorithm. Fig.6.7 shows the structure, the layers and size of the ANN implemented.

The meaning of the individual components is in more details below.

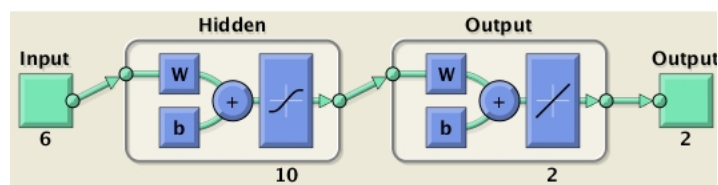


Figure 6.7: ANN structure

Neuron

Neurons are the basic signalling units of the nervous system and each neuron is a discrete cell whose several processes arise from its cell body[30]. The neurons perform some operations to determine the desired output from the input, the weight and the bias are adjusted during the training. From Fig.6.8(a) we can deduce the neuron output for any given vector input $\mathbf{p}=[\mathbf{R}\mathbf{x}\mathbf{1}]$.

$$a = f(\mathbf{W}\mathbf{p} + b) = f(w_{1,1}p_1 + w_{1,2}p_2 + \dots + w_{1,RP}p_R + b) \quad (6.3)$$

The scalar elements of the vector \mathbf{p} are transmitted through a connection that multiplies its strength by the scalar weight w [1]. In this case the neuron includes also a bias b that can be considered as a weight except its input is a constant of value 1. The scalar output (weighted input plus the bias) is the input to the transfer function (f) that generally is a step function or a sigmoid function to obtain the neuron output a . The Sigmoid Transfer function takes the input (with a range of $\pm \infty$) and squashes the output in a range of 0 and 1.

Layer

A layer, as shown in Fig.6.8(b), is composed by the aggregation of one or more neurons and its output is a vector:

$$\mathbf{a} = \mathbf{f}(\mathbf{W}\mathbf{p} + \mathbf{b}) \quad (6.4)$$

The vector \mathbf{a} has dimension equal to the number of the neurons of the layer. In case of multiples layers as for the network in Fig.6.7

$$\mathbf{a}^2 = \mathbf{f}^2(\mathbf{LW}^{2,1}f^1(\mathbf{IW}^{1,1}\mathbf{p} + \mathbf{b}^1) + \mathbf{b}^2) \quad (6.5)$$

where:

element	size	element	size
\mathbf{p}	1x6	\mathbf{a}^2	2x1
$\mathbf{LW}^{2,1}$	2x10	$\mathbf{IW}^{1,1}$	10x6
\mathbf{b}^1	10x1	\mathbf{b}^2	2x1

Feedforward networks often have one or more hidden layers of sigmoid neurons followed by an output layer of linear neurons. Multiple layers of neurons with non-linear transfer functions allow the network to learn non-linear and linear relationships between input and output vectors. The linear output layer lets the network produce values outside the range 1 to +1.

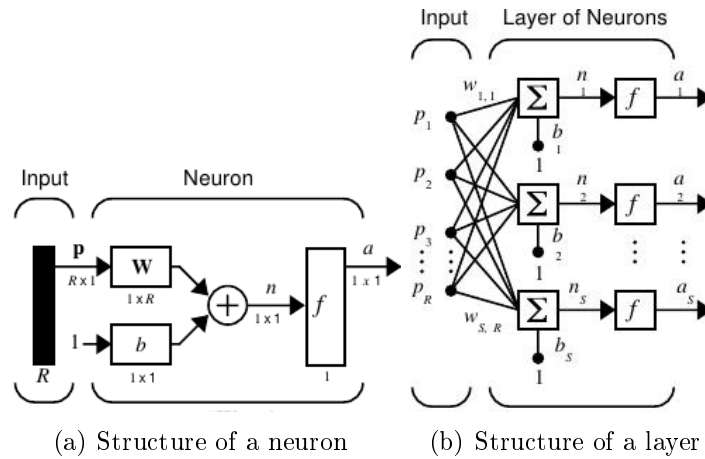


Figure 6.8: Structure for a static network [1].

6.2.2 Training

The network can be trained for function approximation (non-linear regression), pattern association, or pattern classification. The training process requires a set of examples of proper network behaviour comprising network inputs p and target outputs t . During training the weights and biases of the network are iteratively adjusted to optimize the network performance.

The default performance function for feedforward networks is mean square error mse - the average squared error between the network outputs a and the target outputs t . The training algorithms use the gradient of the performance function to determine how to adjust the weights to minimize performance. The gradient is determined using a technique called backpropagation, which involves performing computations backwards through the network.

The simplest implementation of backpropagation learning updates the network weights and biases in the direction in which the performance function decreases most rapidly. The Levenberg-Marquardt algorithm was designed to approach second-order training speed without having to compute the Hessian matrix. When the performance function has the form of a sum of squares (as is typical in training feedforward networks), then the Hessian matrix can be

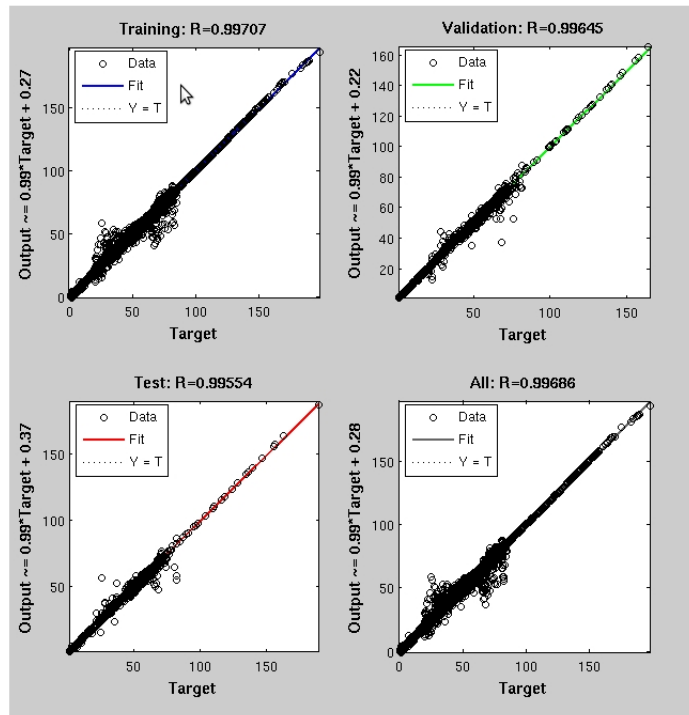


Figure 6.9: ann results

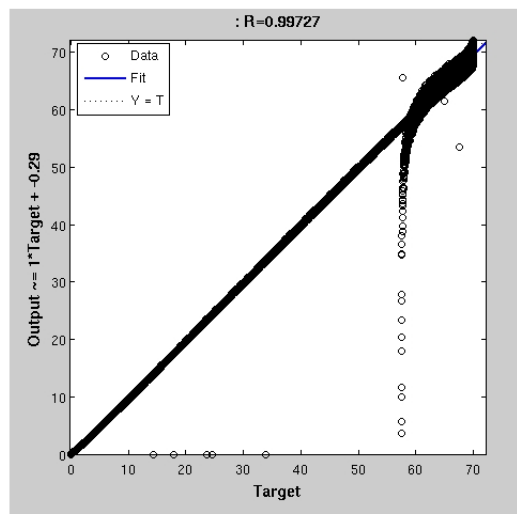


Figure 6.10: Test ann

approximated as

$$\mathbf{H} = \mathbf{J}^T \mathbf{J} \quad (6.6)$$

and

$$\mathbf{g} = \mathbf{J}^T \mathbf{e} \quad (6.7)$$

where \mathbf{J} is the Jacobian matrix that contains first derivatives of the network errors

with respect to the weights and biases, and \mathbf{e} is a vector of network errors.

The Levenberg-Marquardt algorithm uses this approximation to the Hessian matrix in the following Newton-like update [12]:

$$\mathbf{x}_{k+1} = \mathbf{x}_k - [\mathbf{J}^T \mathbf{J} + \alpha \mathbf{I}]^{-1} \mathbf{J}^T \mathbf{e} \quad (6.8)$$

When the scalar α is zero, this is just Newton's method, using the approximate Hessian matrix. When α is large, this becomes gradient descent with a small step size. Newton's method is faster and more accurate near an error minimum, so the aim is to shift towards Newton's method as quickly as possible. Thus, α is decreased after each successful step (reduction in performance function) and is increased only when a tentative step would increase the performance function. In this way, the performance function will always be reduced at each iteration of the algorithm [2].

This algorithm appears to be the fastest method for training moderate-sized feedforward neural networks up to several hundred weights.[12]

6.3 Controller model

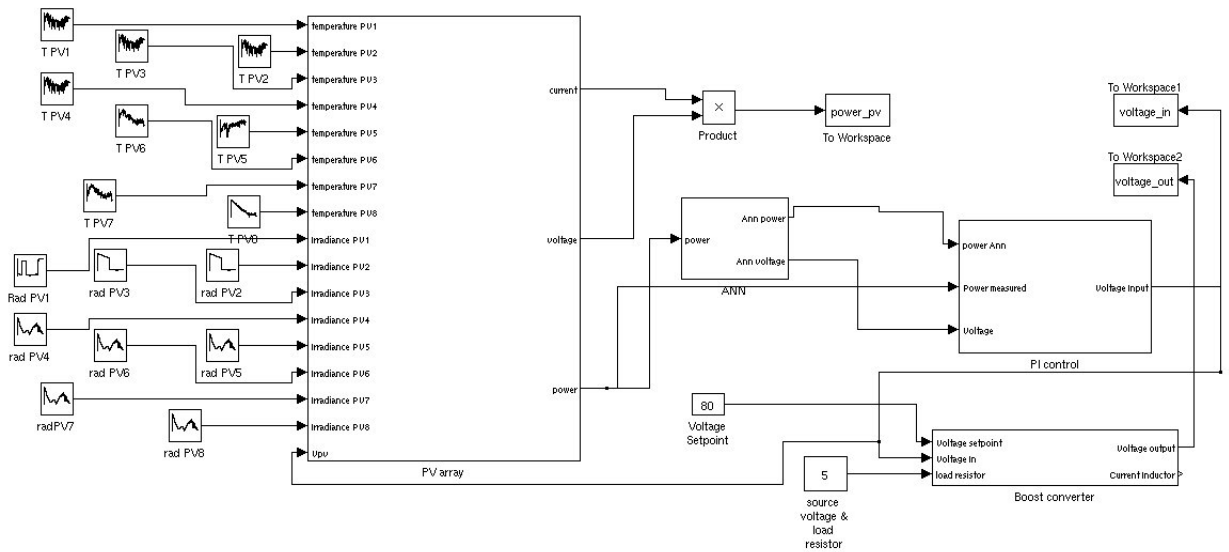


Figure 6.11: Model for the PV array, the ANN, the PI and the boost converter in Simulink

To test the algorithm described in section 6.1 a model for the controller has been developed in Matlab/Simulink. The model includes a PV array, a block for

a feed-forward Artificial Neural Network, a controller system which implements the algorithm guidelines and a model for a boost converter.

6.3.1 PV array

To best if the controller is able to determine V_{mpp} for any real operating condition, the model has been equipped with a PV array composed of the series connection of the eight modules. Each module has been represented as a 1-diode model to reduce the amount of time required for the simulation but all the modules have an independent value of radiation and temperature. With this model it is possible to reproduce partial shading and mismatch. The inputs radiation and temperature are implemented on the sources "The Repeating Sequence Interpolated" which output a discrete-time sequence and then repeat it. The block uses the lookup method "Interpolation-Use end value" to provide an incremental step between data points.

Within these sources, the weather data can be implemented and simulated almost realistically: the temperature and the radiation used in the simulation are the data measured from the PV test facility (recorded every seconds) and they are affected by variations. The measured values have discontinuities between their values, this kind of source in Matlab permits reducing these discontinuities by interpolating the output between any two adjacent points.

6.3.2 ANN

An Artificial Neural Network as been created in Simulink by adding a simple command at the end of the code to generate the desired ANN (*gensim(net,st)* where *st* is the simple time). The ANN has the same structure and function described in the previous section but takes inputs only every 100 seconds so it uses the help of a pulse function to select the desired signal.

6.3.3 PI control block

This block takes as input the two outputs from the ANN (power and voltage) plus the output power measured from the PV array and gives as output the voltage at which the system has to work.

This block includes a PI controller which helps in changing the voltage using a variable voltage step trying to track the MPP. As detailed in section 6.1 the working point is determined first of all from the ANN, and subsequently works on ΔP measured through feedback.

At the start, the output voltage from the control block is a step function with six steps and their value is fixed at 8.4V; 16.5V; 32.7V; 57V; 73.2V; 81.3V. These are the measurement points for the P(V) characteristics which generate the inputs for the ANN. Once the ANN has produced an output, the system then works for one time step at this voltage. Now the working point is V_{mpp}^{ann} and at this voltage the power of the PV array is measured. The difference between the predicted and the measured power is input to the PI controller which generates a signal to add to the set working voltage. To prevent ANN faults or to adapt the operating voltage point due to variations of radiation and temperature, the input to the PI block is switched to the ΔP measured: the difference between the two values of the power measured at two sequential time steps that reflect any changes in radiation and/or temperature. The controller uses a standard PI controller to dynamically control the PV system.

In the classical configuration (Fig.6.12) for a PID (Proportional-Integral-Differential) controller, the control signal $u(t)$ is the sum of three terms. Each of these terms is a function of the tracking error $e(t)$. K_p is the proportional gain and generates feedback proportional to the error. K_i/s is the integral term, and $K_d s$ is the differential gain.

A general PID controller works with the present, past and "future" errors (proportional, integral and derivative terms). Each term is now explained:

Proportional term

The feedback response is:

$$u(t) = K_p e(t) \quad (6.9)$$

where $e(t)$ is the current value of the error. The larger the error, the larger the signal. The feedback response tends to zero as the error does. Thus, if the system drifts a bit from the target, the control does almost nothing to bring it back. This is where the integral term comes in.

Integral term

The feedback response is given by:

$$u(t) = K_i \int_0^t e(\tau) d\tau \quad (6.10)$$

Thus, the system, if stable, is guaranteed to have zero steady-state error. If $e(t)$ is non-zero for any length of time (for example, positive), the control signal gets

larger and large as time

Derivative term

Here the feedback response is:

$$u(t) = K_d \frac{de(t)}{dt} \quad (6.11)$$

The derivative term is not widely used due to noise affecting the vale of the derivative of $e(t)$.

The derivative term has not been included in the controller scheme used in this work.

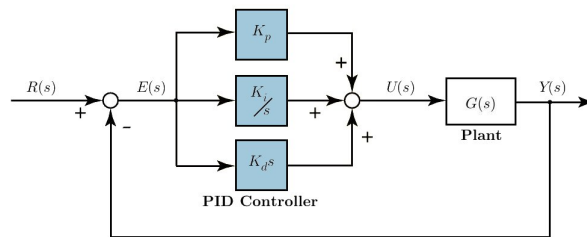


Figure 6.12: PID control system.

6.4 Results

The system described in Sec.6.3 has been tested using real measured data. Some of these results are shown in this section, other results have been included in AppendixD. Fig.6.4 illustrates the results for 2000 seconds of measured data collected on the 31th August 2010. This day has been selected because it exhibits large and fast irradiance changes which are difficult for MPP T algorithms such as Perturb/Observe. As can be seen from Fig6.13(a) the radiation changes include variations of more than 150 Wm^{-2} in less than 20 seconds while the temperature goes through less pronounced changes. Measured temperature for modules PV2, PV4, PV6 and PV8 (reference numbers from Chapter 4) are shown.

Fig6.13(b) presents the results for power and voltage. The voltage is the V_{mpp} at which the system is operating and the power corresponds to the output power from the PV array for the operating voltage applied. It can be noted that the power follows the same shape as the radiation including the peaks, as would be hoped. The voltage response is more complex and needs explanation, step by step.

For the first 200 seconds the voltage slightly decreases due to the increasing temperature of the PV modules; from 200 and 300 seconds the voltage presents a small positive peak (although lower than the previous one) because the temperature briefly reduces followed by another small negative peak due to a local peak in temperature of one of the modules. Another important increase in voltage is at 600 seconds. Here, the negative slope of the radiation (at 500 seconds) affects the PV temperature producing the lowest voltage excursion at 520 seconds but then rising steadily for 200 seconds during which the radiation can be considered constant. In this case the voltage increases between 500 and 600 seconds and then slightly decreases following a similar drop of temperature. The last important local increase voltage is at 1600 seconds when the temperatures of the modules decrease about 5°C.

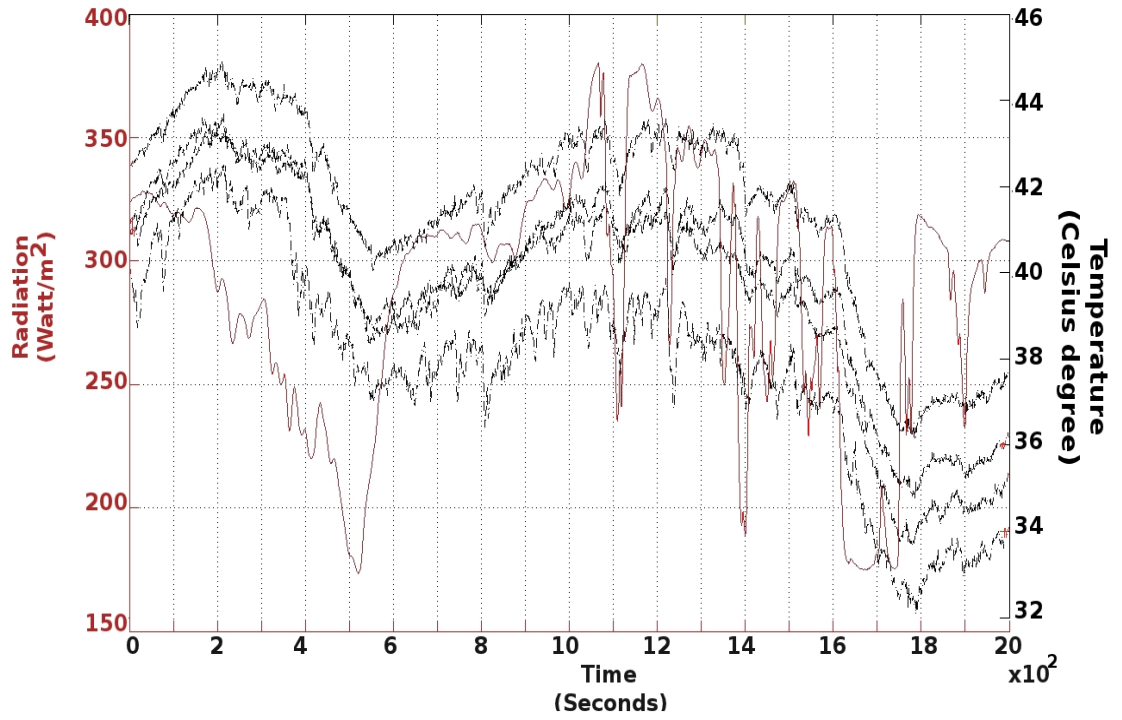
Other measured data where the radiation is almost constant has been used to test the algorithm for the partial shading of the PV array. The PV array model built in Matlab is the one diode model because the algorithm has to be test to detect the MPP for power characteristics which present local maxima. Nevertheless the Matlab model for the PV system has the capability to reproduce power characteristics with more than one peak.

The results shown in Fig.6.14(b) concerns a situation when two modules of the PV array are affected by partial shading. The power characteristic for this specific case presents two local maxima. The V_{mpp} remains almost stable about 50 Volt because there are no significant variations in temperature.

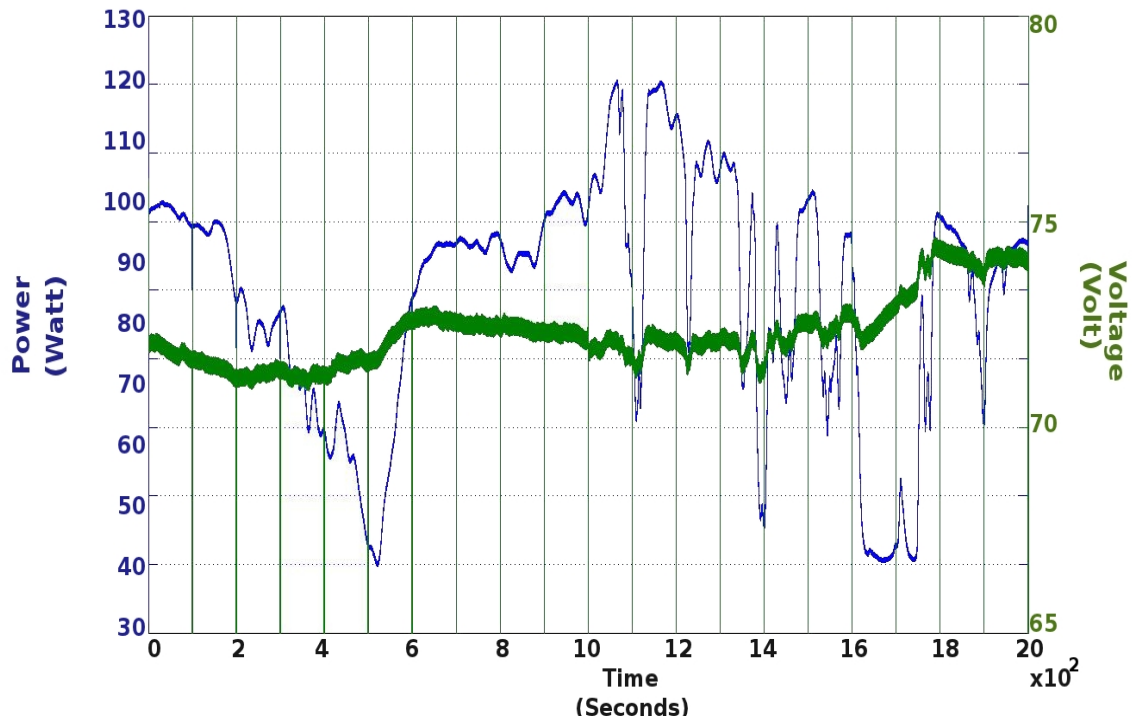
During the first 100 seconds the operating voltage decreases because the radiation is decreasing and the temperature is slightly increasing. The ANN made an error at the first scan, because the two local maxima are very close, predicting a V_{mpp} higher than the true one, but for the second scan it works (at 200 seconds) predicting V_{mpp} accurately.

To estimate the efficiency of the algorithm in predicting the operating point, the output determined by the algorithm has been compared with MPP as modelled for the PV array as shown in Fig.6.15. Aside from the initial error introduced by the ANN for the first 100 seconds the controller is able to detect accurately the MPP.

The same radiation data have been used to test a partial shading of the PV array which involves in three peaks. Incident radiation and temperatures data are detailed in Fig.6.16(a). For this specific case the ANN predicts very accurately the V_{mpp} and the algorithm exhibits only a small error of 1 Watt which represents 1.4% losses at time 80 seconds.

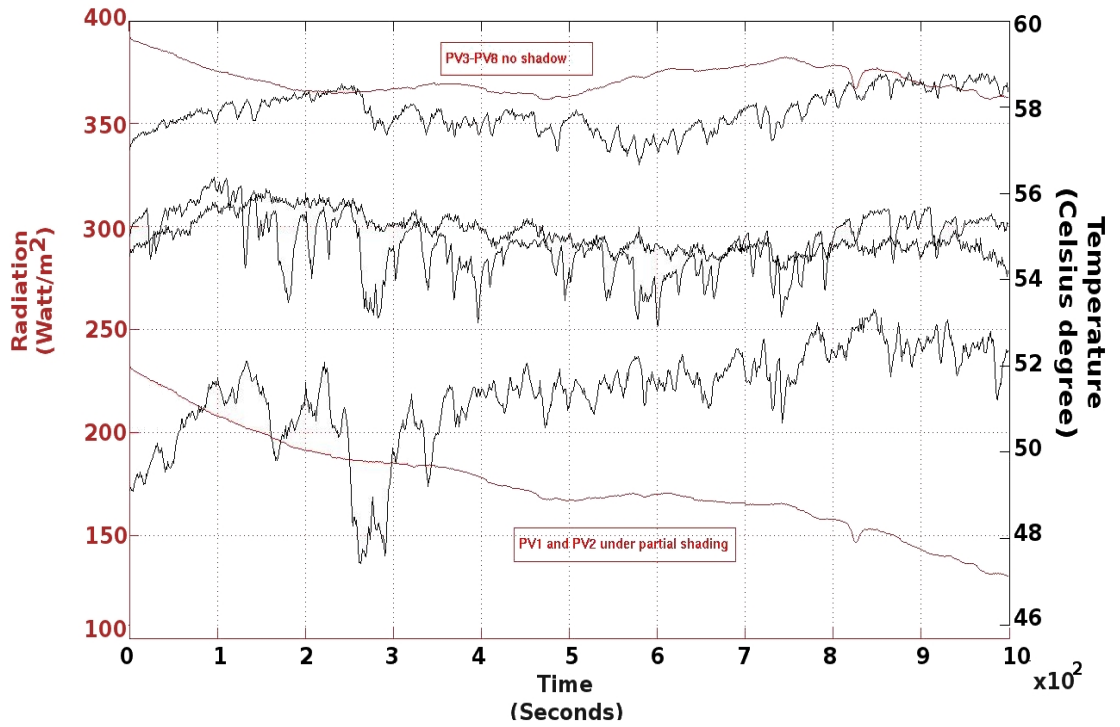


(a) The graph includes the value of the measured radiation considered uniform on the PV array and the measured temperature for the PV modules.

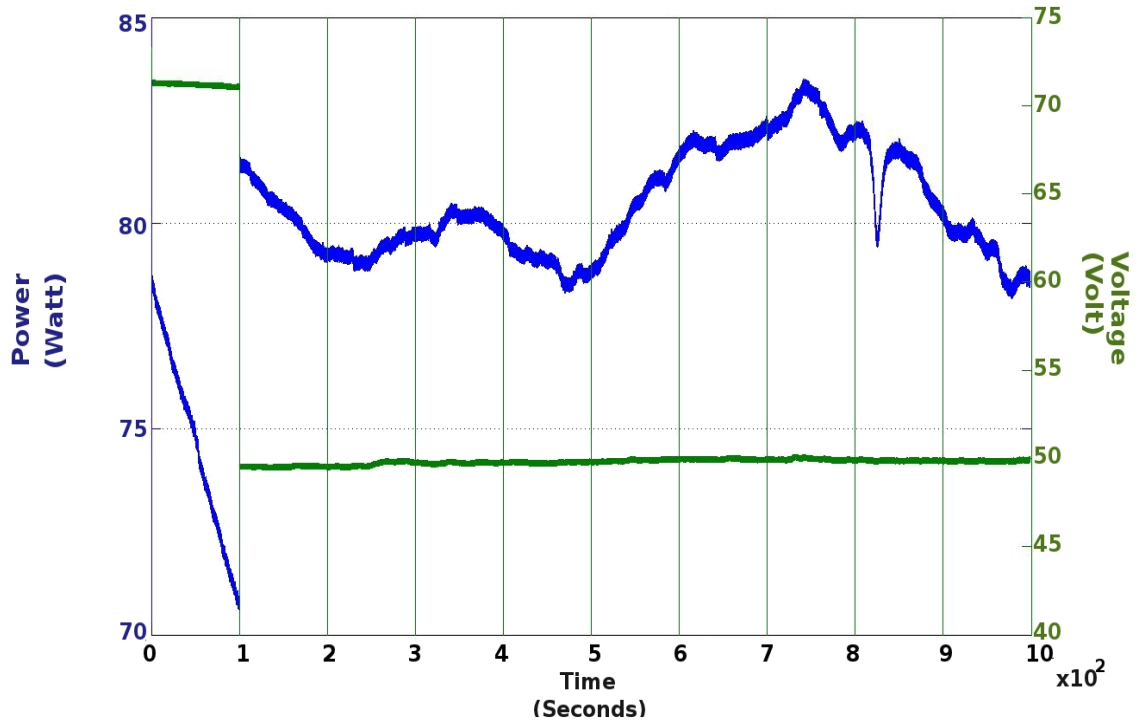


(b) The blue line is the power from the PV array for the calculated operating voltage (green line) from the controller.

Figure 6.13: Results for 2000 seconds of measured data on 31th August 2010.



(a) The graph includes the value of the measured radiation and the radiation falling on the modules affected by partial shading; the graph shows also the values of the temperature for 4 PV modules.



(b) The blue line is the power from the PV array for the calculated operating voltage (green line) from the controller.

Figure 6.14: Simulation of partial shading on 31th August 2010.

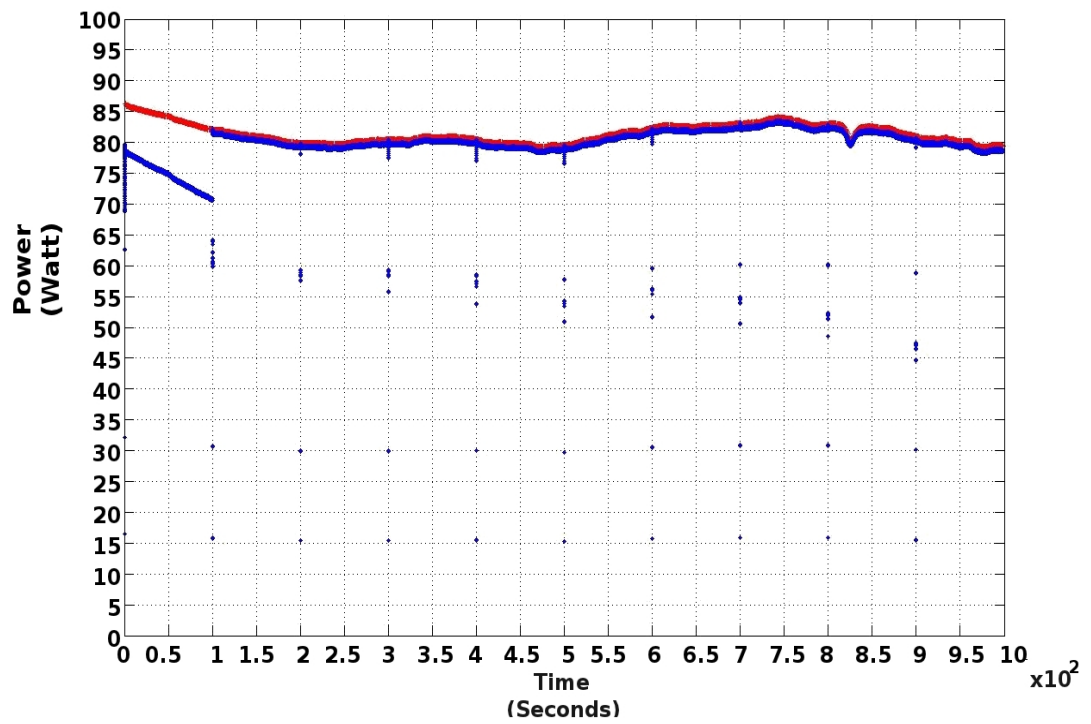
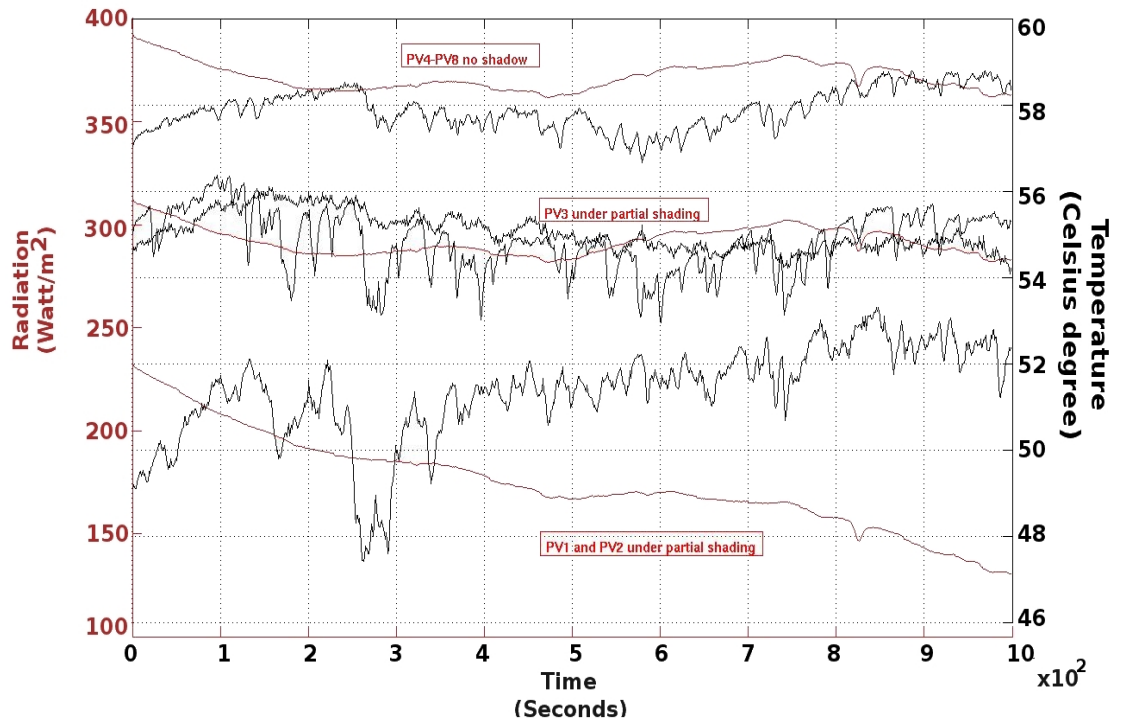
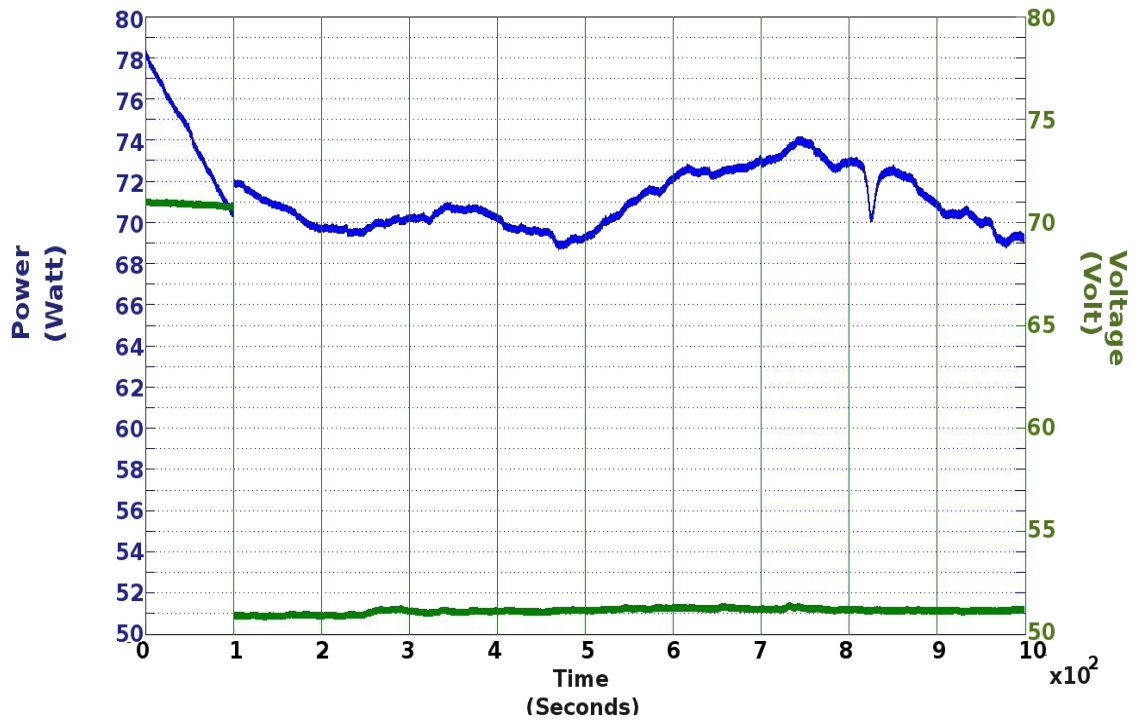


Figure 6.15: Maximum power point for the applied conditions (red line) compared with the MPP tracked by the algorithm (blue line).



(a) Temperature of PV modules and falling radiation as input for the simulation.



(b) The blue line is the power from the PV array for the calculated operating voltage (green line) from the controller.

Figure 6.16: Simulation of partial shading on 31th August 2010 with higher level of the temperature for the modules affected by the shadow.

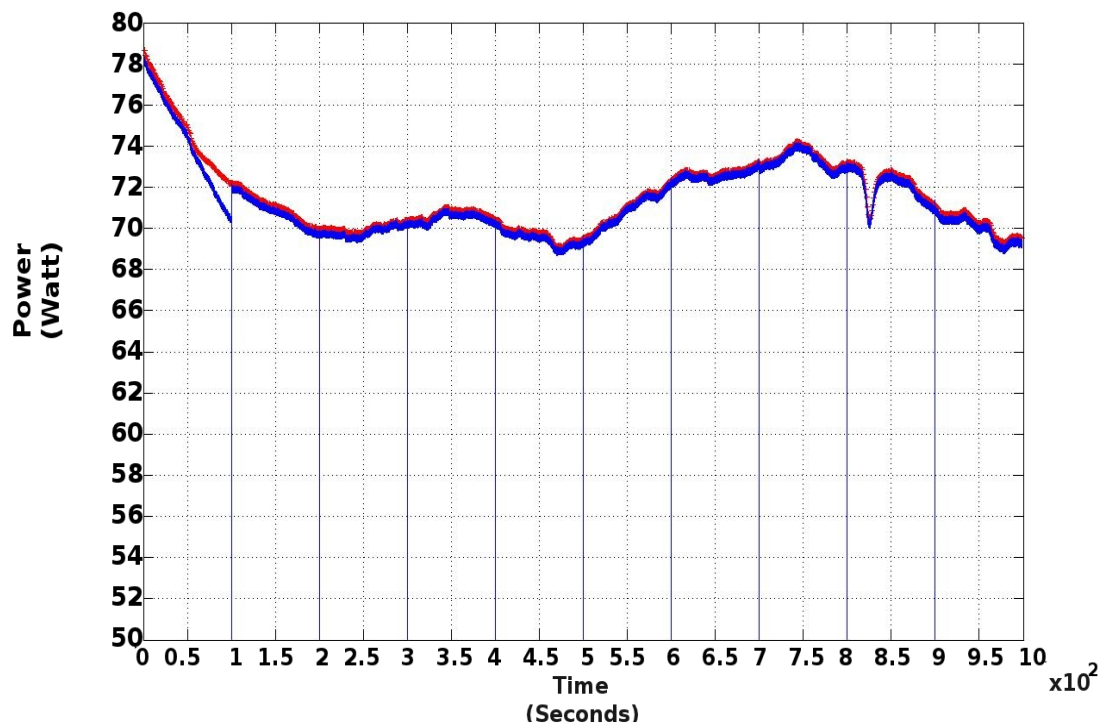


Figure 6.17: Maximum power point for the applied conditions (red line) compared with the MPP tracked by the algorithm (blue line).

For the first 100 seconds the operating voltage is 71V but after that period the operating voltage adjusts down to 51V due to partial shading and the changed values of the incident radiation. Fig.6.17 highlights the performance of the algorithm comparing the MPP calculated for the PV system for the applied conditions (6.16(a)) and the MPP estimated by the algorithm.

6.5 Conclusion

This chapter described the principals behind the algorithm designed to track the MPP under real operating conditions. The algorithm made a good use of an Artificial Neural Network. The algorithm has been implemented in Matlab/Simulink as well as in a simplified array able to reproduce situations of partial shading and mismatch. More results concerning the system response in case of partial shading are presented in AppendixD for when the V_{mpp} is in the lower, middle and higher voltage regions.

The results shows the model for the controller works well and can cope with fast irradiance and temperature as well as dynamically changing shading.

The next chapter will introduce the last part of the research: the converter implementation of the controller using the algorithm.

7

DC/DC converter

This chapter concerns the DC/DC converter implementing the MPP tracker described in the previous chapter. The first part includes an overview of the main types of existing converters with their operating principles.

The second part is about the boost converter, the one selected for this project, with details about its conductive modes (continuous and discontinuous mode) for ideal and real cases.

Particular attention has been paid to the boost converter with a description of control and modulation techniques.

The last part of the chapter illustrates the results obtained by implementing the algorithm with a modelled DC/DC boost converter for a system of the same size as the PV test system, and also for a small system that includes only three PV modules. Results from an experiment which uses a boost converter suitable for a system of three PV modules are presented to demonstrate the algorithm feasibility.

7.1 Overview DC/DC converters topologies

The DC-DC converter functionality is to convert a source of current from one level of voltage to another. Several methods exist for DC-DC voltage conversion. Each of these methods has its specific benefits and disadvantages, depending on a number of operating conditions and specifications.

There are two types of conversion methods, electronic and electrochemical but only the electronic one is considered here. Electronic conversion can be divided into two modes: linear and switch-mode conversions.

7.1.1 Linear conversion

A linear regulator is a voltage regulator based on an active device (such as a bipolar junction transistor, field effect transistor or vacuum tube) operating in its "linear region". The regulating device is made to act like a variable resistor, continuously adjusting a voltage divider network to keep a constant output voltage. The disadvantage of these converters is its low efficiency and the power dissipated as the converter is constantly on and conducting current.

7.1.2 Switch-mode conversion

These converters convert one DC voltage level to another by storing the input energy temporarily and then releasing that energy to the output at a different voltage. The storage may be in either magnetic field (inductors, transformers) or an electric field (capacitors), or both. This conversion method is more power efficient than linear voltage regulation.

The operating point of a PV system depends on many factors: irradiance, wind, ambient temperature, electrical and temperature mismatches and partial shading. As already explained, the response of a PV system depends on its technology and the system setting. V_{mpp} and I_{mpp} are affected differently by the parameters listed above. For fast irradiance changes the V_{mpp} varies slightly compared with the variation of I_{mpp} ; for partial shading the voltage may change up to 40% of its value at STC (depending on the number of the modules affected by partial shading, the string connection and the portion of shaded area of the cells).

Based on the relative magnitudes of supply and load voltages, switch mode converters primarily fall under three broad categories: step up, step down and step up/down.

Step-up

The size of the output voltage is always higher than the supply voltage (boost converters). The details of the operating principle of a boost converter will be introduced in the next sections.

Step-down

The size of the output voltage is always lower than the input voltage (buck converters).

The input-output relation for an ideal buck converter in continuous conduction mode (CCM), i.e. the current through the inductor never falls to zero, does not depend on the inductor value or the switching frequency or the load current and it is given by:

$$\frac{V_o}{V_i} = D \quad (7.1)$$

The output voltage varies linearly with the input voltage. The duty cycle (D) is the ratio between the time where the switch is on and the period (T) and ideally is in a range of $[0,1]$; this implies that $V_o \leq V_i$ this is why the buck converter is also called a step-down converter.

Step up/down

Converter where size of load voltage may be either higher or lower than that of the supply voltage (buck-boost and cuk converters - with polarity reversal; cascade buck-boost and sepic converters).

The functionality of the buck converter is to produce an output voltage lower than the input voltage; the feature of the boost converter is producing an output voltage higher than the input one. In many applications more flexibility is needed, e.g. for battery power application where the fully charged battery voltage starts out greater than the desired output and the converter must operate in the buck mode, but as the battery discharges, its voltage becomes less than the desired output, thus for the discharging the converter must operate in the boost mode.

The functionality of a buck-boost converter is to produce an output voltage which is either greater than or less than the absolute value of the input voltage.

The buck-boost converter can be also realized as a cascade of a boost regulator followed by a buck regulator or a cascade of a buck regulator followed by a boost regulator.

Depending on the requirements of the load, the converters may either step-up or step-down the input voltage to produce a well-regulated load voltage. If the voltage delivered by the PV system is smaller than the peak value of the grid voltage, a voltage boost is needed [49]. The maximum voltage delivered by the roof test array is less than 90 Volt which is lower than the grid voltage (230 Volt). For this reason the boost converter topology has been selected for this study.

7.2 Basics of the boost converter

The basic circuit design of a boost converter is shown in Fig.7.1(a). The boost converter absorbs and injects energy from solar panel to the inverter. The process of absorption and injection of the energy is performed by the combination of four components which are inductor, electronic switch, diode and output capacitor.

Fig.7.1(b) shows the different position of the switch which determines the current flow: when the switch is on, the current builds up in the inductor. The voltage V_i appears across the inductor, and the inductor current increases at a rate equal to V_i/L .

When the switch is opened, the energy stored in the inductor is transferred to the load through the diode. When the switch is opened, the voltage across the inductor is $V_o - V_i$, the current is supplied to the load, and the current decays at a rate equal to $(V_o - V_i)/L$.

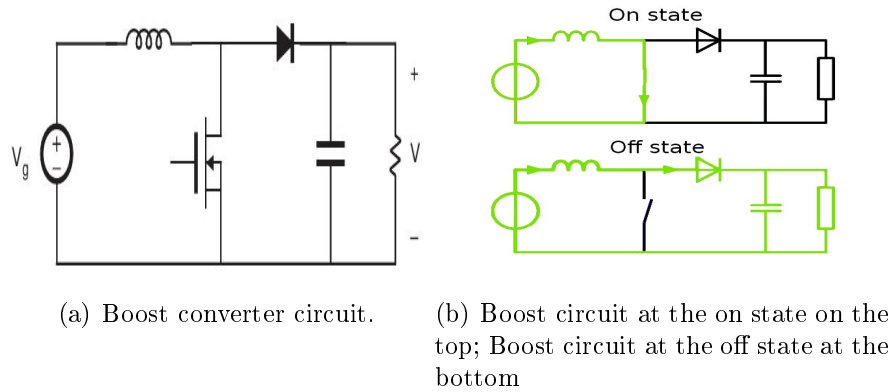


Figure 7.1: Ideal circuit for the boost converter.

7.2.1 Continuous conduction mode

When the boost converter is operating in continuous mode it means the current flowing into the inductor never goes to zero (I_L in Fig.7.2).

The output voltage of the boost converter can be calculated for the steady state (equilibrium condition of a circuit which occurs as the effects of transients are no longer important) with the following procedure:

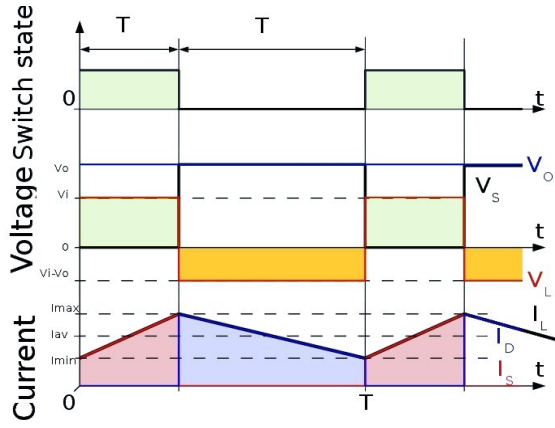


Figure 7.2: Evolution of the current and voltage for a boost converter in continuous conduction mode.

On state

When the switch is closed the current flowing into the inductor (I_L) undergoes a change during the period t as follows:

$$\frac{\Delta I_L}{\Delta t} = \frac{V_i}{L} \quad (7.2)$$

where V_i is the input voltage (or PV voltage) and L is the value of the inductor.

At the end of this period, the variation of the current of the inductor can be calculated from:

$$\Delta I_{L_{on}} = \int_0^{DT} \frac{V_i}{L} dt = \frac{V_i DT}{L} \quad (7.3)$$

T is the commutation period and D represents the portion of the commutation period where the switch is on (*duty cycle*) and ideally is in a range between 0 (the switch never closed) and 1 (the switch remains closed for all the period).

Off state

Switch open. During that time $(1 - D)$ the inductor is not in short circuit and its current can flow through the load. Assuming a zero voltage drop across the diode, and a capacitor large enough for its voltage to remain constant:

$$V_i - V_o = L \frac{dI_L}{dt} \quad (7.4)$$

and the inductor current variation is:

$$\Delta I_{L_{off}} = \int_0^{(1-D)T} dI_L = \int_0^{(1-D)T} \frac{(V_i - V_o)}{L} dt = \frac{(V_i - V_o)(1 - D)T}{L} \quad (7.5)$$

in ideal case, without considering parasitic resistances, and in the steady state condition

$$E = \frac{1}{2}LI_L^2 \quad \Delta I_{L_{on}} + \Delta I_{L_{off}} = 0 \quad (7.6)$$

it follows

$$\Delta I_{L_{on}} + \Delta I_{L_{off}} = \frac{V_i DT}{L} + \frac{(V_i - V_o)(1 - D)T}{L} = 0 \quad (7.7)$$

and this becomes:

$$\frac{V_o}{V_i} = \frac{1}{1 - D} \quad (7.8)$$

From eq.7.8 it can be noted that the output voltage is always bigger than the input voltage; that is why the boost converter is referred to as step-up converter.

7.2.2 Discontinuous conduction mode

When the amount of energy required by the load is small enough to be transferred in a time smaller than the commutation period, the current through the inductor falls to zero during part of the period [5] (discontinuous conduction mode- DCM).

The difference between the continuous and discontinuous conduction mode is in the off period of the switch and it affects the voltage output.

The greatest value of the current in the inductor is:

$$I_{L_{max}} = \frac{V_i DT}{L} \quad (7.9)$$

At the time δT , I_L falls to zero (see Fig.7.3) thus at the off time:

$$I_{L_{max}} + \frac{(V_i - V_o)\delta T}{L} = 0 \Rightarrow \delta = \frac{V_i D}{(V_i - V_o)} \quad (7.10)$$

The load current I_o is equal to the average diode current (I_D). From Fig.7.3, the diode current is equal to the inductor current during the off-state. Therefore the output current can be written as

$$I_o = \bar{I}_D = \frac{I_{L_{max}}\delta}{2} = \frac{V_i DT}{2L} \frac{V_i D}{(V_i - V_o)} = \frac{V_i^2 D^2 T}{2L (V_i - V_o)} \quad (7.11)$$

The relationship between the input and output voltage can be rewritten as:

$$\frac{V_o}{V_i} = 1 - \frac{V_i D^2 T}{2LI_o} \quad (7.12)$$

The output voltage depends, in the DCM, on the voltage input, the current across

the load and the inductor value.

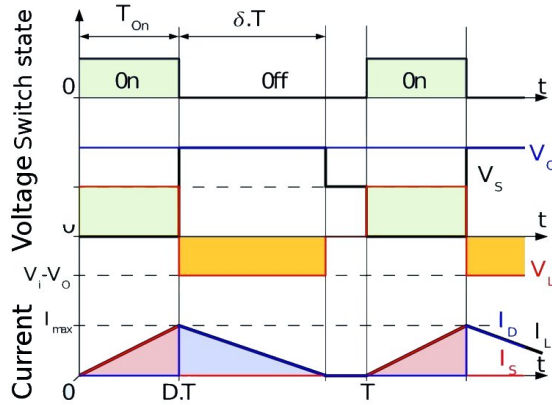


Figure 7.3: Evolution of the current and voltage for a boost converter in discontinuous conduction mode.

7.2.3 Parasitic resistances

For the earlier analysis, all the components have been considered as ideal thus with no power losses. For non ideal case, the components of the converter introduce losses. The inductor has resistance and its magnetic core is not ideal either; the capacitor has resistance, and as current flows in and out of it, dissipates power; the switch has a voltage drop when it is turned on. Also the switch cannot be switched instantly, and thus dissipates power while turning on/off.

In the converter there are two types of noise:

1. conducted noise. Switches create ripple currents in their input and output capacitors. Those ripple currents create voltage ripple and noise on the converter's input and output due to the resistance, inductance, and finite capacitance of the capacitors used.
2. Radiated noise. There are often ringing voltages in the converter, parasitic inductances in components and PCB traces, and an inductor which creates a magnetic field which it cannot perfectly contain within its core

A proper components choice can cut the noise, e.g. PCB layout, and, if that is not enough, additional input or output filtering or shielding [66].

To give an idea of the effect of the parasitic components, the boost converter analysis has been done with the equivalent model of a real inductor considering only a resistor in series. This assumption is acceptable because as an inductor

is made of one long wound piece of wire, it is likely to show a non-negligible parasitic resistance (R_L). Using the state-space averaging method:

$$V_i = \bar{V}_S + \bar{V}_L \quad (7.13)$$

where \bar{V}_S and \bar{V}_L are respectively the averaged voltage across the switch and the inductor over the commutation cycle.

If we consider that the converter operates in steady-state, the average current through the inductor is constant. The average voltage across the inductor is:

$$\bar{V}_L = L \frac{d\bar{I}_L}{dt} + R_L \bar{I}_L = R_L \bar{I}_L \quad (7.14)$$

When the switch is closed (on-state), $V_S = 0$. When it is off, the diode is forward biased and $V_S = V_o$. Thus, the average voltage across the switch is:

$$\bar{V}_S = D \cdot 0 + (1 - D) \cdot \bar{V}_o \quad (7.15)$$

The output current is equal to the inductor current during the off-state. the average inductor current is therefore

$$\bar{I}_L = \frac{\bar{I}_o}{1 - D} \quad (7.16)$$

Assuming the output current and voltage have negligible ripple, the load of the converter can be considered as purely resistive. If R is the resistance of the load, the above expression becomes:

$$\bar{I}_L = \frac{\bar{V}_o}{(1 - D) R} \quad (7.17)$$

Substituting the value of the averaged inductor current into equation 7.14; equation 7.13 can be rewritten as:

$$\frac{V_o}{V_i} = \frac{1}{\frac{R_L}{R(1-D)} + 1 - D} \quad (7.18)$$

The equation above can be reduced to the ideal case if the inductor resistance is zero; an increase of the inductor resistor leads into a decrease of the voltage gain as shown in Fig.7.4.

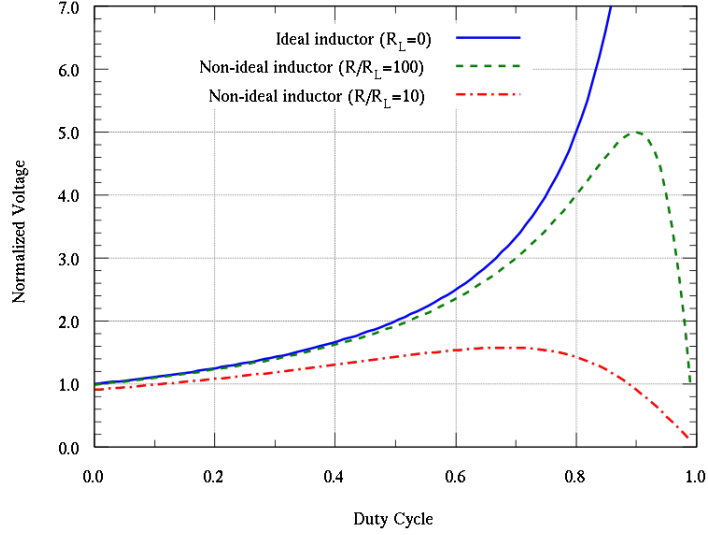


Figure 7.4: Evolution of the output voltage of a boost converter with the duty cycle when the parasitic resistance of the inductor increases.

7.3 Selection of the component for the boost converter

The converter operates in DCM when the current which flows in the inductor falls to zero; to prevent this and forcing the converter to work in the CCM the inductance is calculated such that the inductor current I_L flows continuously and never falls to zero:

$$L_{min} = \frac{(1 - D)^2 DR}{2f} \quad (7.19)$$

where L_{min} is the minimum value of the inductance and f is the switching frequency; therefore the selection of the inductor should be higher than the calculated value.

The output capacitance to give the desired output voltage ripple is given by:

$$C_{min} = \frac{D}{RfV_r} \quad (7.20)$$

where C_{min} is the minimum capacitance and V_r is output voltage ripple factor ($\Delta V_o/V_o$) [42]. The capacitor should be higher than the calculated value to make sure that the converter's output voltage ripple stays within the specific range. The equivalent series resistance (ESR) of the capacitor affects the efficiency, so, the capacitor has to be selected with low ESR to get best performance. ESR can be reduced by connecting capacitors in parallel.

The boost diode reverse voltage rating is limited to the output voltage. It is

also important to consider the diode ability to block the required off-state voltage stress and have enough peak and average current handling ability, fast switching characteristics, low reverse-recovery, and low forward voltage drop.

7.4 Converter control

The control technique of a converter refers to what parameters of operation are monitored and how they are processed to control the modulation of the switch. The way in which the switch is modulated does not regard directly the control technique, but there are some common way to select the modulation as function of the control techniques.

This section gives an introduction of the control techniques, based on voltage and current control and modulation methods, pulse burst modulation and pulse width modulation.

7.4.1 Pulse Burst Modulation - (PBM)

This method uses an oscillator signal which is gated or not gated to the switch each period. Before the beginning of each cycle, comparing the output voltage to an internally generated bandgap reference, the oscillator signal will be gated or not. The decision is latched, so the duty ratio is not modulated within a cycle.

7.4.2 Pulse Width Modulation - (PWM)

Pulse-width modulation uses a rectangular pulse wave. Its pulse width is modulated resulting in the variation of the average value of the waveform. The simplest way to generate a PWM signal is the intersecting method, which requires only a comparator and a sawtooth or a triangle waveform. There are three standards for the PWM: variable frequency constant on-time, variable frequency constant off-time and fixed-frequency.

The modulation method selected for the controller is the PWM with a fixed frequency (4kHz) due to its easy implementation and low cost. The PWM uses a triangle waveform of unitary amplitude.

7.4.3 Voltage control - (VM)

One control technique uses the voltage-mode hysteretic control which is adopted for circuit implementing the PBM for switching modulation.

The advantages of this method include: low-cost, simple and easy architecture, fast load transient response and no need for feedback-loop compensation. A characteristic of this method is possibility to use a varying operating frequency.

The hysteretic control keeps output voltage within the hysteresis band V_{HYS} , if the input voltage $V_i \leq V_{ref} - V_{HYS}$ (on-state) the switch is on and the output voltage increases. Once the output voltage reaches or exceeds the reference $V_{ref} + V_{HYS}$, the switch is turned off and the output voltage decreases [51].

Another technique is the voltage-mode (VM) control which implies the use of PWM. Fig.7.5(a) shows a basic design of this control technique; the measure used to determine the switch modulation is the output voltage. This system includes an error amplifier which monitors the output voltage. The error is amplified with the required frequency compensation to maintain the stability of the control loop. The modulation of the switch is regulated directly by the output of the amplifier. The amplifier has to input: V_{ref} , a voltage reference value, and the output voltage divided down by a ratio-matched resistor divider.

The output voltage is set by the resistor divider ratio and the reference voltage:

$$V_o = V_{REF} \left(1 + \frac{R_2}{R_1} \right) \quad (7.21)$$

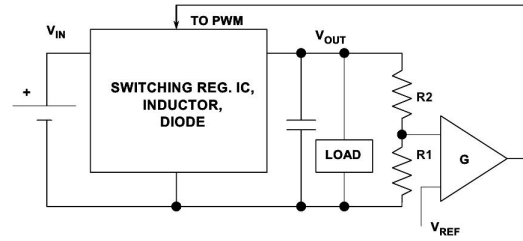
Normally the set of the resistors and the reference voltage are already regulated but some regulators have the resistor divider externally permitting to adjust the voltage output.

Voltage feed-forwarded

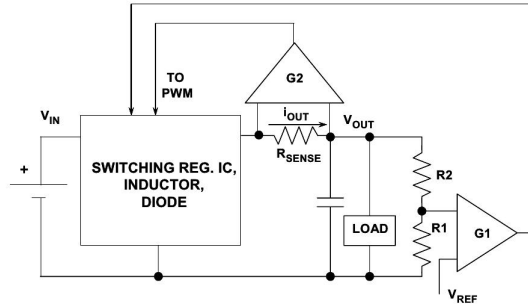
The voltage feed-forwarded is a variation of the VM control technique. With this technique it is possible to adjust automatically the duty cycle as the input voltage changes thus the feedback loop does not need to make an adjustment. This control method can also be used with simple PBM regulators and it is an advantageous technique for applications which have sudden changes in the voltage input. The VM control loop, in general, needs to be compensated to give stability.

7.4.4 Current control - (CM)

As for the VM, in the current-mode control the goal is to regulate the output voltage. The switch is modulated as function of two signals: the current in the inductor and the output error voltage. The general architecture of a CM requires two amplifiers: the first one, G_1 the error amplifier, which works as in the VM



(a) Voltage mode control with PWM.



(b) Current control basics

Figure 7.5: Control techniques basic circuits.

method; the second one, G_2 takes the current sensed at the inductor.

This technique implies two feedbacks, from output current and output voltage. When the switch is closed the current through the inductor starts to rise and creates a voltage across the sense resistor. This voltage is then amplified and fed back to the PWM to turn off the switch. The amplifier G_1 determines the end of the switch on time period determining the limit of the inductor current. CM controls control directly the inductor current rather than controlling the average voltage applied to the LC filter as in VM control; this allows the control to be faster and more stable. Using the inductor current as signal, it is also possible to detect immediately any instantaneous changes in the input voltage. All these advantages weigh more than the cost of the implementation. The disadvantages are the requirement of sensing current and an extra amplifier [42].

The current control with the PWM has been implemented in the controller to adjust the duty cycle so regulating the voltage output. The operating principles have been already presented. The output voltage is sensed and compared with a reference voltage and the current is sensed and fed back. The CM control has been included in the main algorithm control so no additional circuit has been built.

The current and the voltage are sensed by transducers.

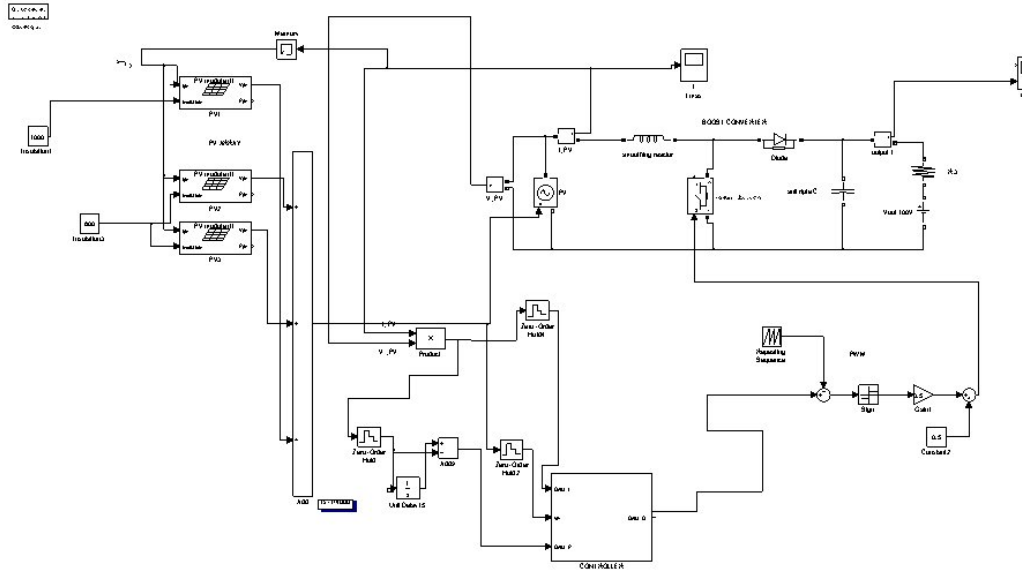


Figure 7.6: System of three PV modules, boost converter with a PWM (sawtooth function) and controller designed to track the MPP.

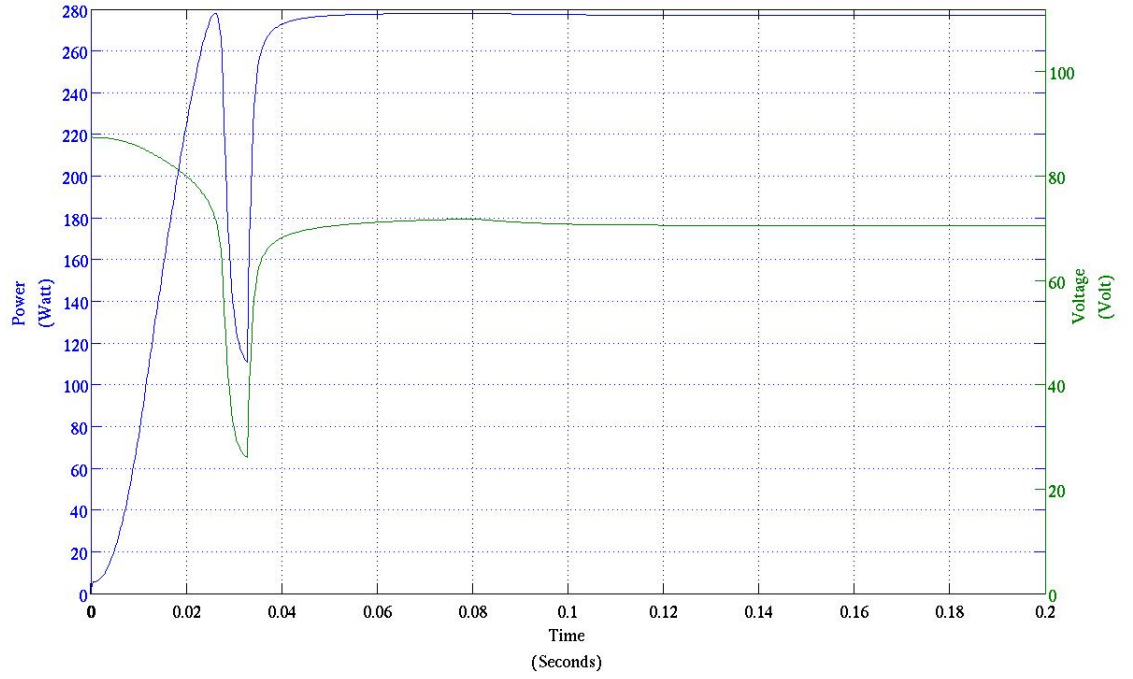
7.5 Test for the designed controller

The algorithm designed and detailed in Chapter 6 has been analyzed for several conditions: partial shading with two, three, four peaks, and fast irradiance changes (results in AppendixD) and also its performance has been verified using real measure data (results in Chapter 6).

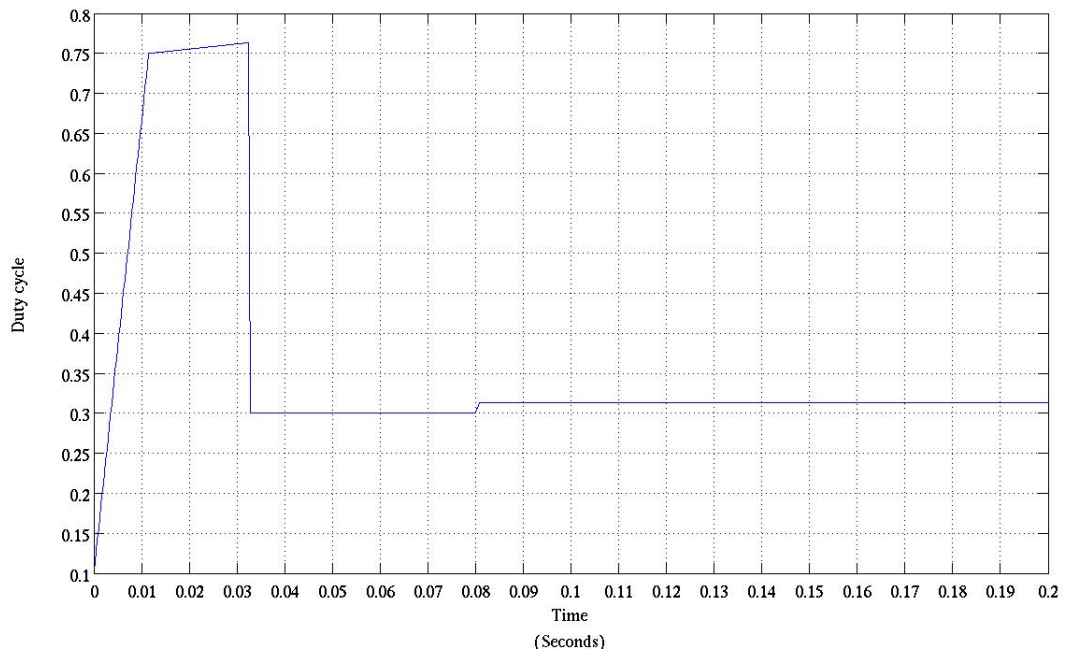
The algorithm shows very good performance in terms of predicting the V_{mpp} for the conditions listed above; also the algorithm presents a fast response which is an important parameter for the efficiency of the MPP tracker. The controller methods described in the previous section use the adjustment of the duty cycle to have the desired input/output relation, thus the algorithm has been adapted to provide the duty cycle as output. Also the algorithm has been adapted to track the MPP even for power lower than the nominal power of the test rig. To accomplish this some changes have been done as explained in the next sections.

7.5.1 Artificial Neural Network

The ANN used in Chapter 6 receives the six inputs (the power measured at desired six voltage values) and returns two output: the V_{mpp} and the MPP predicted. A limitation of the ANN is that has been trained with the data resulting from

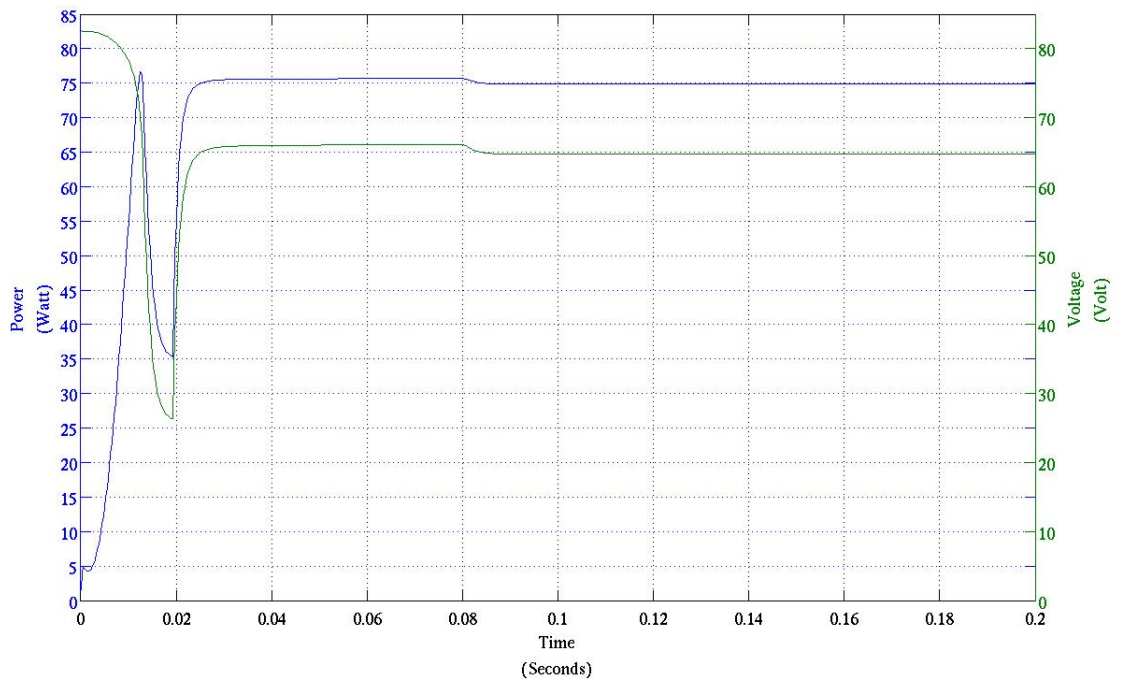


(a) Power (blue line) and Voltage (green) of the PV with the duty cycle calculated by the controller

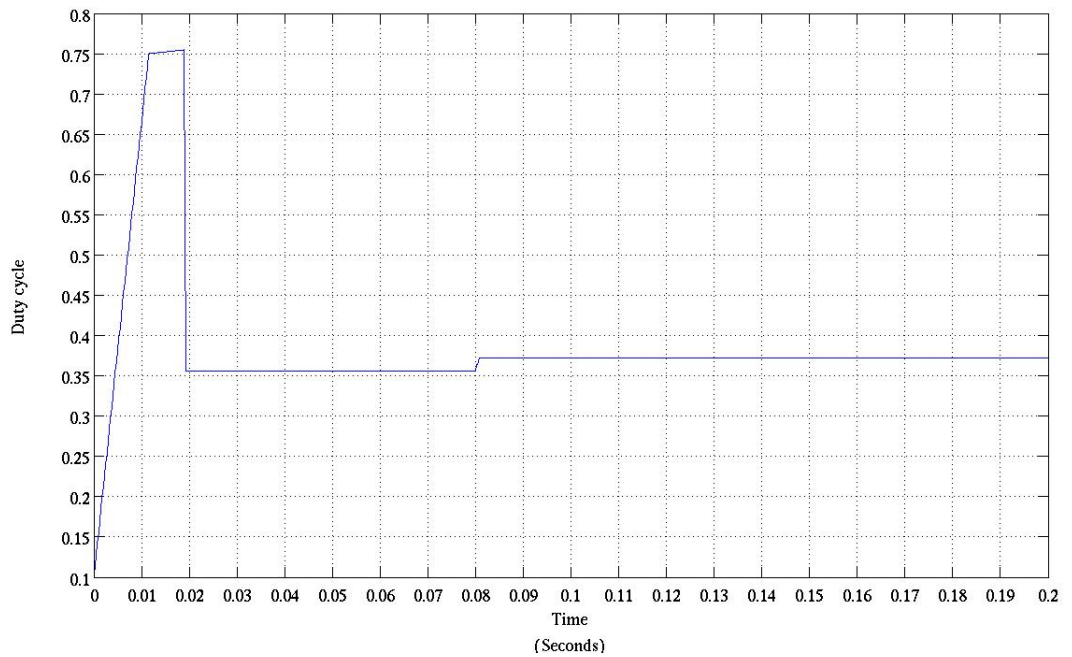


(b) Duty cycle.

Figure 7.7: Simulation of eight PV modules under uniform radiation of 900 Wm^{-2} .

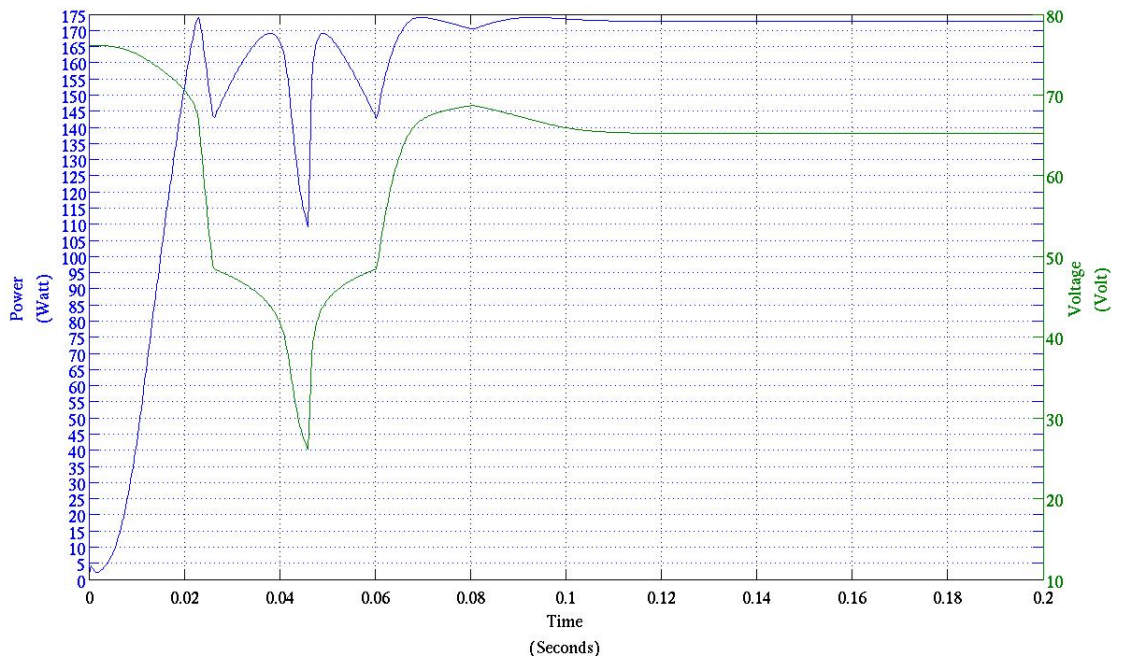


(a) Power (blue line) and Voltage (green) of the PV with the duty cycle calculated by the controller

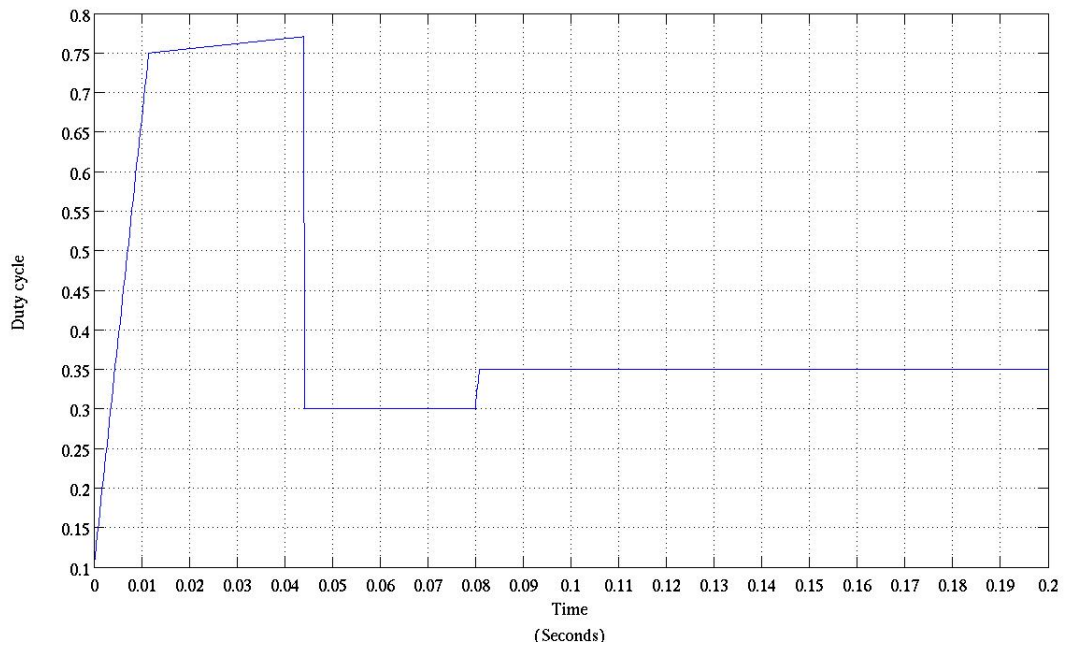


(b) Duty cycle.

Figure 7.8: Simulation of eight PV modules under uniform low radiation (300 Wm^{-2}).

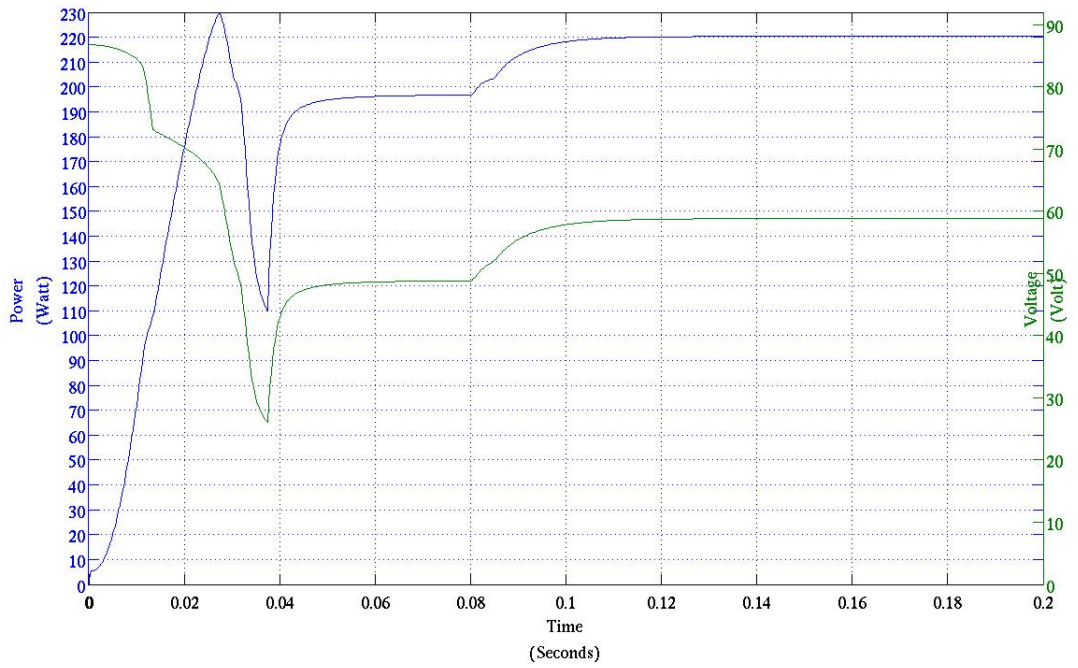


(a) Power (blue line) and Voltage (green) of the PV with the duty cycle calculated by the controller

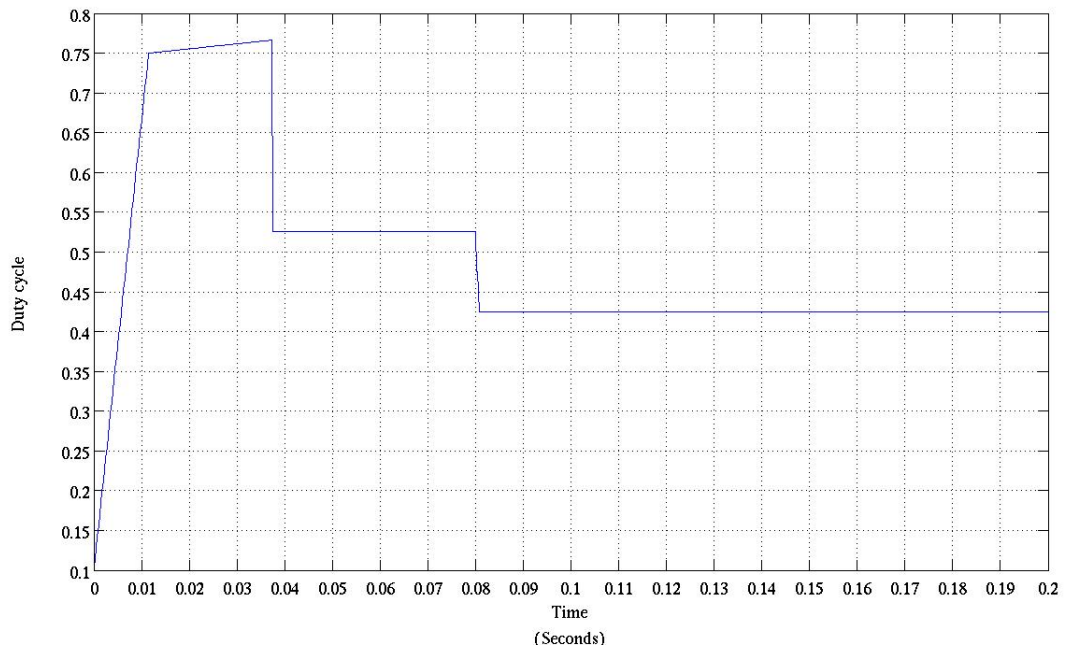


(b) Duty cycle.

Figure 7.9: Simulation of eight PV modules under partial shading. Five modules have a falling radiation of 900 Wm^{-2} , two under 600 Wm^{-2} and one has 400 Wm^{-2} ; this configuration produces three peaks.

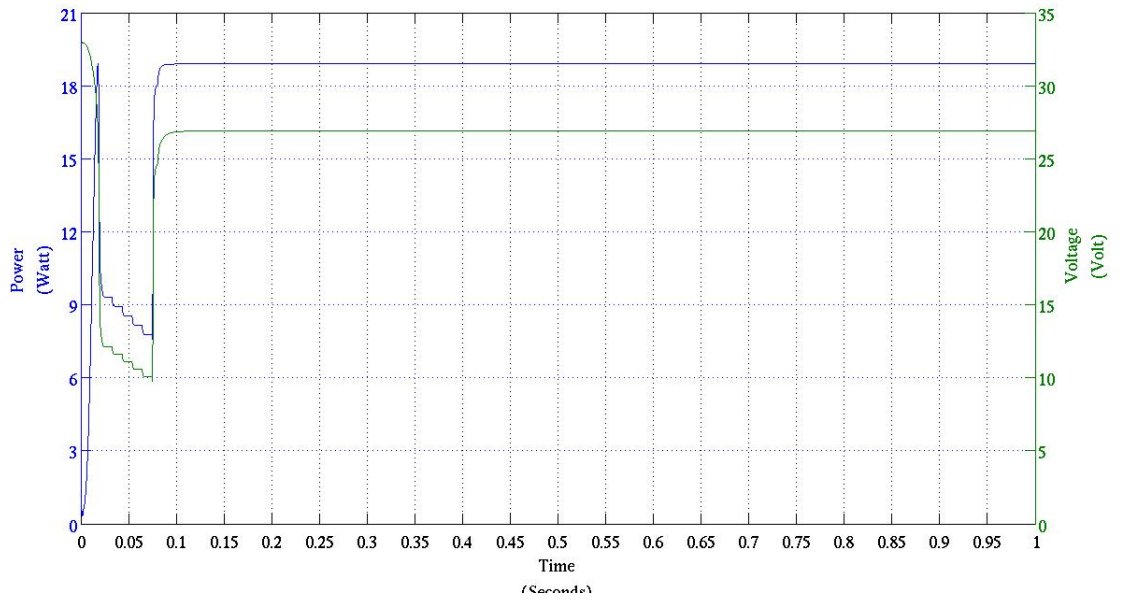


(a) Power (blue line) and Voltage (green) of the PV with the duty cycle calculated by the controller

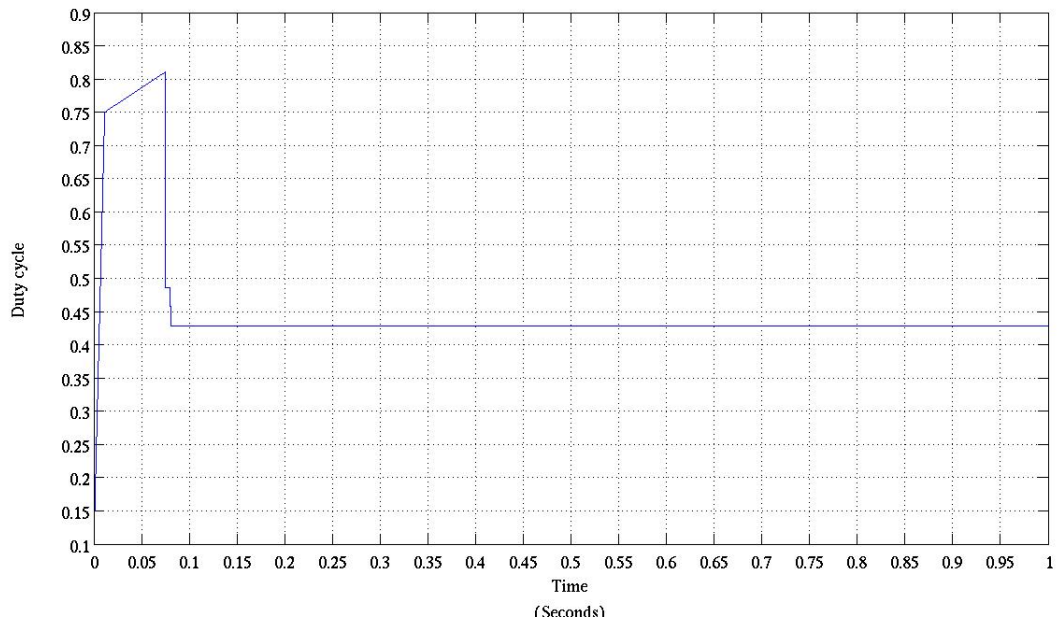


(b) Duty cycle.

Figure 7.10: Simulation of eight PV modules under partial shading. Six modules have a falling radiation of 900 Wm^{-2} , one under 800 Wm^{-2} and one has 300 Wm^{-2} ; this configuration produces three peaks as well.

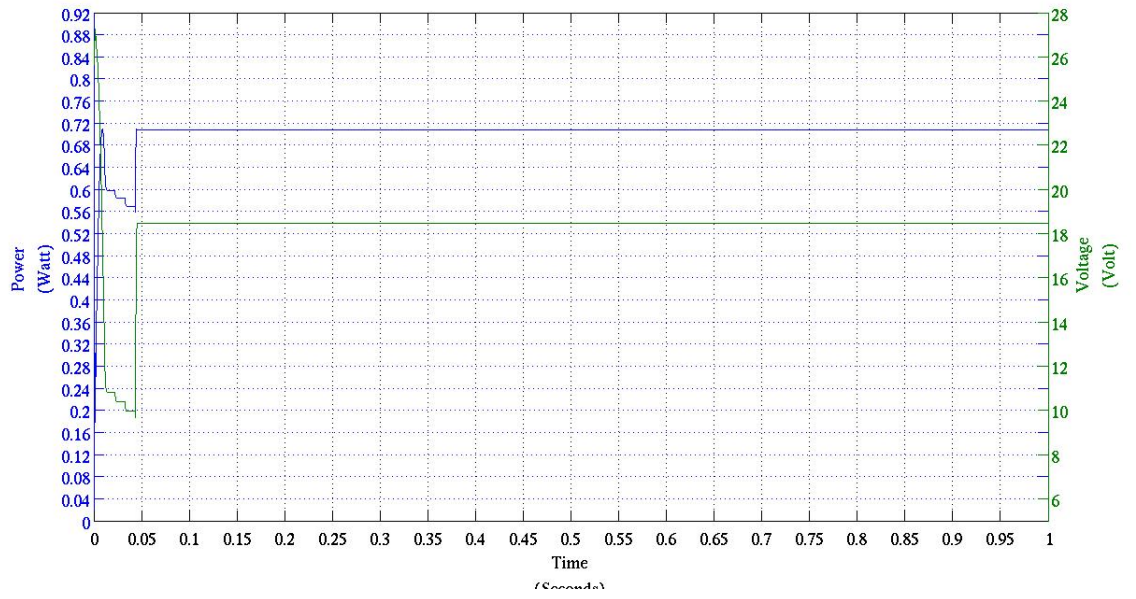


(a) Power (blue line) and Voltage (green) of the PV with the duty cycle calculated by the controller

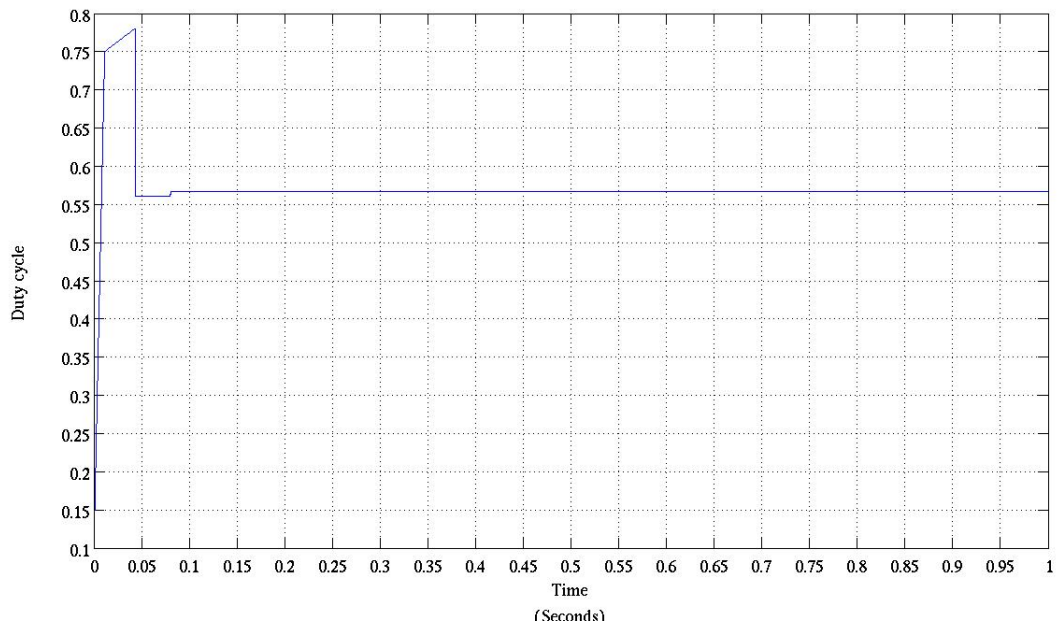


(b) Duty cycle.

Figure 7.11: Simulation of three PV modules under uniform radiation of 1000 Wm^{-2} .

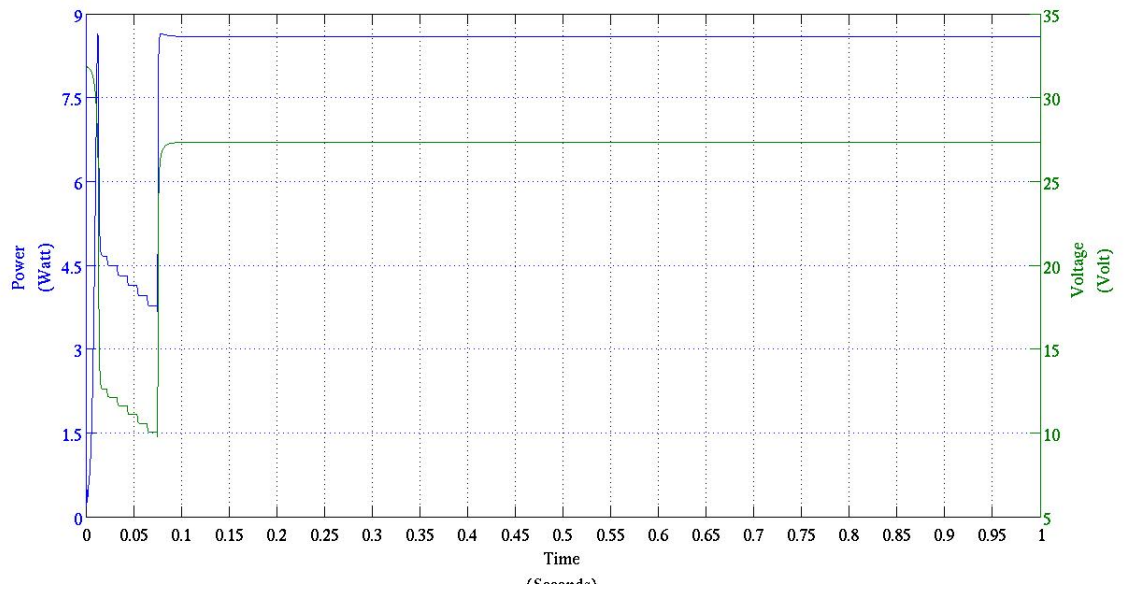


(a) Power (blue line) and Voltage (green) of the PV with the duty cycle calculated by the controller

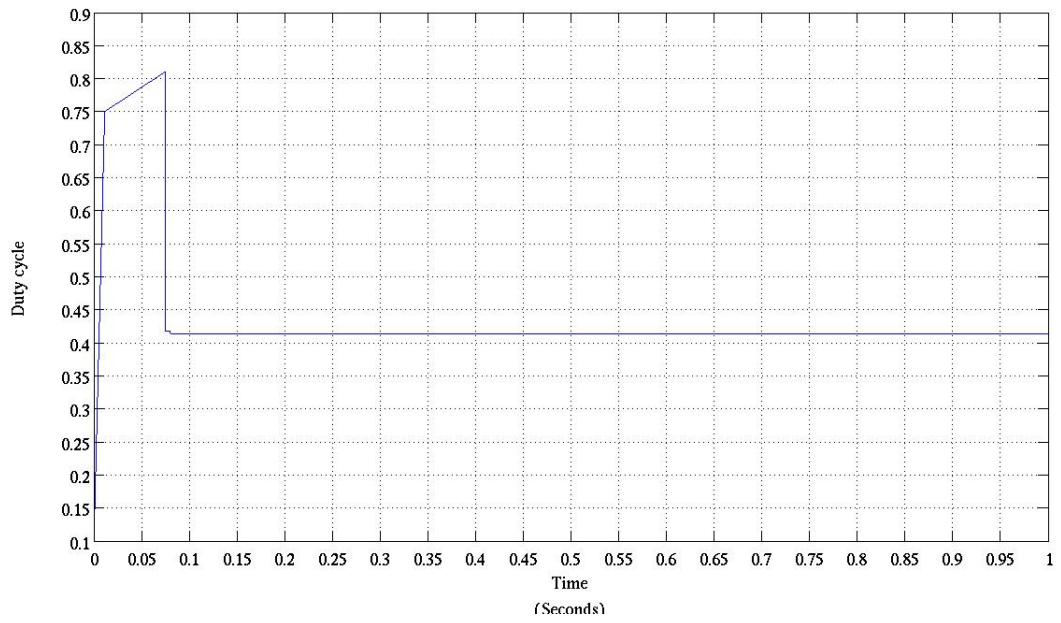


(b) Duty cycle.

Figure 7.12: Simulation of three PV modules under low uniform radiation of 100 Wm^{-2} .

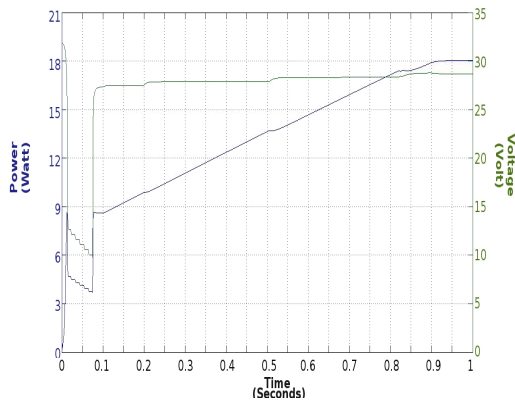


(a) Power (blue line) and Voltage (green) of the PV with the duty cycle calculated by the controller

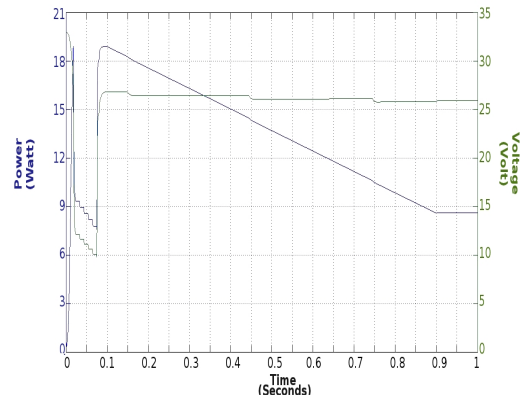


(b) Duty cycle.

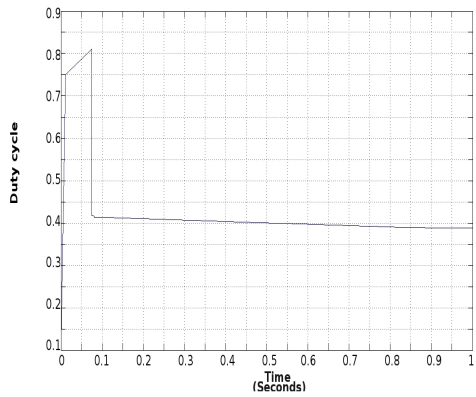
Figure 7.13: Simulation of three PV modules under medium uniform radiation of 500 Wm^{-2} .



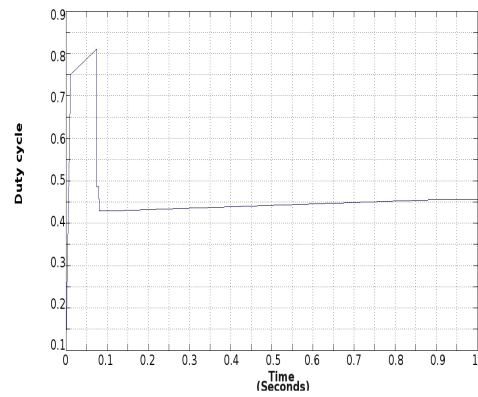
(a) Power (blue line) and Voltage (green) of the PV with the duty cycle calculated by the controller for step-up radiation



(b) Power (blue line) and Voltage (green) of the PV with the duty cycle calculated by the controller for step-down radiation

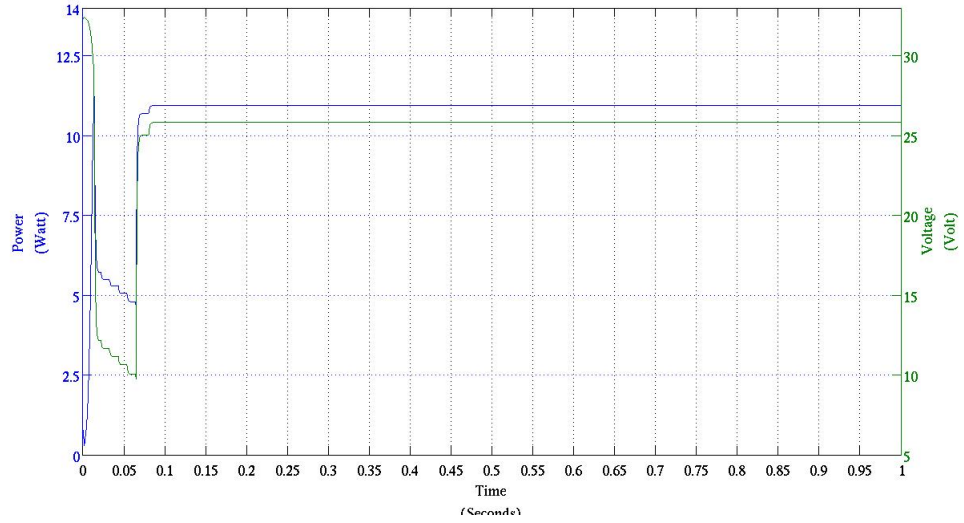


(c) Duty cycle for step-up radiation.

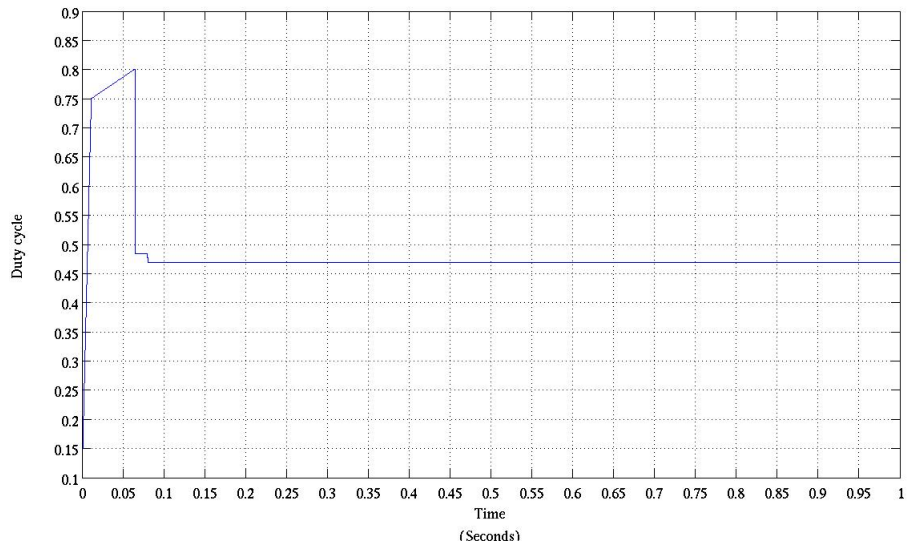


(d) Duty cycle for step-down radiation.

Figure 7.14: Simulation of three PV modules under fast irradiance changes. For the step-up the radiation rises from 500 up to 1000 W/m^{-2} ; the step-down the radiation goes from 1000 to 500 W/m^{-2} .

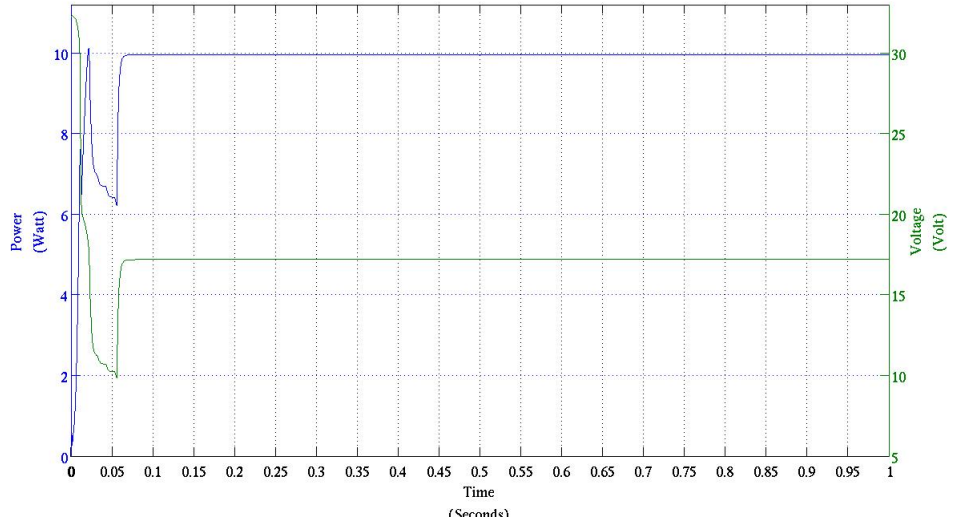


(a) Power (blue line) and Voltage (green) of the PV with the duty cycle calculated by the controller

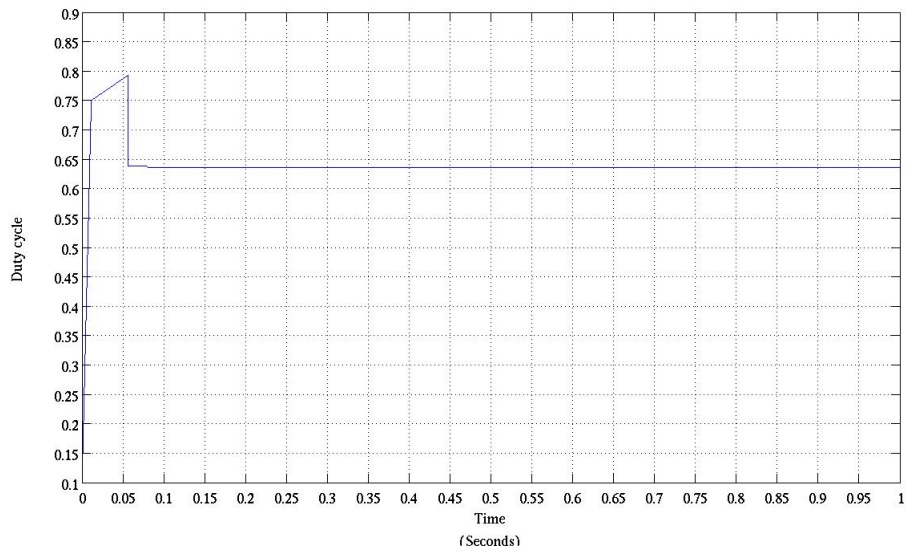


(b) Duty cycle.

Figure 7.15: Simulation of three PV modules under partial shading. The power characteristic presents two local maxima.



(a) Power (blue line) and Voltage (green) of the PV with the duty cycle calculated by the controller



(b) Duty cycle.

Figure 7.16: Simulation of three PV modules under partial shading. The power characteristic presents three local maxima.

the simulations of the PV test system for various conditions (different levels of radiation and temperatures and also partial shading). The ANN, trained with those data, is able to predict the operating point of that particular PV system with its rated power and electrical configuration. To avoid this problem and make the ANN more flexible for any rated power, the data have been normalized with the maximum output power of the PV system, so that the inputs and the outputs of the ANN are values between 0 and 1. The PV system is composed of eight modules connected in series, if the number of the modules increases or decreases, the V_{mpp} will increase or decrease proportionally. Therefore normalizing the data allows to adapt the ANN for any number of the modules connected in series using the same train of data set.

The power measured during the scan is sent to the ANN after being divided by the MPP at STC of the array considered. The power of the PV system, estimated by the ANN, is multiplied by the same constant.

The ANN produces an output only when receives the required six measurements. To do so, the control system has been designed with loops which, once the voltage reaches the desired values, keep the value of the power measured constant for the next 100 seconds.

7.5.2 Scan the power characteristic

The DC converter is a system with two poles and its transient time depends from the components value. The time needed for reaching the desired voltage and measuring the power at the steady state may be too long (several seconds). Thus to make the process of the scan faster, the controller applies a duty cycle that varies from 0.1 up to 0.75 in steps of 0.014 every 0.00025 seconds (switch frequency of the DC/DC converter fixed at 4kHz). The controller continues varying the duty cycle from 0.75 to 0.815 with a smaller step of 0.000159 every $2.5e - 4$ seconds.

The lower two points, corresponding to 8.4 and 16.2 Volt, will never be used as the working voltage of the converter and the PV system current, in that low voltage region, can be considered almost constant. If the low voltage region presents a local maximum, neglecting this local peak will not affect the prediction of the ANN because the power measured at that region is small. For the reason above the controller starts the scan approximatively at V_{oc} and stops at 26.4 Volt. From 26.4 Volt to the short circuit condition (0 volt), the current can be considered constant and the power can be estimated. To extrapolate the power at 16.2 Volt, the controller records the value of the power at 26.4 Volt and then multiply it by 0.628 ($16.2/26.4 = 0.628$). That solution is an approximation and

could introduce an error in the ANN's input, but from the results the ANN can still estimate the proper operating point without significant error.

7.5.3 The duty cycle

The algorithm designed finds the V_{mpp} but the converter is controlled by the duty cycle. The converter used in simulation and in the experiment has a fixed output voltage and a fixed load. After the scan of the P(V) characteristic, the ANN outputs two signals ([0,1]) which correspond to the normalized V_{mpp} and MPP estimated. The duty cycle is given by:

$$D = 1 - \frac{V_i}{V_o} = 1 - \frac{V_{mpp}^{max} ANN_{out}}{V_o} \quad (7.22)$$

where V_{mpp}^{max} corresponds to the maximum operating voltage for the selected PV system and ANN_{out} is the normalized voltage output estimated by the ANN. It is obvious that the equation above does not take into account any parasitic resistances, but the duty cycle is then adjusted by the algorithm as function of the power measured and the power predicted by the ANN as can be noted from the figures of the results.

A modelled boost converter has been used to test the performance of the controller algorithm (Fig.7.6). The tests have been done for a system composed by eight modules and the results are shown from Fig.7.7 to 7.10. Also additional tests have been run for an array composed by only three modules (Fig.7.11 to 7.16).

From the results it can be seen that this algorithm takes a maximum time of 80 milliseconds to track the true MPP and the error is generally less than 1% in power. Only in one case the error reaches the 4% (Fig.7.10(a)). This small error is not a big issue since, in real operating conditions, the parameters affecting the PV behavior are not constant and the algorithm consequently responds to any small variation applying an adjustment to the duty cycle as shown in Fig.7.14(c) and Fig.7.14(d).

7.6 Test with an existing real boost converter

The algorithm has been also tested with a real DC/DC converter to verify its performance with a general DC/DC boost converter.

The specifics of the boost converter are illustrated in table7.1.

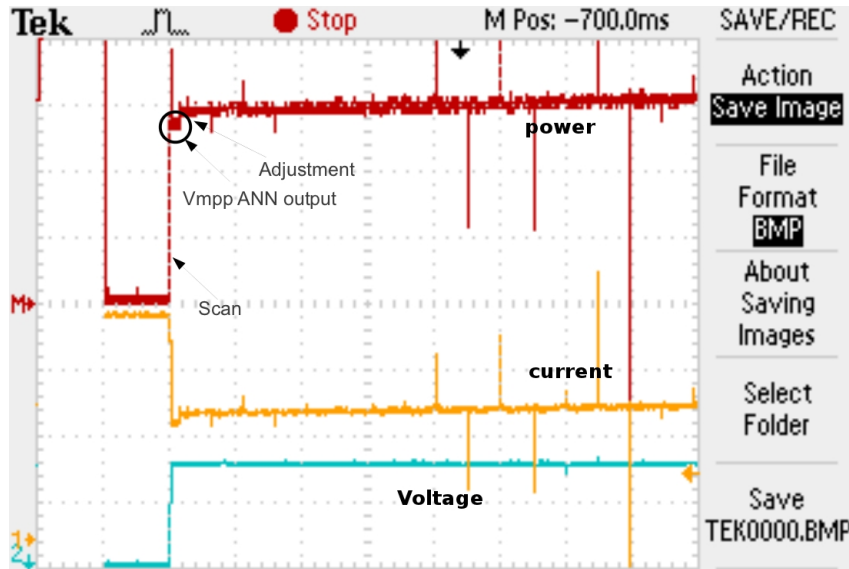


Figure 7.17: Output power (red line), operating voltage (yellow line) and current of the PV array simulator measured by the oscilloscope. Time 0.5 second/division.

Table 7.1: Design specification of the boost converter and circuit parameters.

<i>Parameter</i>	<i>Value</i>
Inductor	0.3H
Smoothing capacitor	2 mF
Output Voltage	45.7 V
Switching frequency	4 kHz

The experiment uses the boost converter, a DSP (Digital Signal Processing) and a PV array simulator. The DSP includes a Infineon TriCore TC1796 microcontroller which implements the algorithm opportunely written in C. The PV array simulator, a E4360 from Agilent, is a dual output programmable dc power source that simulates the output characteristics of a solar array. The modular solar array simulator is primarily a current source with very low output capacitance and is capable of simulating the I(V) curve of different arrays under different conditions.

The test has been done to verify if the algorithm works efficiently with a generic boost converter. From the results, the algorithm has shown a fast response reaching quickly the MPP.

Fig.7.17 shows the output results in terms of power, voltage and current measured by the oscilloscope during the test. The scan is run very fast and is represented by the vertical line. After the controller has ended the scan, the measured

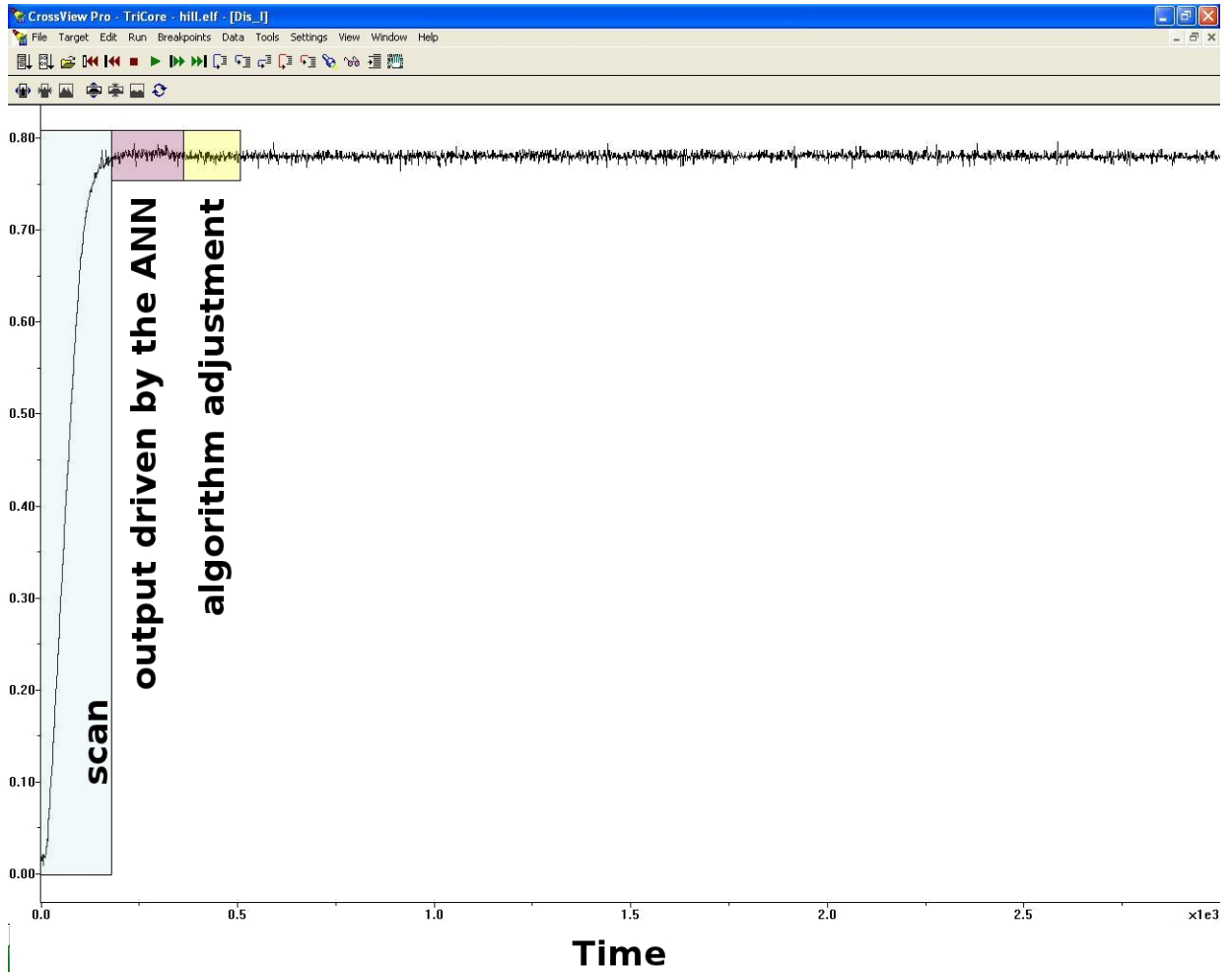


Figure 7.18: The current during the tracking. The graph has been divided in three sections showing the process of the scan, the operating current for the estimated voltage/duty cycle defined by the ANN and the adjustment applied by the controller.

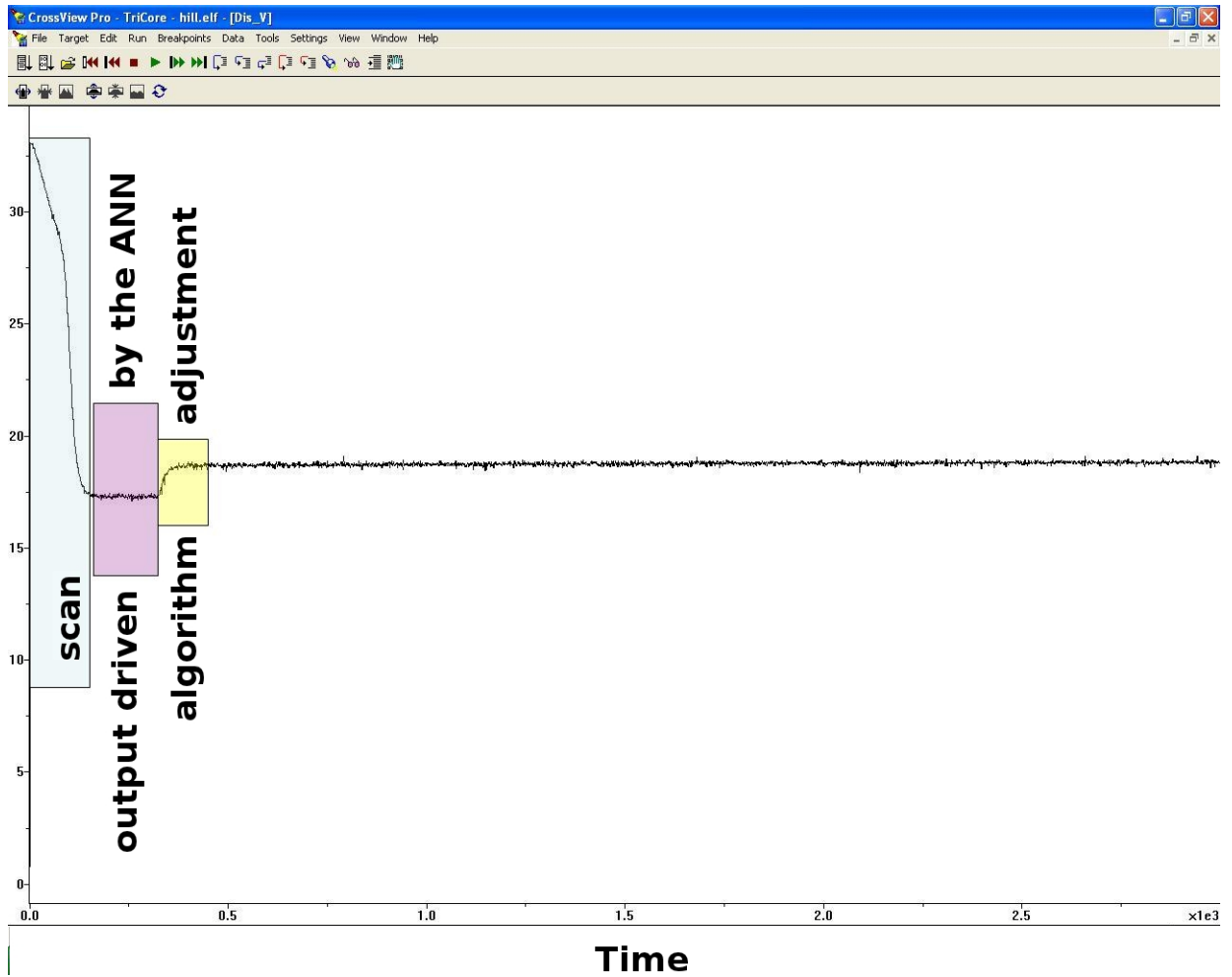


Figure 7.19: The voltage during the tracking. The graph has been divided in three sections showing the process of the scan, the operating voltage estimated by the ANN and the adjustment applied by the controller.

power is fed-back to the ANN and the converter starts working at the voltage calculated by the ANN (controlling the duty cycle).

A second step is detailed in Fig.7.17 where the power is increasing. Details of the current and the voltage of the PV system are shown respectively in Fig.7.18 and Fig.7.19. The controller in fact compares the values of the predicted power from the ANN and the measured one, applying a variable step change to the duty cycle as function of their difference.

The algorithm shows a good response for a general boost converter finding the MPP very quickly (100ms) with a difference of 20ms delay compared to the simulation results.

The boost converter could be tested only for low current and voltage ($MPP=15\text{Watts}$; $I_{mpp}=0.79\text{ Amperes}$; $V_{mpp}=19\text{ Volt}$); the future work includes tests for a DC/DC converter with higher rated power suitable for the PV array installed on the roof of Strathclyde.

7.7 Comparison between the proposed algorithm and the Hill Climbing algorithm

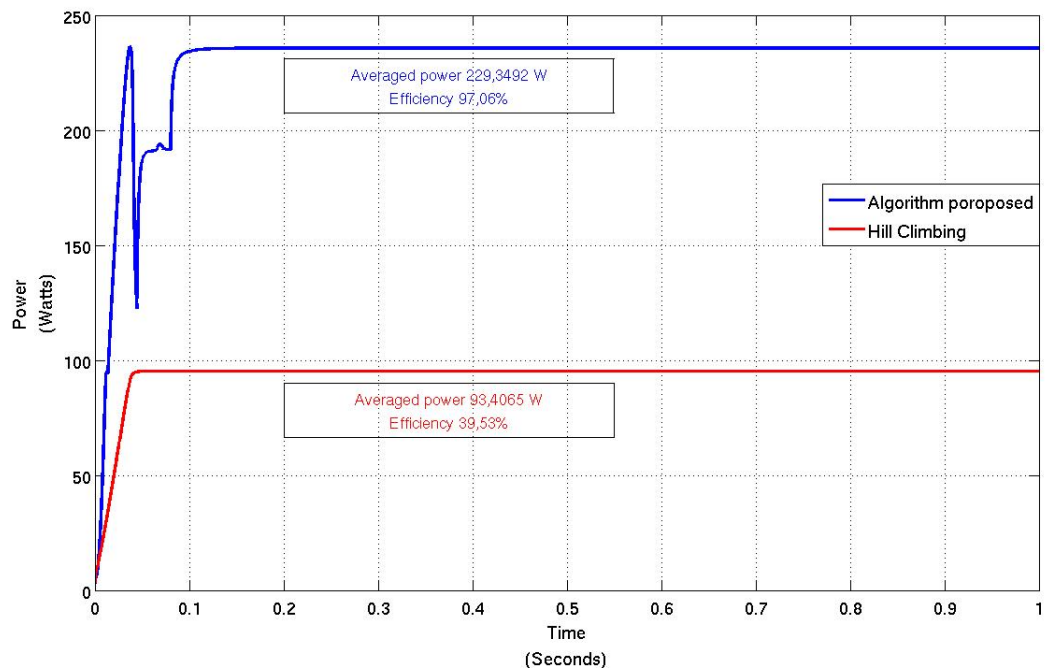


Figure 7.20: The figure shows the comparison between the proposed algorithm and the hill climbing for a partial shaded PV array.

The performance of the proposed algorithm has been compared with the Hill Climbing algorithm sec.2.4.

Fig.7.20 shows the simulation results for a partially shaded array with a power characteristic which exhibits two local peaks. The system (PV, MPPT and boost converter) which includes the proposed algorithm for the MPPT shows an efficiency of 97% compared to the efficiency of the hill climbing which is less than 40%. The major difference results from the contrast between the approaches taken by the two algorithms. The implementation of the ANN effectively tracks the true MPP while the hill climber fixes on the first (local) maximum detected that in this case is far from the global maximum.

Fig.7.21 and 7.22 compare the performance of the two algorithms for fast irradiance changes. The proposed algorithm which implements a variable step as function of the PV power variation shows a higher efficiency.

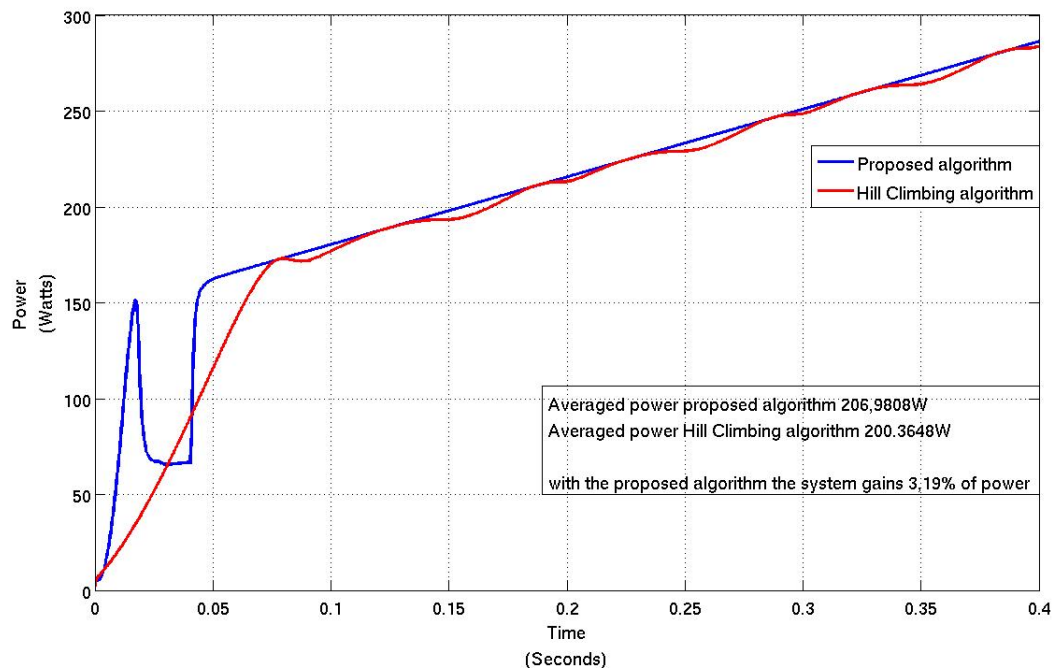


Figure 7.21: The figure shows the comparison between the proposed algorithm and the hill climbing in case of fast irradiance changes. In this specific case the irradiance increases $100Wm^{-2}$

7.8 Conclusion

This chapter has been entirely dedicated to the converter. An overview of the existing converter has been included paying attention on the configuration of the

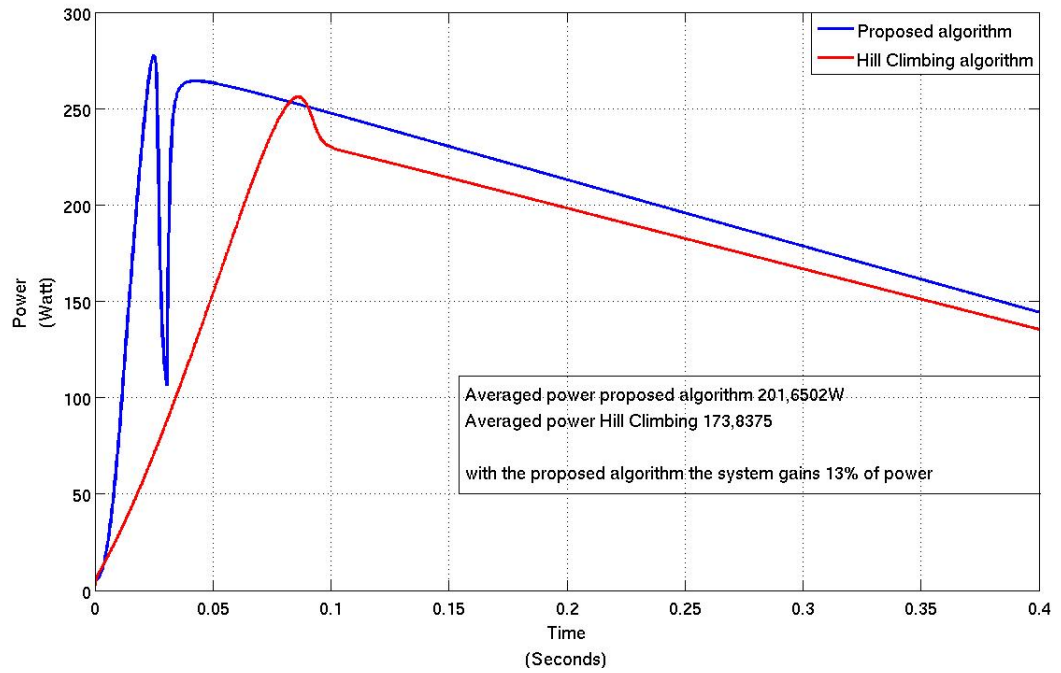


Figure 7.22: The figure shows the comparison between the proposed algorithm and the hill climbing in case of fast irradiance changes. In this specific case the irradiance decreases $100Wm^{-2}$

boost converter including its behavior in CCM and DCM and a brief analysis of the effect of the parasitic components.

Some control and modulation techniques have been detailed explaining how they work and which problems they could have in the implementation.

The last part of the Chapter regards the implementation of the algorithm with a boost converter; it has been also shown how the algorithm can be adapted to different nominal power ranges including results for simulation and experiment.

Summary and conclusions

This PhD thesis examines factors that affect the operational performance of PV systems, with emphasis on power conversion and power point tracking.

The first part of the PhD deals with the behavior of a PV array exposed to real operating conditions of changing and non-uniform irradiance and temperature, identifying key parameters affecting performance and the nature of their influence. This involved an extensive campaign of measurements made using a dedicated PV test rig installed on the roof of the James Weir building at the Strathclyde University, together with extensive instrumentation designed as part of the PhD study.

PV system output measurements were synchronized ambient data measurements (including radiation, temperature, and wind speed), which simplifies the collection and subsequent analysis of the experimental data.

Data collected included all the key ambient and system performance parameters including array current and voltage and module temperatures. This data was used for a comprehensive validation of the highly detailed system performance models developed to account for cell and module mismatch effects. The validated models taken together provide a powerful tool with which to investigate mismatch caused by temperature variations across the array, and radiation variations, caused for example by partial shading, and the impact of this resulting mismatch on system performance.

The issue of shading is very important because it can result in a significant degradation of performance and is a key focus of the research. To better understand the impact of shading, the PV test array was deliberately part shaded during experiments specifically design to assess the impact of shading phenomena. This data was used to validate the representation of partial shading implemented within the models, based on cell by cell sub-models. Together with an algorithm

to geometrically calculate the shading at any given time due to specific shading objects, the model was used to characterize in detail the behavior of a PV array subject to real operating conditions.

The final contribution of note was the development of improved power point tracking. This is important because it is well known that mismatch, and part shading in particular, result in poor tracking performance and a consequent significant loss in overall PV system performance. The validated and final PV model with mismatch and shading modelling was used to help develop a new approach to MPPT, based on a neural net, capable of predicting accurately the location of the maximum power point under real and time varying operational conditions.

The resulting improved MPPT controller was assessed under challenging conditions including I(V) characteristics with up to four local maxima resulting from specific partial shading situations, and with large and rapid Temporal changes in the incident radiation. The controller performed well even under these severe conditions. Simulation results showed that even after a significant disturbance the MPP could be reached within 0.08 seconds. This MPPT controller was implemented on a DC/DC boost converter as used with most PV grid connect.

Tests were undertaken using the fabricated hardware together with an electronic PV simulator to demonstrate successful implementation of the new MPPT controller. These tests included partial shading together with different mean levels of radiation and rapid changes in radiation. Good results were obtained confirming the model based predictions for the performance of the new algorithm developed. In conclusion then an effective approach to MPPT for PV systems exposed to real operational conditions has been developed and proved. Unlike some systems suggested in the literature it requires no additional parameter inputs (such as radiation) that would add cost to the inverter. It this has good commercial potential and can contribute to significant improvements in the performance of a large proportion of PV systems, especially those installed in the built environment such as building integrated PV (BIPV).

An important part of this work is in regard to the impact of shading and an entire chapter has been dedicated to the effect of the partial shading on the PV performance. The results have demonstrated the importance detailed modelling of the shadow path for accurate prediction of the operating point of a PV system.

Based on this detailed modelling it has been possible to develop an ANN based algorithm able to reliably detect the MPP of the PV system for real operating conditions, including partial shading, without the need for additional environmental sensors with all the advantages this brings to commercial application as

indicated above.

A critical point of the ANN is that the network has to be specifically trained for the PV array with which it will be used. The simulation and experimental results have show that this specific controller which includes the use of an ANN may be used for different technologies and different system sizes.

8.1 Future work

The MPPT algorithm has so far only been tested using the PV simulator, albeit with a real DC/DC converter. The natural next stage would be to design a complete grid connection unit including a higher rated DC/DC converter and coupled grid connected inverter, and then to evaluate this using the existing PV test system. Controlled shading would be introduced to test the MPPT when faced with multiple local maxima.

This could be followed by the design and testing of a commercial prototype converter/inverter that meets current EU and International (IEC) Standards.

Appendix A

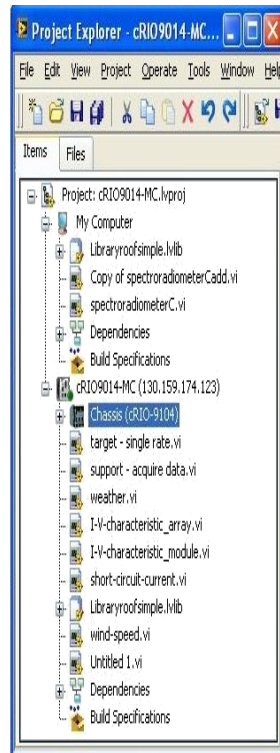
Outdoor test experiment: Labview programming

This appendix is dedicated to the detailed description of the Labview programming mentioned in Chapter 3.

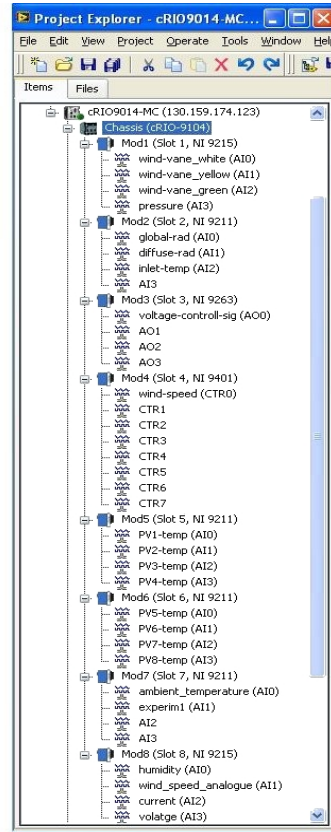
Fig.A.1 shows the all the items in the project tree; the project is divided into different *target* which are in this case:

- "My computer": represents the local computer as a target in the project.
 - "Dependency": it includes files called by other VI (Virtual Instrument) files (code file for Labview) which are not directly included in the main project.
 - "Build specifications": it contains setting for distributing the code in several forms as a toolkit (source distribution), executable (exe), and shared library (DLL)
- "C-RIO9014-MC" hardware connected with the IP address set up for the compact Rio included the chassis connected to it. FigA.1(b) shows all the modules with the detailed channels; for making the code easier to understand, each channel has the name of the quantity measured; in this way it will be possible to change the connection and the code for future work.

Fig.A.1(a) shows all the VIs associated to the project and it includes also all the shared variable which are hidden. The presence of several VIs is justified by the fact more than one experiment and measuring setting is needed.



(a) Main project.



(b) Details of each channel of the CompactRio.

Figure A.1: View of the main screen for controlling the data logger.

Validation of the physical model for PV system

Fig.A.2 shows the VI which controls the power supply and reads the voltage and current from the PV array; this specific VI measures the current and voltage from the array and calculates the power output simply multiplying at each time step the voltage and current. The code is inserted in a *Time Sequence Structure* and executes each frame sequentially; the first frame covers the control of the power supply, the reading measurement and the action of writing the data into a file; the second frame only counts 5 minutes and put the system in standby because the I(V) characteristic is been measured only once every 5 minutes.

In the first frame has been defined a ramp function which controls the output of module 3 channel 0 (NI9263); the output of this channel has been connected to the analogue sensor of the power supply which in 1.3 second produces an output from -1 to 88 Volt (V_{oc}); while the voltage output of the power supply is controlled, the measurements of the current and voltage from the PV are taken from channel 2 and 3 of the module 8 (NI9215) and multiplied to calculate the

power too.

The code related to writing the data into a file has been divided in two: one file records only the electrical data plus the time and the second one collects the weather data needed as global and diffuse radiation, wind speed and direction, pressure and humidity, all the PV temperature; thus the code includes the blocks to open a .dat file (generic data file extension with reduced size) which will be saved in the "home folder" within a specified name and creates a string of data which will be written in the .dat file at the same time the data are collected.

Fig.A.2 doesn't show any of the channels for weather data because all the measurements specified above are included in the block called *variable 2*. This block is what is called *shared variable* and it means this block is outputting some measurement from another VI; in this way it is sure the electrical data are synchronized with the weather data.

An identical VI has been written for collecting the I(V) characteristic from a single module; the main structure remains the same as the one detailed above but there are two differences: the function which defines the control of the power supply is a ramp from -1 to 11 Volt (V_{oc} for a single module) and the second difference is the *shared variable* which includes the same data as *variable 2* unless the PV temperatures, in this test only one PV temperature is needed.

Measuring the short circuit current and the spectrum of the sun

Fig.A.3 is the VI for controlling the power supply which has to maintain the short circuit condition for the PV module and measuring the current flowing. These data have been sent to a shared variable *Short-circuit-current* which is included in the VI that reads the solar spectrum. The other measurements required are taken from the main VI for the weather station and included in the one for the spectroradiometer with the technique of the *shared variables*.

Weather data monitoring

The block diagram (Fig.A.4) shows the code for collecting, the calibrations for the instruments and the recording of all the data. It can be noted also the presence of the shared variables; each scalar value read from the modules has been connected to a block which generates as output an array containing all the information about the measurement. The entire code is inserted in a timed structure that means the entire code is running continuously with a time step of 1000 milliseconds defined inside the timed structure.

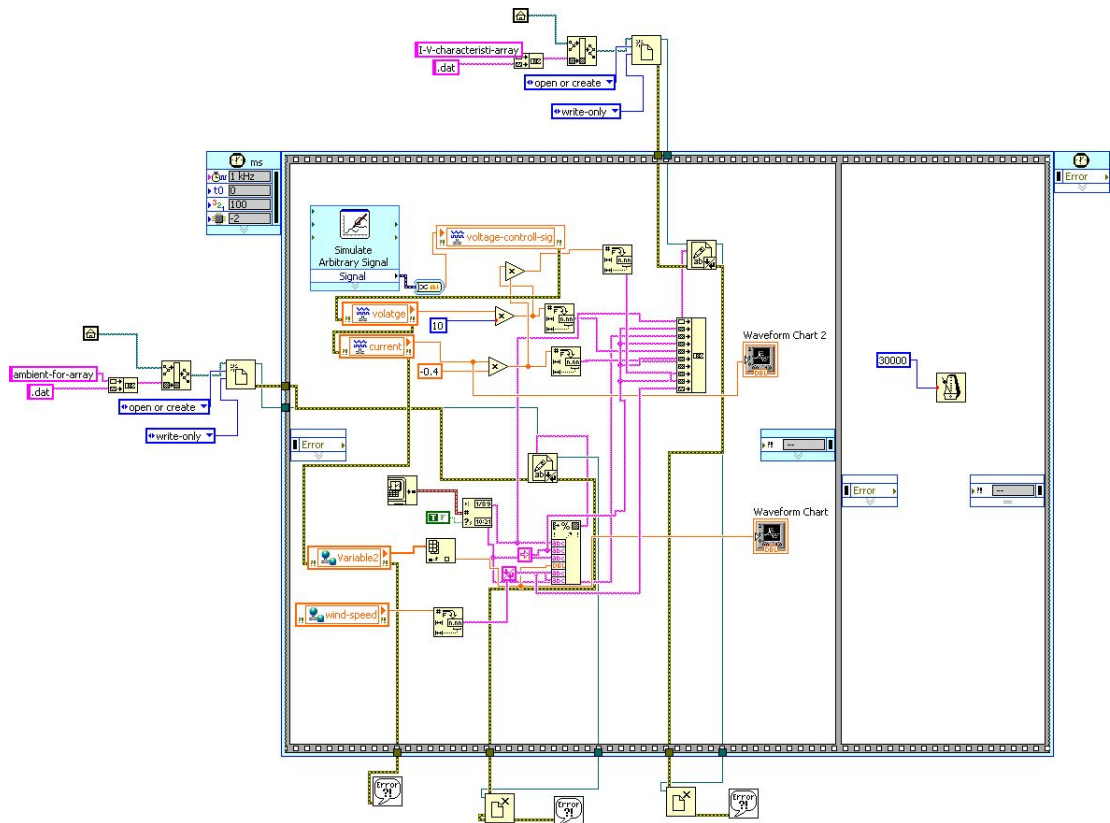


Figure A.2: Block diagram for the measuring the I(V) characteristic from the array.

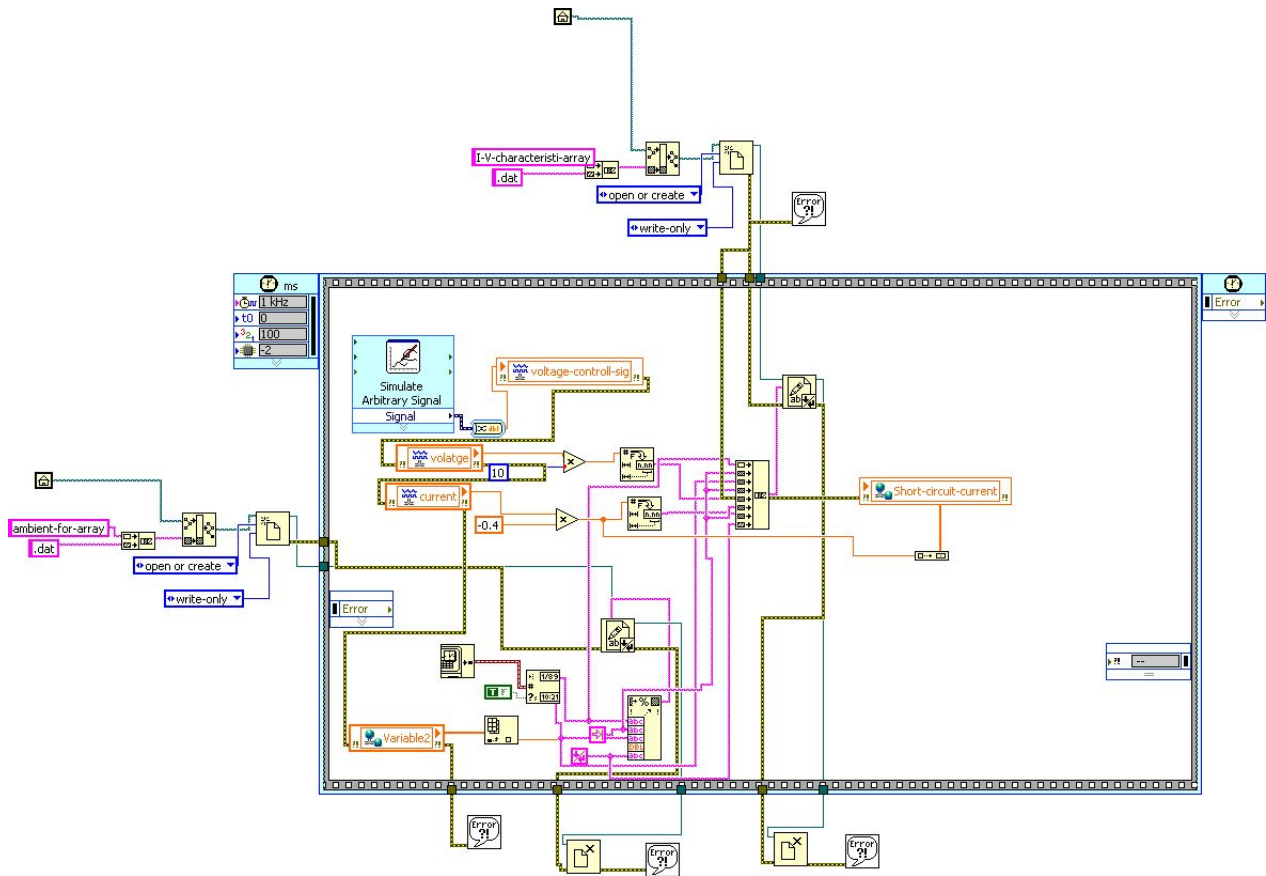


Figure A.3: Block diagram for the measuring the short circuit current of one PV module.

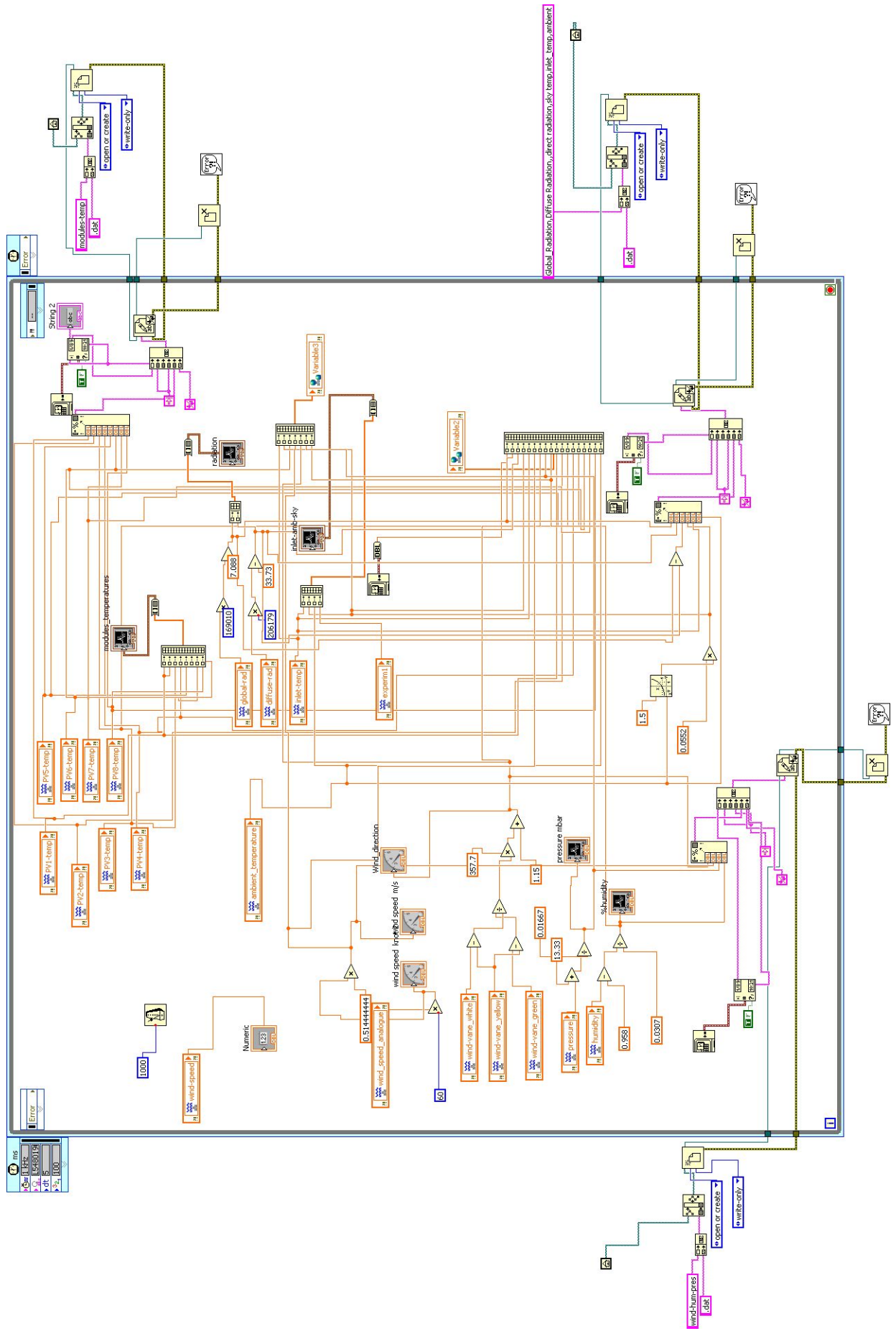


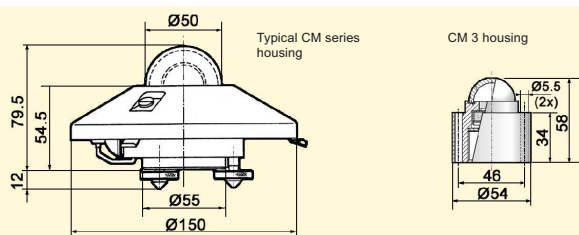
Figure A.4: Block diagram for the monitoring of the weather data.

Appendix B

Roof equipment details

CM Series

PYRANOMETER RANGE



Note: The performance specifications quoted are worst-case and/or maximum values

Kipp & Zonen B.V. reserve the right to alter specifications of the equipment described in this documentation without prior notice

SPECIFICATIONS

	CM 22	CM 21	CM 11	CM 6B	CM 3
ISO CLASSIFICATION / WMO CLASSIFICATION	Secondary Standard High Quality	Secondary Standard High Quality	Secondary Standard High Quality	First Class Good Quality	Second Class Moderate Quality
Response time (95 %)	5 s	5 s	12 s	18 s	18 s
Zero offsets (a) thermal radiation (200 W/m ²) (b) temperature change (5 K/hr)	± 3 W/m ² ± 1 W/m ²	± 7 W/m ² ± 2 W/m ²	± 7 W/m ² ± 2 W/m ²	± 15 W/m ² ± 4 W/m ²	± 15 W/m ² ± 4 W/m ²
Non stability (change/year)	± 0.5 %	± 0.5 %	± 0.5 %	± 1 %	± 1 %
Non linearity (0 - 1000 W/m ²)	± 0.2 %	± 0.2 %	± 0.6 %	± 1.2 %	± 2.5 %
Directional error (at 1000 W/m ²)	± 5 W/m ²	± 10 W/m ²	± 10 W/m ²	± 20 W/m ²	± 25 W/m ²
Temperature dependence of sensitivity	± 0.5 % (-20 to +50 °C)	± 1 % (-20 to +50 °C)	± 1 % (-10 to +40 °C)	± 2 % (-10 to +40 °C)	± 6 % (-10 to +40 °C)
Tilt response (at 1000 W/m ²)	± 0.2 %	± 0.2 %	± 0.2 %	± 1 %	± 2 %
OTHER SPECIFICATIONS					
Sensitivity (µV/W/m ²)	7 - 14	7 - 17	4 - 6	9 - 15	10 - 35
Impedance	10 - 100 Ω	40 - 100 Ω	700 - 1500 Ω	70 - 100 Ω	100 - 200 Ω
Level accuracy	0.1°	0.1°	0.1°	0.5°	1°
Operating temperature	-40 to +80 °C	-40 to +80 °C	-40 to +80 °C	-40 to +80 °C	-40 to +80 °C
Cable length	10 m	10 m	10 m	10 m	10 m
Spectral range (50 % points)	200 - 3600 nm	305 - 2800 nm	305 - 2800 nm	305 - 2800 nm	305 - 2800 nm
Typical signal output for atmospheric applications	0 - 25 mV	0 - 25 mV	0 - 10 mV	0 - 25 mV	0 - 50 mV
Maximum irradiance	4000 W/m ²	4000 W/m ²	4000 W/m ²	2000 W/m ²	2000 W/m ²
Expected daily accuracy	± 1 %	± 2 %	± 3 %	± 5 %	± 10 %
Recommended applications	Scientific research requiring the highest level of measurement accuracy and reliability	Meteorological networks, reference measurements in extreme climates, polar or arid	Meteorological networks, solar energy collector testing, materials testing	Good quality measurements for greenhouse climate control, field testing	Economical solution for routine measurements in weather stations

Options

- Cable extension (5, 10, 15, 20, 25, 100 m) 1,2,3,4,5)
- Connector to extended cable 1,2,3,4,5)
- Various Filter Domes 2,3,4)
- Incorporated temperature sensor, Pt-100 or 10K thermistor 1,2,3)

1) for CM 22 2) for CM 21 3) for CM 11 4) for CM 6B 5) for CM 3

Accessories

- CV 2 Ventilation System 1,2,3,4)
- 2AP Suntracker and Positioner 1,2,3,4)
- CLF 1 levelling fixture 5)
- CM 121B Shadow Ring 1,2,3,4) CLF 1 required for 5)
- SOLRAD Integrator and dataloggers 1,2,3,4,5)
- Various albedo mounting plates 1,2,3,4,5)

SOLAR & ATMOSPHERIC SCIENCE



WWW.KIPPZONEN.COM

Kipp & Zonen B.V.
Röntgenweg 1 2624 BD Delft
P.O. Box 507 2600 AM Delft
The Netherlands

T +31(0)15 2698 000
F +31(0)15 2620 351
E info.holland@kippzonen.com

Your local dealer:

LOW POWER A100L2 ANEMOMETER
(USING LPPL4 ANALOG OUTPUT MODULE)

SPEC SUMMARY



A LOW POWER CONSUMPTION ANALOGUE OUTPUT ANEMOMETER

In response to demand for an anemometer with an analogue voltage output like the proven Porton Anemometer but with reduced current consumption the type PL4 module from the Porton Anemometer has been developed to produce the LPPL4 resulting in an analogue output anemometer suitable for use with data loggers.

- ▶ **TRIED & TESTED 'PORTON ANEMOMETER' MECHANICS AND ROTOR**
- ▶ **0 TO 2½ V OUTPUT FOR 0 TO 150 KNOTS**
- ▶ **5V PULSE/FREQUENCY OUTPUT, 0 TO 1500HZ = 0 TO 150 KNOTS**
- ▶ **VARIANT A100LPC3L2 INCLUDES ANTI-SURGE PROTECTION OPTION**

Specification Summary:

Range of Operation:	Threshold:	0.3Kts (starting speed: 0.4Kts, stopping speed: 0.2Kts)
	Max. windspeed:	150Kts (75m/s)
	Standard measuring range:	0 to 150 Knots
Rotor:	Type:	R30, 3-cup rotor.
	Distance Constant:	2.3m ±10%
Pulse Output:	Rotor speed measurement:	By interruption of optical beam.
	Accuracy:	1% of reading (20 - 110Kts), up to 2% of reading (110 - 150Kts)
	Non-linearity:	0.4% full range output frequency (correction curve supplied).
	Output Range:	0 to 1500Hz for 0 to 150Knots (10Hz per Knot)
	Resolution:	5.15cm.
	5V pulse output:	High 5V±5%, Low <0.2v, min. load res: 20K Ohms. Rise/Fall time approx. 25us, duty cycle 50%(±25%)
Analogue Output:	Nominal Factory Calibration:	0 to 2.500 V DC for 0 to 150 Knots single ended (16.67mV per Knot).
	Output Over-range:	5V ±10%
	Overall Non-linearity:	0.9% full range output for 0 to 150Knots (correction curve supplied for rotor+ratemeter).
	Temperature Coefficient:	±2% of output relative to 15°C value (-30 to +40°C)
	Response Time:	150ms first order lag typical (as Porton A100)
	Effect of supply variation:	±0.2% full range output over full supply range.
	Output Ripple:	Typically 13mV peak to peak at pulse frequency.
	Output Resistance:	Less than 500 Ohms.
	Recommended load resistance:	1M Ohm for calibrated output, (otherwise minimum 5K Ohms).
General:	Operating Temperature Range:	-30 to +70 °C
	Supply Voltage:	6½V to 28V DC
	Power-up Time:	5 sec.
	Current consumption:	2mA max, 1.6mA typical (no output loads).
	Standard Cable:	3m long, 6 core screened 7/0.2mm, PVC insulated.
Connections:	Red = Supply positive, Blue = Supply negative, Green = Analogue output +, Yellow = Analogue output - (Yellow is connected to Blue in the instrument permitting correction for zero offset caused by supply current in long cables), White = Pulse output, Black = Base plate, Screen = Not connected at anemometer.	
Calibration:	Calibration data for the anemometer and rotor are provided at one test speed to an accuracy of 1% at +15°C and +12V DC supply, with analogue output load = 1M Ohm. In-service calibrate/test facility is not fitted.	
Anti-surge options:	A100LPC3L2 variant has an extra surge protection module containing series resistance elements and clamping devices fitted to the base of the module in the standard anemometers. Note that these protection elements slightly affect certain specification parameters.	
Mechanical:	Dimensions, mm / Weight:	195 height x 152 rotor diameter x 55 body diameter. Net Weight: 490g.
	Mounting:	0.25 inch BSW/UNC screw into base (standard tripod fitting).

(Vector Instruments reserves the right to change this specification without notice in line with a policy of continued product improvement)

Vector Instruments, 115 Marsh Road, RHYL, Clwyd, LL18 2AB, United Kingdom.
Tel: (01745) 350700 Fax: (01745) 344206 International Fax: +44 1745 344206.
050-107-06



S-A100/L-LPPL4-5 (G:\NEW-DOCS\A100L2\A100LY3.SAM-19\06\03-DSD)

This instrument incorporates a precision wire-wound potentiometer as shaft angle transducer, enabling wind direction to be accurately determined when used in suitable electronic circuits. The potentiometer has the lowest possible torque consistent with long life and reliability, the small gap at north being filled with an insulating material to ensure smooth operation over the full 360°. The vane-arm assembly is attached by the unique Porton™ gravity fastener, allowing rapid attachment and release; thus improving portability.

Construction is from anodised aluminium alloys and stainless steels for exposed parts. Combined with the hard plastic (upper) plain bearing and precision ball races, the result is an instrument with a long service interval which is suitable for permanent exposure to the weather.

In the marine version,^{#1} body/fin sealing is enhanced and a touching shaft-seal is fitted above the upper (replaceable) bearing for extra protection.

For applications where improved sensitivity is required, a larger vane version^{#2} is available.

An anti-icing heater can also be fitted to extend operation by removing hoare frost around the upper bearing.



Range of Operation

Maximum Wind Speed:	Over 75m/s (150Knots, 170mph)	[60m/s] ^{#2}
Range:	360° mechanical angle, full-circle continuous rotation allowed.	
Temperature range:	-50 to +70 °C	

Performance

Threshold:	0.6m/s (1.2Knot, 1.4mph) [0.75m/s] ^{#1} [0.5m/s] ^{#2} (the vane will commence movement when aligned at 45° to the flow).
Response:	Damped natural Wavelength: 3.4m [3.6m] ^{#2} Damping Ratio: 0.2m [0.24m] ^{#2} Recovery distance: 0.51m [0.54m] ^{#2} Distance constant: 2.3m [2.4m] ^{#2} ±0.5° vane removed and replaced (no measurable backlash movement during use).
Repeatability:	
Life of potentiometer:	5 x 10 ⁷ cycles (10 years typical exposure).
Service Interval:	4 to 5 years.
Accuracy:	±3° in steady winds >5m/s [6m/s] ^{#1} [3.5m/s] ^{#2} (±2° obtainable following calibration).

Electrical

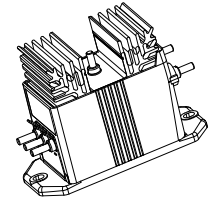
Potentiometer resistance:	1000 Ω ±10%
Maximum dissipation:	0.5W, -50 to +20 °C (de-rate linearly to 0.25W at 70 °C)
Maximum wiper current:	50µA*, (20mA absolute max.)
Supply voltage:	1 to 5V*, (20V absolute max.) across terminals 1 & 3.
Case to pot. voltage:	72V max. (case or screen to any terminal on pot.)
Insulation resistance:	>50MΩ
Temperature coefficient of resistance:	±50 x 10 ⁻⁶ /°C
Electrical continuity angle:	357.7 ±1.5° (2.3° gap at north)
Electrical variation angle:	356.5 ±1.5° (3.5° dead-band)
Resolution:	±0.2°
Independent non-linearity:	±0.25% (unloaded)

Notes: Figures marked * refer to recommended operating conditions.
Bracketed figures marked^{#1,#2} refer to parameters changed when options are fitted, (see options section overleaf).

Voltage Transducer LV 100-100

For the electronic measurement of voltages: DC, AC, pulsed..., with galvanic isolation between the primary circuit (high voltage) and the secondary circuit (electronic circuit).

$$V_{PN} = 100 \text{ V}$$



Electrical data

V_{PN}	Primary nominal voltage rms	100	V
V_{PM}	Primary voltage, measuring range	0 .. ± 150	V
I_{PN}	Primary nominal current rms	100	mA
R_M	Measuring resistance with $\pm 15 \text{ V}$	$R_{M \min}$ $R_{M \max}$	
		@ $\pm 100 \text{ V}_{\max}$	0 170 Ω
		@ $\pm 150 \text{ V}_{\max}$	0 90 Ω
I_{SN}	Secondary nominal current rms	50	mA
K_N	Conversion ratio	100 V : 50 mA	
V_C	Supply voltage ($\pm 5 \%$)	± 15	V
I_C	Current consumption	$< 32 + I_S$	mA

Accuracy - Dynamic performance data

X_G	Overall accuracy @ $V_{PN}, T_A = 25^\circ\text{C}$	± 0.9	%
\mathcal{E}_L	Linearity error	< 0.1	%
I_O	Offset current @ $I_p = 0, T_A = 25^\circ\text{C}$	Typ Max	mA
I_{OT}	Temperature variation of I_O 0°C .. +70°C	± 0.2 ± 0.3	mA
t_r	Response time to 90 % of V_{PN} step	50	μs

General data

T_A	Ambient operating temperature	0 .. +70	$^\circ\text{C}$
T_S	Ambient storage temperature	-25 .. +85	$^\circ\text{C}$
N_p	Turns ratio	1000 : 2000	
P	Total primary power loss	10	W
R_1	Primary resistance @ $T_A = 25^\circ\text{C}$	1	k Ω
R_S	Secondary coil resistance @ $T_A = 70^\circ\text{C}$	55	Ω
m	Mass	790	g
	Standards	EN 50178: 1997	

Features

- Closed loop (compensated) voltage transducer using Hall effect
- Isolated plastic case recognized according to UL 94-V0
- Primary resistor R_1 incorporated within the housing.

Advantages

- Excellent accuracy
- Very good linearity
- Low temperature drift
- Optimized response time
- Wide frequency bandwidth
- No insertion losses
- High immunity to external interference.

Applications

- AC variable speed drives and servo motor drives
- Static converters for DC motor drives
- Uninterruptible Power Supplies (UPS)
- Power supplies for welding applications.

Application domain

- Industrial.

Current Transducer LTSR 6-NP

For the electronic measurement of currents: DC, AC, pulsed, mixed, with galvanic isolation between the primary circuit (high power) and the secondary circuit (electronic circuit).

$$I_{PN} = 6 \text{ At}$$



Electrical data

I_{PN}	Primary nominal current rms	6	At
I_{PM}	Primary current, measuring range	0 .. ± 19.2 ¹⁾	At
I_p	Overload capability	250	At
V_{OUT}	Output voltage (Analog) @ I_p	2.5 ± (0.625 · I_p / I_{PN})	V
	$I_p = 0$	2.5 ²⁾	V
V_{REF}	Reference voltage (internal reference), Ref _{OUT} mode	2.5 ³⁾	V
	Reference voltage (external reference), Ref _{IN} mode	1.9 .. 2.7 ⁴⁾	V
G	Sensitivity	104.16	mV/A
N_s	Number of secondary turns (± 0.1 %)	2000	
R_L	Load resistance	≥ 2	kΩ
$C_{L,max}$	Maximum capacitive loading	500	pF
R_{IM}	Internal measuring resistance (± 0.5 %)	208.33	Ω
TCR_{IM}	Temperature coefficient of R_{IM}	< 50	ppm/K
V_C	Supply voltage (± 5 %)	5	V
I_C	Current consumption @ $V_C = 5 \text{ V}$	Typ 28 + $I_s^{5)}$ + ($V_{OUT} R_L$)	mA

Accuracy - Dynamic performance data

X	Accuracy @ I_{PN} , $T_A = 25^\circ\text{C}$	± 0.2	%
	Accuracy with R_{IM} @ I_{PN} , $T_A = 25^\circ\text{C}$	± 0.7	%
ϵ_L	Linearity error	< 0.1	%
		Max	
TCV_{OUT}	Temperature coefficient of V_{OUT} / V_{REF} @ $I_p = 0$		
	- 40°C .. + 85°C	150	ppm/K
TCG	Temperature coefficient of G	- 40°C .. + 85°C	50 ⁶⁾ ppm/K
V_{OM}	Magnetic offset voltage @ $I_p = 0$,		
	after an overload of 3 x I_{PN}	± 7	mV
	5 x I_{PN}	± 8	mV
	10 x I_{PN}	± 10	mV
TCV_{REF}	Temperature coefficient of internal V_{REF}		
	@ $I_p = 0$		
	- 10°C .. + 85°C	50	ppm/K
	- 40°C .. - 10°C	100	ppm/K
t_{ta}	Reaction time @ 10 % of I_{PN}	< 100	ns
t_r	Response time to 90 % of I_{PN} step	< 400	ns
di/dt	di/dt accurately followed	> 15	A/μs
BW	Frequency bandwidth (0 .. - 0.5 dB)	DC .. 100	kHz
	(- 0.5 .. 1 dB)	DC .. 200	kHz

Notes: ¹⁾ Only in ref_{OUT} mode or with external REF less than 2.525 V and greater than 2.475 V. For external REF out of these limits see leaflet. ²⁾ V_{OUT} is linked to V_{REF} , by conception the difference between these two nodes for $I_p = 0$ is maximum ± 25 mV, 2.475 V < V_{OUT} < 2.525 V. ³⁾ In Ref_{OUT} mode at $T_A = 25^\circ\text{C}$, 2.475 V < V_{REF} < 2.525 V. The minimal impedance loading the ref pin should be > 220 kΩ. Internal impedance = 600 Ω. For most applications you need to buffer this output to feed it into an ADC for example. ⁴⁾ To overdrive the REF (1.9 V .. 2.7 V) max ± 1 mA is needed. ⁵⁾ $I_s = I_p / N_s$. ⁶⁾ Only due to TCR_{IM} .

Features

- Closed loop (compensated) multirange current transducer using the Hall effect
- Unipolar voltage supply
- Isolated plastic case recognized according to UL 94-V0
- Compact design for PCB mounting
- Incorporated measuring resistance
- Extended measuring range
- Access to the internal voltage reference
- Possibility to feed the transducer reference from external supply.

Advantages

- Excellent accuracy
- Very good linearity
- Very low temperature drift
- Optimized response time
- Wide frequency bandwidth
- No insertion losses
- High immunity to external interference
- Current overload capability.

Applications

- AC variable speed drives and servo motor drives
- Static converters for DC motor drives
- Battery supplied applications
- Uninterruptible Power Supplies (UPS)
- Switched Mode Power Supplies (SMPS)
- Power supplies for welding applications.

Application Domain

- Industrial.

BOP MODEL TABLE

MODEL (1) (5)	d-c OUTPUT RANGE		CLOSED LOOP GAIN		OUTPUT IMPEDANCE			
	E _o max.	I _o max.	VOLTAGE CHANNEL G _v (V/V)	CURRENT CHANNEL G _i (A/V)	VOLTAGE MODE SERIES R	VOLTAGE MODE SERIES L (2)	CURRENT MODE SHUNT R	CURRENT MODE SHUNT C (3)
100 WATT								
BOP 20-5M	± 20V	± 5A	2.0	0.5	80μΩ	20μH	40kΩ	0.05μF
BOP 50-2M	± 50V	± 2A	5.0	0.2	0.5mΩ	100μH	50kΩ	0.05μF
BOP 100-1M	± 100V	± 1A	10.0	0.1	2.0mΩ	200μH	100kΩ	0.05μF
200 WATT								
BOP 20-10M	± 20V	± 10A	2.0	1.0	40μΩ	50μH	20kΩ	0.1μF
BOP 36-6M	± 36V	± 6A	3.6	0.6	120μΩ	50μH	36kΩ	0.1μF
BOP 50-4M	± 50V	± 4A	5.0	0.4	0.25mΩ	100μH	50kΩ	0.05μF
BOP 72-3M	± 72V	± 3A	7.2	0.3	0.48mΩ	200μH	72kΩ	0.05μF
BOP 100-2M	± 100V	± 2A	10.0	0.2	1.0mΩ	200μH	100kΩ	0.05μF
BOP 200-1M(4)	± 200V	± 1A	20.0	0.1	4.0mΩ	1.2mH	200kΩ	0.03μF
400 WATT								
BOP 20-20M	± 20V	± 20A	2.0	2.0	20μΩ	50μH	20kΩ	0.2μF
BOP 36-12M	± 36V	± 12A	3.6	1.2	60μΩ	50μH	36kΩ	0.2μF
BOP 50-8M	± 50V	± 8A	5.0	0.8	125μΩ	100μH	50kΩ	0.15μF
BOP 72-6M	± 72V	± 6A	7.2	0.6	240μΩ	200μH	72kΩ	0.1μF
BOP 100-4M	± 100V	± 4A	10.0	0.4	500μΩ	200μH	100kΩ	0.1μF

(1) For factory installed digital interfaces add appropriate suffix. See page 55.

(2) For determining dynamic impedance in voltage mode.

(3) For determining dynamic impedance in current mode.

(4) Same size as 400W models.

(5) To specify digital display, substitute the suffix letter "D" for the suffix letter "M."

FEATURES

- Source and sink 100% of their current rating. See Figure 1.
- Separate control circuits for voltage and current with automatic crossover to current and voltage limits.
- All controls and flag signals accessible through a 50-terminal user-port at the rear.
- Zeroable preamplifier available for scaling and summing external signals.
- Optional digital displays. Specify by substituting the suffix "D" in place of the "M."



For high power bipolar power supplies, see Series BOP High Power, page 44.

For high voltage bipolar power supplies, see Series BOP-HV, page 56.

The tabulation of the effective series resistance and inductance in voltage mode, and the effective shunt resistance and shunt capacitance in current mode, is done to allow a calculation of the output impedance versus frequency.

BOP accept plug-in cards for remote digital control

- BIT 4882 provides 12-bit IEEE 488.2 talk-listen control with SCPI support.
- BIT 4886 provides 16-bit IEEE 488.2 talk-listen control with SCPI support.
- BIT TMA-27 connect BOP to Kepco's single-address multiple instrument serial bus for long range (>300m) control from IEEE 488.2, RS 232 or VXI-based hosts.
- BIT 488B or BIT 488D offer listen-only GPIB support in binary or Hex format.

Cards may be factory installed. See page 55 for appropriate suffix designations.



KEPCO, INC. • 131-38 Sanford Avenue • Flushing, NY 11352 USA • Tel: (718) 461-7000 • Fax: (718) 767-1102
 Email: hq@kepcopower.com • www.kepcopower.com/bop.htm

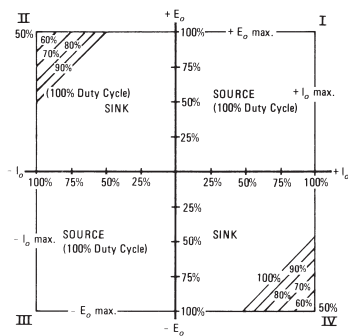


FIGURE 1
Output Source-Sink plot

TABLE 1
Source current measured worst case, 125V a-c.

MODEL	CURRENT (Amps)
BOP 20-5M	2.6
BOP 20-10M	5.5
BOP 20-20M	11.0
BOP 36-6M	5.1
BOP 36-12M	10.6
BOP 50-2M	2.6
BOP 50-4M	4.8
BOP 50-8M	9.5
BOP 72-3M	5.0
BOP 72-6M	10.8
BOP 100-1M	2.6
BOP 100-2M	4.8
BOP 100-4M	9.2
BOP 200-1M	5.5

CE BOP are CE marked per the Low Voltage Directive (LVD), EN61010-1.



KEPCO, INC. • 131-38 Sanford Avenue • Flushing, NY 11352 USA • Tel: (718) 461-7000 • Fax: (718) 767-1102
Email: hq@kepcopower.com • www.kepcopower.com/bop.htm

BOP GENERAL SPECIFICATIONS

SPECIFICATION	RATING/DESCRIPTION	CONDITION
INPUT		
a-c Voltage	95-113, 105-125, 190-226, 210-250V a-c	User selectable
Current	See Table 1	Max load, 115V a-c
Frequency	47-65Hz	Range
OUTPUT		
d-c Output	Bi-direction, series pass	Transistor (1)
Type of stabilizer	Automatic crossover	Voltage/current
Voltage	0 to 100% of rating (bipolar)	Adjustment range for temp 0-55°C
Current	0 to 100% of rating (bipolar)	
Sink	See source/sink plot	Duty cycle
Error Sense	0.5V per load wire	Voltage allowance
Isolation Voltage	500V d-c or peak	Output to ground
Leakage Current	<5 microamperes	rms at 115V a-c 60Hz
Output to Ground	<50 microamperes	p-p at 115V a-c 60Hz
Series Connection	500V	Max voltage off ground
Parallel Connection	Current sharing	Use master-slave connection
OVP	Not available	
CONTROL		
Type	Voltage Current	Variable input, fixed gain
Voltage/ Current	Local	10-turn zero-center pot
Remote Analog		-10V to +10V
Local Digital		Serial bus or GPIB or VXI
Remote Digital		Use SN or SNR interface
Bounding	±Volt/current local	Four screwdriver trimmers
	±Volt/current remote	0 to 10 volts
Dynamics	See dynamic spec table	Fast only
User Amplifiers	Uncommitted gain 20K	Two provided
References	±10 volts, 1mA	Two provided
Options (built-in)	GPIB hex card	Suffix -488B
For user added card refer to "BIT" models page 55	GPIB BCD card	Suffix -488D
	Long range serial card/VXI	Suffix -TMA
	Talk-listen 4882 card (SCPI)	Suffix -4882
	Talk-listen 4886 card (SCPI)	Suffix -4886
	Serial RS 232	Suffix -232
MECHANICAL		
Input Connection	Detachable IEC type 3-wire	All models
Output Connections	Front signal/output	Binding posts
	Rear user port	50-terminal connector
	Rear output	Barrier strip
Meters	Two 2 1/2" horiz., 2% zero center analog	Front panel
Indicators	Four LEDs	Voltage/Current/Bounding
Mounting (in std 19" racks)	Use RA 37 rack adapter	3/4 rack size
	Mounting "ears" supplied	Full rack size
Cooling	Forced air	Exhaust to rear
Dimensions inches (HxWxD) add mm	5 7/32 x 12 17/32 x 17 3/64 132.6 x 318.3 x 435.4	3/4 rack size
2 1/2" to rear inches mm	5 7/32 x 19 x 20 3/64 132.6 x 482.6 x 510	Full rack size
Finish; Fed Std 595	Light gray, color 26440	Front panel
Weight (packed for shipment)	47lb (21.4Kg)	3/4 rack size (100W)
	53lb (24.1Kg)	3/4 rack size (200W)
	76lb (34.5Kg)	Full rack size

(1) 200V model uses FET.

BOP DYNAMIC SPECIFICATIONS

MODEL	BANDWIDTH (f-c to f-3dB) KHz (minimum) Mode		RISE & FALL TIME 10%-90% µsec (maximum) Mode		LARGE SIGNAL FREQUENCY (min) RESPONSE KHz Mode		SLEWING RATE (minimum) Mode		RECOVERY STEP LOAD µsec (maximum) Mode	
	V	I	V	I	V	I	V	I	V	I
100 WATT										
BOP 20-5M	18	12	20	30	17	13	5V/µsec	0.15A/µsec	25	10
BOP 50-2M	18	12	20	30	17	13	5V/µsec	0.15A/µsec	25	10
BOP 100-1M	18	11	17	22	18	11	11V/µsec	70mA/µsec	40	25
200 WATT										
BOP 20-10M	18	6	20	60	17	7	2V/µsec	0.4A/µsec	80	20
BOP 36-6M	16	13	20	27	15	14	3V/µsec	0.5A/µsec	50	35
BOP 50-4M	23	14	14	25	15	11	4.5V/µsec	0.25A/µsec	40	30
BOP 72-3M	20	15	18	26	17	12	10V/µsec	0.15A/µsec	30	30
BOP 100-2M	22	15	18	26	17	12	10V/µsec	0.15A/µsec	30	30
BOP 200-1M	4.0	2.5	110	150	4.0	2.5	5V/µsec	15mA/µsec	150	120
400 WATT										
BOP 20-20M	9.5	10	35	35	8	10	1V/µsec	1.25A/µsec	100	75
BOP 36-12M	20	10	16	30	19	10	4V/µsec	0.75A/µsec	50	30
BOP 50-8M	24	10	14	35	24	11	7.5V/µsec	0.5A/µsec	40	30
BOP 72-6M	19	9.5	18	40	20	11	9V/µsec	0.4A/µsec	50	20
BOP 100-4M	18	14	22	30	16	10	10V/µsec	0.25A/µsec	40	30

BOP STATIC SPECIFICATIONS

INFLUENCE QUANTITY	OUTPUT EFFECTS(1)				PREAMPLIFIER(4) OFFSETS		REFERENCE ± 10V
	VOLTAGE MODE		CURRENT MODE		ΔE _{io}	ΔI _{io}	
	TYPICAL	MAXIMUM	TYPICAL	MAXIMUM			
Source (min.-max.)	<0.0005%	0.001%	<0.002%	0.005%	<5µV	<1nA	<0.0005%
Load (NL-FL)	<0.001%	0.002%	<0.5mA	1mA	—	—	<0.0005%
Time (8-hour drift)	<0.005%	0.01%	<0.01%	0.02%	<20µV	<1nA	<0.005%
Temp., per °C	<0.005%	0.01%	<0.01%	0.02%	<20µV	<1nA	<0.005%
Ripple and Noise (2)	rms	<1mV	3mV(5)	<0.01%	0.03%	—	—
	p-p(3)	<10mV	30mV(5)	<0.1%	0.3%	—	—

- (1) Output effects, expressed as a percentage, are referred to the maximum rated output voltage or current.
(2) Measured with the common terminal grounded so that the common mode current does not flow through the load.
(3) Peak-to-peak ripple is measured over a 20Hz to 10MHz bandwidth.
(4) The output effect can be calculated by the relationship:
 $\Delta E_o = \pm \Delta E_r (R_f/R_i) \pm \Delta E_{io} (1+R_f/R_i) \pm \Delta I_{io} (R_f)$ where R_f is the feedback resistor, and R_i is the input resistor from the reference, E_r .
(5) For BOP 200-1M the maximum ripple and noise is 5mV rms and 50mV p-p.

The tabulated offsets, more particularly their change as a function of source, time and temperature, allow a user to calculate performance of the uncommitted amplifier(s) with user specified input and feedback components. The formula for this is given in the static specifications table footnote.



KEPCO, INC. • 131-38 Sanford Avenue • Flushing, NY 11352 USA • Tel: (718) 461-7000 • Fax: (718) 767-1102
Email: hq@kepcopower.com • www.kepcopower.com/bop.htm

Appendix C

Programming: data manipulation and shadow calculation

This appendix includes all the codes written in bash and Matlab for assisting the simulation and validation of the model for the PV the outdoor test experiment.

BASH is a command processor language that is typically run in a text window, allowing the user to type commands which cause actions. Bash can also read commands from a file, called a script. Like all Unix shells, it supports file-name wildcarding, piping, here documents, command substitution, variables and control structures for condition-testing and iteration. The keywords, syntax and other basic features of the language were all copied from sh. Bash is a POSIX shell but with a number of extensions.

AWK is a data extraction and reporting tool that uses a data-driven scripting language consisting of a set of actions to be taken against textual data (either in files or data streams) for the purpose of producing formatted reports. The language used by awk extensively uses the string datatype, associative arrays (that is, arrays indexed by key strings), and regular expressions.

SED (stream editor) is a Unix utility that parses text and implements a programming language which can apply transformations to such text. It reads input line by line (sequentially), applying the operation which has been specified via the command line (or a sed script), and then outputs the line. The script C.1, written in bash, takes as input the file *\$file* which contains the values of the short circuit of each cell (considering the partial shading) and the name of the cell (first row of the input file). The short circuit current has been calculated as function of the portion of the cell surface that is shaded and the incident radiation.

The incident radiation has been derived from the measured incident global and diffuse irradiance on the horizontal plane, the incident angle and the solar

azimuth calculated as a function of the time of the measurement. The output files are as many as the number of the cells (specified from the number of the columns in the input file); the name of each file is a number which refers to the cell and module number as in Fig.4.8 page 60; the generated files are composed of two columns: the first one is the ascending time in seconds; the second is the value of the short circuit current of the cell previously calculated in Matlab taking into account the partial shading. The output files maintain constant the value of the I_{sc} for one second. The script generate a folder in which all the files can be grouped.

Listing C.1: Generate function for PSpice

```

1
2  #!/bin/bash
3  for file in $@;
4
5
6  do
7
8      mkdir pspice.d;
9      for ((i=1; i<144; i++))
10     do
11         name=$(cat $file | awk ' NR == 1 {print $'i'}')
12         cat $file | awk ' NR != 1 {print 2*NR-4"
13             "$'i'"\"r"; print 2*NR-3"\"$'i'"\"r"}'>
14             pspice.d/$name.txt
15     echo pspice.d/$name
16     done;
17 done;

```

The code C.2 is used to select the data for the simulation when the Labview code for controlling the weather station did not synchronized the ambient data with the measured I(V) characteristic. Once the code for the c-RIO has been re-written with the latest version of Labview (2009) it is equipped with *shared variables* and the script is no longer required.

From C.2 the script takes three files input: the *time input file* which selects the time of each I(V) measurement; *data file1* which contains the temperature measured on the back of PV modules, one second time step; *data file2* which contains the values of the diffuse and global radiation measured every second.

The script creates a variable, *time*, and selects the temperatures and the

radiation values measured at the same time as the I(V) characteristic.

Listing C.2: Selection of the measured data

```
1  #!/bin/bash
2
3  time_input_file="transducer100301.dat"
4  data_file1="Temperature100301.txt"
5  data_file2="Pyranometer100301.txt"
6
7  strings $time_input_file > $time_input_file.clear
8  times=$(awk '{print $2}' $time_input_file.clear | uniq)
9  rm $time_input_file.clear
10 if [ -f $data_file1.clear ];then rm $data_file1.clear; fi
11 if [ -f $data_file2.clear ];then rm $data_file2.clear; fi
12
13 for time in $times;
14 do
15     awk '$1=="$time"' {print; exit}'
16     $data_file1 >> $data_file1.clear
17     awk '$2=="$time"' {print; exit}'
18     $data_file2 >> $data_file2.clear
19 done;
```

The model described in Chapter 4 uses two current sources to represent the available current generated by a solar cell: the first one takes into account only the part of the current generated by the incident radiation and the proportion of shading; the second one considers the contribution of the temperature to the process of the generation of the current since the band gap energy, E_G , decreases and more photons have enough energy to create electrons-holes pairs.

The value of the current has been kept constant for the simulation time step (one second) and has been calculated from:

$$I_T = (T_{cell} - T_{ref}) \frac{dI}{dT} \quad (C.1)$$

where dI/dT is $3.13 \text{ mA}^\circ\text{C}^{-1}$. The script C.3 creates a file for each module giving a name that records module's position in the array.

Listing C.3: Generation of the files containing the adjustment of the cell's current due to the temperature

```
1
```

```

2  #!/bin/bash
3  for file in $@;
4  do
5
6      mkdir Ppice-temp.d;
7
8
9      cat $file | awk -F',' 'NR!=1 {print 2*NR-4"
      "($7-20)*0.00313"\r"; print 2*NR-3"
10         ($7-20)*0.00313"\r"}'>Ppice-temp.d/1a.txt
11      cat temperature.csv | awk -F',' 'NR!=1 {print 2*NR-4"
      "($11-20)*0.00313"\r";
12         print 2*NR-3"
      "($11-20)*0.00313"\r"}'>Ppice-temp.d/2a.txt
13      cat temperature.csv | awk -F',' 'NR!=1 {print 2*NR-4"
      "($10-20)*0.00313"\r";
14         print 2*NR-3"
      "($10-20)*0.00313"\r"}'>Ppice-temp.d/3a.txt
15      cat temperature.csv | awk -F',' 'NR!=1 {print 2*NR-4"
      "($6-20)*0.00313"\r";
16         print 2*NR-3"
      "($6-20)*0.00313"\r"}'>Ppice-temp.d/4a.txt
17      cat temperature.csv | awk -F',' 'NR!=1 {print 2*NR-4"
      "($5-20)*0.00313"\r";
18         print 2*NR-3"
      "($5-20)*0.00313"\r"}'>Ppice-temp.d/5a.txt
19      cat temperature.csv | awk -F',' 'NR!=1 {print 2*NR-4"
      "($9-20)*0.00313"\r";
20         print 2*NR-3"
      "($9-20)*0.00313"\r"}'>Ppice-temp.d/6a.txt
21      cat temperature.csv | awk -F',' 'NR!=1 {print 2*NR-4"
      "($8-20)*0.00313"\r";
22         print 2*NR-3"
      "($8-20)*0.00313"\r"}'>Ppice-temp.d/7a.txt
23      cat temperature.csv | awk -F',' 'NR!=1 {print 2*NR-4"
      "($4-20)*0.00313"\r";
24         print 2*NR-3"
      "($4-20)*0.00313"\r"}'>Ppice-temp.d/8a.txt;
25  done;

```

From the measured characteristic, some parameters have to be collected to compare them with the simulated values. The following script illustrates how to create a folder (*mkdir \$file*) which includes the files for the MPP values (power, current and voltage), the short circuit current and the open circuit voltage.

Listing C.4: Selection of the useful parameters from the measured I(V) characteristic.

```

1
2
3 #!/bin/bash
4 for file in $@;
5 do
6
7 mkdir $file.d;
8
9 cat $file | awk -F',' 'BEGIN{i=0;}
10     {if(i<361)
11         {if($4>0 && $4<0.1)
12             {print $1,"$2","$3","$4","$5\r";i=0}}
13             }>prova.csv
14 cat $file | awk -F',' 'BEGIN{minutes=-1;P=0}
15     {if(minutes==$2) {if($6>P)
16         {P=$6;I=$5;V=$4;h=$1;m=$2;s=$3}}
17         else {print
18             h","m","s","P","I","V\r";minutes=$2;P=0;}
19             }>$file.d/main_parameter_measured.csv;
20 cat prova.csv | awk -F',' 'BEGIN{minutes=-1;}
21     {if(minutes==$2) {}
22         else {print ;minutes=$2}
23         }>$file.d/Isc.csv;
24 cat $file | awk -F',' 'BEGIN{i=0;}
25     {if(i<361)
26         {if($5<=0) {print $1,"$2","$3","$4","$5\r";i=0}}
27         }>prova1.csv;
28
29 cat prova1.csv | awk -F',' 'BEGIN{minutes=-1;}
30     {if(minutes==$2) {} else {print ;minutes=$2}
31         }>$file.d/Voc.csv;
32

```

```
33
34 done;
```

The output from the simulation is a text file containing time, power, current and voltage values for each of the temperatures simulated. Given the large quantity of data, looking at a characteristic at each time step is not possible. Thus key values have been selected: I_{sc} , P_{max} , I_{mpp} and V_{mpp} . The role of the script C.5 is selecting these parameters for the various temperatures.

Listing C.5: Selection of the results from the simulation

```
1 #!/bin/bash
2 for file in $@;
3 do
4     mkdir $file.d;
5
6     cat $file | awk 'BEGIN{i=0; Pmax=0}
7     NR!=1 {if($1>=i)
8         {if ($1<i+1)
9             {if ($int((i)/2+2)>Pmax)
10                {Pmax=$int((i)/2+2); Imax=$int((i)/2+17);
11                  Vmax=$40}
12             }
13            else {i=i+2; print $1"_"Pmax"_"Imax"_"Vmax;Pmax=0}
14           }
15     }'>$file.d/main_parameter.csv;
16     cat $file | awk 'BEGIN{i=0; I=0}
17     NR!=1 {if($1>=i)
18         {if ($1<i+1)
19             {if($32==0) {I=$int((i)/2+17)}} else {i=i+2; print
20                I;I=0}}}'>$file.d/Isc.csv;
21 done;
```

In section 5.3 page 95 the model for the calculation of the coordinates of the shadow created by a surrounding object as function of the location, the time, the position of the object and the PV surface has been described. The following code written in Matlab calculates these coordinates for every location, position, time and time step.

Listing C.6: Calculation of the shadow coordinates projected on the PV array from an object

```

function S=shading_point_yearly()
phi=48.76; %latitude
lambda=9.183; %local
    longitude
lambda_zone=30; %zone
    longitude
5 for i=1:2:3 %select day
    of the year
beta=40
    delta(i)=(23.45*sind((360/365)*(284+i)));
    %declination angle radiant
    B(i)=(360*(i-81)/364); %B
10 Et(i)=9.87*sind(2*B(i))-7.53*cosd(B(i))-1.5*sind(B(i));
    %equation of the time
    v=[500:5:800]; %select the minute of the day and time
    step
    Ts(i,:)=v+4*(lambda_zone-lambda)+Et(i);
    omega(i,:)=(0.25*Ts(i,:)-180); %hour angle
15 theta(i,:)=cosd(phi)*cosd(delta(i))*cosd(omega(i,:))+
    +sind(phi)*sind(delta(i));
    zenith(i,:)=acosd(theta(i,:));
    elevation(i,:)=90-zenith(i,:);
    azimuth(i,:)=sign(omega(i,:))*abs(acosd((theta(i,:)*
20 *sind(phi)-sind(delta(i)))/(sind(zenith(i,:))*cosd(phi))))
    s1(i,:)=cosd(azimuth(i,:)).*cosd(elevation(i,:));
    s2(i,:)=sind(azimuth(i,:)).*cosd(elevation(i,:));
    s3(i,:)=sind(elevation(i,:));
end
25 %day and time size matrix
total_time=i*size(v,2);
MX1=reshape(s1',1,total_time);
MX2=reshape(s2',1,total_time);
30 MX3=reshape(s3',1,total_time);
s=[MX1; MX2; MX3];
    %define the point of the shading surface

```

```

    r0=[10200 2100 0]
35  r1=[10500 2100 0];
    r2=[10500 2100 2400];
    r3=[10200 2100 2400];

    %define the points of the shaded surface
40  p1=[8050 2514.3 1540.4]
    p2=[8050 3157.1 2306.4]
    p3=[10300 3157.1 2306.4]
    p4=[10300 2514.3 1540.0]

    %calculation of the vector perpendicular to the
45  %solar generator plane C

    for k=1:total_time
        j=p2-p1;
        x=p4-p1;
50  a=cross(j,x);
        A(:,k)=(a);
        vect1=r0-p1;
        vect2=r1-p1;
        vect3=r2-p1;
55  vect4=r3-p1;
        C(:,k)=(vect1);
            Ca(:,k)=(vect2);
        Cb(:,k)=(vect3);
        Cc(:,k)=(vect4);
60  end

        P=(dot(A,C)./(dot(A,s)));
        Pa=(dot(A,Ca)./(dot(A,s)));
        Pb=(dot(A,Cb)./(dot(A,s)));
        Pc=(dot(A,Cc)./(dot(A,s)));
65  for j=1:total_time
            for f=1:3
                D=(P(j).*s(:,1:j));
                D1=(Pa(j).*s(:,1:j));
                D2=(Pb(j).*s(:,1:j));
70  D3=(Pc(j).*s(:,1:j));
                R0(:,j)=(r0);
                R1(:,j)=(r1);
                R2(:,j)=(r2);

```

```

75     R3(:,j)=(r3);
        P0(f,j)=R0(f,j)-D(f,j);
        P1(f,j)=R1(f,j)-D1(f,j);
        P2(f,j)=R2(f,j)-D2(f,j);
        P3(f,j)=R3(f,j)-D3(f,j);
80     S1=[(P1(:,:))' (P0(:,:))' (P3(:,:))' (P2(:,:))'];
        S1(:,3)=0
        S1(:,6)=0
        S1(:,9)=0
        S1(:,12)=0

85     S=S1
            end
        end
end

```

The last code written in Matlab is used to calculate the proportion each cell of the PV array that is shaded. It takes as input the coordinates calculated by the previous code (C.6) and return a matrix of 144 columns (total number of the cells) and as many rows as the time selected for the simulation.

Listing C.7: Calculation of the shading percentage on the surface of each cell of the PV array

```

function shading_perc=shading_percentage2_figure()

R=zeros(18*8,4*3);
x1=(ones(8,1)*(805:12.5:1017.55))';
5 R(:,1)=x1(:);
y1=(ones(18,1)*(251.43:8.035:307.675));
R(:,2)=y1(:);
x2=(ones(8,1)*(817.5:12.5:1030))';
R(:,4)=x2(:);
10 y2=(ones(18,1)*(251.43:8.035:307.675));
R(:,5)=y2(:);
x3=(ones(8,1)*(805:12.5:1017.5))';
R(:,7)=x3(:);
y3=(ones(18,1)*(259.465:8.035:315.71));
15 R(:,8)=y3(:);
x4=(ones(8,1)*(817.5:12.5:1030))';
R(:,10)=x4(:);
y4=(ones(18,1)*(259.465:8.035:315.71));

```

```

R(:,11)=y4(:);
20
    %shadow coordinates
    matrice=shading_point();
    time=size(matrice,1);

25
    for tempo=1:time

        K_vector(tempo)={matrice(tempo,1:12)};
        nshadow=size(K_vector,2);

30
    end

    close all

35
    for shadow=1:nshadow
        npoint_shadow=size(K_vector{shadow},2)/3;
        K=zeros(0,3);

40
        x_cell=unique([R(:,1); R(:,4)]);
        y_cell=unique([R(:,2); R(:,8)]);
        dx_cell=x_cell(2)-x_cell(1);
        dy_cell=y_cell(2)-y_cell(1);

45
        %division of the space
        xmin=min(K_vector{shadow}(1:3:3*npoint_shadow));
        xmax=max(K_vector{shadow}(1:3:3*npoint_shadow));
        ymin=min(K_vector{shadow}(2:3:3*npoint_shadow));
        ymax=max(K_vector{shadow}(2:3:3*npoint_shadow));
50
        x_cell=unique([x_cell;
            [max(x_cell):dx_cell:(xmax+dx_cell)
             min(x_cell):-dx_cell:(xmin-dx_cell)]']);
        y_cell=unique([y_cell;
            [max(y_cell):dy_cell:(ymax+dy_cell)
             min(y_cell):-dy_cell:(ymin-dy_cell)]']);
        for i=1:npoint_shadow

            if(i==npoint_shadow)

```



```

55         j=1;
        else
            j=i+1;
        end

60         %looking for interseption point
        %and the cells

        x_shadow1=x_cell(x_cell<max(K_vector{shadow}([i
            j]-1)*3+1)) & x_cell>min(K_vector{shadow}([i
            j]-1)*3+1));

65         if(max(K_vector{shadow}([i j]-1)*3+1)<max(x_cell)
            && max(K_vector{shadow}([i
            j]-1)*3+1))>min(x_cell))
            x_shadow1=[x_shadow1; max(K_vector{shadow}([i
            j]-1)*3+1)];
        end
        if(min(K_vector{shadow}([i j]-1)*3+1)<max(x_cell)
            && min(K_vector{shadow}([i
            j]-1)*3+1))>min(x_cell))
70         x_shadow1=[min(K_vector{shadow}([i j]-1)*3+1))
            ; x_shadow1];
        end

        y_shadow1=interp1(K_vector{shadow}([i
            j]-1)*3+1),K_vector{shadow}([i
            j]-1)*3+2),x_shadow1);
        z_shadow1=interp1(K_vector{shadow}([i
            j]-1)*3+1),K_vector{shadow}([i
            j]-1)*3+3),x_shadow1);

75         shadow1_ok=find(y_shadow1<max(y_cell) &
            y_shadow1>min(y_cell));
        x_shadow1=x_shadow1(shadow1_ok);
        y_shadow1=y_shadow1(shadow1_ok);
        z_shadow1=z_shadow1(shadow1_ok);

80         y_shadow2=y_cell(y_cell<max(K_vector{shadow}([i

```

```

j]-1)*3+2)) & y_cell>min(K_vector{shadow}([i
j]-1)*3+2));

if(max(K_vector{shadow}([i j]-1)*3+2)<max(y_cell)
& max(K_vector{shadow}([i
j]-1)*3+2))>min(y_cell))
y_shadow2=[y_shadow2; max(K_vector{shadow}([i
j]-1)*3+2)];
85 end
if(min(K_vector{shadow}([i j]-1)*3+2)<max(y_cell)
& min(K_vector{shadow}([i
j]-1)*3+2))>min(y_cell))
y_shadow2=[min(K_vector{shadow}([i j]-1)*3+2))
; y_shadow2];
end

90 x_shadow2=interp1(K_vector{shadow}([i
j]-1)*3+2),K_vector{shadow}([i
j]-1)*3+1),y_shadow2);
z_shadow2=interp1(K_vector{shadow}([i
j]-1)*3+2),K_vector{shadow}([i
j]-1)*3+3),y_shadow2);

shadow2_ok=find(x_shadow2<max(x_cell) &
x_shadow2>min(x_cell));
95 x_shadow2=x_shadow2(shadow2_ok);
y_shadow2=y_shadow2(shadow2_ok);
z_shadow2=z_shadow2(shadow2_ok);

100 x_shadow=[x_shadow1; x_shadow2];
y_shadow=[y_shadow1; y_shadow2];
z_shadow=[z_shadow1; z_shadow2];
K=[K; [x_shadow y_shadow z_shadow]];
end

105 x_shadow=[];
y_shadow=[];
z_shadow=[];

```

```

110     for x=x_cell'

        cell_ok=find(K(:,1)==x);
        y=sort(K(cell_ok,2));
        for i=1:(length(y)/2)
            y_shadow=y_cell(y_cell>y(2*i-1) &
                y_cell<y(2*i));
115         ncell=length(y_shadow);
            x_shadow=x*ones(ncell,1);

            z_shadow=zeros(ncell,1);
            K=[K; [x_shadow y_shadow z_shadow]];
120         end
    end

    K=unique(K,'rows');

125     ncell=size(R,1);
    for i=1:ncell
        %look for shadow point in each cell
        points=find(K(:,1)>=R(i,1) & K(:,1)<=R(i,10) &
            K(:,2)>=R(i,2) & K(:,2)<=R(i,11));

130         if(length(points)>=3)
            [index,shadow_area]=convhulln(K(points,[1
                2]));%calculates area
            else
                shadow_area=0;
            end
135         [index,cell_area]=convhulln([R(i,[1 4 7 10])'
            R(i,[1 4 7 10]+1)']]);
            shading_perc(shadow,i)=shadow_area/cell_area;
        end

        %plot the results
140     figure(shadow)
        cla;
        subplot(1,2,1)
        for i=1:ncell
            rectangle('Position',

```

```

[R(i,1),R(i,2),R(i,10)-R(i,1),R(i,11)-R(i,2)];
145 end
hold on
for i=1:npoint_shadow
    if(i==npoint_shadow)
        j=1;
150    else
        j=i+1;
    end
    plot(K_vector{shadow}([i
        j]-1)*3+1),K_vector{shadow}([i j]-1)*3+2),'b-');
end
155 plot(K(:,1),K(:,2),'r*')
hold off
subplot(1,2,2)
for i=1:ncell
    rectangle('Position',
        [R(i,1),R(i,2),R(i,10)-R(i,1),R(i,11)-R(i,2)]);
160 end
hold on
for i=1:ncell
    if(shading_perc(shadow,i)~=0)
        text(R(i,1),mean([R(i,2)
            R(i,8)]),sprintf('%.2f',shading_perc(shadow,i)));
165    end
end
hold off
end
end

```

Appendix D

Additional results of the proposed algorithm

This Appendix contains a part of the test run for checking the capability of the algorithm described in Chapter 6 to track the maximum power point under real operating conditions.

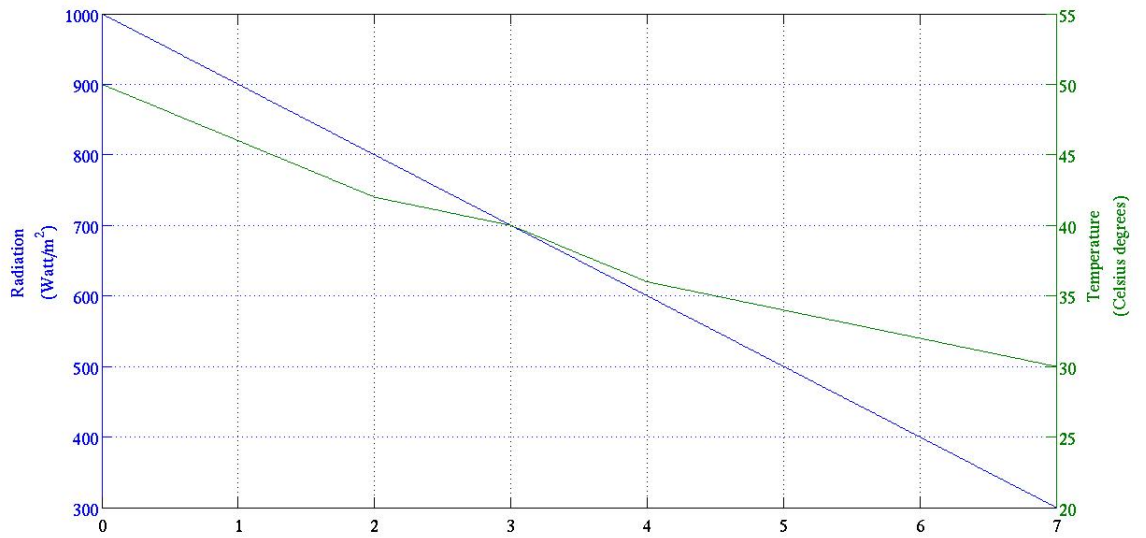
Some examples have been included in the chapter but in these pages more detailed results are presented.

The first results show the V_{mpp} and the MPP tracked by the algorithm in the case of fast irradiance changes (Fig.D.1(b) and D.2(b)). The radiation has a variation of $100 \text{ W/m}^{-2}\text{s}^{-1}$ and the temperatures vary by 3°C per second, and are in the range 30 and 50°C .

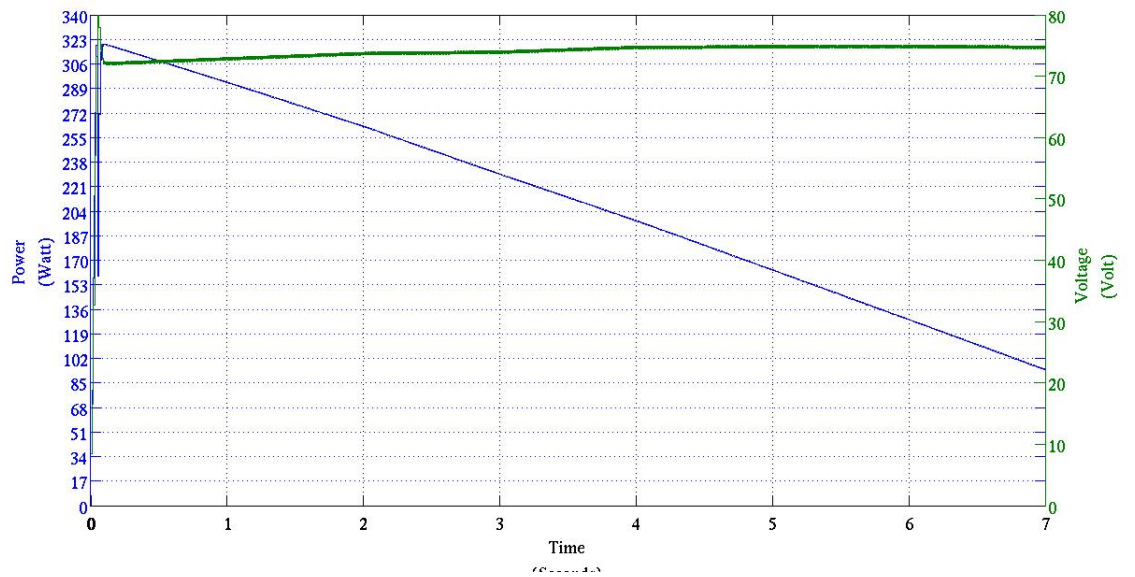
From Fig.D.3 to Fig.D.7 the response of the algorithm to different cases of partial shading is shown. Each results includes the power characteristic for the radiation and temperature simulated to check if the control algorithm is able to detect the true maximum.

The partial shading studied involved two, three and four local maxima with rapid movement of the voltage of the MPP.

The results show very good prediction of the V_{mpp} for every case; the maximum error (less than 5 Watts) concerns the case of a power characteristic with three peaks (Fig.D.5(a)) but that error represents the 2% of the MPP.

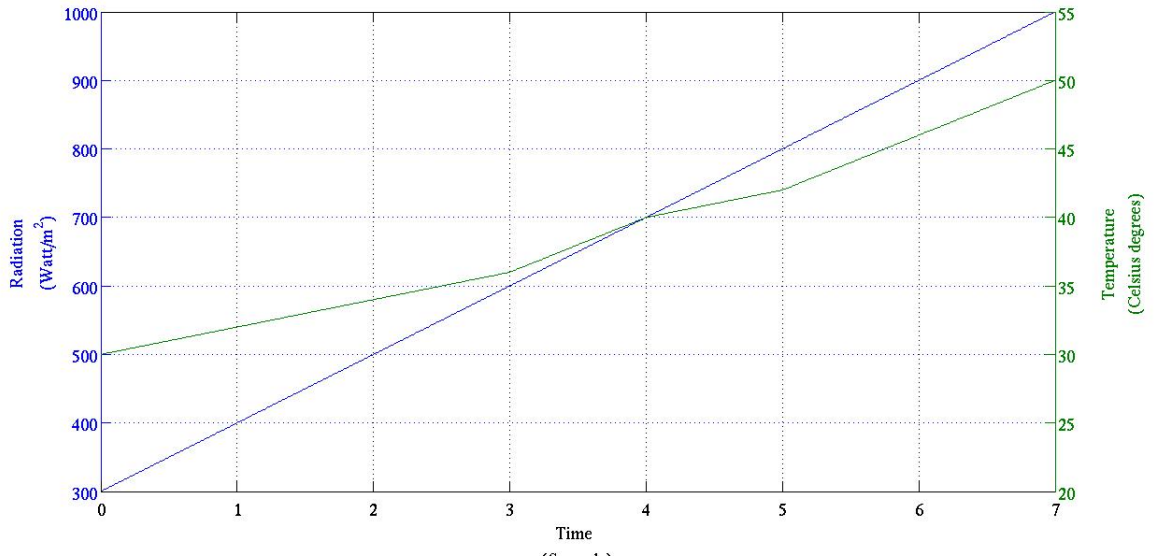


(a) Ramp down: radiation and temperature uniform for the array.

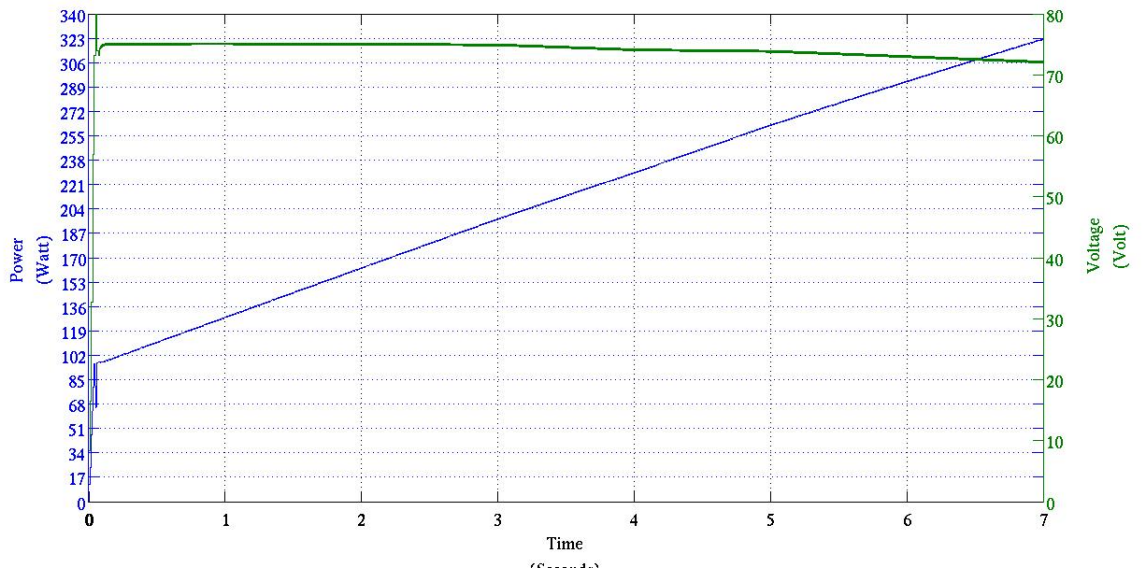


(b) Ramp down: the blue line is the output power of the PV array for the calculated operating voltage (green line) from the algorithm.

Figure D.1: Simulation of a ramp down.

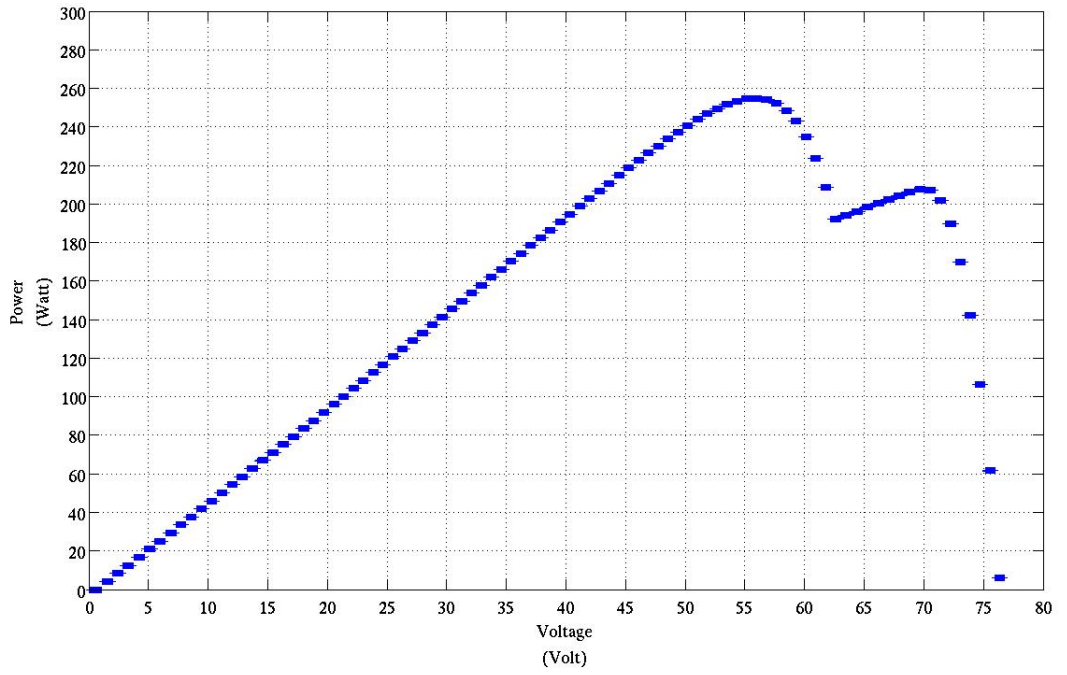


(a) Ramp up: radiation and temperature uniform for the array.

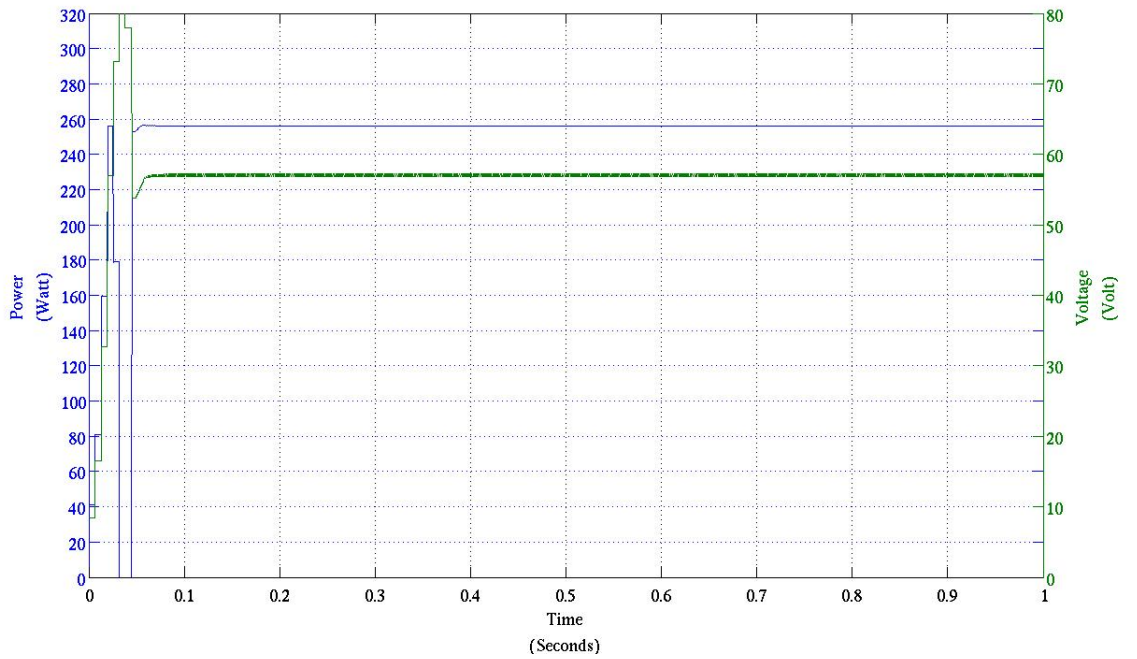


(b) Ramp up: the blue line is the output power of the PV array for the calculated operating voltage (green line) from the algorithm.

Figure D.2: Simulation of a ramp up.

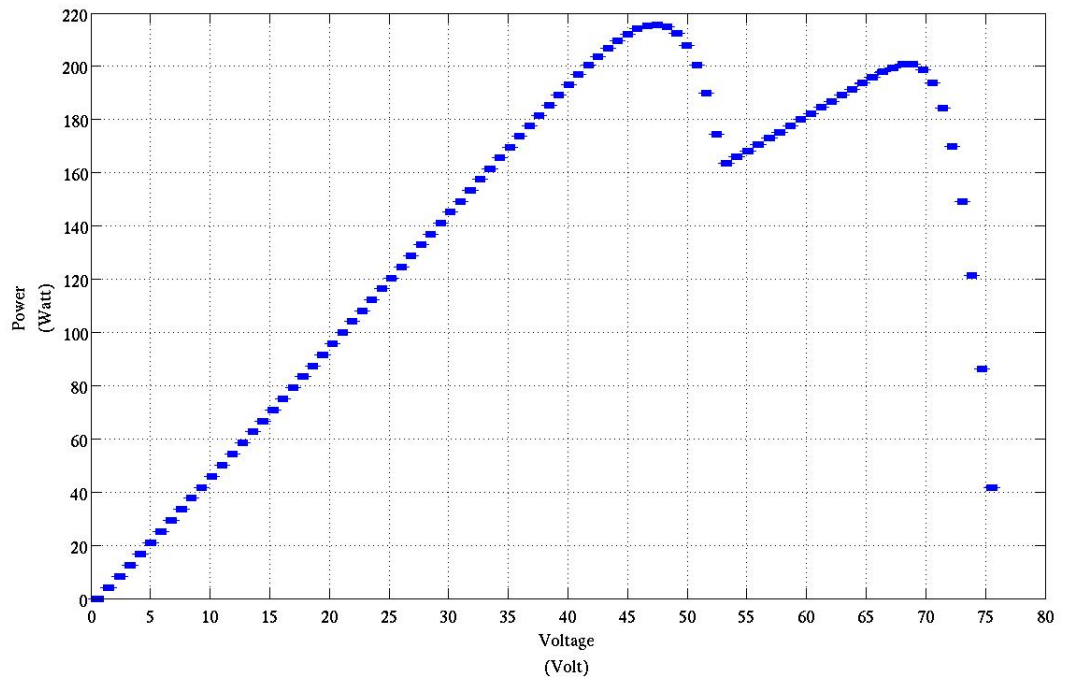


(a) Power characteristic.

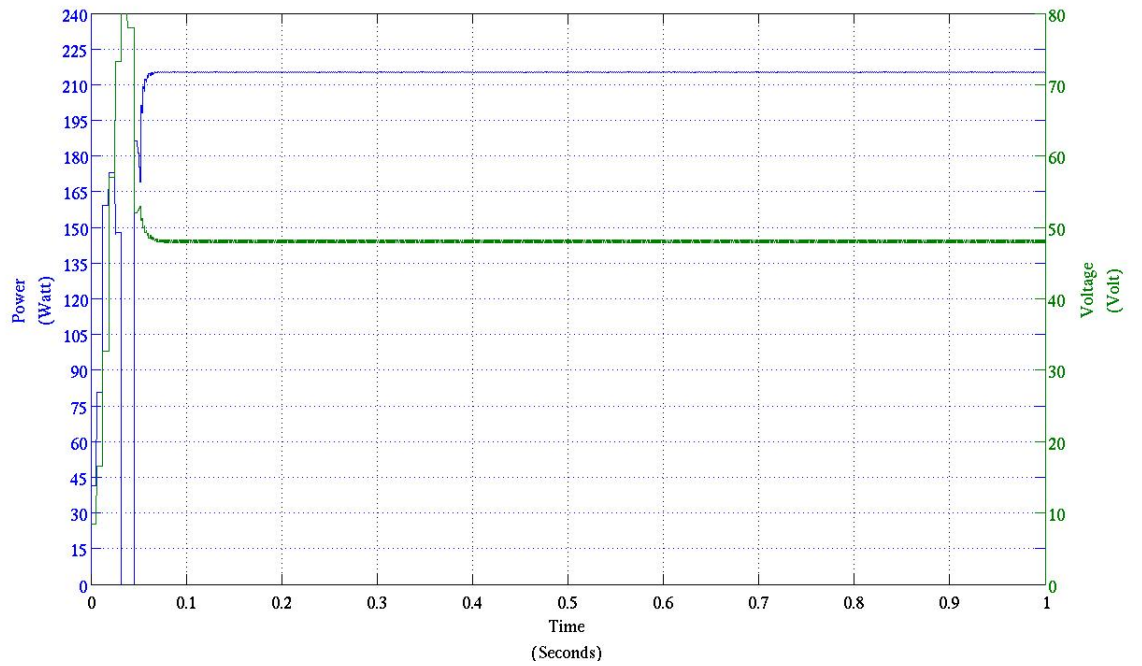


(b) The power (blue line) from the PV array for the calculated operating voltage (green line) from the algorithm.

Figure D.3: Simulation of a partial shading involving two peaks on the power characteristic.

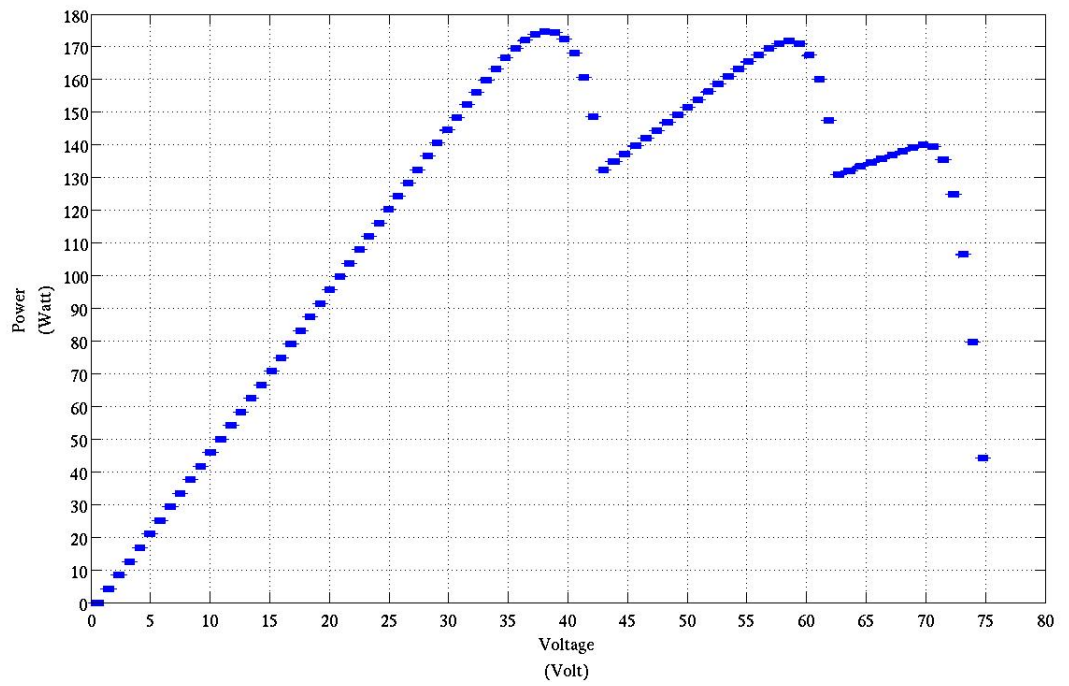


(a) Power characteristic.

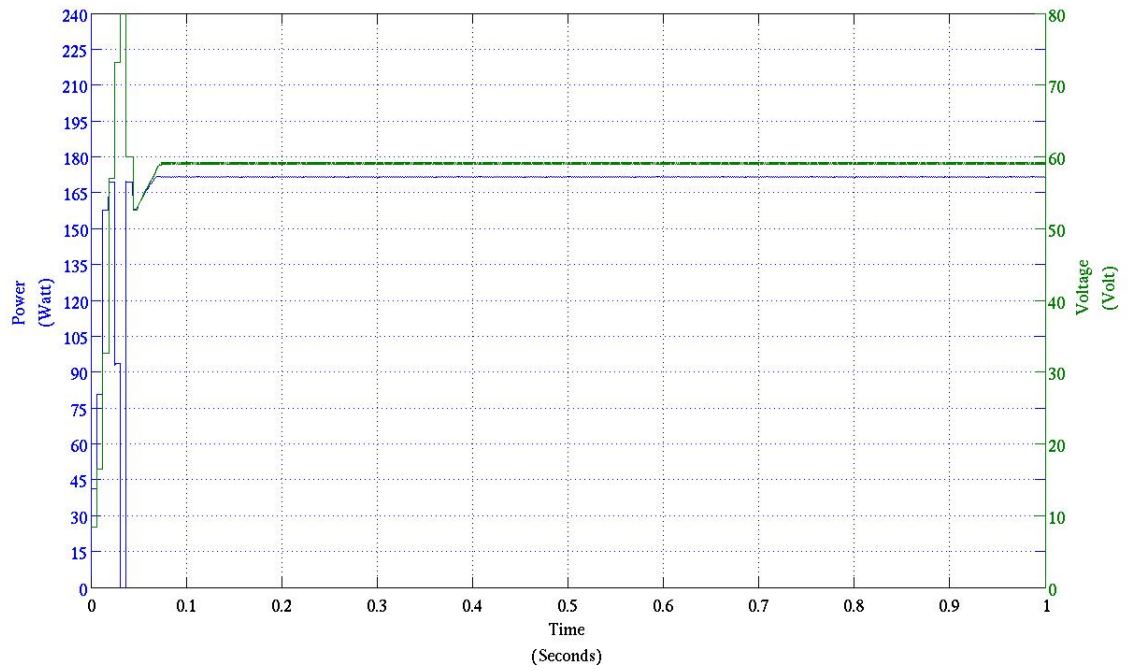


(b) The power (blue line) from the PV array for the calculated operating voltage (green line) from the algorithm.

Figure D.4: Simulation of a partial shading involving two peaks on the power characteristic.

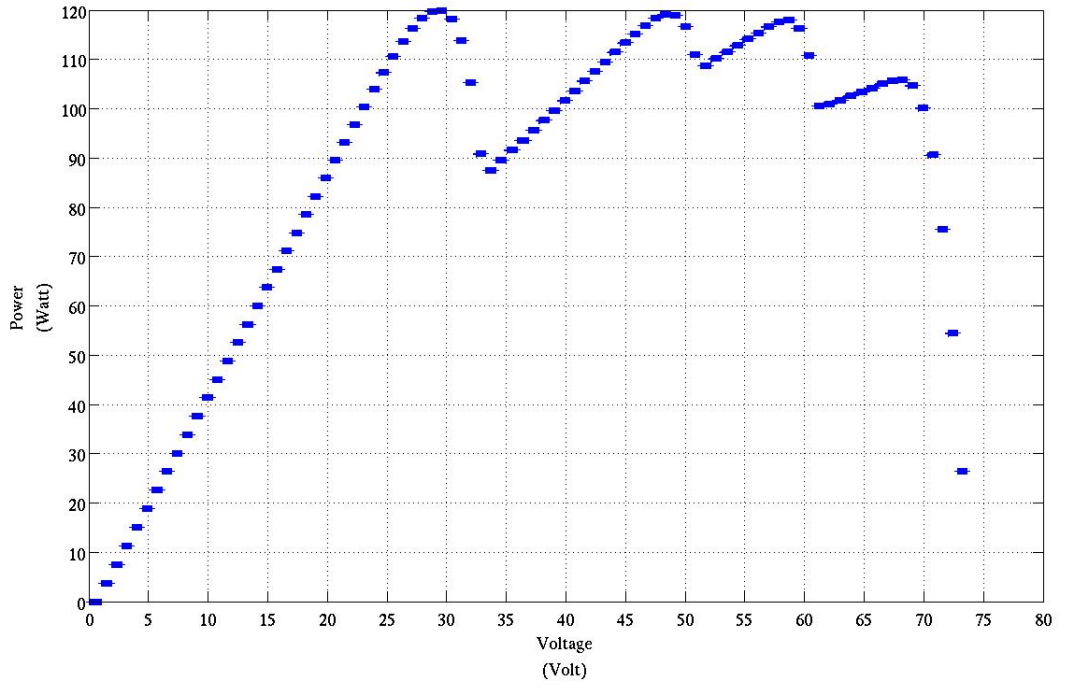


(a) Power characteristic.

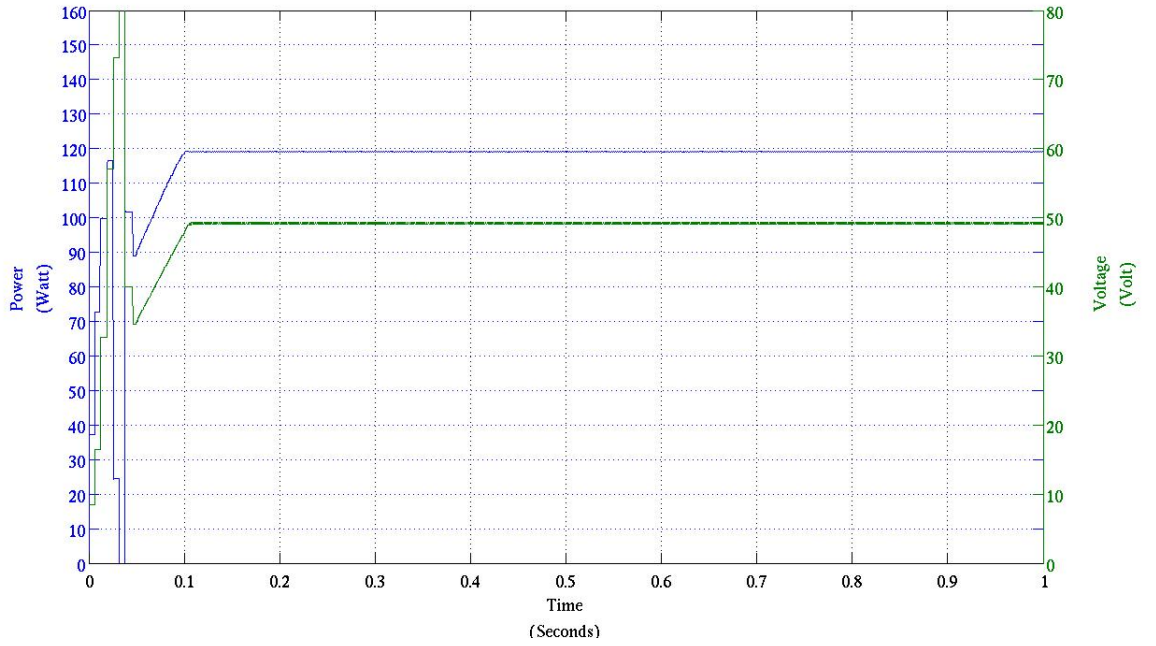


(b) The power (blue line) from the PV array for the calculated operating voltage (green line) from the algorithm.

Figure D.5: Simulation of a partial shading involving three peaks on the power characteristic.

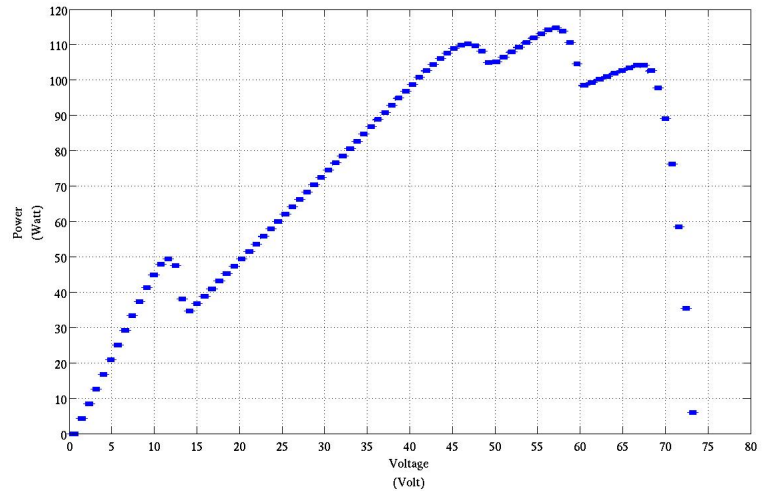


(a) Power characteristic..

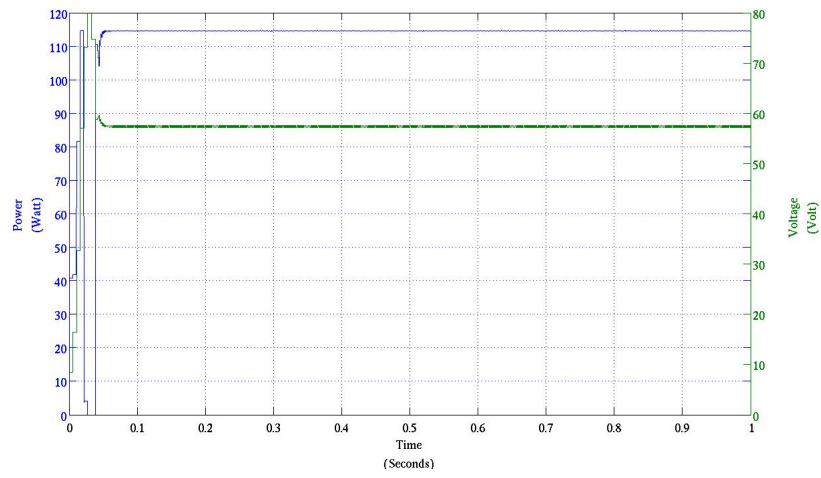


(b) The power (blue line) from the PV array for the calculated operating voltage (green line) from the algorithm.

Figure D.6: Simulation of a partial shading involving four peaks on the power characteristic.



(a) Power characteristic.



(b) The power (blue line) from the PV array for the calculated operating voltage (green line) from the algorithm.

Figure D.7: Simulation of a partial shading involving four peaks on the power characteristic.

Bibliography

- [1] A Brief Introduction to Neural Networks. *www.mathworks.co.uk*.
- [2] Hojjat Adeli and Shih-Lin Hung. *Machine learning: neural networks, genetic algorithms, and fuzzy systems*. Wiley, USA, 1995.
- [3] Al-Amoudi, A. and Zhang, L. Application of radial basis function networks for solar-array modelling and maximum power-point prediction. *Generation, Transmission and Distribution, IEE Proceedings-*, 147(5):310 –316, sep 2000.
- [4] Alonso, R. and Ibaez, P. and Martinez, V. and Roman, E. and Sanz, A. An innovative perturb, observe and check algorithm for partially shaded PV systems. In *Power Electronics and Applications, 2009. EPE '09. 13th European Conference on*, volume , pages 1 –8, sept. 2009.
- [5] Anuja, S.K. and Satheesh Kumar, R. A High Efficient DC-DC Converter with Soft Switching for Stress Reduction. *IJCA Proceedings on International Conference on VLSI, Communications and Instrumentation (ICVCI)*, (9):19–24, 2011. Published by Foundation of Computer Science.
- [6] apps1.eere.energy.gov/buildings/energyplus/.
- [7] Bianchini, M. and Frascioni, P. and Gori, M. Learning without local minima in radial basis function networks. *Neural Networks, IEEE Transactions on*, 6(3):749 –756, may 1995.
- [8] J. W. Bishop. Computer Simulation of the Effects of Electrical Mismatches in Photovoltaic Cell Interconnection Circuits. *Solar Cells*, 25:73–89, 1988.
- [9] Luis Castañer and Santiago Silvestre. *Modelling photovoltaic system using PSpice*. Wiley, England, first edition, 2002.
- [10] Alexis de Medeiros Torres, Fernando L. M. Antunes, and Fernando Soares dos Reis. An artificial neural network-based real time maximum power tracking controller for connecting a pv system to the grid. *Industrial*

Electronics Society, IECON '98. Proceedings of the 24th Annual Conference of the IEEE, 4:554–558, 1998.

- [11] C. Deline. Partially shaded operation of a grid-tied pv system. *34th IEEE Photovoltaic Specialist Conference Philadelphia*, 2009.
- [12] Howard Demuth and Mark Beale. *Neural Network Toolbox for use with MATLAB*. MathWorks Inc, England, fourth edition, 2000.
- [13] Maria Carla Di Vincenzo and Prof. David Infield. Maximum power point analysis for partially shaded arrays. *7th Photovoltaic Science Application and Technology*, 2011.
- [14] Maria Carla Di Vincenzo and Prof. David Infield. Artificial Neural Network for real time modelling of photovoltaic system under partial shading. *2nd IEEE International Conference on Sustainable Energy Technology*, 2010.
- [15] John A. Duffie and William A. Beckman. *Solar Engineering of Thermal Processes*. John Wiley, third edition, 2006.
- [16] Trishan Eswam and Patrick L. Chapman. Comparison of photovoltaic array maximum power point tracking techniques. *IEEE Transactions on Energy Conversion*, 22:439–449, June 2007.
- [17] N. Femia, G. Petrone, G. Spagnuolo, and M. Vitelli. Perturb and observe MPPT technique robustness improved. In *Industrial Electronics, 2004 IEEE International Symposium on*, volume 2, pages 845 – 850, may 2004.
- [18] Martin K. Fuentes. A Simplified Thermal Model for Flat-Plate Photovoltaic Arrays. *Sandia National Laboratories report*, 1987.
- [19] Garg, H.P. and Prakash, J. *Solar Energy fundamentals and applications*. Tata McGraw-Hill, India, first edition, 2006.
- [20] Adolf Goetzberger and Valker U. Hoffman. *Photovoltaic Solar Energy Generation*. Springer, Germany, first edition, 2005.
- [21] Volker Hanitsch and Rolf Quaschnig. Shade Calculations in Photovoltaic Systems. *ISES Solar World Conference*, 1995.
- [22] W. Herrmann, W. Wiesner, and W. Vaaßen. Hot Spot Investigations on PV Modules - New Concepts for a Test Standard and Consequences Module Design with Respect to Bypass Diode. *Photovoltaic Specialists, Conference Record of the Twenty-Sixth IEEE*, 1997.

- [23] T. Hiyama and K. Kitabayashi. Neural network based estimation of maximum power generation from pv module using environmental information. *Energy Conversion, IEEE Transactions on*, 12(3):241 –247, sep 1997.
- [24] Hiyama, T. and Kouzuma, S. and Imakubo, T. and Ortmeyer, T.H. Evaluation of neural network based real time maximum power tracking controller for PV system. *Energy Conversion, IEEE Transactions on*, 10(3):543 –548, sep 1995.
- [25] A. Hovinen. Fitting of the solar cell IV-curve to the two diode model. *Physica Scripta*, 1994:175, May 1994.
- [26] <http://www.globalwarmingart.com>.
- [27] Huang, Keya and Li, Wenshi and Huang, Xiaoyang. MPPT of Solar Energy Generating System with Fuzzy Control and Artificial Neural Network. In *Information Technology, Computer Engineering and Management Sciences (ICM), 2011 International Conference on*, volume 1, pages 230 –233, sept. 2011.
- [28] Y.H. Ji, H. Park, J.G. Kim, and C.Y. Won. C-language Based PV array simulation technique considering effects of the partial shading. *IEEE IC on Industrial technology*, 2009.
- [29] A. D. Jones and C.P. Underwood. A thermal model for photovoltaic systems. *Solar Energy*, 70(4), 2000.
- [30] E.R. Kandel, J.H. Schwartz, and T.M Jessell. *Principles of Neural Science*. Appleton & Lange, Norwalk, third edition, 1996.
- [31] Min-Huei Kim, M.Goday Simões, and Bimal K.Bose. Neural Network-based estimation of power electronic waveform. *IEEE transaction power electronics*, 11, 1996.
- [32] D. L. King, W. E. Boyson, and J. A. Kratochvil. Photovoltaic Array Performance Model. *Sandia National Laboratories*, 2004.
- [33] Søren Bækhoj Kjær. *Design and Control of an Inverter for Photovoltaic Applications*. PhD thesis, Aalborg University, May 2005.
- [34] David Kriesel. A Brief Introduction to Neural Networks. *www.dkriesel.com*, 2005.

- [35] Zhihong Lin, Xiaokang Huang, and W.B. Berry. Temperature dependence on the energy band gap selection in two cell, for terminal tandem solar cell design. *Photovoltaic Specialists Conference IEEE*, 1991.
- [36] Stefan Marko and Ivan Darul'a. Large Scale Integration of Renewable Electricity Production into the Grids. *Journal of ELECTRICAL ENGINEERING*, 58:58–60, 2007.
- [37] Par T. Markvart and Luis Castañer. *Practical Handbook of Photovoltaics: Fundamentals and Applications*. Elsevier, England, first edition, 2003.
- [38] Martin A. Green. *Solar cells: operating principles, technology, and system applications*. Englewood Cliffs, NJ: Prentice-Hall, UK, first edition, 1998.
- [39] Mashaly, H.M. and Sharaf, A.M. and Mansour, M. and El-Sattar, A.A. A photovoltaic maximum power tracking using neural networks. In *Control Applications, 1994., Proceedings of the Third IEEE Conference on*, volume , pages 167 –172 vol.1, aug 1994.
- [40] Daniel R. Matroni. Photovoltaic System Acceptability in the Future. Technical report, WORCESTER POLYTECHNIC INSTITUTE, May 2011.
- [41] Robert W. Miles, Guillaume Zoppi, and Ian Forbes. Inorganic photovoltaic cells. *Materials today*, 10(11), 2007.
- [42] Ned Mohan, Tore M. Undeland, and Williams P.Robbins. *Power Electronics: Converters, Applications, and Design*. John Wiley&Sons, USA, third edition, 2003.
- [43] National Center for Photovoltaics (NCPV) and National Renewable Energy Laboratory's (NREL's). Archive for July–December 2007, 2007.
- [44] Jenny Nelson. *The Physics of Solar Cells*. Imperial College Press, England, first edition, 2003.
- [45] Volker Quaschnining and Rolf Hanitsch. Influence of shading on electrical parameters of solar cells. *Photovoltaic Specialists Conference, Conference Record of the Twenty Fifth IEEE*, page 1287, May 1996.
- [46] R. Ramaprabha and B.L. Mathur. Intelligent Controller based Maximum Power Point Tracking for Solar PV System. *International Journal of Computer Applications*, 12:37–41, January 2011.

- [47] Ramaprabha, R. and Gothandaraman, V. and Kanimozhi, K. and Divya, R. and Mathur, B.L. Maximum power point tracking using GA-optimized artificial neural network for Solar PV system. In *Electrical Energy Systems (ICEES), 2011 1st International Conference on*, volume , pages 264 –268, jan. 2011.
- [48] S.H. Raushenbach. Electrical output of shadowed solar arrays. *IEEE Transactions on Electron Devices*, 18:483–490, 1971.
- [49] Fritz Schimpf and Lars E. Norum. Grid connected Converters for Photovoltaic, State of the Art, Ideas for Improvement of Transformerless Inverters. *Nordic Workshop on Power and Industrial Electronics*, 1:6, 2008.
- [50] L. ShashuaBar, M.E. Hoffman, and Y. Tzimir. Integrated thermal effects of generic built forms and vegetation on the UCL microclimate. *Building and Environmental*, 2006.
- [51] Chunping Song. Optimizing accurancy of hysteretic control. *Journal of Power Electronics Technology*, 2006.
- [52] Syafaruddin, Takashi Hiyama, and Engin Karetepe. Polar coordinated fuzzy controller based real-time maximum-power point control of photovoltaic system. *IET Renewable Power Generation*, 34:2597–2606, 2009.
- [53] R.J. Van Overstraeten and R.P. Mertens. *Physics Technology and Use of Photovoltaics*. Adam Hilgher, 1986.
- [54] Julie Vesz. Assessment of Photovoltaic Modules Under Real Operating Conditions. *Rapport de Stage de 4eme anee*, 2008.
- [55] Chen Wenying, Lin Yongjun, Liu Weiliang, and Liu Shuang sai. Polar coordinated fuzzy controller based real-time maximum-power point control of photovoltaic system. *Advanced Materials Research*, 34:2597–2606, 2009.
- [56] Chen Wenying, Lin Yongjun, Liu Weiliang, and Liu Shuang sai. Research on MPPT of PV Systems Based on BP Neural Network. *Advanced Materials Research*, 466-467:2597–2606, 2012.
- [57] Martin Wolf and Hans Rauschenbacht. *Series resistance effect on solar cell measurements*. Pergamon Press, Great Britain, first edition, 1963.
- [58] Xuanzhi Wu. High-efficiency polycrystalline CdTe thin-film solar cells. *Solar Energy*, 77:803–814, 2004.

- [59] Yu-En Wu, Chih-Lung Shen, and Chia-Yu Wu. Research and improvement of maximum power point tracking for photovoltaic systems. In *Power Electronics and Drive Systems, 2009. PEDS 2009. International Conference on*, volume , pages 1308 –1312, nov. 2009.
- [60] P. Würfel. *Physics of Solar Cells: From Principles to New Concepts*. Wiley-WCH, 2005.
- [61] www.cadence.com/products/orcad/.
- [62] www.eko-usa.com.
- [63] www.ni.com/white-paper/3068/en.
- [64] www.pveducation.org.
- [65] Miro Zeman. Solar Cells. Technical report, Delft University of Technology, 2005.
- [66] Hank Zumbahlen. *Linear Circuit Design Handbook*. Elsevier, USA, first edition, 2008.